THE UNIVERSITY OF MANITOBA

NUCLEAR MAGNETIC RESONANCE IN THE HIGHLY ANISOTROPIC RARE EARTH-Co_5 COMPOUNDS

by

HENRY P. KUNKEL

A THESIS

SUBMITTED TO THE FACULTY OF GRADUATE STUDIES

IN PARTIAL FULFILLMENT OF THE REQUIREMENTS FOR THE DEGREE

OF DOCTOR OF PHILOSOPHY

DEPARTMENT OF PHYSICS

WINNIPEG, MANITOBA

NOVEMBER, 1984

NUCLEAR MAGNETIC RESONANCE IN THE HIGHLY ANISOTROPIC RARE EARTH-Co_5 COMPOUNDS

BY

HENRY P. KUNKEL

A thesis submitted to the Faculty of Graduate Studies of the University of Manitoba in partial fulfillment of the requirements of the degree of

DOCTOR OF PHILOSOPHY

Acknowledgement

I wish to thank my supervisor Dr. C. W. Searle for the guidance and support given to me during the course of this project. I would also like to thank the other members of the magnetic resonance group, Dr. J. Davis, Dr. S. Kupka and Dr. I. Maartense for their helpful suggestions and comments. I also wish to acknowledge the many other members of the Physics department, both fellow graduate students and staff members, for the useful discussions and for the encouragement which made the completion of this thesis possible.

November 20,1984

TABLE of CONTENTS

		page
table of contents		i
abstract		iii
Chapter 1	Introduction	1
CHAPTER 2	Magnetic Properties of the Rare-Earth-Transition Metal Intermetallic Compounds	8
2.1	Introduction	8
2.2	Magnetic Coupling in the Rare Earth-Transition Metal Compounds	14
2.3	The Rare Earth Compounds with Ni and Co	25
2.4	The Nature of the Co Moment in the Rare Earth-Cobalt Compounds	32
2.5	Magnetic Ordering in the Ni and Co Compounds	38
2.6	The Rare Earth-Iron Compounds	40
2.7	The Structure of the Rare Earth-Cobalt Compounds	41
CHAPTER 3	Principles of Nuclear Magnetic Resonance	48
3.1	Introduction	48
3.2	The Basic Principles of NMR	51
3.2.1	The Quantum Mechanical Picture of Nuclear Magnetic Resonance	52
3.2.2	Classical View of Nuclear Magnetic Resonance	55
3.3	Pulse Methods	61
3.3.1	Free Induction Decay	62
3.3.2	Double Pulse Methods	64
3.3.3	Measurement of T_1	65
3.3.4	The Formation of Spin Echoes	66
3.3.5	Multiple Pulse Methods	67
CHAPTER 4	Nuclear Resonance in Ferromagnetic Materials	70
4.1	Introduction	70
4.2	The Observation of NMR in Magnetically Ordered Materials	73
4.3	Domain Wall Enhanced Nuclear Magnetic Resonance	78
4.4	Enhancement in Pulse NMR Experiments	81
4.5	The Distortion of Lineshapes due to the	

	Enhancement Effect	83
4.6	NMR Spectra in Ordered Magnetic Materials with an Anisotropic Hyperfine Field	85
4.7	The M-M Model for the Domain Wall Composite Lineshape	93
CHAPTER 5	Experimental Procedure and Results	99
5.1	Introduction	99
5.2	Experimental Apparatus	102
5.3	Additional Experimental Considerations	107
5.4	Sample Preparation	114
5.5	Preliminary Experimental Results	118
5.6	The External Modulation of the Spin-Echo Decay Envelope	121
5.7	Origin of the Spin-Echo Modulation Effect - The Longitudinal Enhancement Mechanism	138
5.8	Experimental Identification of Domain-Wall-Centre and Domain-Wall-Edge NMR Resonances in Magnetically Ordered Materials	146
5.9	Experimental Results for the RCo_5 Compounds	159
5.10	The Observation of Quadrupole Splitting Effects and its Correlation with the Longitudinal Enhancement Measurements	174
CHAPTER 6	Discussion	185
6.1	Introduction	185
6.2	The Basic Principles of the Analysis	193
6.3	The Calculation of the Modulation Spectrum and the Identification of NMR Resonance Peaks	197
6.4	Calculation of the Effect of a Perpendicular Magnetic Field on the Echo Amplitude	216
6.5	The Discrete-Wall Model and the Hyperfine Field Distribution within the Domain Wall	229
6.6	The Nature of the "Anomalously" large Longitudinal Enhancement Factor	240
6.7	The Relationship between the Magnetocrystalline Anisotropy and the Anisotropy in the Hyperfine Field	253
6.8	The Absolute Intensity of the Co^{59} Resonances	272
CHAPTER 7	Conclusion	276
References		281

ABSTRACT

The NMR spectra of magnetic materials containing domain walls and having a large anisotropy in the hyperfine field show two NMR peaks arising from a single site; one peak arising from nuclei located at the domain wall centre and the other peak arising from nuclei located at the domain wall edge. The identification of the origin of the observed peaks therefore gives a simple measurement of the total anisotropy in the hyperfine field. Techniques have been developed to identify the nature of the various peaks observed in the Co^{59} NMR resonances in the RCo_5 compounds.

The modulation of the spin echo decay envelope by an external a.c. field has been observed. An enhancement of the external longitudinal modulating field resulting from the anisotropy in the hyperfine field has been identified. This is analogous to the enhancement of a transverse r.f. field by the isotropic hyperfine field which is characteristic of NMR in ferromagnetic materials. The observation of quadrupole splitting effects has been correlated with the rate of change of the hyperfine field in the domain wall as measured by the modulation experiment.

The orbital contribution to the anisotropy in the hyperfine field consists of two contributions; one arising from the anisotropy in the crystal field and the other from an anisotropy in the spin-orbit interaction. A phenomenological model is presented which can consistently account for the data available on the anisotropy in the

hyperfine field, the anisotropy in the magnetization and the magnetocrystalline anisotropy. The correlation between the anisotropy in the hyperfine field and the magnetocrystalline anisotropy represents an interesting new procedure for the study of the magnetocrystalline anisotropy and would therefore be of particular use in the fabrication of improved permanent magnetic materials.

Chapter 1

Introduction

The development of the RCo_5 type of permanent magnet material began in 1935 with the discovery by Urbain, Weiss and Trombe of the ferromagnetism of gadolinium (1). Studies of the other elements in the lanthanide series of rare earth metals followed but the unavailability of pure rare earth metals made the progress extremely slow.

As a result of the need to know more about the rare earth metals for the Atomic Energy Development Program, methods were developed to produce them in quantity and this stimulated the study of the rare earth metals in solid solution. Nesbitt, Wernick and Corenzwit (2) first published data on the saturation magnetization of the iron-gadolinium and cobalt-gadolinium systems in 1959. In 1960 Hubband, Adams and Gilfrich (3), working with the $GdCo_5$ compound, recognized the relationship between a large magnetocrystalline anisotropy and a large coercivity, determined that the easy axis of magnetization was parallel to the hexagonal axis and used particle alignment to increase the magnetization. In 1966 Hoffer and Strnat (4) reported the extremely large magnetocrystalline anisotropy of YCo_5 and extensive studies of the series of RCo_5 compounds containing Y, Sm, Ce, La, Nd, Pr and a commercial mixture of the rare earth metals known as mischmetal (MM) followed. Out of these studies developed a series of permanent magnetic

alloys possessing both a high remanent magnetization and a high coercivity. This is illustrated in Fig. 1.1 where the demagnetization curves of several RCo_5 compounds is shown along with several other common magnetic materials for comparison.

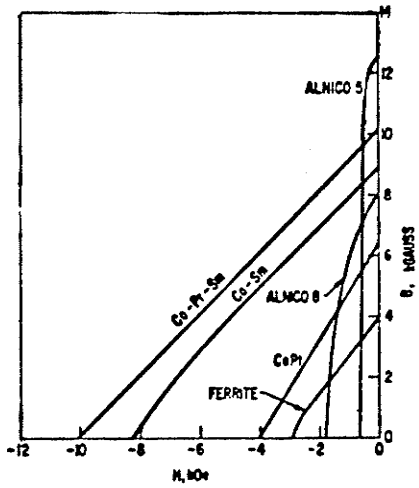

Fig. 1.1 Comparison of the demagnetization curves of two rare-earth-Co alloys with several commercial magnets.

Magnetocrystalline anisotropy is the tendency for the magnetization to lie along certain crystallographic directions. The existance of crystalline anisotropy can be demonstrated experimentally by examining the magnetization curves of a single crystal. The magnetization curve represents the component of the magnetization in the direction of the applied field plotted as a function of field. It is apparent that smaller fields are required to magnetize the crystal along certain directions than along other directions. These are referred to as the easy and hard directions respectively.

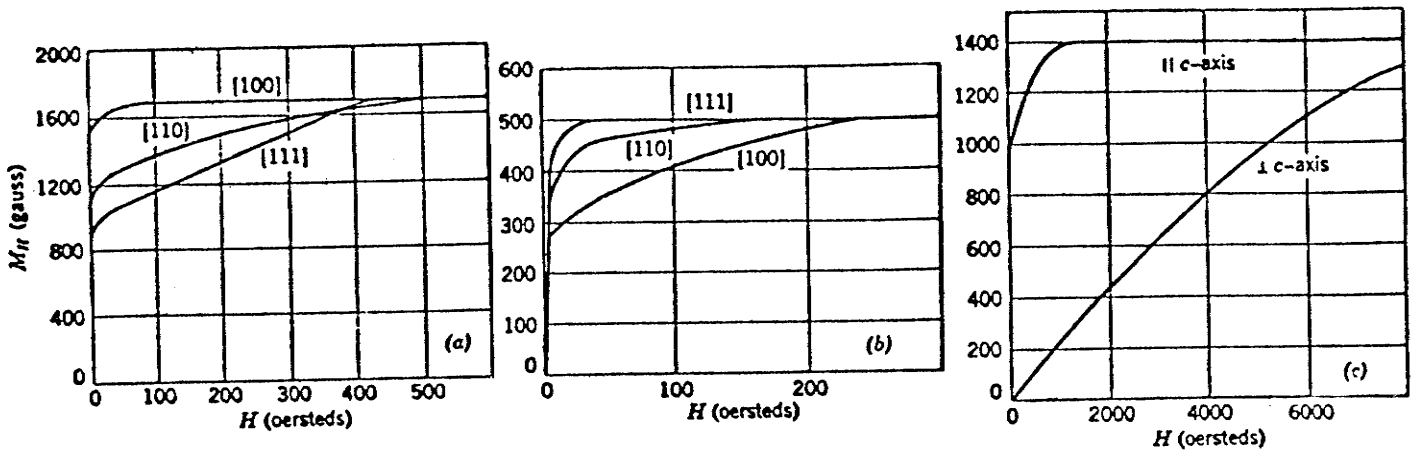

Fig. 1.2 Magnetization curves of single crystals of (a) iron, (b) nickel and (c) cobalt with the applied fields along the directions indicated (Ref. 5).

The crystalline anisotropy energy is defined as the work required to make the magnetization lie along a certain direction relative to the easy direction. The anisotropy energy is usually written in a power series of trigonometric functions of the angles the magnetization vector makes with respect to the crystal axes. For a cubic material such as iron the anisotropy energy is given by

$$E = K_1 \{\alpha_1^2 \alpha_2^2 + \alpha_2^2 \alpha_3^2 + \alpha_3^2 \alpha_1^2\} + K_2 \alpha_1^2 \alpha_2^2 \alpha_3^2 + \qquad (1.1)$$

where the α's are the direction cosines between the direction of magnetization and the cubic edges and the K_i are the anisotropy constants of degree i. For an hexagonal lattice such as cobalt the easy direction is the hexagonal c-axis and the anisotropy energy may be written as

$$E = K_1 \sin^2\theta + K_2 \sin^4\theta \qquad (1.2)$$

where θ is the angle between the direction of magnetization and the c-axis. The easy direction is determined by the values of the anisotropy constants K_1 and K_2.

If $K_1 > 0$ easy axis

$K_1 < 0$ and $K_1 > -2K_2$ easy cone

$K_1 < 0$ and $K_1 < -2K_2$ easy plane

The magnetocrystalline anisotropy of the RCo_5 compounds is determined by a contribution from the cobalt sublattice and by a contribution from the rare earth sublattice. At high temperatures the measured values of K_1 are positive and have comparable values for all compounds, including the compounds YCo_5, $LaCo_5$ and $CeCo_5$ which possess no rare earth magnetic moment, and therefore it is likely that the major contribution to K_1 is from the Co sublattice. At low temperatures the K_1 values are different for various RCo_5 compounds not only in magnitude but also in sign. The easy axis (c-axis) is kept for some compounds such as $SmCo_5$, $GdCo_5$ and $ErCo_5$ but a transition takes place to a cone of easy axes ($PrCo_5$ and $HoCo_5$) or to an easy plane ($NdCo_5$, $TbCo_5$, $DyCo_5$).

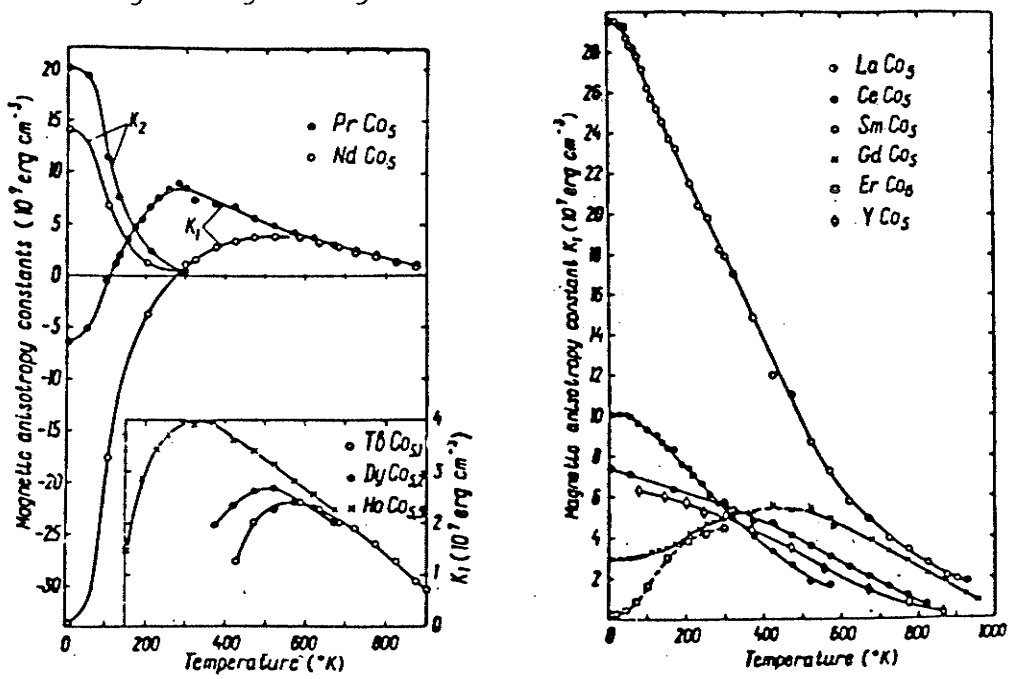

Fig. 1.3 Temperature dependence of the anisotropy constants of the RCo_5 compounds (Ref. 6).

Table 1.1 shows selected magnetic properties of some RCo_5 compounds.

TABLE 1.1

RCo_5	M_s (kG)	T_c ^oC	Density (g/cm^3)	K_1 10^7 ergs/cm^3	H_A (kOe)
YCo_5	10.6	923	7.60	5.5	130
$LaCo_5$	9.1	843	8.03	6.3	175
$CeCo_5$	7.7	648	8.56	5.2	170
$PrCo_5$	12.0	883	8.33	6.9	145
$NdCo_5$	12.3	903	8.39		
$SmCo_5$	10.7	998	8.60	11.2	290
$GdCo_5$	3.6	1008	8.86		270

For a ferromagnetic material to be useful as a permanent magnetic material it, first of all, must have a high spontaneous magnetization, M_s, at room temperature so that it can produce a remanent flux of useful magnitude. The theoretical upper limit of the energy product, $(BH)_{max}$ is given by $4\pi^2 M_s^2$ in cgs units and is therefore determined by M_s. A second requirement, which actually follows from the first, is for a high Curie temperature. Finally a large intrinsic coercive force is needed. Such high coercive forces are expected of a material with a very large magnetocrystalline anisotropy, ideally with a single easy axis. When such an anisotropy exists, a high coercive force can be obtained whether the material is used in the form of single-domain particles or whether domain walls are present and the important reversal process is wall motion or domain nucleation (7,8). Figure 1.4 shows schematic hysteresis loops for both a low and a high

coercivity material as well as the hysteresis loop for a single domain particle.

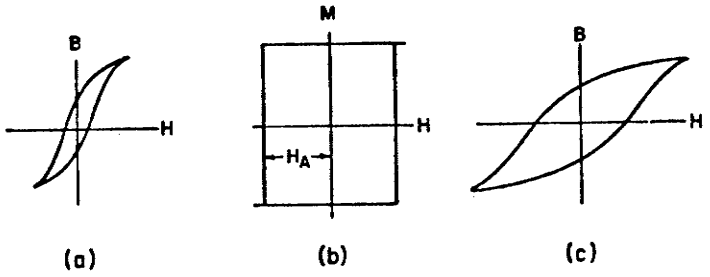

Fig. 1.4 Schematic hysteresis loops for (a) a low coercivity material, (b) a spherical single domain particle and (c) a high coercivity material.

The relationship between the coercive force and the wall energy and therefore K_1 is an important aspect of the magnetization reversal in the RCo_5 compounds and is one of the principle motivations behind this investigation. More information is needed on the dependence of K_1 on deviations from stoichiometry and the result of both magnetic and non-magnetic substitutions. Some macroscopic studies have been reported on single crystals and these will be referred to in chapter six. The general approach that has been taken for these materials is to assume that the Co sub-lattice contribution to K_1 is constant throughout the series and is given by K_1 for YCo_5. The difference between this value and the value for another member of the RCo_5 series was then attributed to the rare earth sub-lattice. However, of much greater interest would be a microscopic examination of this problem since a microscopic understanding of the origin of the magneto-crystalline anisotropy and the effects of composition would not only be of fundamental interest but also would lead to a much more precise procedure for preparing high quality permanent magnetic materials. Neutron diffraction, the Mossbauer effect and NMR are possible techniques that might be used to obtain microscopic information

on these systems. The particular technique that we have used is spin-echo NMR which has certain advantages, which will be described later, over the other two techniques.

Before a microscopic experimental study can be carried out the necessary experimental techniques will have to be developed. Also we will have to determine which experimental parameter we can use to best measure the microscopic contribution of the Co sub-lattice to the magnetocrystalline anisotropy and then the analytical techniques will have to be developed to interpret the experimental results.

The two quantities which were considered were the signal intensity and the anisotropy in the hyperfine field at the Co^{59} sites. Because of the large number of factors that are involved in determining the signal intensity and the generally small strength of the observed signals it was decided that the anisotropy in the hyperfine field was the most appropriate parameter to study. An important advantage to using domain wall NMR is that it allows one to sample the hyperfine field as a function of angle without the application of an external field.

Before we present our experimental results, however, we will present a general discussion of the magnetic properties of the rare earth intermetallic compounds in chapter two, introduce the general principles of NMR and in particular spin-echo NMR in chapter three and review the present state of NMR in ferromagnetic materials with domain walls in chapter four.

CHAPTER 2

Magnetic Properties of the Rare-Earth-Transition Metal Intermetallic Compounds

2.1 Introduction

Magnetic ordering exists in a large number of the rare-earth intermetallic compounds, at least over some temperature range. In the compounds that include a non-magnetic element such as aluminum, zinc and copper, the Curie temperatures are usually low, i.e. less than 100^{o} K which indicates that the exchange interactions between rare-earth atoms is small. When the other component of the compound is magnetic, such as the 3d transition elements Fe and Co, the magnetic ordering temperature can become quite large, and it is necessary to consider also the exchange interactions between the transition metal atoms and between the transition metal and rare-earth atoms.

Due to the small spatial extent of the 4f wave function, there is very little overlap of the wave functions between neighbours and the magnetic interaction between the ions must arise from an indirect exchange involving the polarization of the conduction electrons. This mechanism is referred to as the Ruderman-Kittel-Kasuya-Yoshida (RKKY) interaction. The mechanism was initially conceived by Ruderman and Kittel (1) in order to explain NMR (Knight shift) results obtained for metallic Cu-Mn alloys. A short time later Kasuya (2) noted that direct exchange was an inadequate coupling mechanism for gadolinium and suggested that the Ruderman-Kittel proposal was capable of describing

the interaction. The exchange interaction between the localized 4f electrons and the itinerant conduction electrons produces an imbalance in the net spin density which is maximum in the vicinity of the magnetic ion and decreases in an oscillatory manner as the distance from the magnetic ion increases. The spin polarization can be appreciable at distances of ten or more times the radius of the 4f shell and therefore the interaction is of long range. The oscillatory character of the spin polarization also implies that both parallel and anti-parallel coupling is possible between the localized moments.

The interaction between the spins of the conduction electrons and the localized electrons is given by the Hamiltonian

$$H = -J_e \, S_1 \cdot S_c \tag{2.1}$$

where J_e is the effective exchange integral. A second order perturbation calculation (1-3) gives the following expression for the net spin density, ρ.

$$\rho = -[9\pi z^2 J_e S_1 / 4E_F] F(x) \tag{2.2}$$

where z is the number of conduction electrons per atom, E_f is the Fermi energy, and

$$F(x) = x^{-4}(x \cos x - \sin x) \tag{2.3}$$

Here $x = 2k_f r$ and k_f is the radius of the Fermi sphere and r is the distance from the magnetic ion. Figure 2.1 illustrates the variation of the spin density with distance from the magnetic ion for the case $J_e < 0$. A second magnetic ion with $J_e < 0$ will experience positive coupling (ferromagnetic alignment) if it is at a distance at which the spin density is negative, i.e. at positions N_2 and N_4 in Fig. 2.1. Negative or anti-ferromagnetic coupling will result if the interionic

distance corresponds to a positive spin density (positions N_1 and N_3).

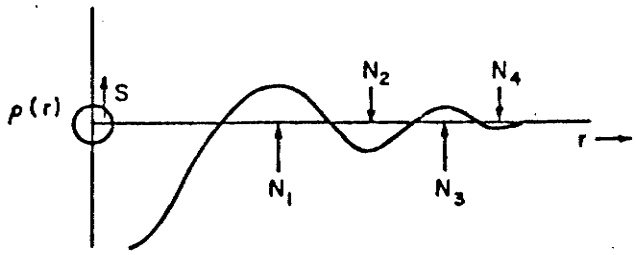

Fig. 2.1 Spin density, $\rho(r)$, versus distance from the magnetic ion for the case $J_e < 0$.

An ion in a solid will experience an interaction resulting from all the surrounding magnetic ions. In the molecular field approximation the Weiss constant, θ, is a measure of the interaction. De Gennes (4) has considered an assembly of ions interacting via the RKKY mechanism and obtained the following expression for the Weiss constant

$$\theta = -\{3\pi z J_e^2 (g-1)^2 J(J+1)/4E_F\} \Sigma F(x) \qquad (2.4)$$

The quantity $\Sigma F(x)$ is obtained by summing the RKKY function, $F(x)$, over all the surrounding ions with the origin at the site of one of the magnetic ions. In the molecular field approximation the magnitude of the Weiss constant is identical to the ordering or Curie temperature and thus the ordering temperature is also given by the above expression. The type of ordering which occurs depends on the sign of $\Sigma F(x)$. The ordering will be anti-ferromagnetic if this sum is positive and ferromagnetic if it is negative.

The ordering temperatures of an isostructural series of rare-earth compounds in which the R-R interactions are dominant provide strong support for the principle of the RKKY mechanism. Since the majority of the rare earths will have the same valancy; z, E_f and

F(x) will be constant throughout the series and if J_e is constant then the ordering temperature will vary linearly with the quantity $(g-1)^2 J(J+1)$, the so-called de Gennes function. This linearity is observed in such series as the rare-earth-aluminum compounds.

It should be noted that the sign of θ is dependent on the electron concentration. As the number of conduction electrons increases, k_f increases, and θ oscillates between positive and negative values. Thus the electron concentration can determine whether ferromagnetic or anti-ferromagnetic coupling will occur. This feature is of considerable importance for the production of compounds of a particular magnetic structure.

The conduction electron polarization causes an increase in the experimentally determined ionic moment which is simply given by

$$\mu_p = \mu_B \int \rho(r)dr = \mu_B \frac{3zJ_e}{4E_F} (g_J-1)J \qquad (2.5)$$

In the presence of a magnetic field the Zeeman energy per ion becomes $(g\mu_B + \mu_p)H$ and the g value of the ion is shifted by an amount

$$\Delta g = \frac{3zJ_e}{4E_F} (g_J-1)J \qquad (2.6)$$

When the rare earths are combined with 3d transition metals the exchange interaction between the transition metal atoms is much larger than the R-R interactions. This is a direct consequence of the much larger spatial extent of the 3d wave functions as compared to the 4f wave functions of the rare earth elements. An idea of the strength of the transition metal interactions can be obtained from the ordering temperatures of rare-earth-transition metal compounds in which the rare earth does not have a magnetic moment, e.g. La, Y, or Lu. Figure 2.2 shows the composition dependence of the magnetic ordering temperature

and the moment per 3d atom for various compounds of non-magnetic rare earth elements with nickel, cobalt or iron. The decrease in ordering temperature with decreasing 3d atom content for the R-Co and R-Ni compounds appears to be related to the corresponding decrease in 3d moment. However, for the R-Fe compounds a decrease in the iron moment corresponds to an increase in the ordering temperature.

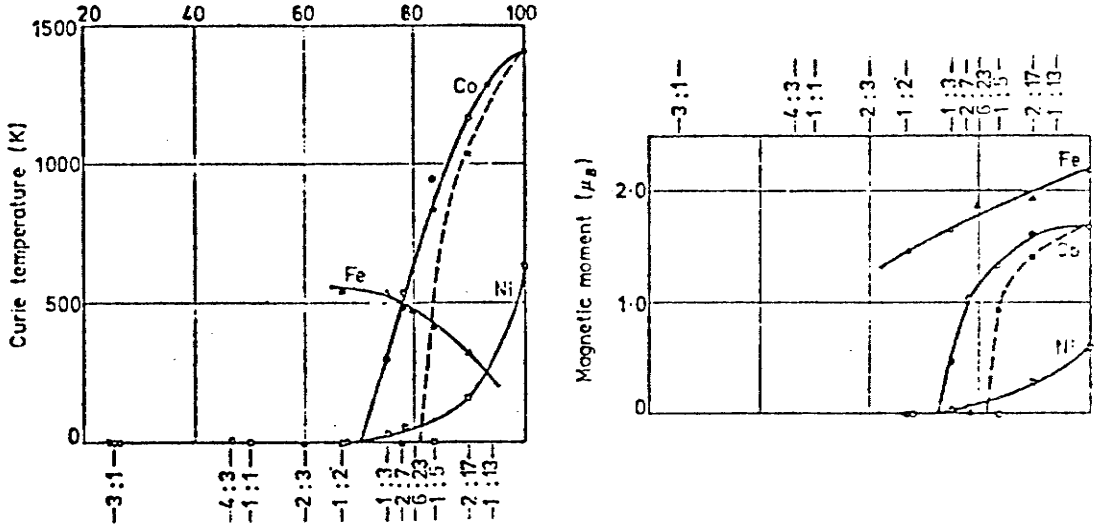

Fig. 2.2 Curie temperature and magnetic moment per transition metal atom versus molar fraction of transition metal. The compounds are the La,Th-Co, Y-Ni, and Y-Fe series. (From Ref.8[9]).

The large spatial extent of the 3d wave functions indicates that there will be a strong overlap of the wave functions of neighbouring atoms, which leads to the formation of energy bands. In order for the system to have a net moment the band must be split so that the populations of the two sub-bands with spin-up and spin-down electrons becomes unequal. The strong exchange interaction between the 3d electrons can result in such a situation. In general, one of three possibilities, shown schematically in Fig. 2.3, exists. The upper limit in energy for a 3d electron is given by the Fermi energy (E_f).

When E_f is higher than the top of the 3d band, both sub-bands would be completely filled and the net moment would be zero. This would also be the case if the Fermi level were below the top of the band but the effective exchange interaction between the 3d electrons were too small to produce a relative shift of the sub-bands. This situation is shown in Fig. 2.3 (a). Figure 2.3 (b) shows one possibility that could occur when there is a relative shift of the sub-bands. The net moment is given by the difference $\sum_{E} N(E)\uparrow - N(E)\downarrow$ i.e. the difference of the shaded areas in the figures. In this case only one of the 3d sub-bands is unsaturated. It is also possible to have a net moment when both 3d sub-bands are unsaturated. Such a situation is shown in Fig. 2.3 (c).

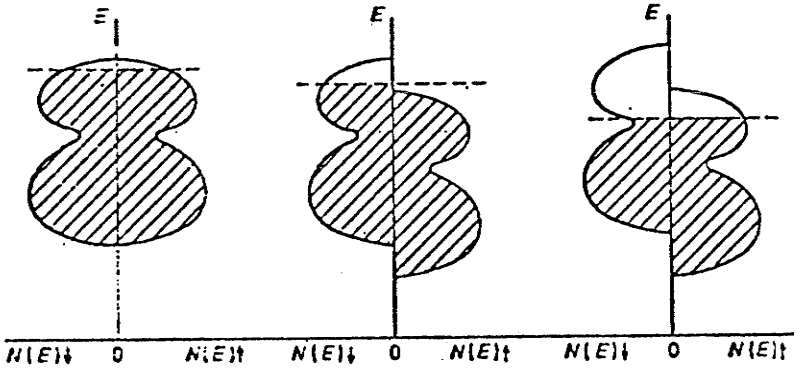

Fig. 2.3 Schematical representation of the density of states of the 3d electrons with spin-up $N(E)\uparrow$ and spin-down $N(E)\downarrow$. The Fermi level E_F is indicated by the dashed line.

When the number of 3d electron in a compound is raised by chemical substitution, a corresponding increase in the Fermi level results. In the situation represented by Fig. 2.3 (b), a lowering of the 3d moment results whereas in the situation of Fig. 2.3 (c) an initial increase in the 3d moment is produced. Thus it can be concluded that the magnetic moment of the R-Ni and R-Co compounds are due to the incompleteness of one of the 3d sub-bands, whereas for the Fe compounds

both 3d sub-bands are incomplete. The situation corresponding to Fig. 2.3 (a) in which there is no splitting of the sub-bands is encountered in compounds like YCo_2, YNi_2, $LaNi_5$, YNi_5 and $ThNi_5$. The fact that YNi_5 is a Pauli paramagnet at all temperatures although Y_2Ni_{17} as well as Y_2Ni_7 and YNi_3 are magnetically ordered compounds at low temperature is strange in terms of the itinerant electron model. The lack of a moment by the Ni atoms in YNi_5 has been attributed by Gignoux et al (5) to the fact that the Fermi level is in a minimum of the density of states.

2.2 Magnetic Coupling in the Rare Earth-Transition Metal Compounds

One of the most common methods of obtaining information about the coupling between magnetic moments is magnetic dilution. The magnetic atom in a given compound is gradually replaced by a different, usually non-magnetic, atom in such a way that the crystal structure is maintained. In general, magnetic dilution produces a reduction in exchange fields. Investigations on pseudobinaries can therefore give important information about properties like superconductivity and electrical resistivity as well as about crystal field splitting.

The effect of a change in valence electron concentration on the magnetic properties can also be studied using a series of pseudobinary compounds in which a non-magnetic component is replaced by a different non-magnetic component of a different valence. This can produce a much more drastic change in the magnetic properties than a simple magnetic dilution.

Intermetallics between the rare earth elements and aluminum have been extensively studied since they form easily and possess many interesting properties. As a result they are probably the best characterized of the rare earth intermetallics. The known compounds are R_3Al, R_2Al, RAl, R_3Al_2, RAl_2, RAl_3, R_3Al_{11}, and RAl_4. All of the lanthanides combine with aluminum to form the cubic Laves phase structure, RAl_2.

$CeAl_2$ was first formed and characterized in the early 1940's (6,7). However, the existence of the entire series was not established until 1960, in the work by Wernick and Geller (8). A detailed study of the bulk magnetic properties of the entire series was conducted by Williams et al (9) and Wallace et al (14,15).

The first studies of $R_{1-x}R'_xAl_2$ ternary systems were conducted by Williams et al (9) in 1962. Using bulk magnetization measurements on several R,R' combinations they inferred the coupling mode between the rare earth atoms to be ferromagnetic when R and R' are both heavy or light and anti-ferromagnetic coupling when one is light and one is heavy. As a result of the difference in the LS coupling in heavy and light rare earth elements, this coupling corresponds to the situation in which the spins of R and R' always couple parallel. It follows that all the RAl_2 compounds should be ferromagnetic. One exception does, however, exist in the case of $EuAl_2$ as was established in 1968 by Mader and Wallace (10). The peculiar behavior of Eu in $EuAl_2$ is a consequence of the fact that in this compound Eu is divalent, whereas the other rare earths are trivalent. The divalency of Eu is clearly indicated by its lattice parameter. The lattice

parameters of the RAl_2 compounds decrease with increasing atomic number as a result of the lanthanide contraction. The unit cell of $EuAl_2$ is anomalously enlarged in comparison with the other members of this series.

If the RKKY formalism is applicable to systems containing lanthanide elements, the magnetic structure would be dependent on the electron concentration. This idea was initially developed theoretically by Mattis (12) and has been confirmed experimentally for some systems, but in other cases it does not seem to be the case. Sekizawa and Yasukochi (13), for instance, found that anti-ferromagnetic GdAg (e.c.=2) could be transformed into a ferromagnetic material by a substitution of In for Ag to give $GdAg_{0.5}In_{0.5}$ (e.c. = 2.5). Presumably $EuAl_2$ is anti-ferromagnetic because it has a lower electron concentration than the other members of that series. Mader and Wallace (14) confirmed this by observing that the ternaries $Eu_{1-x}La_xAl_2$ were anti-ferromagnetic for $x < 0.2$ and ferromagnetic for $x > 0.6$. Swift and Wallace (14) have been able to account for these results using the RKKY formalism (Eqn.2.4).

For a metal which is a Pauli paramagnet the nuclear magnetic resonance is observed at a lower field than the same nucleus in an insulator. This is the so-called Knight shift. The nucleus then sees an internal field which is generated by the Fermi contact interaction produced by the polarized conduction electrons resulting from the external field. The Knight shift in this case is positive. In 1960, Jaccarino et al (15,16) found that K for Al^{27} in the RAl_2 compounds was an order of magnitude larger than the Knight shift for a Pauli

paramagnet and its sign varied according to whether R was a light or heavy lanthanide. They observed that K was positive for light lanthanides and negative for the heavy lanthanides. Assuming a Hamiltonian of the form given by equation (2.1) the Knight shift is given by (15-18)

$$K = K_o[1 + J(g-1)\chi_f|2g\mu_B{}^2] \qquad (2.7)$$

where g is the Landé factor, χ_f is the susceptibility of the 4f shell, K_o is the contribution to K of the Pauli susceptibility and J is given by $J = 6\pi z J_e \Sigma F(x)$.

Buschow et al (19) have used Eqns. 2.4 and 2.7 to evaluate J_e and k_f, the effective radius of the Fermi sphere. Using a value for the radius of the Fermi sphere given by the free electron model ($k_f = \{3\pi^2 N/V\}^{1/3}$, assuming each rare-earth atom contributes three electrons to the conduction band, results in a negative value for Θ. This indicates anti-ferromagnetic coupling, however, and with the exception of $CeAl_2$ and $EuAl_2$ the RAl_2 compounds are ferromagnetic. As a result Buschow et al adjusted k_f to a value less than k^o_f to obtain a positive Θ. Using Eqns. 2.4 and 2.7 to solve simultaneously for k_f and J_e they obtained $k_f = 0.94\ k^o_f$ and $J_e = -0.9$ eV for $GdAl_2$.

The fact that J_e is negative deserves some comment since, if it were a true exchange integral, it would be positive. Knight shift measurements such as those described above have resulted in both positive and negative values of J_e. Clearly J_e is not a pure exchange integral but rather it is a composite parameter dependent upon the chemical nature of the system as a consequence of the variations in the band structure, the negative contributions to J_e originating from

interband mixing (20).

Similar work has been done by Alfieri et al (21) on $GdAg_{1-x}Zn_x$ and $GdCu_{1-x}Zn_x$ ternaries and by Pierre (22) on $TbCu_{1-x}Zn_x$. In each case the substitution of Cu or Ag by Zn produced a change from anti-ferromagnetic to ferromagnetic coupling. Pierre (23) using a procedure similar to Swift and Wallace, found that this behaviour could be accounted for if it was assumed that $k_f \sim .85\ k^o_f$.

In some cases the RKKY model is not capable of describing the experimental results correctly. This is due in part to the approximations made in the model and in part also to the existence of a second interaction scheme between the rare-earths.

The RKKY formalism constitutes a free electron treatment. The choice of a value for k_f different from k^o_f in the procedure of Buschow et al presumably takes into account some of the inadequacies of this treatment. i.e. The details of the band structure are in some ways incorporated into the choice of k_f.

The equiatomic rare earth-zinc compounds have relatively high magnetic ordering temperatures, approximately room temperature in the case of GdZn. Magnetic ordering is anti-ferromagnetic or ferromagnetic, depending on whether R is a light or heavy rare-earth element. Magnetic dilution of GdZn to produce a change in the valence electron concentration has been studied by Alfieri et al (21), replacing Zn with Ag and In. Their results are shown in Fig. 2.4 along with the calculated results of Oppelt et al (24,25). The qualitative agreement with experiment obtained by Oppelt et al was based on the RKKY model

using Yosida's modification (3). Yosida took account of the finite mean free path (ρ) of the conduction electrons by multiplying F(x) in Eqn. 2.2 by $\exp(-r/\rho)$. The calculated result shown in Fig. 2.4 used a value of ρ equal to five times the lattice parameter and a value of k_f 10 per cent smaller than the free electron value.

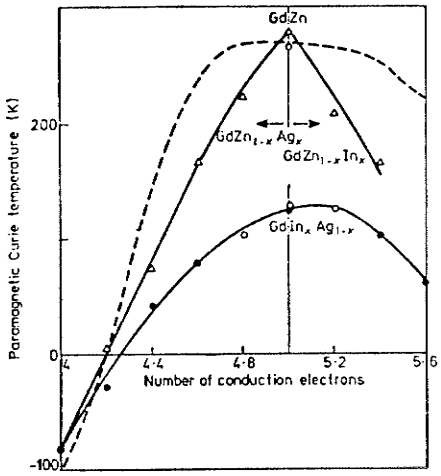

Fig. 2.4 Paramagnetic Curie temperatures of several series of pseudobinary compounds versus concentration. (From Ref. 21,24,25 as presented by Buschow Ref.89)

Eckrich et al (26) have studied the magnetic dilution of GdZn with non-magnetic La and Y. The results show a non-linear decrease in the Curie temperature in disagreement with the RKKY model (Fig. 2.5).

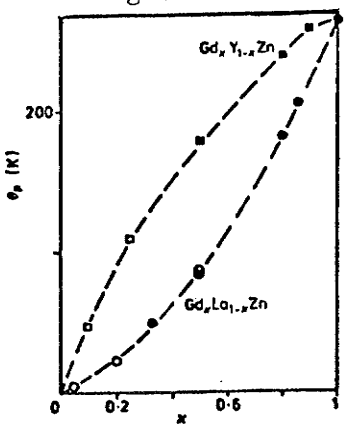

Fig. 2.5 The concentration dependence of the Curie temperature in $Gd_{1-x}Y_xZn$ and $Gd_{1-x}La_xZn$. The open symbols are paramagnetic Curie temperatures and the closed symbols are ferromagnetic Curie temperatures T_c. (From Ref. 26).

Buschow et al (27), in connection with the work of Oppelt et al, have suggested that better agreement could be obtained if different mean free paths were used for all the pseudo-binary compounds. Stronger potential scattering in the pseudo-binaries would lead to smaller ρ values and a sharper peak in the calculated curve of Fig. 2.4. Large potential scattering could also account for the relatively low ordering temperatures of the $GdIn_{1-x}Ag_x$ series. A decreasing mean free path with increasing Gd content could also account for the non-linear depression of the Curie temperatures observed in the $Gd_{1-x}La_xZn$ compounds.

Alternatively it was suggested by Buschow and Schinkel (28) that a large participation of the 5d electrons in the 4f-4f exchange coupling could account for the observed effects. The variation in the Curie temperature would result from the sensitivity of the 5d-5d interaction on the lattice constant. This latter view has gained support from NMR measurements taken on these same systems.

The hyperfine field that is measured in an NMR experiment, after correcting for the contributions due to the demagnetization and Lorentz fields, is composed of the following contributions:

$$H_{hf} = H_{cp} + H_{ce} + H_{orb} \qquad (2.8)$$

In this expression H_{cp} and H_{orb} represent the hyperfine field due to the core polarization and the orbital moment respectively, and H_{ce} is the contribution due to the conduction electron polarization. H_{ce} is composed of a contribution H_{op} which represents the conduction electron polarization caused by the spin at the atomic site under

consideration and another contribution H_N arising from conduction electron polarization due to the neighbouring sites in the lattice. The term H_N is usually referred to as the transferred hyperfine field and the examination of this quantity can provide valuable information on the magnetic coupling between localized moments. A local sampling of the conduction electron spin polarization can often be obtained using NMR or Mossbauer effect measurements. The local conduction electron spin polarization splits the nuclear Zeeman levels by means of the Fermi contact interaction, and produces the transferred hyperfine field observed. The sign and magnitude of this field are given in the simplified RKKY approach by

$$H_N = \frac{9\pi n^2 A(o) J(o) |\langle S_z \rangle|}{2E_F \, g_N \, \mu_N} \sum_i F(2k_F r_i) \qquad (2.9)$$

In the above expression g_N is the nuclear g value and μ_N is the nuclear magneton. The quantity A(0) is the hyperfine field coupling constant, defined by the interaction A(0) S·I between the conduction electron spin moment S and the nuclear spin moment I.

Since H_N is expected to vary linearly with the Gd concentration, H_N can be obtained from the (linear) concentration dependence of the hyperfine field measured in a series of pseudo-binary compounds like $Gd_{1-x}Y_xAl_2$ (29). A more direct and reliable means of determining H_N is to dope the compound with a non-magnetic rare-earth, such as La, and study the NMR at this site. Since both the H_{cp} and H_{op} are absent, the transferred field H_N can be determined directly (26,30,32). In some instances it was possible to observe a satellite structure which could be explained in terms of transferred

fields from nearest-neighbour magnetic atoms and contributions from more remote magnetic neighbours (31,33,34). Dormann et al (30,33) have, in fact, found that in GdZn the relatively high Curie temperature is incompatible with the sign and magnitude of the transferred hyperfine field. Dormann et al concluded that whenever T_c is high the dominant contribution to the exchange interaction between the localized 4f moments proceeds via the 5d electrons. Although the s and d electron polarizations both contribute constructively to the magnetic coupling, these contributions to the transferred hyperfine field subtract since the hyperfine coupling constants of s electrons is positive and that of d electrons is negative.

The work of Jaccarino et al (15), Jaccarino (16), Peter (35) and Gossard et al (36) on the RAl_2 systems showed that the conduction electron polarization due to the rare-earth ion is negative with respect to the spin of the ion both locally and at the neighbouring Al site. Since in the Laves phases the R-R and R-Al distances are comparable it is reasonable to expect that the polarization is also negative at the neighbouring rare-earth site which will result in a ferromagnetic rare-earth sub-lattice. This is consistant with the conclusions reached from bulk magnetization measurements done on ternary $R_{1-x}R'_xAl_2$ systems.

The anti-parallel coupling between the rare-earth and the transition metal spins was explained by Wallace (37) assuming a negative polarization of the s conduction electrons at the transition ion site. This would not be too surprising, at least for the Laves phases, since the transition metal ions lie at equivalent sites to the Al ions in

RAl_2. Wallace assumed that the rare earth-transition metal distances in these compounds were such that an anti-ferromagnetic s-4f interaction is always favoured. In the model the s-3d interaction was taken as positive since Stearns (38) has found it to be in certain systems containing iron. This automatically leads to anti-parallel coupling of the rare-earth spins and the transition ion spins. This situation is shown in Fig. 2.6 from which it is evident that this coupling mechanism will automatically lead to ferromagnetism in the light rare-earth compounds and ferrimagnetism in the heavy rare-earths.

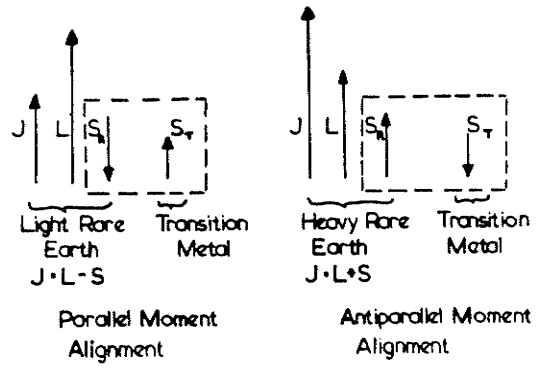

Fig. 2.6 The relative spin orientation in the rare earth-transition metal compounds.

The Knight shift at the nucleus of the non-magnetic component element of various rare-earth intermetallic compounds differing widely in composition, crystal structure and the nature of the non-magnetic component has been measured by various investigators (39-45). In all cases the conduction electron polarization was found to be negative at the site of the non-magnetic component. This is rather surprising since, with the RKKY model in mind, one would expect that the variety of different electron concentrations and interatomic spacings would lead to positive polarizations as well. The values of J(0) obtained when plotted against the corresponding value of k_f were found to be

positive for small values of k_f and increasingly negative for high k_f. de Wijn et al (42) interpreted this as indicating that interband mixing was dominant at high electron concentrations, in qualitative agreement with the theoretical predictions of Watson et al (20).

Accordingly, Campbell (46) has proposed a different model to account for the anti-ferromagnetic 4f-3d coupling consistantly observed in the rare-earth-transition metal compounds. Campbell suggests that the 4f rare-earth spins create a positive local 5d moment through ordinary 4f-5d exchange. The coupling between the spins then arises via the 3d-5d interaction. Campbell argues that the rare-earths can be considered to belong to a first half of a transition metal series, as far as their d electron is concerned. Since Fe, Co and Ni belong to the second half, the 5d-3d interaction will be negative and anti-ferromagnetic 4f-3d coupling will result.

Shidlovsky and Wallace (47) have studied the series $GdCo_{5-x}Al_x$ and $GdCo_{5-x}Cu_x$ in the expectation that the replacement of Co with Cu or Al would raise the electron concentration and change the Gd-Co coupling from anti-ferromagnetic to ferromagnetic. This, however, was not found to be the case, possibly because of the more complex nature of the exchange coupling between the Gd and the Co spins. Unfortunately, the anti-ferromagnetic coupling eliminates the heavy rare-earth Co compounds as candidates for use as permanent magnetic materials.

The first rare earth-transition metal compounds to be structurally identified were $CeNi_2$ and $CeCo_2$ which were investigated by Fulling et al (48) in 1942. Since then a vast number of such rare-earth intermetallics have been isolated. The rare-earth nickel system is particularly rich in the existence of intermetallic compounds, with at least eight stable phases having been positively identified. Each of these has been thoroughly characterized, both structurally and magnetically, in part due to their close relationship to the important R - Co compounds. However, in most of the R - Ni compounds Ni is non-magnetic, electrons apparently being transferred from the rare-earth to nickel until the nickel 3d band is filled. This makes the R - Ni compounds magnetically simpler since the transition metal sub-lattice is non-magnetic. As a result the study of the R - Ni compounds, in particular RNi_5, will contribute to a better understanding of the magnetically more complex RCo_5 compounds.

Pure nickel has approximately 0.6 vacancies per atom in its d band. Alloying nickel with an electron-rich metal such as copper reduces its moment in direct proportion to the copper content (49). This has been interpreted as resulting from the filling of the nickel 3d band with electrons supplied by Cu. Similar affects have been observed in intermetallic compounds such as $MgNi_2$ (50).

The cubic Laves phases, RNi_2, in many ways resemble the RAl_2 compounds. The magnetic interactions involve only the R sub-lattice, but are transmitted through a transition metal sub-lattice with a filled d shell. This has been established by saturation magnetization measurements on these compounds in the paramagnetic state (51-53). The

effective moments that were measured agreed well with the value, $g[J(J+1)]^{1/2}$, that is expected for a free tripositive rare-earth ion.

Wallace et al (54) have studied the system $R_{1-x}R'_xNi_2$ and determined that the coupling systematics are the same as in RAl_2, i.e. the spins always couple parallel. This leads to ferromagnetism when R and R′ are both light or heavy rare-earth elements and anti-ferromagnetism otherwise.

The magnetic properties of the RNi_5 compounds were first investigated by Nesbitt et al (55). The weakly or non-magnetic nature of nickel in these systems was again inferred by noting the agreement of the measured moments with the expected rare-earth component alone (at least for the heavy rare-earth compounds). The Pauli paramagnetism observed for $LaNi_5$ and $LuNi_5$ also supports this conclusion.

It appears, however, that Ni is non-magnetic in these compounds by only a very small margin. Neutron diffraction experiments (56) on $ErNi_5$ and $TbNi_5$ have confirmed that Ni is non-magnetic in these heavy rare-earth compounds. However, addition of Co to the heavy rare-earth $DyNi_5$ compound, has produced results that could only be reasonably interpreted if the dilution confers a moment on the nickel, presumably as a result of the competition for electrons between Ni and Co and resulting in an incomplete Ni d shell (57,58).

The marginal nature of the band filling in the heavy RNi_5 compounds follows rather naturally from the fact that nickel has approximately 0.6 vacancies per atom in its d shell. Thus for the RNi_2 series there are 1.2 vacancies per formula unit and for the RNi_5 series there are 3.0 vacancies per formula unit to be filled in

each case by the three valence electrons supplied by the rare-earth. The marginal nature of the band filling in the Haucke phase compounds (RNi_5) is thus quite apparent.

Susceptibility measurements on the light RNi_5 compounds such as $NdNi_5$ (59) seem to indicate that Ni carries a moment in these compounds. This in itself may be an indication of the marginal band filling in these compounds.

Wallace at al (57) have also studied the $R_{1-x}R'_xNi_5$ ternaries and observed the same coupling systematics as found in the Laves phase systems. The consistent coupling mode found in so many of the rare-earth compounds is a strong indication for a common coupling mechanism such as that suggested by Dormann et al (33) who suggested that the dominant contribution to magnetic coupling proceeds via the 5d electrons.

Bulk magnetic measurements (60,61) on the R_2Ni_{17} compounds, another of the more important compounds formed between the rare-earths and nickel, indicate that the Ni is magnetic in these compounds. This can readily be accounted for since the low concentration of rare-earth atoms would supply insufficient electrons to completely fill the Ni d-band. Y_2Ni_{17} and Lu_2Ni_{17} have Ni moments of 0.27 and 0.29 μ_B, respectively. The above model, assuming that each Ni atom lacks 0.6 electrons to fill its d-shell, would supply six electrons from the two rare-earth atoms to the seventeen nickel atoms and result in 0.25 holes/atom remaining in good agreement with experiment. These investigations also lead to the conclusion that the R - Ni coupling is consistent with the coupling expected in rare earth-transition metal

compounds, i.e. ferromagnetic when R is light, and anti-ferromagnetic when R is heavy.

The first investigation of the magnetic properties of the rare earth-cobalt compounds which produced reliable results was conducted by Nesbitt et al (62) in 1959. They studied a series of Gd-Co compounds and found that the Gd and Co sub-lattices coupled anti-ferromagnetically. Nassau et al (63) examined a series of RCo_5 compounds and also found that the coupling mode, for both light and heavy rare-earths, conformed with what is expected.

Seven intermetallic compounds have been identified in total in the rare earth-cobalt series. These are R_3Co, R_4Co_3, RCo_2, RCo_3, R_2Co_7, RCo_5 and R_2Co_{17}. Two of these compounds possess more than one stable phase and it is extremely difficult to obtain single phase samples in these cases. The R_2Co_{17} compound is found with both a Th_2Zn_{17} (rhombohedral) and Th_2Ni_{17} (hexagonal) structure, and R_2Co_7 possesses both a Ce_2Ni_7 (hexagonal) and Gd_2Co_7 (rhombohedral) structure.

Interest in the ternary systems, especially those based on the RCo_5 system, arises for a variety of reasons. Alloying is useful in attempts to achieve the mechanical properties required for the fabrication of permanent magnets and also can be used to convert the peritectically formed binary into a congruent melting material. In addition there is, of course, no reason that the binary should have optimal magnetic properties. The ternaries have, of course, often been used to obtain information on the coupling systematics. Nassau et al (63) studied the Gd-Y-Co ternaries and found a rise in moment as Y

replaced Gd, providing additional evidence that the Gd-Co coupling is anti-ferromagnetic. Wallace et al (64) have conducted a systematic study of the $R_{1-x}R'_xCo_5$ ternaries using several different R,R′ combinations and found that the best accounting of the measured moments could be obtained, using reasonable ionic moments, if the heavy lanthanides couple anti-parallel to cobalt, the light lanthanides couple parallel to cobalt, and the heavy-heavy and light-light coupling is parallel and anti-parallel respectively. Again this coupling scheme is consistent with that found in other rare-earth compounds.

However, substantial deviations between the calculated and measured values is found for ternaries containing light lanthanides. This discrepancy appears to originate from the assumption of fixed ionic moments for calculating the magnetic moments. Bleaney (65) appears to have been the first to suggest that the cobalt moment may depend on the nature of the rare-earth element it is combined with. The exchange field of the lanthanide sub-lattice is presumed to produce a substantial induced moment on the cobalt. The variable moment of Co was confirmed by neutron diffraction studies (66,67).

The magnetic properties of the RCo_2 compounds have also been quite thoroughly studied (53,66). The coupling systematics are found to be in accord with those found in the RCo_5 compounds. Several of these have been examined by neutron diffraction techniques (52,68,69) and the results have confirmed the coupling mode inferred earlier from bulk magnetization measurements. These results have also directly shown the variation of the cobalt moment with the rare-earth element.

Magnetic studies of the R_2Co_{17} compounds result in the same

coupling modes that one has grown to expect in the rare-earth compounds, especially the rare earth-transition metal compounds. The large saturation moments of the R_2Co_{17} with the rare-earths of Ce through Sm as well as their extremely high Curie temperatures make these compounds excellent candidates for the fabrication of permanent magnets. The magnetic moments per formula unit are given in Table 2.1 (66,70).

Table 2.1

Rare Earth	Magnetic Moment (μ_B/f.u.)
Ce	26.1
Pr	32.9
Nd	32.1
Sm	23.6
Gd	14.4
Tb	10.8
Dy	8.3
Ho	7.8
Er	10.6
Tm	13.6
Lu	27.4

The results shown in Table 2.1 clearly show that it is the light rare-earths which are the best candidates for permanent magnetic materials. The large total magnetic moment that they possess is a strong indication of ferromagnetic coupling between the rare-earth and Co sub-lattice. The compound Lu_2Co_{17} has no rare-earth moment and we can compute that the total Co moment is 27.4 μ_B/f.u. or 1.62 μ_B/atom. Pr_2Co_{17} and Nd_2Co_{17} have moments in excess of this, from which we can conclude that the Co sub-lattice is coupled ferromagnetically to the rare-earth sub-lattice. Ce_2Co_{17} also does not have a Ce moment. The reduced value of the moment is a consequence of the quadravalent state of Ce. The small value for Sm_2Co_{17} is

difficult to explain. It could result from a coupling system which is not ferromagnetic. However, Sm is extremely volatile, and consequently Sm compounds are the most difficult to prepare. The low value of the moment could also have been produced by a low quality sample.

Unfortunately, from the point of view of the manufacture of permanent magnetic materials, most of the light R_2Co_{17} compounds have unfavourable anisotropies since the moments lie in the basal plane. Sm_2Co_{17} has an easy axis, however, and appears therefore to be the best candidate for use as a permanent magnet.

The variable cobalt moment, suggested by Bleaney, appears to be essential to the understanding of the magnetic properties of the cobalt compounds. Lemaire et al (66,71) have examined the influence of the rare-earth exchange field on the cobalt moment by studying the cobalt moments in the Y-Co and Gd-Co series. Figure 2.7 shows the variation of the cobalt moment with the atomic compositon of the rare-earth component, as obtained by Lemaire et al (71). It is evident that the Co moment decreases with increasing rare-earth concentration and the Co moment is large when its rare-earth partner is magnetic. The first effect is due to electron transfer from the rare-earth to the Co, thus decreasing the cobalt moment as the band is filled; the second effect is due to the magnetic induction suggested by Bleaney. If elemental Co is assumed to be in a $3d^{8.3}$ configuration with one half band filled, the reduction in the cobalt moment due to electron transfer is given by the solid line in Fig. 2.7. This is in good qualitative agreement with the Y-Co series.

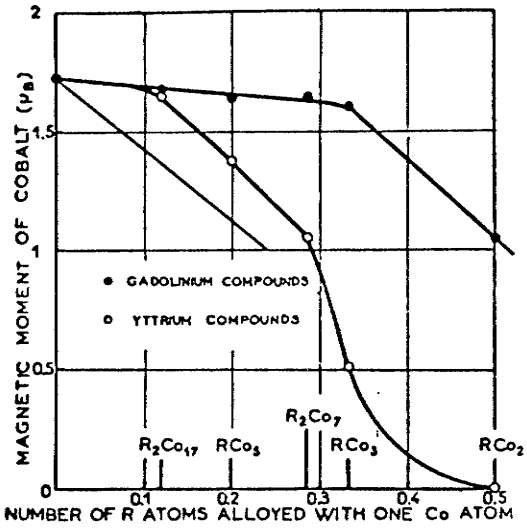

Fig. 2.7 Variation of the magnetic moment of Co in its intermetallic compounds with Y and Gd. (After Lemaire Ref.71).

2.4 The Nature of the Co Moment in the Rare Earth-Cobalt Compounds

Magnetic dilution is an important tool in the study of not only the nature of the exchange coupling between the various moments, but also can be used to obtain information on the nature of the magnetic moments themselves. An important consideration in such a study is, of course, that the crystal structure is preserved.

Several studies have been conducted, using various pseudo-binary systems, to obtain a better understanding of the nature of the transition metal moments. Piercy and Taylor (72) and Taylor (73) have studied the systems $Dy_{1-x}Y_xFe_2$ and $Gd(Co_{1-x}Ni_x)_2$ respectively, and found a non-linear variation of the transition metal moment with composition. In both series the transition metal moment changed significantly over a small composition range, which is difficult to understand on the basis of electron transfer to localized 3d states.

Piercy and Taylor (74) have also studied the system $Y(Fe_{1-x}Co_x)_2$ which was considered more nearly analogous to the classic Fe-Co system studied in the original work on collective electron ferromagnetism. Figure 2.8 shows the results that they obtained, the sudden collapse of the transition metal moment at a composition of approximately 20 per cent iron being the most striking feature. In an attempt to explain this behaviour Piercy and Taylor proposed that the 3d states of the iron, cobalt and nickel atoms in these compounds form a band which produces an itinerant electron moment. The reduction in transition metal moment was interpreted in terms of the filling of the 3d band as cobalt is added to the system. The collapse of the moment can be attributed to the disappearance of the splitting of the 3d sub-bands due to the combined effects of the decrease in the moment due to band filling and the resulting variation of the rare earth-transition metal and transition metal-transition metal exchange interaction.

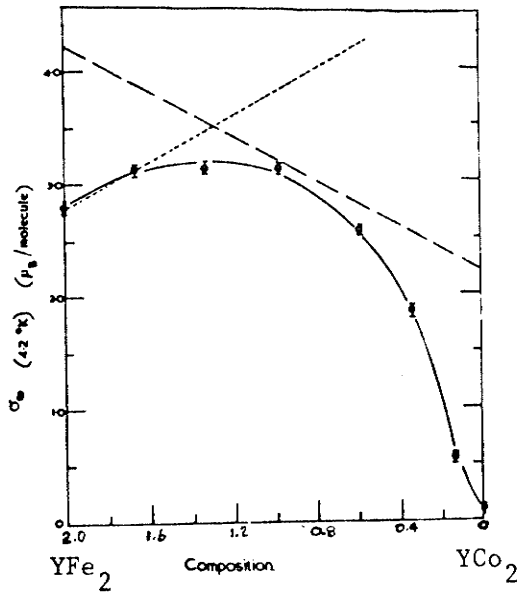

Fig. 2.8 The variation of the transition metal moment in the $Y(Fe,Co)_2$ pseudobinary, with increasing electron concentration. (After Piercy and Taylor Ref. 74).

In most of the series of compounds containing Fe dilution with Co or Ni leads to an initial increase in the magnetic moment per transition metal ion. After passing through a maximum, further dilution results in a continuous decrease of the transition metal moment. In the series of the type $Y(Co_{1-x}Ni_x)_n$ the 3d moment decreases monotonically. The behaviour of the Fe containing ternaries results from the fact that in these compounds the spin up and spin down sub-bands are both unfilled. The Fermi level is located at a minimum in the spin-down density of states as shown in Fig. 2.3 (c). Increasing the 3d electron concentration fills the spin-up band and therefore increases the net magnetic moment. When the spin-up band is full further dilution with Ni or Co adds electrons to the spin-down sub-band and the moment decreases.

Examination of the magnetic data for a series of rare earth-transition metal phases indicates that the transition metal moment increases with increasing transition metal content in the compound. In these compounds the accurate determination of the moments associated with the two types of ions in the ordered state is quite difficult, except for the case of the yttrium compounds and to a lesser extent the gadolinium compounds. Generally the lanthanide moments are considerably lower than their theoretical gJ values as a result of the crystal field interaction. Poldy (75) has examined a series of pseudo-binary compounds in the Y-Fe and Y-Co phases and found a strong indication that the moment behaviour in the compounds is similar to the behaviour found

in Fe-Co-Ni metal alloys. These results, shown in Fig. 2.9, represent additional evidence favouring an itinerant transition metal moment.

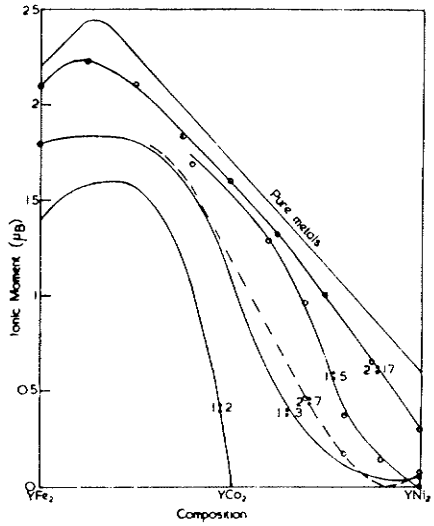

Fig. 2.9 The transition metal moment in the pseudobinary compounds in the Y(Fe,Co) and Y(Co,Ni) systems. (After Poldy Ref. 75).

However, attempts have also been made to explain the magnetic behaviour shown in Fig. 2.2 by means of a localized moment model. Buschow (76) and also Burzo (77) have discussed the magnetic properties of rare earth-transition metal compounds in terms of the Friedel model (78). In another work Burzo et al (79) have used Jaccarino and Walker's local environment model (80) to explain the transition metal moment collapse in the series $Gd(Co_{1-x}Ni_x)_2$. Figure 2.10 shows a calculated fit by Burzo et al to the available experimental data at that time. In their analysis the authors assumed that only those Co atoms would possess a magnetic moment that are surrounded by at least three out of a possible six nearest-neighbour Co atoms.

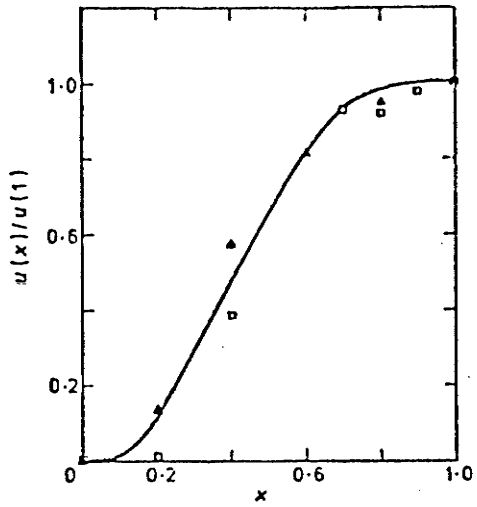

Fig. 2.10 Concentration dependence of the 3d moment in $GdNi_{2-2x}Co_{2x}$ normalized to the Co moment in $GdCo_5$.(From Taylor Ref.73 □, Burzo Ref.77 ▲, and calculated fit by Burzo Ref.79).

Friedel et al have extended the usual band model to allow for the formation of localized moments within a band picture. They showed that a local spin polarization about a transition metal ion could be stable when the Stoner condition for ferromagnetism is satisfied. Blandin and Friedel (81) suggested that the magnetic interactions modify the density of d states $\rho_d(E_f)$ so that the Stoner condition $\rho_d(E_f)U > 1$ is fulfilled. The critical magnitude of the interaction which would lead to a magnetic moment would correspond to a certain number of nearest-neighbour cobalt atoms. The appearance of a magnetic moment is most likely to occur in a nearly magnetic ion such as Co than in an atom such as nickel.

Brouha and Buschow (82,83) have studied the magnetic properties of $La(Co_{1-x}Ni_x)_5$ and $Y(Co_{1-x}Ni_x)_5$ and found that they were able to explain the concentration dependence of the magnetic moment in terms of the rigid band model only for the compounds with a fairly high

Co concentration. They suggested that, since in YNi_5 and $LaNi_5$ the 3d band is incompletely filled and magnetically unsplit, this was due to the collapse of the 3d band in regions of higher Ni concentration. Increasing the Ni content, therefore, would not only add electrons to the unsaturated spin-down band (Fig. 2.3 (b)), but also would affect the magnetic splitting so that in regions of high Ni concentration filling of both sub-bands would occur (Fig. 2.3 (a)). A surprisingly good description of the concentration dependence of the magnetic moment in these series was obtained by Buschow et al (84) in terms of the model of Jaccarino and Walker. Burzo (85) has reported that the paramagnetic behaviour of some rare earth-cobalt compounds was consistent with a localized transition metal moment.

The experimental work that has been done thus suggests that the magnetic behaviour of the cobalt atoms in rare-earth compounds is both complex and of great interest. Evidence not only exists for a localized character to the moments but the sensitivity of these moments on the rare earth content and the valence electron concentration are indications of an itinerant transition metal moment. Such behaviour can certainly be justified in the Friedel model. The Friedel model also gives some insight into why the local environment model of Jaccarino and Walker has given such surprisingly good descriptions of the concentration dependence of the transition metal magnetic moment in various pseudo-binary series.

The local environment model is not always capable of explaining the observed magnetic properties. Cannon et al (86) have found that the Jaccarino-Walker model is not able to explain the concentration

dependence of the Co moments in $Gd_{1-x}Y_xCo_2$. Gignoux et al (5) have investigated the magnetic properties of the $Gd_{1-x}Y_xNi_5$ series. The Curie temperature varied linearly with Gd concentration up to x = 0.75. The Ni moment, obtained from magnetization measurements, increased strongly with Gd concentration and reached a value of 0.16 μ_B per Ni atom. The authors indicated, however, that the variation of the Ni moment with Gd concentration could not be exclusively explained by the local environment effects alone.

Since Ce and Th when combined with 3d transition elements are tetravalent and have no magnetic moment, they can be used in series like $Y_{1-x}Ce_xM_n$ to study the effect of the valence electron concentration on the magnetic properties of these compounds. Buschow and van Stapele (87) examined the $Y_{1-x}Ce_xFe_2$ series and found that the Fe moment decreased only slightly with the addition of Ce. The Curie temperature decreased rather dramatically from 545 K to 230 K. Miskinis et al (88) studied the $Gd_{1-x}Ce_xFe_2$ and $Gd_{1-x}Th_xFe_2$ series and reported that there was no change in the nature of the Gd-Fe coupling in these pseudo-binary compounds.

These results serve to illustrate the truly complex nature of not only the transition metal moment but also of the magnetic coupling that occurs between the various elements in the rare earth-transition metal intermetallic compounds.

2.5 Magnetic Ordering in the Ni and Co Compounds

The magnetic ordering temperature of both the cobalt and nickel

compounds increase with increasing transition metal concentration relative to the RM_2 compound. At a given concentration the ordering temperature is given by

$$T_{order} = A+\alpha G \qquad (2.10)$$

where A and α are constants and G is the de Gennes function defined earlier. Figure 2.11 shows the variation of the Curie temperature with the de Gennes function for the cobalt compounds. The intercept with the temperature axis corresponds to the constant A and is related to the transition metal-transition metal interaction. The strength of the interaction obtained from the constant A will not be the same as the transition metal-transition metal strength in compounds formed with magnetic rare-earth, since the rare-earth sub-lattice induces an increase in the transition metal moment which results in an increase in the M-M exchange interaction.

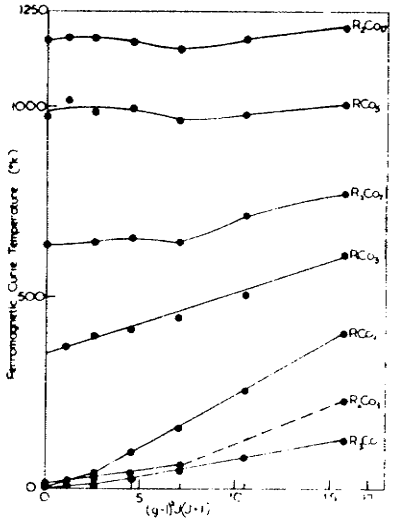

Fig. 2.11 The variation of the Curie temperature with the de Gennes function for the cobalt compounds.

The high Curie temperatures indicate the dominance of the Co-Co interactions over the R-R interactions. Figure 2.12 shows the Curie temperature for several rare-earth series. It is apparent that, as the

proportion of Co in the compound decreases, the R-R interaction becomes more important. However, in spite of this the Co interaction remains important even in the RCo_2 series. The Curie temperature for $GdNi_2$ which has only R-R interactions is 85 K as compared to 408 K for $GdCo_2$. The higher T_c for the cobalt compound clearly indicates the importance of the Co-Co interaction.

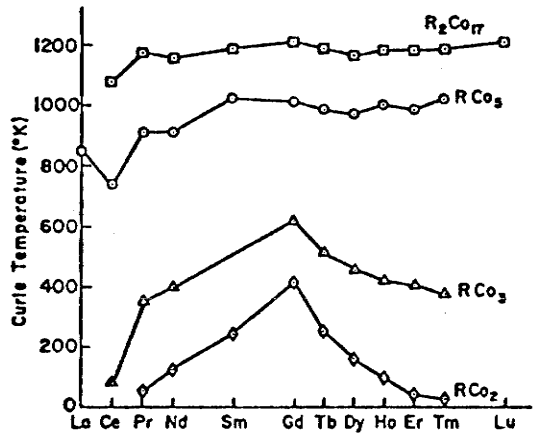

Fig. 2.12 The Curie temperatures for several rare earth cobalt series.

2.6 The Rare Earth-Iron Compounds

To complete this chapter it would seem appropriate to comment on the rare earth-iron compounds, specifically on their usefulness as permanent magnetic materials.

The rare-earths form fewer compounds with iron than with nickel or cobalt. The compounds that do form, however, show the same variable moment property found in the rare earth-cobalt compounds. In Gd_2Fe_{17} the iron moment is $2.1\mu_B$ while in $GdFe_2$ it is $1.6\mu_B$. In $LuFe_2$, where Lu is non-magnetic, the Fe moment is $1.45\mu_B$, indicating that in $GdFe_2$ the Gd induces a moment of $0.15\mu_B$ on the Fe. In these

respects the iron compounds resemble the cobalt compounds. However, all the RFe_2 compounds possess substantial transition metal moments, whereas the Co compounds do not. This difference between the behaviour of Fe and Co is probably a consequence of the fact that in Co one of the d sub-bands is filled and electron transfer from R causes a rapid decline in moment. In Fe both sub-bands are unfilled and electron transfer occurs into both and the decrease in the number of unpaired spins is considerably slower.

Although the rare earth-Fe compounds have generally similar magnetic properties to the rare earth-Co compounds, their usefulness as permanent magnets is not very promising. The reasons are that the iron compounds have Curie temperatures considerably lower than the cobalt compounds, and, in addition, no rare earth-Fe compound exists which is the technological equivalent of the RCo_5 systems. Moreover, the light rare-earth systems, in which ferromagnetic coupling is expected, either do not form or form only as phase mixtures. The heavy rare-earth systems couple anti-ferromagnetically and have magnetizations which are too small to be useful. Therefore, the most significant application of iron in rare earth-based magnets seems to be in the formation of ternaries in partnership with cobalt. As seen in Fig. 2.9 the addition of Fe can increase the average transition metal moment in R-Co compounds.

2.7 The Structure of the Rare Earth-Cobalt Compounds

The large magnetic moment that some of the rare earth elements

have at low temperature and the strong magnetic coupling of the 3d transition elements is the main reason for the study of alloys made from these elements. The physical properties of a solid solution generally are consistent with what would be expected on the basis of a linear interpolation between the properties of the parent materials. Because of the large difference in atomic radii between the rare earth elements and the 3d transition elements, very little terminal solid solubility exists in these systems and one is therefore forced to study the intermetallic compounds in order to discover materials which would be of practical importance.

The physical properties of the intermetallic compounds need not have anything in common with the properties of the component elements. For instance, it is possible that non-magnetic parent materials would produce magnetic intermetallic compounds. This may also be the case for numerous other properties such as superconductivity, magnetocrystalline anisotropy, mechanical hardness, and the ability to absorb hydrogen gas. The number of compounds formed between rare earth and transition metals is enormous and therefore the investigation of the properties of these compounds is a formidable task.

A characteristic feature of the rare earth-transition metal binary systems is the existence of intermetallic compounds. The number of compounds tends to increase with increasing atomic number of the rare earth and therefore the decreasing radius as a result of the lanthanide contraction. For a given rare earth the number of compounds tends to increase as the number of 3d electrons of the transition metal increases. The primary factor which controls the formation and

stability of compounds in these systems, however, is the size factor. As many as ten intermetallic compounds have been identified in a single system.

The intermetallic compounds which have outstanding permanent magnet properties are the hexagonal $CaCu_5$ phases of the rare earth-Co system. The preparation of such a compound, however, by the solidification of a stoichiometric melt may result in a mix of several intermetallic compounds. This may be understood by the examination of the phase diagram. Figure 2.13 shows the phase diagram for the Gd-Co system. If a melt of 83.4 atomic % Co ($GdCo_5$) is cooled the first solid phase produced is Gd_2Co_{17}. At the melting temperature of $GdCo_5$ (1335^o C) diffusion of atoms is still appreciable and the Gd_2Co_{17} particles react with the Co-deficient melt to form the $GdCo_5$ phase (peritectic reaction). However, from the phase diagram it can be seen that close to its melting point the phase $GdCo_5$ is richer in Co concentration than the stoichiometric composition. Thus the central part of each grain will be Co rich. Since the cooling rate is generally quite large for an arc melted button the excess Co will not have sufficient time to diffuse to the outer parts of the grains. When solidification is complete the grains will be surrounded by material which is deficient in Co, i.e.: the Gd_2Co_7 phase. Vacuum annealing at temperatures in the range 800-1100^o C will produce single-phase material, while annealing at lower temperatures will result in eutectoid decomposition. Similar decompositions of the RCo_5 phases also occur in other R-Co systems. As the rare earth atom becomes heavier the temperature range over which the RCo_5 compound is stable becomes

smaller until it is entirely absent for systems in which R is an element beyond Tm.

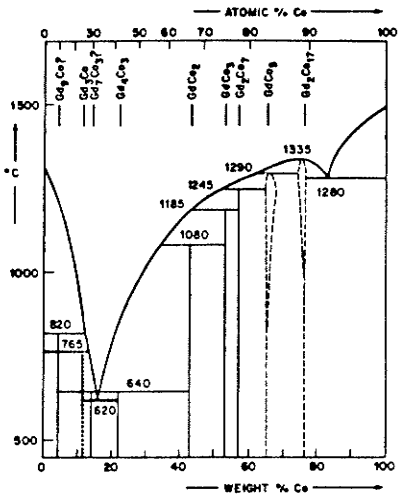

Fig. 2.13 Phase diagram for $GdCo_5$.

Another important feature of the RCo_5 phase is that it exists over a significant range of Co concentrations. Samples annealed and quenched are single phase between the compositions $GdCo_{4.8}$ and $GdCo_{5.6}$ (92). X-ray diffraction measurements have shown that, inside the homogeneous region, the lattice parameters are strongly dependent on the composition. Increasing the Co concentration results in a contraction of "a" and an expansion of the "c" lattice parameter of the hexagonal crystal structure (92).

Figure 2.14 shows the phase diagrams for YCo_5 and $SmCo_5$. Since the outer electron configuration for all the rare earth elements are quite similar, a chemical similarity also exists which results in a fairly uniform behaviour when the rare earth elements are combined with other elements. Thus if one member forms an intermetallic compound of a given composition and crystal structure all other members are likely to behave in the same manner. The physical properties including the

magnetic properties can vary quite markedly, however, within such a series of compounds, as a result of the filling up of the inner 4f electron shell which produces a large variation in the spin and orbital moment. An important subclass of these compounds are those in which the rare-earth element has no magnetic moment (La, Lu, Y, and Ce). This makes it possible to study the origin and nature of the 3d electron magnetism, using techniques such as nuclear magnetic resonance, the Mossbauer effect and the diffraction of polarized neutrons, on systems that have high atomic order. The disadvantage of using mixtures of 3d transition metals is that they form solid solutions.

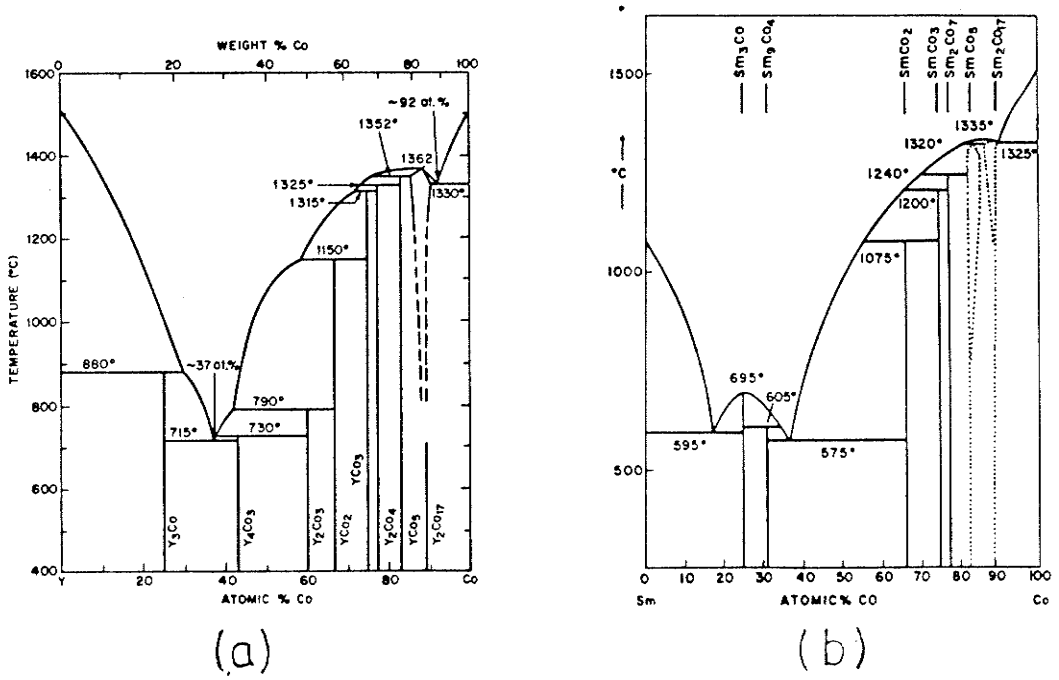

Fig. 2.14 Phase diagrams for (a) YCo_5 and (b) $SmCo_5$.

Table 2.2 presents a survey of the types of structures that are found in the rare earth transition metal systems. M indicates the transition metals which form the particular structure.

TABLE 2.2

Compound	Lattice symmetry	Structure type	M
R_3M	Orthorhombic	Al_3Ni	Ni,Co
R_7M_3	Hexagonal	Th_7Fe_3	Ni
R_4M_3	Hexagonal	Ho_4Co_3	Co
RM	Orthorhombic	FeB	Ni
RM_2	Cubic	$MgCu_2$	Ni,Co,Fe,Mn
RM_2	Hexagonal	$MgZn_2$	Mn
RM_3	Hexagonal	$CeNi_3$	Ni
RM_3	Rhombohedral	$PuNi_3$	Ni,Co,Fe
R_2M_7	Hexagonal	Ce_2Ni_7	Ni,Co
R_2M_7	Rhombohedral	Gd_2Co_7	Ni,Co
R_6M_{23}	Cubic	Th_6Mn_{23}	Fe,Mn
RM_5	Hexagonal	$CaCu_5$	Ni,Co
R_2M_{17}	Hexagonal	Th_2Ni_{17}	Ni,Co,Fe
R_2M_{17}	Rhombohedral	Th_2Zn_{17}	Co,Fe
RM_{12}	Tetragonal	$ThMn_{12}$	Mn

Most of these structures are, in fact, related to the hexagonal $CaCu_5$ lattice by several atomic substitutions accompanied by layer shifts. The hexagonal $CaCu_5$ structure is shown in Fig. 2.15. Two different types of atomic layers exist in this structure. One layer contains both M and R atoms whereas in the next layer only M atoms are found. As a result this structure contains two inequivalent transition metal, M, sites.

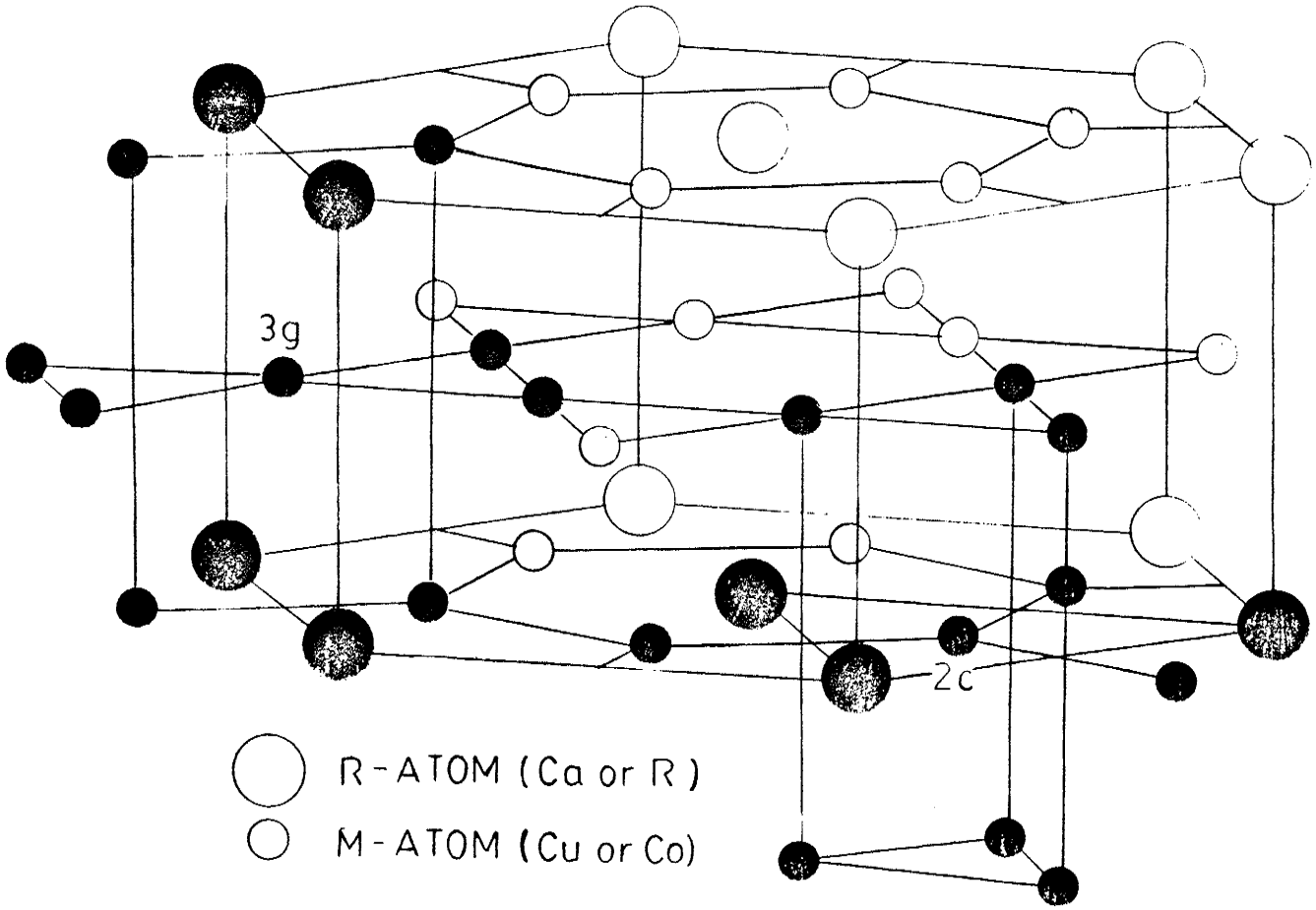

Fig. 2.15 The hexagonal $CaCu_5$ structure showing the two inequivalent Cu sites and the local atomic environment.

CHAPTER 3

Principles of Nuclear Magnetic Resonance

3.1 Introduction

The majority of nuclei possess angular momentum along with an associated magnetic dipole moment. These quantities were first introduced to explain the hyperfine splitting observed of atomic spectral lines. The nuclear magnetic moments will interact with a magnetic field producing quantized energy levels given by

$$E_m = -\gamma\hbar m_I H \tag{3.1}$$

where γ_N is the gyromagnetic ratio, or the ratio between the magnetic moment and the angular momentum, $\vec{\mu} = \gamma_N \hbar \vec{I}$, the eigenvalues of I_z are given by m_I which takes possible values from +I, I-1 to -I, and H is the magnetic field intensity defining the axis of quantization for the nuclear spins. These are the nuclear Zeeman energy levels, analogous to the magnetic splitting observed in electron spin systems. In terms of the nuclear magneton β which is defined by $\beta = e\hbar/2M$ where M is the mass of the proton, and the nuclear moment μ given by $g\beta I$ where g is the nuclear g-factor which will vary from nucleus to nucleus, the nuclear Zeeman energy levels are given by

$$E_m = -g\beta H m_I \tag{3.2}$$

For a proton g = 5.586 and since I = 1/2, the proton has a magnetic moment of 2.793 nuclear magnetons. The neutron, although uncharged, has a negative γ_N and g, and a magnetic moment of -1.913 nuclear magnetons.

The basis of nuclear magnetic resonance experiments are induced transitions between the possible energy levels of the system by the application of a suitable perturbation; for instance, a time-varying magnetic field perpendicular to H. Transitions, of course, will only occur if the natrix elements between initial and final states are non-zero. For the time varying magnetic field the only allowed transitions are between neighbouring energy levels (i.e. $\Delta m = \pm 1$).

The obvious initial application of NMR was in the accurate determination of the magnetic moments of nuclei. A comparison of the resonant frequencies of two different nuclei in the same magnetic field would give the relative value of their gyromagnetic ratios or their magnetic moments if the nuclear spins are known. The value of I can often be found from the hyperfine structure of electronic spectra. Once the nuclear magnetic moment is accurately known, for example the proton moment, then the resonance frequency can be used to measure the value of a magnetic field. Magnetic resonance magnetometers, using nuclei with appropriate γ_N values to keep the resonance frequency at a convenient value for detection, can be used to measure a wide range of magnetic field values.

It should be noted that in the above applications correction factors have to be used to allow for the diamagnetic screening of the surrounding electrons which would cause the effective field seen by the resonant nuclei to differ from the applied field. For these applications the presence of the electrons is certainly a nuisance. However, for the chemist or solid state physicists the need for such corrections provides a sentitive means of studying the details of the

actual electronic motion in atoms and molecules in gases, liquids and solids.

The magnetic interaction between the electrons and the nuclei, i.e. the hyperfine interaction, results in an additional shift in the NMR resonance frequency. This same interaction shifts also the electron resonance frequence in an E.S.R. experiment. The measurement of these shifts, as a function of temperature, pressure or composition is a very useful means of studying the electronic structure. It should be noted that nuclear resonance also provides a means of studying electric effects in molecules and solids. In re-orientating the nucleus relative to the applied magnetic field in a resonance experiment, work must also be done against electric forces which tend to maintain the same nuclear orientation. The magnetic and electric components of the resonance energy may often be separated, giving useful information on the electrical environment of the nucleus.

The resonance of nuclei in ordered magnetic materials is a major area of study. The hyperfine interaction is in general very much larger than any applied field and the resonance may be observed without the use of an external field. The need of a diamagnetic correction is thus avoided and a direct measurement of the internal fields in ordered magnetic materials is thus possible, which can then be related to the electronic structures of these materials and thus to the nature of ferromagnetism itself.

The first successful magnetic resonance experiment was conducted by Rabi et al (1) in 1939, using the molecular beam magnetic resonance method. However, molecular beams consist of discrete non-interacting

particles, and it was much more interesting to be able to observe resonance effects in bulk matter. Gorter (2) attempted to do this in LiF using a calorimetric method designed to measure the heating caused by energy absorption. The first successful nuclear magnetic resonance experiments in bulk matter were reported in 1946 by Block, Hansen and Packard (3) using protons in water, and by Purcell, Torrey and Pound (4) using protons in solid paraffin. The techniques used, however, were different, and as they are best described by different viewpoints of the magnetic resonance phenomena, one a classical picture of precessing spins, the other, the quantum mechanical viewpoint of transitions between energy levels, both viewpoints will be briefly described in the next section.

3.2 The Basic Principles of NMR

The general theory of magnetic resonance can be developed from two different viewpoints. The quantum mechanical description was first developed by Bloembergen, Purcell and Pound (5). The classical description, which led to the use of the word "resonance" in the description of the phenomena, was developed initially by Bloch (6). The two approaches are, in fact, complementary and each is useful in the descriptions of certain aspects of magnetic resonance. The basic theory is applicable to electron-spin resonance (E.S.R.) as well as to nuclear magnetic resonance.

3.2.1 The Quantum Mechanical Picture of Nuclear Magnetic Resonance

In the development of the quantum mechanical viewpoint, one considers an ensemble of nuclear spins in a uniform magnetic field H. In order to ensure internal thermal equilibrium some form of spin-spin coupling is necessary to allow energy transfer through the system. The spins will then be distributed among the possible energy levels according to a Boltzmann distribution. The ensemble is then said to be at a spin temperature T_s determined by the Boltzmann distribution. The concept of spin temperature is very useful in describing the physical processes involved in nuclear magnetic resonance.

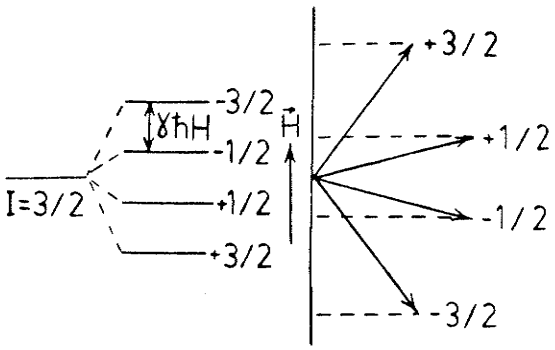

Fig. 3.1 Energy levels and the space quantization picture for nuclei in a magnetic field, H. The vectors represent either angular momentum in units of h or magnetic moment in units of $\gamma_N h$ (or $g\beta$).

Before the Zeeman field is applied the various spin levels are degenerate and equally populated. At the instant the field is applied the spin temperature is therefore infinite. In order that this temperature fall to the temperature of the surroundings, the spin system must lose heat and hence there must be some form of contact between the spin ensemble and the surroundings (the lattice). The fluctuating electric and magnetic fields at the spin sites produced by the vibrational motion of atoms, molecules or ions, and by the orbital and spin motion of electrons, can produce the required interaction if there

are components of this motion with a frequency corresponding to the transition energy between neighbouring levels. The equilibrium populations are therefore given by the Boltzmann distribution with T_s equal to the lattice temperature. The characteristic time determining the rate of spin cooling is known as the spin-lattice relaxation time T_1; a short T_1 meaning good thermal contact with the lattice.

In order to treat the spin ensemble as a system at internal thermal equilibrium, there must be a mechanism for maintaining a uniform spin temperature throughout the ensemble, and thus some kind of spin-spin interaction is necessary to allow the transfer of energy from one spin to another. This interaction is primarily magnetic in nature, but quadrupolar and electron-nuclear effects can also contribute. Strong spin-lattice interactions may, in some cases, also help to induce thermal equilibrium since each spin is independently coupled to the lattice.

The source of the magnetic relaxation is the interaction of a nuclear dipole with the magnetic field of neighbouring dipoles. Each dipole, therefore, sees a total field composed of the isotropic component (external field) and the vector sum of all the local fields produced by neighbouring dipoles. In a solid this broadens the line while in liquids and gases the dipole-dipole interaction is considerably reduced by the thermal motion. Liquid line-shapes are therefore determined by the isotropic interactions.

How quickly a spin system comes to equilibrium within itself is described by the spin-spin relaxation time T_2. Since large interactions result in larger line-widths and faster relaxation to

equilibrium, it follows that T_2 has some relationship with the inverse of the line-width. In practice the measured line-widths are composed of not only the true dipole-dipole interaction, but also contains a contribution from the field inhomogeneity over the volume of the sample.

If an external radiation field is applied when there is thermal equilibrium between the spins and the lattice, the excess spin population of the lower level will result in more upward than downward transitions and a net absorption of energy. This will change the relative populations of the levels and thus increase the spin temperature. The spin lattice interaction, on the other hand, will try to maintain the spin temperature at the lattice temperature. The net result of these two competing processes can be described by the equation

$$\frac{dn}{dt} = -2Pn + \frac{n_o - n}{T_1} \tag{3.3}$$

where n is the population difference at time t and n_o is the population difference at equilibrium. P is the transition probability induced by the radiation field and given by

$$P_{m \rightleftarrows m-1} = \tfrac{1}{4}\gamma^2 H_1^{\,2}(I+m)(I-m+1)\, g(\nu) \tag{3.4}$$

where $g(\nu)$ is the line-shape function representing the distribution in energy of the transitions between $|m\rangle$ and $|m-1\rangle$. When the two processes balance the equilibrium population difference is given by

$$n_{eq} = \frac{n_o}{1 + 2\,PT_1} \tag{3.5}$$

The factor of $1+2PT_1$ by which n_{eq} is smaller than n_o is called the saturation factor. If $2PT_1 \ll 1$ the applied radiation field has a negligible effect on the population of the levels and the spin

temperature remains equal to the lattice temperature. For particular values of H_1 and T_1 the equilibrium rate of absorption of energy will be

$$\left(\frac{dE}{dt} \right)_{eq} = \frac{n_o \hbar \omega P}{1 + 2\,PT_1} \tag{3.6}$$

For small H_1, i.e. $2PT_1 << 1$, the rate of energy absorption is proportional to H_1^2. As the strength of H_1 increases the rate decreases and asymptotically approaches $n_o \hbar\omega/2T_1$. Experimentally, however, as a result of saturation, the detected signal approaches zero as H_1 becomes large. The detected signal normally is not the power absorption but rather a quantity related to the transverse magnetization produced by H_1.

Substituting Eqn. 3.4 for P into Eqn. 3.5 shows that the saturation factor is maximum at the peak of the resonance absorption curve. Saturation therefore would decrease the peaks more than the wings and therefore have a line broadening effect.

3.2.2 Classical View of Nuclear Magnetic Resonance

A fundamental problem in magnetism is the description of the behaviour of a free spin in a uniform magnetic field. This problem can be treated classically as well as quantum mechanically and provides an alternative view of the resonance phenomena.

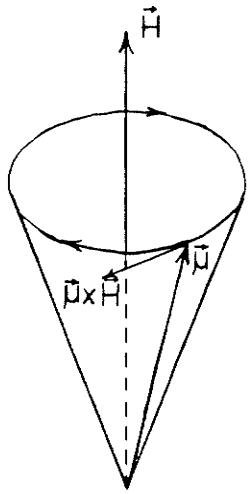

Fig. 3.2 Classical picture of a magnetic moment $\vec{\mu}$ precessing around a magnetic field, $\vec{H}$.

Classically a magnetic moment $\vec{\mu}$ in a field $\vec{H}$ experiences a torque of $\vec{\mu} \times \vec{H}$ which is also equal to the rate of change of its angular momentum. Since $\vec{\mu} = \gamma_N \hbar \vec{I}$, the equation of motion for the magnetic moment is

$$\frac{d\vec{\mu}}{dt} = \gamma_N \vec{\mu} \times \vec{H} \tag{3.7}$$

The use of a rotating co-ordinate system to solve the above equation was developed by Bloch (6) and Rabi, Ramsey and Schwinger (7). The time derivative of a time-dependent vector in a non-rotating frame of reference is given by

$$\frac{d\vec{A}}{dt} = \frac{\partial \vec{A}}{\partial t} + \vec{\omega} \times \vec{A} \tag{3.8}$$

where $\frac{\partial A}{\partial t}$ is the derivative computed in the rotating frame and ω is the angular velocity of the rotating frame. Combining Eqns. 3.7 and 3.8 yields the equation of motion of the magnetic moment in the rotating frame

$$\frac{\partial \vec{\mu}}{\partial t} = \gamma_N \vec{\mu} \times (\vec{H} + \frac{\vec{\omega}}{\gamma}) \tag{3.9}$$

where $(\vec{H} + \vec{\omega}/\gamma_N)$ is the effective field in the rotating co-ordinate system. For a field $H = H_o$, constant in time, the effective field vanishes in a frame rotating with $\omega = -\gamma_N H_o$ and the magnetic moment is fixed in this frame. Therefore, with respect to the laboratory frame the moment precesses with the Larmor frequency given by $\omega = -\gamma_N H_o$.

This result can be used to interpret the effect of the rotating magnetic fields used in nuclear magnetic resonance experiments. The rotating field H_1 is perpendicular to H_o and rotates with an angular velocity $-\omega$. Selecting the axis of the rotating system so that H_1 lies along the x-axis gives an effective field in the rotating frame of

$$\vec{H}_{eff} = (H_o - \frac{\omega}{\gamma_N})\,\hat{k} + H_1\hat{i} \qquad (3.10)$$

which is constant in time. Therefore the motion of the system is much simpler in the rotating co-ordinate system. The moment precesses about $\vec{H}_{eff}$ with an angular velocity $\gamma_N|H_{eff}|$. As seen in Fig. 3.3 the angle between $\vec{H}_{eff}$ and $\vec{H}_o$ is given by

$$\cos\theta = (\omega - \omega_o)/\gamma H_{eff} \qquad (3.11)$$

where $\omega_o = \gamma_N H_o$. When $\omega = \omega_o$, $\theta = 90^o$ and the moment can precess about $H_{eff} = H_1$, until it becomes anti-parallel to H_o. This frequency can be considered as the resonance frequency of the system.

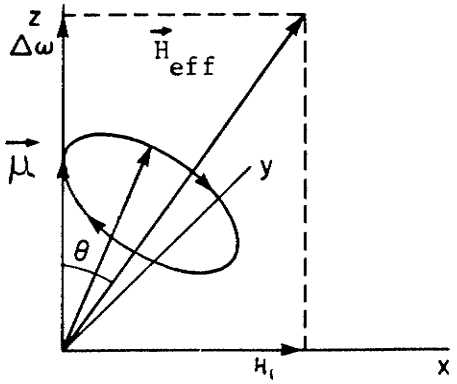

Fig. 3.3 The motion of the nuclear magnetic moment in the rotating frame.

It should be noted that it is possible to go to a second rotating co-ordinate system which rotates about $\vec{H}_{eff}$ such that the effective field in the doubly rotating system is reduced to zero. The problem then becomes trivial since with zero field there is no change in the orientation of the magnetic moment. Although oscillating rather than rotating fields are usually used in nuclear magnetic resonance experiments, the above procedure can be used to analyse these problems since an oscillating field is equivalent to two opposite rotating fields and only the component rotating in the same sense as the Larmor precession has an important effect.

Bloch (6) in 1946 proposed, for the description of the magnetic properties of ensembles of spins in an external field, a set of simple phenomenologically derived equations. These have proved to be not only of general qualitative use, but at least for liquids, have provided a correct quantitative description of the behaviour of this phenomenon.

Instead of considering a single dipole of moment $\vec{\mu}$, Bloch considered a collection of spins with a net magnetization $\vec{M}$ per unit volume in a field $\vec{H}$. In thermal equilibrium with the lattice, $\vec{M}$ has a magnitude M_o and is parallel to $\vec{H}$. The equation of motion of the nuclear magnetization is given by

$$\frac{d\vec{M}}{dt} = \gamma_N \vec{M} \times \vec{H} \qquad (3.12)$$

The trend of the magnetization towards equilibrium is described by the equation

$$\frac{dM_z}{dt} = \frac{M_o - M_z}{T_1} \qquad (3.13)$$

where T_1 is the longitudinal relaxation time. A component of the nuclear magnetization perpendicular to H_o, resulting from the application of an r.f. pulse for example, would decay at a rate given by the equations

$$\frac{dM_x}{dt} = -\frac{M_x}{T_2} \quad \text{and} \quad \frac{dM_y}{dt} = -\frac{M_y}{T_2} \tag{3.14}$$

where T_2 is the transverse relaxation time. It is assumed that the motion due to the presence of an applied d.c. field and a smaller r.f. field would be described by the equation

$$\frac{d\vec{M}}{dt} = \gamma\vec{M} \times \vec{H} - \frac{M_x\hat{i} + M_y\hat{j}}{T_2} - \frac{M_z - M_o}{T_1}\hat{k} \tag{3.15}$$

in the laboratory frame. In a frame rotating at the same rate as the applied r.f. field, ω, there is an effective static field

$$\vec{H}_{eff} = (H_o + \frac{\omega}{\gamma})\hat{k}' + H_1\hat{i}' \tag{3.16}$$

The equation of motion in the rotating frame is

$$\frac{d\vec{M}}{dt} = \gamma(\vec{M} \times \vec{H}_{eff}) - M_x'\hat{i}' + M_y'\hat{j}' - \frac{M_z - M_o}{T_1}\hat{k}' \tag{3.17}$$

The steady state solution is given by where $\Delta\omega = \omega - \omega_c$.

$$\begin{aligned} M_x' &= \frac{\Delta\omega\gamma H_1 T_2^2}{1 + (\Delta\omega T_2)^2 + \gamma^2 H_1^2 T_1 T_2} M_o \\ M_y' &= \frac{\gamma H_1 T_2}{1 + (\Delta\omega T_2)^2 + \gamma^2 H_1^2 T_1 T_2} M_o \\ M_z &= \frac{1 + (\Delta\omega T_2)^2}{1 + (\Delta\omega T_2)^2 + \gamma^2 H_1^2 T_1 T_2} M_o \end{aligned} \tag{3.18}$$

The transverse components in the laboratory frame are given by

$$\begin{aligned} M_x &= M_x' \cos\omega t - M_y' \sin\omega t \\ M_y &= M_x' \sin\omega t + M_y' \cos\omega t \end{aligned} \tag{3.19}$$

These components of the magnetization in the laboratory frame are functions of time and can induce a signal in a coil at the frequency ω. Bloch introduced the notation $u = M'_x$ and $v = -\gamma/|\gamma| \; M'_y = \pm M'_y$. Experimentally it is possible to detect u and v separately or in any combination of the two quantities. For negligible saturation, i.e. for $\gamma_N^2 H_1^2 T_1 T_2 \ll 1$, v is given by

$$v = -\pi |\gamma_N| H_1 M_o f(\Delta\omega) \tag{3.20}$$

where $f(\Delta\omega)$ is the normalized Lorentz shape function with half-width $1/T_2$. With saturation, v still has a Lorentz shape but becomes broadened such that

$$\frac{1}{T_2'} = \frac{1}{T_2}(1 + \gamma_N^2 H_1^2 T_1 T_2)^{\frac{1}{2}} \tag{3.21}$$

For small values of H_1, v is proportional to H_1, it is maximum when $\gamma_N^2 H_1^2 T_1 T_2 = 1$ and then decreases to zero as H_1 is increased further. Since $v_{max} = \frac{1}{2}(T_2/T_1)^{1/2} M_o$ and normally $T_2 < T_1$, the steady state transverse magnetization is less than M_o.

The function u is an odd rather than an even function of $\Delta\omega$, vanishes at resonance, and has a maximum and a minimum on either side of the resonance for $\Delta\omega = \pm 1/T'_2$. As H_1 increases, u_{max} grows steadily to an asymptotic value of $M_o/2\,(T_2/T_1)^{1/2}$.

The r.f. power absorbed by the spin system is given by

$$P = \frac{dE}{dt} = -\vec{M} \cdot \frac{d\vec{H}}{dt} \tag{3.22}$$

In the rotating frame $d\vec{H}/dt = \omega H_1 \hat{j}'$ and therefore the power absorbed becomes $\omega H_1 v$ which is the reason the quantity v is referred to as the absorption component. The quantity u, representing the dispersive component, remains finite for large H_1, and therefore when searching for signals in samples with unknown relaxation times it is advantageous to use strong r.f. fields and to detect this dispersive component.

It often happens that the inhomogeneity of the applied field

results in a spread in Larmor frequencies and consequently a linewidth much greater than that predicted by Eqns. 20 or 21. The dependence of v on H_1, that is, the saturation behaviour, is quite different in this situation since v then approaches an asymptotic value of $M_o T_2^*/(T_1 T_2)^{1/2}$ where $1/T_2^* = \gamma_N \Delta H$ is the half-width of the field inhomogeneity. It can therefore be concluded that it is not correct to account for the inhomogeneity by introducing into the Bloch equations a resultant transverse relaxation time. The fundamental difference in nature between the broadening expressed by $1/T_2$ in the Bloch equations and the broadening produced by inhomogeneities can be more clearly demonstrated using the spin echo methods.

3.3 Pulse Methods

The pulse technique was first introduced by Torrey (8) and Hahn (9). It is particularly useful for measurements to be made of T_1 and T_2 when other methods are unreliable or impractical, since the pulse methods allow a straight-forward measurement of the relaxation times. The major disadvantage of pulse techniques is that it requires more elaborate equipment than the steady state methods. The motion, except during the actual pulses, consists of a simple free precession of the spins, and therefore, the Bloch equations are simplified by the absence of H_1. The pulse methods can best be understood using a reference frame rotating at the precession frequency $\omega_o = -\gamma_N H_o$. The equilibrium magnetization $\vec{M}$ lies parallel to H_o in the z′ direction as shown in Fig. 3.4. At resonance $\vec{H}_{eff} = \vec{H}_1$ and the application of the field

$\vec{H}_1$ at frequency ω_o in the x′ direction means that in the rotating frame M′ precesses about H_1 in the y′-z′ plane as shown in Fig. 3.4 (b). The angle θ through which M′ moves depends on the length of time, Δt, the r.f. field is applied. Two cases are of particular interest. When $\theta = \pi/2$, the pulse length is $\Delta t = \pi/(2\gamma_N H_1)$ and after this "90°" pulse the magnetization lies in the x′-y′ plane. For $\theta = \pi$, the pulse is of length $\pi/\gamma_N H_1$, and after this pulse the magnetization is inverted provided $\Delta t \ll T_1$.

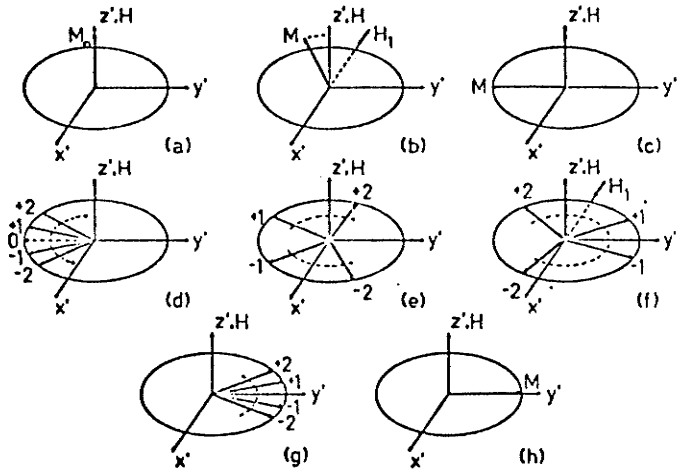

Fig. 3.4 Diagram illustrating the formation of both the free induction and the spin echo in the rotating frame as referred to in the text.

3.3.1 Free Induction Decay

Free induction decay is observed after the application of a 90° pulse to a spin system initially in thermal equilibrium. Ideally, the pulse duration is short compared to T_2 so transverse relaxation can be neglected during the pulse. This is easily satisfied for liquids, but for solids it is only satisfied if Δt ~ microseconds.

After a 90^{o} pulse the vector M′, of magnitude M_o, is rotating in the laboratory x-y plane and is therefore able to induce a voltage at the Larmor frequency in a coil in the x-y plane. Any particular spin will see a field, $H_o + h_1$, where h_1 is the local field resulting from dipole-dipole coupling, hyperfine interactions and the field inhomogeneity. Only those spins with $h_1 = 0$ will actually be stationary in the rotating frame. The others will gradually move relative to this set of spins, either clockwise or anti-clockwise, depending on the sign of h_1. The spins are often conveniently divided into groups of spins lying in a field range $H_o + \Delta h_1$ referred to as spin isochromats.

The vectors representing the individual spin isochromats fan out as shown in Fig. 3.4 (d) and so the net magnetization in the x′-y′ plane gradually falls to zero as does the induced voltage in the detecting coil. A pure exponential decay results from the application of an r.f. pulse exactly at the resonance frequency of a single type of nucleus.

If the r.f. frequency is slightly different from the Larmor frequency of the nuclei, then after the 90^{o} pulse M rotates relative to the rotating frame. The detector displays the interference signal between the exponentially decaying value of M_{xy} and the reference r.f. signal. For systems containing several nuclei of the same species, but differing in Larmor frequency because of chemical shifts and spin-spin coupling, interference effects can occur which are much more complex. For a single multiplet this "interferogram" is a regular beat pattern as illustrated in Fig. 3.5 (a) with the period of the beat pattern related

to the reciprocal of the frequency differences in the spectrum. For more complex spectra the FID interferogram is too complex to analyse by inspection. However, the free induction decay and the continuous wave spectrum obtained by conventional field or frequency sweep are Fourier transforms of each other (10), and this is the basis of the Fourier transform NMR method.

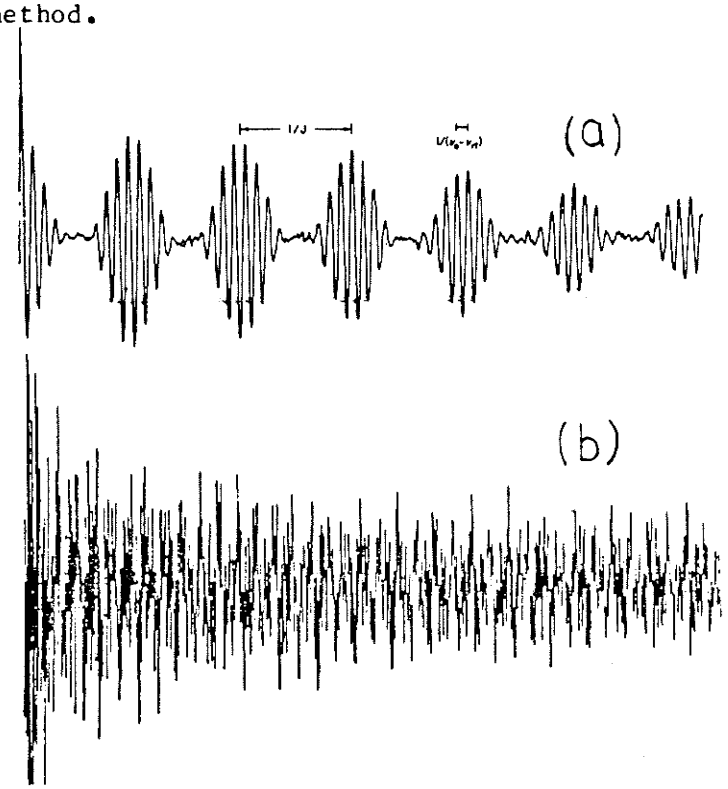

Fig. 3.5 Free induction decay interferograms illustrating the simple case of a single multiplet (C^{13} resonance CH_3I) (a) and a much more complicated case (C^{13} in progesterone) (b).

3.3.2 Double Pulse Methods

Any source of local field variations will contribute to the dephasing process responsible for free induction decay. The observed free induction time constant is related to the Bloch transverse

relaxation time T_2 and the inhomogeneity time $T_2^* \sim 1/\gamma\Delta H$ by the equation

$$\frac{1}{T_m} = \frac{1}{T_2} + \frac{1}{T_2^*} \tag{3.23}$$

If field inhomogeneity is the dominant source of dephasing then the size of the transverse magnetization of each spin isochromat is constant. However, if $T_2 < T_2^*$ then spin flips cause a rapid decrease in the size of the spin isochromats and a subsequent drop in the signal. It is assumed here, that T_1 is sufficiently long so as not to contribute to a reduction in the transverse magnetization.

3.3.3 Measurement of T_1

Either a 90°-τ-90° or 180°-τ-90° pulse sequence may be used to measure T_1. In both cases a second pulse is applied at a time τ after the first pulse. This second 90° pulse turns the component M_z which is growing at a rate of $M_z = (1 - \exp(-\tau/T_1))$ for the first case, and $M_z = (1-2\exp(-\tau/T_1))$ for the second into the x'-y' plane and a free induction signal is observed with amplitude M_z. The measurement of M_z as a function of τ gives a measure of T_1. For a wide-band spectrum, however, T_m may be less than the recovery time of the receiver from the shock of the pulse and the free induction decay will not be observable and therefore T_1 measurements are not possible using pulse methods.

4.3.5 The Formation of Spin Echoes

One of the most important sequences is the 90°-τ-180° double pulse sequence first proposed by Hahn (9) which leads to the formation of "spin echoes" and which can be used to measure T_2 without the additional contribution from field inhomogeneity. The effect of the first 90° pulse is identical to that discussed for the observation of free induction. The effect of a 180° pulse in the x′ direction will flip the individual isochromats through 180° about the x′ axis, but the direction and rate of precession will be unchanged (Fig. 3.4 (f)). The isochromat vectors now begin to come into phase along the y′ axis as shown in Fig. 3.4 (g). After a time τ after the second pulse the vectors coalesce so that the resulting value of M'_y is large and a correspondingly large voltage will be induced in the receiving coil in the laboratory frame. If transverse relaxation did not occur, the echo amplitude would be just as large as the initial value of the free induction following the 90° pulse. Otherwise each spin isochromat has a transverse magnetization which decreases with a time constant T_2, while the total transverse magnetization (i.e. free induction signal) decreases with a time constant T_m. The dephasing caused by field inhomogeneity is reversible however and therefore the echo amplitude decreases as $\exp[-2\tau/T_2]$ and T_2 can be determined from a plot of peak echo amplitude as a function of τ. In principle it is necessary to use a separate pulse sequence for each value of τ and to wait between pulse sequences an adequate time ($\sim 5T_1$) for restoration of equilibrium.

It should be noted that the sharpness of the echo will depend on the speed at which the isochromat components coalesce. The width of the

echo will therefore be inversely related to the linewidth. The resonance curve itself can be obtained by extrapolating the echo amplitude back to $\tau = 0$ to obtain the equilibrium magnetization. Plotting the equilibrium magnetization as a function of frequency will yield the resonance curve. It should also be noted that the spin echo is 180° out of phase with the r.f. pulses. Figure 3.6 shows a schematic diagram illustrating the spin-echo effect.

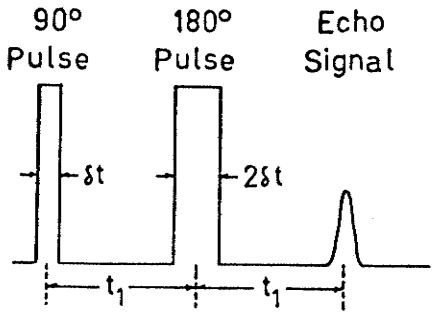

Fig. 3.6 A schematic diagram of the 90° and 180° r.f. pulses and the spin echo.

3.3.5 Multiple Pulse Methods

Many other ingeneous pulse sequences have been developed which have specific experimental applications. Any process which causes the spin isochromats to be dephased in a non-reversible manner will reduce the size of the echo. The diffusion of atoms through the sample to regions where H_o is different due to field inhomogeneity is one such process. Carr and Purcell (11) showed that a simple modification of Hahn's spin-echo method could reduce the effect of diffusion on the determination of T_2. This method, commonly referred to as a Carr-Purcell sequence, consists of a 90°-τ-180°-2τ-180°-2τ-180°

sequence. The advantage of this method is that the waiting time between sequences required in the unmodified spin-echo method is eliminated. Pulse methods can also be used to measure diffusion rates.

An inhomogeneity in H_1 can have a serious cumulative effect when using multi-pulse sequences. Meiboom and Gill (12) proposed a method of overcoming this problem which uses the same pulse sequence as the Carr-Purcell technique, but the 180° pulses are applied along the positive y′ axis, i.e. 90° out of phase with the initial 90° pulse.

In solids, static dipolar interactions between neighbouring nuclei and the resulting dipolar broadening make the observation of smaller interactions such as chemical shifts, Knight shifts and electron-coupled nuclear interactions impossible. The Hamiltonian for a dipolar interaction is

$$H_d = \sum_{i<j} \sum 2r_{ij}^{-3}(1 - 3\cos^2\theta_{ij})[\vec{\mu}_i \cdot \vec{\mu}_j - 3(\vec{\mu}_z)_i(\vec{\mu}_z)_j] \qquad (3.26)$$

where $\vec{r}_{ij}$ is the vector joining nuclei with magnetic moments $\vec{\mu}_i$ and $\vec{\mu}_j$, and has an angle θ_{ij} with respect to H_o which is along the z axis. For rapid random motion $(3\cos^2\theta_{ij} - 1)$ averages to zero. This term also goes to zero with sufficiently rapid rotation of the sample about an angle of $54^\circ\ 44'$. However, for strong interactions, speeds of ~ 10^5 rev/sec are required which is not experimentally feasible. Waugh et al (13) have shown that in the rotating frame the spins can be rotated in this way by the following pulse cycle: $[90^\circ_{x'}, 2\tau, 90^\circ_{-x'}, \tau, 90^\circ_{y'}, 2\tau, 90^\circ_{-y'}, \tau]$. At the end of the cycle $\vec{M}$ is again along the z′ axis and during the cycle it has spent one-third of its time along each axis. Since $\vec{\mu}_i \cdot \vec{\mu}_j$ depends only on the

relative orientations, this term is unaffected by the rotation of $\vec{M}$. However, the second term must be averaged over the three orientations and becomes $1/3\ \vec{\mu}_i \cdot \vec{\mu}_j$ and thus $H_d = 0$.

CHAPTER 4

Nuclear Resonance in Ferromagnetic Materials

4.1 Introduction

The first successful nuclear magnetic resonance experiments in bulk materials were reported in 1946 by Bloch, Hansen and Packard (1) using protons in water, and by Purcell, Torrey and Pound (2) using protons in solid paraffin. Since that time both the steady state techniques developed by these workers, as well as pulsed NMR methods, have been used extensively to measure the hyperfine fields of transition metal ions in insulating materials such as the magnetic oxides. A full understanding of the nature of the hyperfine field for these transition metal ions seems to be of fundamental importance for the interpretation of the NMR spectra obtained for more complicated materials such as metals and intermetallic compounds.

Gossard and Portis (3) were the first to report the observation of nuclear magnetic resonance in a ferromagnet. A strong resonance was detected at room temperature in a sample of f.c.c. cobalt powder. The possibility of observing nuclear magnetic resonance in ferromagnetic materials provided a new technique for the investigation of ferromagnetism.

Because of the small magnitude of the nuclear moments, the application of NMR is limited in general to the study of materials in which the resonant nuclear moments are present in relatively high

numbers. The usefulness of this technique depends on the modification of the frequency, line shape and relaxation behaviour of the resonance which arise from the static as well as dynamic hyperfine effects. The large abundance of resonant nuclei required would appear to make the NMR technique especially useful for the study of the hyperfine interactions in solids. However, the small r.f. skin depth as well as the large linewidths limits the signal strengths in metals.

The Hamiltonian of a nuclear spin I and an electronic spin S in a magnetic field H_o can be written as

$$H = -\gamma_n \hbar \vec{I} \cdot \vec{H}_o - \gamma_e h \vec{S} \cdot \vec{H}_o + \vec{I} \cdot [A] \cdot \vec{S} \qquad (4.1)$$

where A is the symmetric second rank hyperfine tensor. In general, the correlation time τ_c of the electron spin fluctuations is shorter than the nuclear Larmor precession period in the electronic field ($\tau_c^{-1} > |AS/h|$). The nuclear magnetization, therefore, responds only to the average electronic field, which is proportional to the average value of the spin, $\langle S \rangle$. Therefore, the effective nuclear Hamiltonian is

$$H_n = -\gamma_n \hbar \vec{I} \cdot \vec{H}_o + \vec{I} \cdot [A] \cdot \langle S \rangle \qquad (4.2)$$

For an isotropic A the resonance frequency becomes

$$\omega_o = |\gamma_n H_o - (A/\hbar)\langle S_z \rangle| \qquad (4.3)$$

In the paramagnetic state $\langle S \rangle$ averages to zero and an external field must be applied in order to observe a resonance. For S-state ions $\langle S^z \rangle$ is then proportional to χH_o, where χ is the magnetic susceptibility. Since $\langle S \rangle$ is usually small compared to the instantaneous value of S, the amplitude of the spin fluctuations $\delta S = S - \langle S \rangle$ is very large. The observation of NMR is possible, however, only if the field seen by the nuclear spins has a sufficiently sharp value.

That is, it is necessary that the spectral intensity of the spin fluctuations at the nuclear frequency ω_o be sufficiently small. For times less than the correlation time, τ_c, the effect of the fluctuations can be considered negligible. Therefore, the highest frequency for which the spectral intensity has a significant magnitude is given by the cut-off frequency $\omega_c \approx \tau_c^{-1}$. The correlation function $G_{ij}(\tau)$ is related to the spectral density function $J_{ij}(\omega)$ by

$$G_{ij}(\tau) = \frac{1}{2\pi} \int_{-\infty}^{\infty} J_{ij}(\omega) \exp(i\omega\tau) d\omega \tag{4.4}$$

However, the integrated intensity is given by $\langle(\delta S)^2\rangle$ and

$$\langle(\delta S)^2\rangle = G(o) = \int_{-\infty}^{\infty} J(\omega) d\omega \approx 1/3S(S+1) \tag{4.5}$$

Therefore, the integrated intensity is independent of τ_c and it follows that $J(\omega_o)$ becomes smaller as τ_c decreases because the fluctuations are distributed over a wider frequency range.

In dilute paramagnetic crystals τ_c is usually not sufficiently small to observe a resonance. In concentrated crystals, however, the electronic exchange interaction $H_E = -\sum_{ij} J_{ij} S_i S_j$ may greatly decrease the electronic correlation time, and thus narrow the resonance. Because of the requirement of a high exchange frequency, NMR experiments involving magnetic ions are easier to observe in materials having a relatively high ordering temperature. For example, NMR has been observed for Co^{59} in CoO and $KCoF_3$ (4) and for Mn^{55} in MnO, MnS and MnSe (5). Since transferred hyperfine fields are usually much smaller than direct hyperfine fields, the requirement of a high exchange frequency is considerably reduced for the observation of the resonance

of a non-magnetic ion with magnetic neighbours, as is the situation for F^{19} in K_2NaCrF_6, $KMnF_3$ and $KNiF_3$ (6).

Below the magnetic ordering temperature the long range electronic spin ordering results in a time-averaged <S> which is non-zero even without an applied magnetic field. In the absence of quadrupolar interactions the nuclear Hamiltonian is given by

$$H_n = -\gamma_n \hbar \vec{I} \cdot \vec{H}_{eff} \tag{4.6}$$

where

$$\vec{H}_{eff} = \vec{H}_o + \vec{H}_{dip} + \vec{H}_{hf} \tag{4.7}$$

The dipolar and hyperfine fields are proportional to the thermal average value of the electronic magnetic moment. The NMR frequency, therefore, can be used to measure the average magnetization at specific lattice sites as a function of variables such as temperature, pressure and magnetic field. This would be particularly useful in anti-ferromagnetic systems since the macroscopic magnetization vanishes with no external field.

4.2 The Observation of NMR in Magnetically Ordered Materials

The observation of NMR in the ordered state is facilitated by a large enhancement of the transverse r.f. field which is associated with the large magnitude of <S>. This conclusion was arrived at by Portis and Gossard (7) after a study of the saturation behaviour of the f.c.c. Co resonance.

Redfield, (8) in his paper on the nuclear resonance in metals, found that the response of the nuclei to the r.f. field was linear up

to field intensities corresponding to the condition $\gamma^2 H_1^2 T_1 T_2 \sim 1$, the usual Bloch result. At higher intensities, he obtained the surprising result that the resonance line became narrow and the absorption signal saturated while the dispersion signal continued to increase linearly. This is referred to as intermediate saturation. Final saturation develops when the r.f. field becomes comparable to the linewidth. At r.f. fields greater than this the dispersion line broadens and the signal saturates. Redfield also found that if the signal is measured as a function of modulation frequency in the intermediate saturation region, the signal decreases at higher modulation frequencies. The frequency at which the signal is reduced to $1/\sqrt{2}$ of its low frequency value corresponds to the spin-lattice relaxation rate. Redfield also showed that the apparent spin-lattice relaxation increases as the sample enters intermediate saturation. The Redfield analysis assumed that the linewidth is determined by spin-spin relaxation.

Portis and Gossard observed a dispersive line-shape and could detect no change in linewidth or line-shape at the lowest powers possible. They concluded that the line was inhomogeneously broadened and the variation in the sample losses was produced primarily by the real part of the susceptibility. Portis and Gossard did, however, observe the expected effect of saturation on the spin-lattice relaxation time, but for a value of the saturation parameter $\gamma^2 H_1^2 T_1 T_2$, six orders of magnitude less than expected. Either the relaxation times are very much longer than expected, or the r.f. fields seen by the nuclei are very much larger than the applied r.f. field. An observation of

final saturation confirmed that the driving field seen by the nuclei was enhanced by a factor of approximately 1000.

In order to explain the lineshape Portis and Gossard suggested that although the dominant sample losses are associated with wall motion (9), the torques exerted by the nuclei back on the wall could modulate these losses by as much as several per cent of the total wall losses. In an earlier paper Gossard and Portis (3) had reported that the resonance signal drops off much more rapidly than does the square of the transverse susceptibility, from which they concluded that domain wall processes make an important contribution to the resonance signal.

The mechanism producing the tremendous enhancement of the driving field is the indirect excitation of the nuclei via the electron-nuclear hyperfine coupling. The enhancement factor is directly proportional to the angle through which $\langle S \rangle$ (and therefore H_{hf}) is turned by the transverse r.f. field. In a magnetic crystal the resonant response thus depends on the magnetization process in the material.

In multi-domain samples the primary magnetization process is the displacement of the domain walls. Only nuclei located within domain walls will be excited under these circumstances. For single-domain ferromagnetic particles or for magnetically saturated samples the principal magnetization process is rotation of the magnetization.

The simplest case of this type of indirect excitation corresponds to excitation of the nuclear resonance in a single domain particle, in which the nuclear spins are quantized along an axis defined by the direction of the electronic magnetization. This direction

coincides with the direction of the magnetizing field, H, which consists of both the effective anisotropy field H_A and the external field H_o. It is also assumed that the electron resonance frequency is much larger than the nuclear magnetic resonance frequency. The application of a small transverse r.f. field, H_x, then produces an angular rotation of H_{hf}, the hyperfine field, of

$$\theta = \tan^{-1} H_x/H \approx H_x/H \tag{4.8}$$

The resulting transverse component of the hyperfine field varies at the excitation frequency and produces an effective driving field of

$$\begin{aligned} H_x^{eff} &= H_x + H_{hf}^x = H_x + H_{hf} \sin\theta \\ &= H_x + \frac{H_{hf}}{H} H_x = (1 + \eta) H_x \end{aligned} \tag{4.9}$$

The driving field is enhanced by a factor $\eta = H_{hf}/H$, which is directly proportional to the hyperfine field and inversely proportional to the field supplying the restoring torque. Since usually $H_{hf} >> H$, the enhancement factor can be quite large. Gossard and Portis (3) generously estimated η to be of the order of 100 in f.c.c. Co and initially accounted for the strength of the observed absorption in this manner. However, this value of η turned out to be at least an order of magnitude too small.

Thus the resonance enhancement in unmagnetized ferromagnetic materials such as f.c.c. Co must be the result of a different magnetization process. Nuclei lying in the domain walls will be driven by r.f. fields sufficiently large to account for the observed enhancement factors, as will be shown in the next section.

Gossard et al (10) have developed an expression for the nuclear

magnetic absorption in ferromagnetic materials, and found that the steady state signal intensity is not simply proportional to χ_n'' x $(H_x^{eff})^2$ and thus $\chi_n''\eta$ because of the hyperfine coupling between the electronic and nuclear magnetizations.

The absorption rate for the combined electron-nuclear system is given by

$$\overline{P} = \tfrac{1}{2}\,\mathrm{Re}\{i\omega(H_n m_x + H_e M_x)\} \tag{4.10}$$

where H_n and H_e are the effective transverse fields seen by the transverse components of the nuclear and electronic magnetizations m_x and M_x, respectively. The magnetizations are related to the effective fields by the complex transverse susceptibilities χ_n and χ_e.

$$m_x = \chi_n H_n \quad \text{and} \quad M_x = \chi_e H_e \tag{4.11}$$

H_n is given by Eqn. 4.9 and H_e is given by

$$H_e = H_x + H_{hf}(m_x/|M|) \approx H_x \tag{4.12}$$

Since the nuclear resonance frequency ω_o is generally far from the electronic ferromagnetic resonance, χ_e will be diagonal and the power absorption is given by

$$\overline{P} = \tfrac{1}{2}\omega_o H_x^2\{\chi_n''[1 + \eta^2] + \chi_e''[1 + 2(\chi_n'/\chi_e')\eta^2]\} \tag{4.13}$$

The absorption rate at ω_o therefore contains two components. The first is the ordinary nuclear absorption χ_n'', enhanced by the hyperfine coupling. The second part consists of the electronic losses, χ_e'', which are modulated by the real part of the nuclear susceptibility, χ_n'. At high power levels the nuclear resonance therefore has a dispersive shape since χ_n'' saturates more easily than χ_n'.

The mechanism producing the large enhancement of an external r.f. field by the motion of a domain wall can be understood by considering a spherical particle with a single domain wall at its centre.

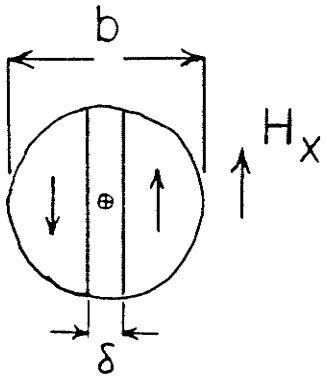

Fig. 4.1

The direction of the magnetization in the domains is assumed to be an easy direction. When an external field, H_x, is applied parallel to the wall's surface, the wall will be displaced along a direction perpendicular to the wall. If the effect of internal imperfections is small, the wall displacement will be limited by the increase in demagnetizing energy. For a particle of radius b

$$\frac{z}{b} \approx \frac{H_x}{\frac{1}{2}DM_s} \tag{4.14}$$

where D is the demagnetizing factor and M_s is the saturation magnetization. Each spin in the wall is rotated through an angle

$$\theta = \pi z/\delta \tag{4.15}$$

where δ is the width of the 180° wall. The magnitude of the r.f. field at the nucleus will be

$$\begin{aligned} H_{xn} &\approx \theta H_{hf} \\ &\approx \frac{2\pi}{\delta} \frac{H_x b}{DM_s} H_{hf} \end{aligned} \tag{4.16}$$

The enhancement factor is therefore

$$\eta = \frac{H_{xn}}{Hx} \qquad (4.17)$$

$$= \frac{2\pi}{\delta} \frac{b}{DM_s} H_{hf}$$

Using appropriate values of the constants gives $\eta \sim 1200$ in reasonable agreement with the experimental results for Co.

To obtain a theoretical expression for the NMR signal intensity due to domain-wall enhancement, Gossard et al (10) considered the equation of motion for the domain wall

$$\mu \frac{d^2z}{dt^2} + \beta \frac{dz}{dt} + \alpha z = 2M_s H_x - \frac{dU}{dz} \qquad (4.18)$$

where z is the position of the wall, μ is the wall mass, β is the damping constant, and α is the stiffness constant of the wall. The right-hand-side of Eqn. 4.18 represents the pressure on the wall, where M_s is the saturation magnetization and H_x is the external applied field. The second term is due to the hyperfine interaction which has an energy density given by

$$U = - \frac{H_{hf}}{M_s} (\vec{M}_s \cdot \vec{m}) \qquad (4.19)$$

The above result assumes that for small amplitude motion the damping will not seriously modify the magnetization in the wall (11).

The important consideration in wall-enhanced NMR is the way in which the nuclear spins modify the equation of motion of the wall. For small amplitude periodic motion the pressure on the wall is given by (11)

$$- \frac{dU}{dz} = 2H_{hf}^2(\chi_n' - i\chi_n'')z \int \left(\frac{d\theta}{dz} \right)^2 dz'$$

$$= (\varepsilon' - i\varepsilon'')z \qquad (4.20)$$

Then for a periodic driving field the wall displacement is obtained from a solution of Eqn. 4.18

$$z = -\frac{2M_s H_x}{(\alpha - \varepsilon' - \omega^2\mu) + i(\omega\beta + \varepsilon'')} \tag{4.21}$$

The energy dissipation is given by

$$P = \tfrac{1}{2}\mathrm{Re}\{2i\omega z M_s H_x\}$$

$$\approx 2\omega_n M_s^2 H_x^2 \frac{\omega\beta + \varepsilon''}{\mu^2(\omega_w^2 - \omega_n^2 - \frac{\varepsilon'}{\mu})^2 + (\omega\beta + \varepsilon'')^2} \tag{4.22}$$

where $\omega_w = (\alpha/\mu)^{1/2}$ is the wall resonance frequency. Equation 4.22 can be simplified to

$$P \approx P_o[1 + m\chi_n'] \tag{4.23}$$

where

$$P_o = 2\omega_n^2 M_s^2 H_x^2 \frac{\beta}{\mu^2} \frac{1}{(\omega_w^2 - \omega_n^2)^2}$$

$$m = \frac{1}{\omega_w^2 - \omega_n^2} \frac{2H_{hf}^2}{\mu} \int \left(\frac{d\theta}{dz'}\right)^2 dz' \tag{4.24}$$

Equation 4.23 clearly shows that the steady-state NMR signal has a dispersion-like character. The index m changes its sign depending on whether the wall resonance frequency, ω_w, is larger or smaller than the nuclear resonance frequency ω_n. Hirai et al (12) have studied the nuclear resonance signal in α-Fe_2O_3 and found that the observed signal originates from two types of walls. One type, called a movable wall, is predominant in well-annealed samples around zero field. It has a relatively small stiffness constant, α, and a correspondingly small wall resonance frequency. Hirai found that the detected signal had a negative phase and therefore for these walls $\omega_w < \omega_n$. The second type

of wall is one that is trapped at some sort of impurity in the crystal. This type is more difficult to sweep out of the sample with an external field and for hematite the wall stiffness constant was so large that $\omega_w > \omega_n$. The detected signal had positive phase. For a particular external field (applied along c-axis and parallel to the applied r.f. field) Hirai found that the NMR signal consisted of two signals of opposite phase superimposed. The NMR signal with $m > 0$ had a narrower linewidth than the signal with $m < 0$ because the latter (corresponding to the mobile walls which have a larger enhancement factor) had already suffered from saturation broadening.

4.4 Enhancement in Pulse NMR Experiments

In pulse NMR experiments the enhancement has two effects. The magnitude of the required driving field is reduced by a factor $(1 + \eta_1)$ and also, after the removal of the excitation, the precessing nuclear magnetization induces through the hyperfine interaction a coherent precession of the electronic magnetization. The total transverse magnetization is $m_x(1 + \eta_2)$ and the enhancement of the induced signal in the receiver coil is therefore given by $1 + \eta_2 = 1 + \Delta M/\Delta m$. .

For the domain enhancement mechanism the driving and the response enhancement factors, η_1 and η_2, are equal. This is not the case for domain wall enhancement, however. A general expression for the driving field enhancement for domain walls can be obtained using Eqn. 4.18. For this calculation the pressure due to the hyperfine

interaction can be neglected and therefore setting $\epsilon' = \epsilon'' = 0$ in Eqn. 4.21 allows the effective r.f. field at the nucleus to be determined.

$$H_x^{eff} \approx H_{hf} \frac{d\theta}{dz'} z = 2H_{hf}M_s \frac{d\theta}{dz'} \frac{(\alpha - \mu\omega^2) - i\beta\omega}{(\alpha - \mu\omega^2)^2 + \beta^2\omega^2} H_x \qquad (4.25)$$

where θ is the angle between the electronic spin in the domain wall and the easy axis and z' is the direction of the wall displacement. For a 180^o wall

$$\frac{d\theta}{dz'} \approx \frac{1}{\delta} \sin\theta \qquad (4.26)$$

and therefore the rate of spin rotation in a wall is not uniform as assumed in the simple calculation first considered. Then

$$|\eta_1| = \frac{H_x^{eff}}{H_x} = \frac{2H_{hf}M_s \sin\theta}{\mu\delta[(\omega_w^2 - \omega_n^2)^2 + (\beta/\mu)^2\omega_n^2]^{\frac{1}{2}}} \qquad (4.27)$$

where δ is the wall thickness, ω_n is the nuclear resonance frequency and $\omega_w = (\sigma/\mu)^{1/2}$ is the wall resonance frequency.

The response enhancement factor, $\eta_2 = \Delta M/\Delta m$, results from the interaction of the oscillatory component of the nuclear magnetization (transverse to the hyperfine field or the electronic magnetization) with the domain wall through the second term on the right hand side of Eqn. 4.18. The pressure on the wall is given by

$$H_{hf} \int \frac{d\theta}{dz'} m_\perp(z')dz' \qquad (4.28)$$

and the resulting displacement in the wall in anology with Eqn. 4.22 is

$$z = H_{hf}\langle m_\perp \rangle \frac{(\alpha - \mu\omega_n^2) - i\beta\omega_n}{(\alpha - \mu\omega_n^2)^2 + \beta^2\omega_n^2} \qquad (4.29)$$

where $$\langle m_{\perp} \rangle = \frac{1}{\delta} \int_{-\infty}^{\infty} m_{\perp}(z') \sin\theta \, dz'$$

The oscillating total magnetic moment produced by the wall displacement per unit volume is $\Delta M = 2M_s Az/V$, where A is the wall area and V is the volume of the particle. The response enhancement factor is then given by

$$\eta_2 = \frac{\Delta M}{\Delta m} = \frac{\Delta M}{\langle m_{\perp} \rangle}$$

$$= \frac{2H_{hf}M_s A}{V} \frac{1}{\mu[(\omega_w^2 - \omega_n^2)^2 + (\beta/\mu)^2\omega_n^2]^{\frac{1}{2}}} \qquad (4.30)$$

It should be noted that η_2 is smaller than η_1 by the factor $A\ell/V$.

4.5 The Distortion of Lineshapes due to the Enhancement Effect

Domain wall enhancement of the NMR signals in ferromagnetic materials has made it possible to observe many weak resonances. It has been particularly useful in the study of impurities in ferromagnetic metals. However, the enhancement mechanism often resulted in unknown distortions of line-shapes and intensities. In particular it then becomes difficult to use intensities to identify sites.

Mendis and Anderson (13) suggested that steady state fast passage techniques would allow a direct measurement of the distribution of hyperfine fields without distortion by enhancement effects. This suggestion was based on the analysis by Portis (14) of the effects of fast passage on the electron spin resonance signal. Portis obtained a power series expression in the parameter ϵ for the dispersive part of the r.f. susceptibility.

$$\chi'(\omega) = \tfrac{1}{2}\pi\chi_o\omega \frac{d}{d\omega_o}\left\{\frac{2}{\pi}\int_o^\infty \frac{\omega' G(\omega',\omega_o)d\omega'}{\omega'^2 - \omega^2} \times \gamma H_m \cos(\omega_m t)\right.$$

$$\left. + \tfrac{1}{4}\pi\chi_o\omega \cos\phi_1 \sin(\omega_m t - \phi_1) \times \varepsilon G(\omega-\omega_o) + O(\varepsilon^3)\right. \qquad (4.31)$$

The parameter $\epsilon = \omega_m H_m T/H_1$, where ω_m is the modulation frequency, H_m is the modulation field, T is the relaxation time, and H_1 is the r.f. field seen by the resonant spins. $G(\omega-\omega_o)$ is the normalized distribution function of local magnetic fields around $\omega_o = \gamma H_o$ and $\phi_1 = \tan^{-1}(\omega_m T)$. The first term is the derivative of the dispersion signal associated with the distribution in the local fields which is in phase with the modulation. The second term is the rapid passage contribution to the signal which is directly proportional to the distribution and approximately 90^o out of phase with the modulation. The second term thus gives a direct measure of the hyperfine distribution and can easily be detected in ESR using a bridge spectrometer.

The situation for NMR in ferromagnetic materials is more complex, since as was indicated in section 4.2, the detected signal has two contributions. Usually the effective r.f. field at the nucleus is large enough to saturate χ_n'' and one detects only χ_n' via its modulation of the intrinsic wall losses. The observed signal is then proportional to the sample losses, $\chi_n' \eta^2 H_{rf}^2$, where η is the r.f. enhancement factor.

It was indicated in Eqns. (4.25) and (4.26) that the enhancement depends on $d(\theta)/dz'$ which in turn depends on the structure of the domain wall. For a 180^o wall $d(\theta)/dz'$ is largest at the wall

center. When the wall is displaced a distance z by the application of a magnetic field, the electronic spins will rotate through an angle (ϑ) = $d(\theta)/dz'$ z generating a transverse r.f. field at the nucleus of magnitude $H_{hf}\theta$. However, if the hyperfine field is anisotropic the enhancement factor will not only depend on the position within the wall but also is an implicit function of the resonant frequency. Butler (15) has re-examined the fast passage derivation including the frequency dependence of H_1. The fast passage signal is then proportional to $\eta(\omega)\ G(\omega - \omega_o)$ which may be considerably different than the distribution in local fields alone, in ferromagnets with significant anisotropy in their hyperfine fields. We will present a simple argument in chapter 6 that indicates that pulse NMR is not prone to this type of distortion.

Butler also found that large values of γH_1 will also distort the spectra. When γH_1 becomes comparable to any splitting, the spectrum is smeared so that the lines are no longer resolved. This is, in fact, the case for both steady state and pulse NMR.

4.6 NMR Spectra in Ordered Magnetic Materials with an Anisotropic Hyperfine Field

The observation of two NMR peaks from a single site in a magnetically ordered material containing domain walls was first reported in the early 1970's (16-21). This possibility was first suggested by Turov, Tankeyev and Kurkin (22,23) following a general theoretical treatment of the problem of NMR in a multi-domain ferromagnetic which concluded that for an anisotropic hyperfine field it is possible that there exist two resonances enhanced by wall motion, one arising from

nuclei at the wall centre and one arising from nuclei at the wall edge. The steady state spectra obtained consisted of a single, broad, intense resonance (called the "b" resonance) and a quadrupole split (2I narrow peaks were observed where I is the nuclear spin) so-called "a" resonance. Of particular interest is that the b resonance could not be observed using the spin-echo technique for the Cr^{53} resonance in $CrBr_3$ (21),and the Mn^{55} and P^{31} resonances in MnP (17). Similar results were obtained for MnB (16), MnBi (18) and hcp Co (20) although in reference (18) an additional sharp peak was observed with the spin-echo technique which presumably was the b resonance although it was not identified as such, and in reference (20) no transient experiments were reported. The explanation for the failure to observe the transient b resonances was that either the relaxation times T_1 (17) or T_2 (21) was considerably shorter for the b resonance. This is consistent with the prediction made by Winter (24) and Weger (25) concerning relaxation effects in domain walls and thus was a preliminary indication that the b resonance was a wall centre resonance.

It had been believed, initially, (26,27) that the so-called "a" and "b" resonances of $CrBr_3$, for instance, were domain rotation enhanced and wall displacement enhanced, respectively. Later it was felt that the b resonance came from the motion of spins in domains of closure (28). Closure domains are energetically unfavourable, however, because of the large values of K/J where K is the anisotropy energy and J is the exchange energy.

To unambiguously determine the location of the spins which contribute to the resonances, several different approaches have been

taken. Cobb et al (21) used two steady-state techniques, the fast passage (29) and rotary-saturation (8,30) methods, to measure η and found that the enhancement factors measured for both resonances were much too large to be accounted for by any other process except domain wall motion.

Nagai et al (17) studied the Mn^{55} and P^{31} resonances in the intermetallic compound MnP which has an orthorhombic crystal structure with an easy axis of magnetization along the c-axis. Neutron diffraction measurements indicated that all Mn moments are equivalent in the ferromagnetic state (31,32). Figure 4.2 shows the observed resonances at two different temperatures with the low frequency Mn^{55} resonance consisting of five well-resolved lines with an equal spacing. The lines were of comparable intensity but strongly dependent on the relative orientation of the r.f. field to the domain walls, the strongest signal occurring with H_{rf} applied along the c-axis. The relative intensity was independent of the direction of the r.f. field, however. If any of the resonances were enhanced by the domain rotation mechanism the intensity would be strongest for H_{rf} perpendicular to the c-axis. It was also observed that the application of a field parallel to the c-axis decreased the intensity of all resonances much more quickly than predicted for domain rotation enhanced signals (Eqn. 4.9). It, therefore, was concluded that all resonances were enhanced by domain wall motion.

In order to finally identify the orientation of the electronic spins in the domain wall whose nuclei contribute to the observed resonances, Cobb et al (21) measured the field dependence of the "a" and

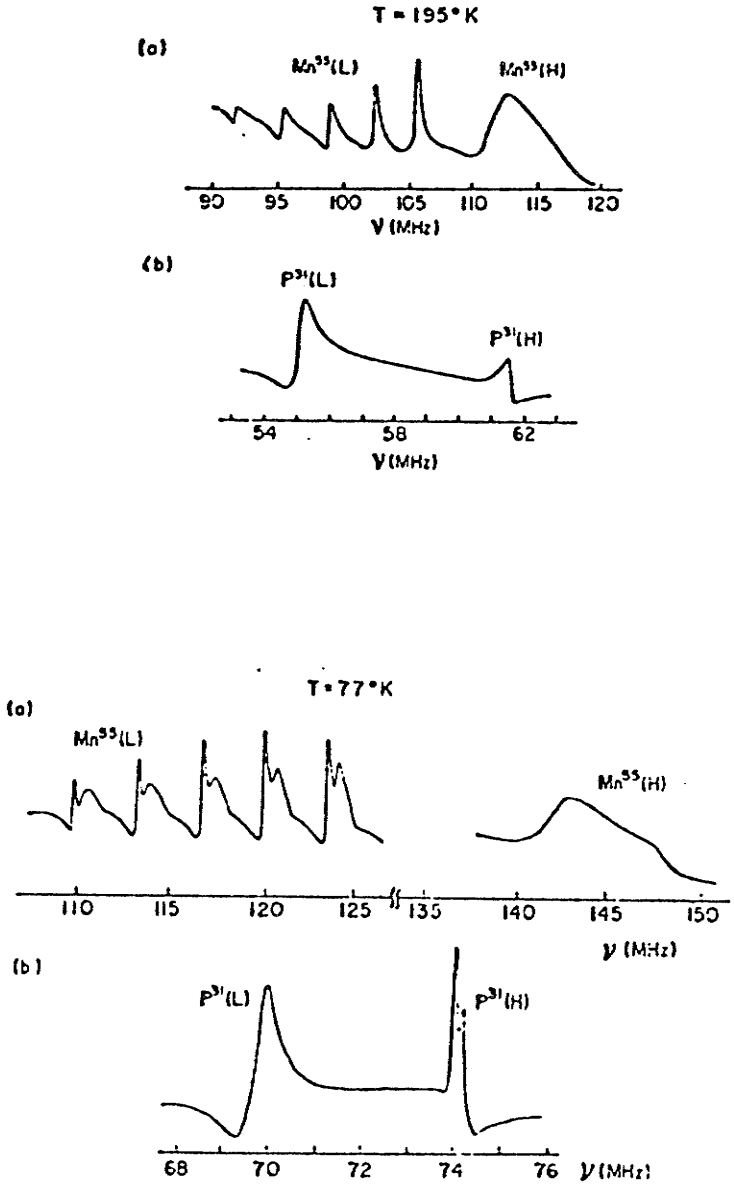

Fig. 4.2 The Mn^{55} and P^{31} resonances in the intermetallic compound MnP as obtained by Nagai et al (Ref. 17).

"b" resonance frequencies for a field applied parallel and perpendicular to the c-axis. The difference in the degree of penetration of the external field due to demagnetizing effects allows the orientations to be determined. This, in fact, is closely related to the technique we have used for the identification of resonances observed in the RCo_5 compounds which will be discussed in the next chapter. Cobb et al, also found that the field dependence of the quadrupole splitting produced results consistent with the frequency measurements. The application of a field perpendicular to the c-axis varied the splitting of the "a" resonance consistent with an angular dependence.

$$\Delta\nu(\theta) = \frac{e^2qQ}{4h} (3 \cos^2 \theta - 1) \qquad (4.32)$$

where q is the electric field gradient, Q is the quadrupole moment and is the angle between the electronic spin moment and the c-axis and is given by $\sin\theta = H_o^{\perp}/(H_A + H_d^{\perp})$. For $\theta = 90^o$, $\Delta\nu(\pi/2) = 1/2\ \Delta\nu(0)$ as expected and it was also observed that the b resonance developed a quadrupole splitting as the field increased with a field independent splitting of exactly $1/2\ \Delta\nu(0)$. Hence the "a" resonance must be associated with nuclei of spins at the wall edge and the "b" resonance with spins at the wall centre.

An important type of NMR experiment on ordered magnetic materials involves the measurement of the temperature dependence of the zero-field frequency. In many situations the hyperfine coupling constants are independent of temperature over a large enough range of temperature. The measured frequency is then proportional to the sub-lattice magnetization, and can therefore be compared at low

temperatures with the predictions of the spin-wave theory, since

$$\nu(T) = \nu(0)[1 - (\langle n \rangle / \langle S \rangle_{T=0})] \sim T^{3/2} \qquad (4.33)$$

at low temperature where $\langle n \rangle$ is the thermal average value of the spin deviation. In cases where the hyperfine coupling constants are not constant because of thermal expansion it is useful to combine temperature dependence measurements with pressure dependence measurements of the NMR frequencies (33-35). Calculations by Suhl (36) and Winter (24) first indicated that the temperature dependence of the magnetization in the wall should decrease more rapidly than the magnetization in the domain. The important effects influencing the wall magnetization are (1) scattering of spin waves by walls, (2) propagation of spin waves entirely within the walls, and (3) thermal excitations of wall translations. Calculations indicated a linear temperature dependence of the difference between the wall and domain magnetizations is expected.

Nagai et al (17) observed the temperature dependence of the resonant frequencies and found that the Mn^{55} (L) and P^{31} (H) frequencies vary with temperature nearly proportional to the saturation magnetization, while the Mn^{55} (H) and P^{31} (L) NMR frequencies decreased at a significantly faster rate. These results thus indicated that the Mn^{55} (L) and P^{31} (H) resonances were domain-wall-edge resonances and the Mn^{55} (H) and P^{31} (L) resonances were domain-wall-centre resonances.

The Co^{59} resonance in hcp Co was first observed by Koi et al (37), who found that the domain-wall-centre resonance occurred at 228 MHz. Kawakami et al (20) first identified the wall edge resonance in

1972 by measuring the temperature dependence of the two observed resonances. Magnetic (38,39) and neutron diffraction (40) measurements showed that the easy direction of magnetization in hcp Co rotates from the c-axis to a direction in the c-plane between 519 K and 598 K. The observed temperature variation of the wall edge resonance would reflect this spin rotation by increasing in frequency and becoming equal to the wall centre frequency as the spin rotation is completed.

Interestingly the anisotropy in the hyperfine field decreased with increasing temperature indicating that an anisotropy in the spin magnetic moment in the wall is not the major contributor to the anisotropy in the hyperfine field. Using Winter's theory Kawakami estimated this at 0.2 kOe at 500° C compared to a residual anisotropy , $H_{//} - H_{\perp}$ of 5 kOe. At 4.2 K the measured anisotropy was $H_{//} - H_{\perp} = 8$ kOe.

Perlow et al (41) investigated the Mossbauer effect of Fe^{57} in a single crystal of hcp cobalt and measured a quadrupole splitting of .064 mm/sec. and strangely found the hyperfine field to be isotropic. They indicated that for a non-cubic material the anisotropy in the hyperfine field arises from the following contributions; (1) the dipolar field H_d due to the spin moment of the 3d electrons, (2) the field H_L due to the orbital moment of the 3d electrons, and (3) the field H_s produced by the contact interaction of the s electrons which are polarized by the 3d electrons. Perlow et al showed that for hcp Co the last term is negligible and were forced to postulate an accidental cancellation of the dipolar and orbital contributions to account for the isotropic hyperfine field observed.

Kawakami et al (20) used the expressions of Perlow to analyse their data. The dipolar field is given by

$$H_d = \mu_B n_h \langle 3\cos^2\theta - 1\rangle\langle r^{-3}\rangle \approx \mu_B q \qquad (4.34)$$

where μ_B is the Bohr magneton, q is the electric field gradient, and n_h is the number of holes in the 3d band (1.7), $\langle 3\cos^2\theta - 1\rangle$ is the asymetry in the spin density distribution obtained from neutron diffraction (42), and $\langle r^{-3}\rangle$ is taken as the free atom value (43). The dipolar field obtained at 4.2 K was $(H_{\parallel} - H_{\perp})_d = 2.3$ kOe. Similarly the orbital hyperfine field is given by

$$H_L = \mu_B n_h (g - 2)\langle r^{-3}\rangle \qquad (4.35)$$

where g is the electronic g-factor. The orbital contribution to the anisotropy in the hyperfine field is therefore

$$\Delta H_L = (H_{\parallel} - H_{\perp})_L = \mu_B n_h (g_{\parallel} - g_{\perp})\langle r^{-3}\rangle \qquad (4.36)$$

The anisotropy in the g-factor, $g_{\parallel} - g_{\perp}$, can be estimated from the anisotropy in the magnetization, $M_{\parallel} - M_{\perp}$, by measuring the magnetization parallel and perpendicular to the c-axis (44). Using this and $g_{\parallel} = 2.17$ (45) gives $(H_{\parallel} - H_{\perp})_L = +5.4$ kOe at 4.2 K.

Of particular interest is the fact that ΔH_L is over twice as large as the anisotropy in the dipolar hyperfine field ΔH_d. These authors also noted that the total anisotropy and the quadrupole splitting (Eqn. 4.32) had approximately the same temperature dependence as the deviation of the ratio of the lattice constants c/a from ideal, i.e. $(8/3)^{1/2} - c/a$.

From Eqn. 4.34 and Eqn. 4.32 it follows that ΔH_d also has approximately the same temperature dependence and consequently the orbital contribution to the anisotropy is also dominant at high

temperature. This is an important point and will be referred to later in our examination of the relationship between the anisotropy in the hyperfine field and the magnetocrystalline anisotropy.

4.7 The M-M Model for the Domain Wall Composite Lineshape

Murray and Marshall (46) developed a simpler approach than the formalism of Turov et al for the treatment of NMR in multi-domain ferromagnets. For a 180^{o} wall in a uniaxial ferromagnet the power spectrum is given by a sum over all sites in the wall.

$$P(\nu) = \int_{0}^{\pi} q(\theta) f(\nu-\nu') d\theta \tag{4.37}$$

where $q(\theta)$ is the strength of the signal coming from nuclei in the wall whose quantization direction has an angle θ with respect to the easy direction and $f(\nu - \nu')$ is the "local" lineshape function. The variation of the signal with θ is given by

$$q(\theta) = k\eta^{2}(\theta) H_{rf}^{2} n(\theta) \tag{4.38}$$

where $\eta(\theta) = \eta_{o} \sin\theta$ is the enhancement factor as a function of angle, k is a constant, H_{rf} is the applied r.f. field and $n(\theta)$ is the angular distribution of spins. Since the number of spins per unit distance is a constant, $n(z) = n_{o}/d$ where n_{o} is the number of spins in a domain wall and d is the domain wall thickness. Then $n(\theta)$ is given by

$$n(\theta) = \frac{n_{o}}{d} \frac{dz}{d\theta} \tag{4.39}$$

Since a 180^{o} wall is described by the equation (47)

$$\sin \theta = \operatorname{sech} (\pi z/\delta) \tag{4.40}$$

where $\delta = \pi (J/K)^{1/2}$ is the domain wall thickness,

$$\frac{dz}{d\theta} = - \frac{\delta}{\pi \sin \theta} \tag{4.41}$$

and

$$n(\theta) = \frac{n_o \delta}{\pi d} \left| \frac{1}{\sin \theta} \right| \tag{4.42}$$

Therefore for a steady-state NMR spectra $q(\theta) \propto |\sin\theta|$.

Murray and Marshall assumed that the intrinsic linewidth was independent of position in the wall and therefore independent of frequency and θ. However, in order to reproduce the general features of the observed spectra, Cobb et al (21) and Butler (48) found that it is essential to include a position-dependent linewidth within the wall, as was first proposed by Turov et al (23). Assuming a linewidth $\Delta = \Delta(\theta)$ which depends on the position in the wall and a Lorentzian line-shape gives a "local" distribution function

$$f(\nu - \nu') = \frac{\Delta}{\pi} \frac{1}{\Delta^2 + (\nu - \nu')^2} \tag{4.43}$$

where $\Delta(\theta) = \Delta_d + \delta f(\theta)$, Δ_d is the constant linewidth at the domain wall edge and $f(\theta)$ is the angular dependence.

The origin of the θ-dependent linewidth was taken by Turov et al (23) to be thermal magnon scattering (T_1 process) associated with the low-energy excitations peculiar to the wall which would make the line-shapes strongly temperature dependent. These authors were concerned with very low nuclear abundance which would preclude an indirect coupling of the nuclei. Cobb et al assumed that these same

excitations are responsible for a strong indirect coupling of nuclei through a Suhl-Nakamura interaction (49,50) since they observed no significant change in the composite line-shape with temperature. The amplitude of these excitations varies as $\sin^2\theta$, being largest at the wall centre and zero at the wall edge (21), and therefore one can expect a position dependent linewidth. However, because of the anisotropic hyperfine interaction, the number of nuclei that can interact and therefore the range of the interaction, also depends on θ. The exact form of the angular dependence is thus expected to be quite complicated.

Since the magnetization (spins) within the domain wall makes varying angles (θ) with respect to the c-axis, the hyperfine field and quadrupole splitting will vary from site to site within the wall. This variation will result in an angular variation in the resonant frequency of the nuclei in the wall, and as a result ν' in Eqn. 4.43 becomes angular dependent.

The hyperfine field distribution in a ferromagnetic is given by

$$H_{hf} = \bar{A}\langle S\rangle \qquad (4.44)$$

where $\langle S\rangle$ is the thermal average of the electronic spin and $\bar{A}$ is the hyperfine coupling tensor. For a crystal with uniaxial symmetry $\bar{A}$ is diagonal with $A_{xx} = A_{yy} = A_{\perp}$ in the co-ordinate system with the z-axis along the crystallographic c-axis. When the electronic spin direction makes an angle θ with respect to the c-axis, the angle θ' between the hyperfine field and the c-axis is given by

$$\tan\theta' = H_{\perp}/H_{||} \tan\theta \qquad (4.45)$$

where $H_{||} = A_{zz}\langle S\rangle$ and $H_{\perp} = A_{\perp}\langle S\rangle$ define the hyperfine field with the electronic spins parallel to the c-axis and perpendicular to the c-axis

respectively. The magnitude of the hyperfine field is given by

$$H_{hf} = \{H_{||}^2 \cos^2 \theta' + H_{\perp}^2 \sin^2\theta'\}^{\frac{1}{2}} \approx H_{||} + H_a \sin^2 \theta' \tag{4.46}$$

where $H_a = H_{||} - H_{\perp}$ and it is assumed that $H_a \ll H_{||}, H_{\perp}$.

In the presence of both an anisotropic hyperfine interaction and an electric quadrupole interaction the nuclear spin Hamiltonian is given by

$$H = -\gamma\hbar I \cdot H_{hf} + \frac{e^2qQ}{4I(2I-1)} [3I_z^2 - I(I+1) + \zeta(I_x^2 - I_y^2)] \tag{4.47}$$

where x, y, and z represent the principal axis of the electric field gradient (EFG), eq = V_{zz} is the EFG along the z-axis and $\zeta = (V_{xx} - V_{yy})/V_{zz}$ is the asymmetry parameter. The frequency corresponding to the transition between the m and m-1 states is, to first order in the EFG, given by (51,52)

$$\nu_m' = \nu_{||} + (\nu_{||} - \nu_{\perp}) \sin^2 \theta' + \nu_Q(m - \tfrac{1}{2}) \times (3\cos^2\theta - 1 + \zeta \sin^2\theta \cos(2\phi)) \tag{4.48}$$

where $\nu_{||}$(c-axis) = $\gamma H_{||}/2\pi$, $\nu_{\perp}$(b-axis) = $\gamma H_{\perp}/2\pi$ and ν_Q = $3e^2qQ/4I(2I-1)h$.

Since the large enhancement of the r.f. field in ferromagnets usually saturates the absorptive component of the nuclear susceptibility, the power absorption usually arises from the dispersive part of the nuclear susceptibility. The observed power spectrum is given by

$$P(\nu) \propto \int_0^{\pi} \sum_m \frac{|\sin\theta|(\nu - \nu_m')}{(\Delta_d + \delta f(\theta))^2 + (\nu - \nu_m')^2} d\theta \tag{4.49}$$

Figure 4.3 (a) shows the measured spectrum for Cr^{53} in $CrBr_3$ as

obtained by Cobb et al. Figure 4.3 (b) shows the predicted spectrum assuming a constant linewidth through the wall, which exhibits not only a quadrupole splitting on the "a" resonance but also on the "b" resonance, inconsistent with experiment. Figure 4.3 (c) shows the predicted spectrum assuming a $\sin^2\theta$ position dependent linewidth and adjusting Δ_d and δ to reproduce the resonance line-shape. The absence of quadrupolar structure on the "b" resonance implies that Δ must be comparable with the separation between quadrupolar components. Since the linewith is of dynamical origin, the domain wall edge resonance would have a smaller Δ, more easily resolved quadrupole splitting, and also a large value to T_2. The domain wall centre resonance would have a much larger Δ, which could result not only in the absence of a resolved quadrupole splitting but a smaller T_2 could also account for the failure to observe either a free-induction or spin-echo effect if T_2 were smaller than the amplifier recovery time.

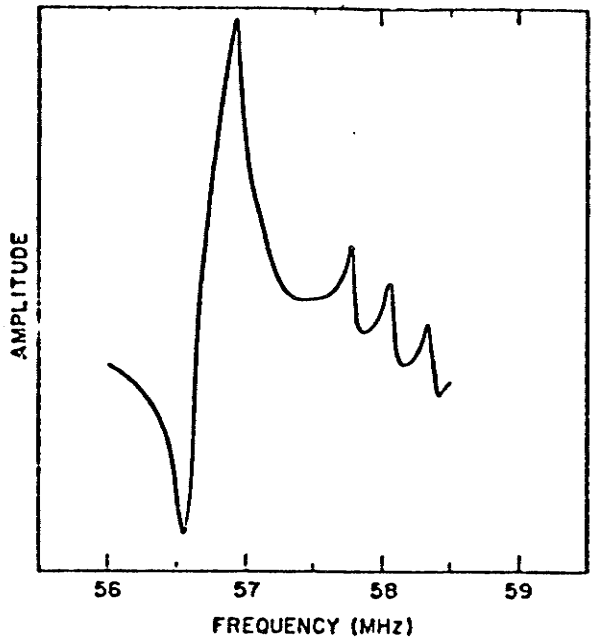

(a)

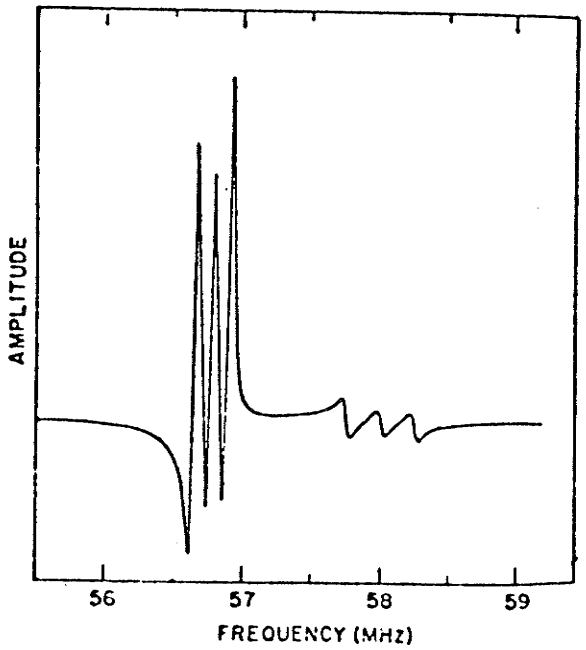

(b)

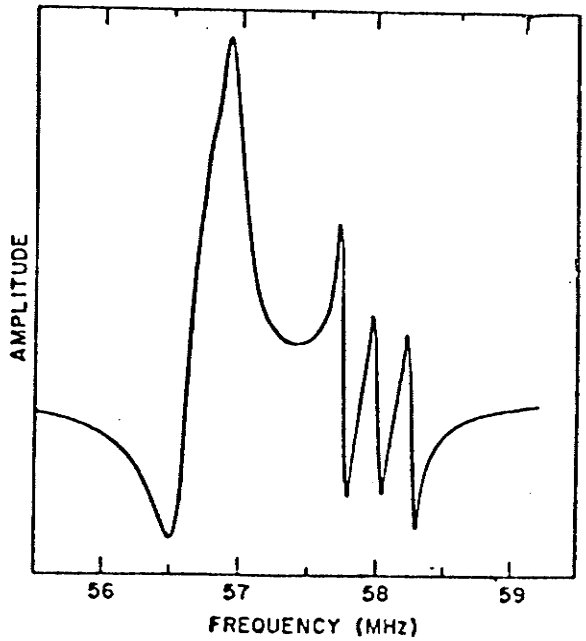

(c)

Fig. 4.3 The Cr^{53} resonance in $CrBr_3$ as obtained by Cobb et al (Ref. 21) (a).The calculated spectrum assuming a constant linewidth through the wall (b). The calculated spectrum assuming a position dependent linewidth (c).

CHAPTER 5

Experimental Procedure and Results

5.1 Introduction

Superficially, steady-state and pulsed NMR spectrometers are quite similar in that they both require a transmitter for generating the r.f. field, a preamplifier-receiver-detector system for processing the nuclear signal and sample circuitry to contain the sample and to couple the sample to both the transmitter and the receiver (1,2). The requirements for these basic units are quite different, however, for the steady-state or continuous wave (c.w.) and the pulsed NMR spectrometers. The pulsed transmitter must generate kilowatts of power during a pulse to give an r.f. field in the range of 10 - 400 G at the sample. A c.w. transmitter usually generates less than one watt since an r.f. field of 10^{-4} G is only required in a typical steady-state experiment. The power requirements of a pulsed spectrometer used to investigate ferromagnetic materials are not as great because of the enhancement effect resulting from electronic magnetization processes.

There are several other basic requirements of a NMR pulsed spectrometer which generally makes it a more complex instrument than the c.w. spectrometer. The pulses must be sufficiently short so that no relaxation takes place during the pulse interval. In the case of the broader lines from solids this requirement becomes more difficult to achieve. In addition the pulse shapes must be as rectangular as

possible, with the rise and particularly the fall time short compared with the pulse width. In a single coil system it is desirable to have a coil with a large Q in order to obtain the largest possible r.f. field amplitude. It has been shown that the field in a sample coil is given by (1)

$$H_1 \simeq 3(PQ/\nu_o V)^{\frac{1}{2}}$$
$$\simeq 3.7(PT_r/V)^{\frac{1}{2}} \qquad (5.1)$$

where P is the transmitter power in watts, Q is the quality factor of the sample circuit, ν_o is the resonance frequency in megahertz, V is the volume of the coil in cubic centimeters and T_r is the rise and fall time, in micro-seconds, of the r.f. pulse envelope at the sample. Also, the high Q is desirable for good signal detection sensitivity after the pulse. The signal-to-noise in a pulsed NMR experiment is given by (1)

$$S/N \propto \xi\gamma I(I + 1)\ (QV\nu_o T_2/\beta T_1)^{\frac{1}{2}} \qquad (5.2)$$

where ξ is the filling factor of the receiver coil, γ is the gyromagnetic ratio of the nucleus, I is the spin-quantum number of the nucleus, T_1 and T_2 are the spin-lattice and spin-spin relaxation times and B is the bandwidth of the receiver-detector system. However, the r.f. pulses produce "ringing" in high Q circuits which decays slowly and thus cancels the advantage obtained from the use of short pulses. Pulse-damping circuits or diode arrangements are often used to

reduce this ringing and to sharpen the tail of the pulses. Crossed-coil systems have the advantage that the transmitter and receiver coils are separated so that the respective Q values can be independently chosen for the transmitter and receiver and ringing effects are not as troublesome.

The pulsed NMR receiver must be able to withstand large overvoltages and recover very rapidly from overload. The recovery time of the receiver must be as small as possible (a few microsec.) in order to observe the resonance signal as soon as possible after the pulse. The effect of the pulses on the receiver is reduced by isolating it from the transmitter using either crossed-coil networks or diode systems.

In order to avoid signal distortion the amplifier-detector system must have a large enough band-width to reproduce the rapid time dependence of the resonance signal.

A versatile pulse-programming system is also required to gate the r.f. transmitter to generate the desired pulse sequence of one, two or more r.f. pulses. The duration of each pulse must be continuously variable to give a 90°, 180° or other spin rotation. The separation between pulses must also be controllable over an extremely large range from microseconds to possibly minutes. A free-running oscillator is desirable since it is often necessary, as in the modified Carr-Purcell experiments mentioned in chapter three to control the phase coherence of the r.f. pulses so that the pulses start with H_1 in the same (or known) phase orientation in the rotating frame. If phase sensitive detection is used the gate unit must also provide a reference signal.

The simplest detection system is the diode detector. A

disadvantage of this detector is that its response is not linear and it must therefore be calibrated. Since it is insensitive to the phase of the signal it cannot be used for either Fourier transform experiments or pulse techniques requiring a definite phase relationship between pulses such as the Meiboom-Gill sequence. A much more versatile detection method employs a phase-sensitive detector. It also has a smaller effective bandwidth than a diode detector and therefore a better signal-to-noise ratio.

The use of an averaging device to improve the signal-to-noise ratio in pulsed experiments is common. Multiple repetition of the experiment can significantly improve the signal-to-noise ratios because of the averaging effect on the noise, the improvement being proportional to the square root of the number of repetitions. There are two main averaging devices. The computer of average transients (CAT) is a multi-channel device for digitally averaging a periodic signal. Alternatively a boxcar integrator may be used which is essentially a capacitor store accessed by an electronic gate. The boxcar output reads only the smoothed value of the magnitude of the signal at the particular instant chosen for the gate to open and is thus a single channel device. The gate may be swept to recover an entire signal (echo shape) or to follow the time development of the spin-echo amplitude.

5.2 Experimental Apparatus

The pulsed NMR (spin-echo) experiments were performed using the model 6600 variable-frequency r.f. generator and receiver manufactured

by Matec Inc. With the model 765 r.f. plug-in unit a peak power of 500 watts is available over a frequency range of 90-300 MHz, the transmitter being of the pulsed oscillator type producing incoherent pulses with continuously variable widths between 0.5 and 5.0 microsec. The minimum observable signal with the superheterodyne receiver is approximately 4 microvolts with an overall bandwidth of 2 MHz. The detector is of the diode type and the maximum overall gain from receiver input to detected output is approximately 100 db.

Normally the transmitter and receiver are connected to the external load by means of separate co-axial cables. Matching devices (double stub tuners or stub stretchers) may be employed at the output of the plug-in and at the input to the load for optimum power transfer, and in the receiver cable for optimum signal transfer. As these devices were not available cable lengths were adjusted to optimize the detected signal, thereby nominally adjusting the length of the cables to an odd multiple of half-wavelengths. It is assumed that the adjustment of the pulse widths for maximum echo amplitude can compensate for any frequency variation of the transmitter output and the efficiency of coupling of the transmitter and receiver to the sample circuitry. The calibration of the receiver sensitivity at each frequency using an r.f. pulse of known amplitude obtained from an r.f. signal generator will also compensate for any variation in the coupling to the sample circuitry. (This will be described in the next section.)

Two types of sample circuits were used in these experiments. One consisted of a single coil system which was part of a tunable L-C circuit. The sample was placed inside the coil which consisted of 3 or

4 turns of copper wire. Alternatively, and, in fact, in most instances, a cylindrical cavity was used which had a resonant frequency which could be varied by adjusting a capacitance at one end. Whereas the L-C circuit was placed inside a liquid He dewar to obtain the low temperature spectra, for the cavity the tail of the dewar was inserted into the cavity to apply the excitation externally. Figure 5.1 illustrates the external cavity with the cryostat tail inserted and S representing the sample. The tuning capacitance is formed between a brass disc fastened to the top of a central post and the cavity front, which screws into the cavity on very fine threads. Gross tuning is accomplished by replacing the brass disc with a disc of different area. The r.f. magnetic field in the cavity is in a mode cylindrically symmetric with respect to the axis of the cavity. The r.f. pulse is applied to a single loop of wire as shown in the figure, and the signal is detected by a similar loop on the opposite side of the cavity.

Figure 5.2 is a block diagram of the spectrometer system used in the measurements of the spin-echo decay envelopes. The repetition rate of the experiments must be considerably slower than the spin-lattice relaxation time so that the system returns to thermal equilibrium after each two-pulse sequence. For hcp Co T_1 for the domain wall edge resonance is on the order of several milliseconds restricting the repetition rate to less than 100 pulse sequences per second. We used a repetition rate of 60 Hz.

The receiver is calibrated using the pulse modulated r.f. signal generator, the output of which is applied to the transmitter side of the sample circuit. The signal generator's output voltage is kept

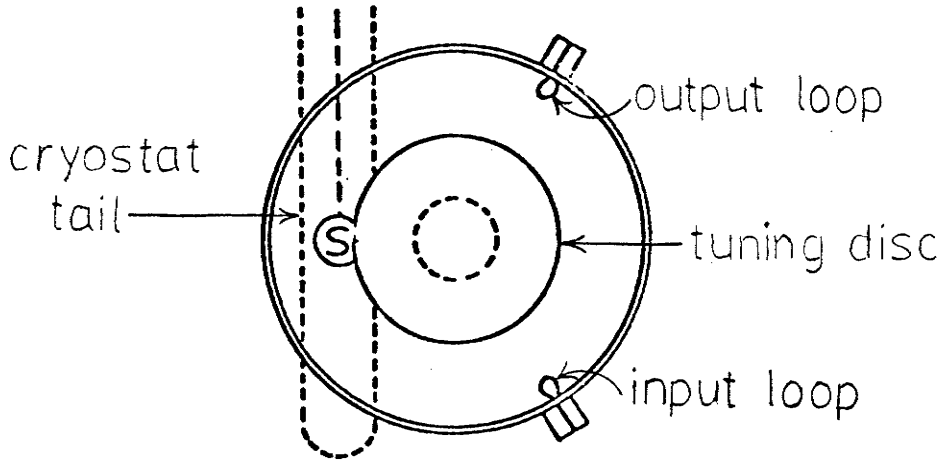

Fig. 5.1 The r.f. cavity with the cryostat tail inserted and s represents the sample.

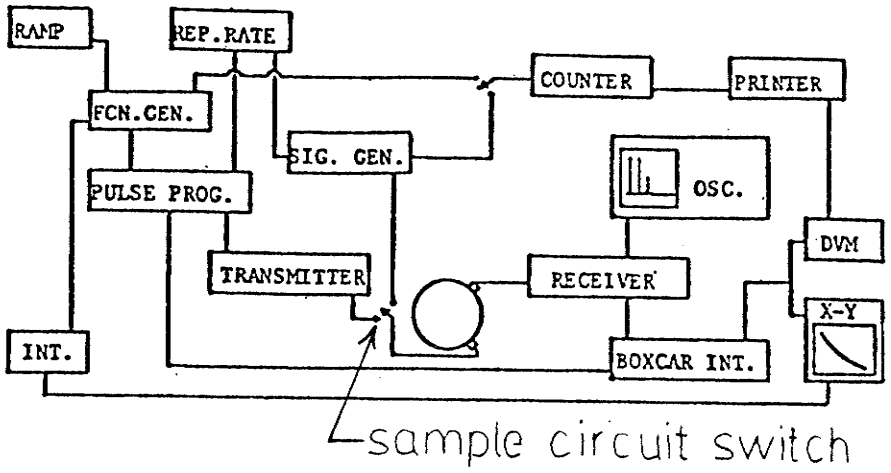

Fig. 5.2 Block diagram of the spin-echo spectrometer system.

fixed throughout the experiment and selected so that it will not saturate the receiver in parts of the spectrum where the gain is largest (i.e. where the resonance is weak). The signal generator output pulse is timed to occur at the same time as the initial position of the echo so that the boxcar integrator and the digital voltmeter can be used to measure the receiver gain as well as the echo amplitude, depending upon the position of the switch to the sample circuit (see Fig. 5.2).

The triggers for the r.f. pulses as well as for the boxcar's gate positioning pulse are obtained from a square wave which has a repetition rate which varies linearly as a result of the application of a ramp voltage to the VCG input of the function generator. In this way the pulse separation can be continuously varied over a range of more than 100 microsec. and the boxcar gate position can be adjusted to automatically track the echo position at twice the pulse separation. The gate of the boxcar integrator has a width (~15 nanoseconds) which is much less than the width of the echo, and when properly positioned the boxcar will record the echo maximum amplitude.

The area of the positive half of a square wave period is proportional to the period and thus the output of the square-wave integrator can be applied to the x-axis of an x-y recorder. The digital counter measures the period of the square wave which is related to the pulse separation, and this is recorded by the digital printer. The boxcar output is applied to both the x-y recorder and the digital voltmeter to obtain a continuous record of echo amplitude versus pulse separation. This, along with the receiver gain, is sufficient to obtain the NMR spectrum when repeated over the entire frequency range.

5.3 Additional Experimental Considerations

In the case where spin diffusion and relaxation effects can be neglected during the r.f. pulses and during the free induction decay (FID) or spin-echo, the free induction and spin-echo are related to the Fourier transform of the resonance line if the resonance line is narrower than the bandwidth of the r.f. pulses. In ordered magnetic materials, however, the resonance is strongly broadened by sample inhomogeneities and is usually much broader than the r.f. pulse bandwidth. This is particularly true for magnetic materials containing domain walls and having a large anisotropy in the hyperfine field. The echo and fid will then reflect the frequency spectrum of the pulse rather than that of the actual nuclear resonance spectrum. Therefore, to obtain the entire spectrum it must be sampled as a function of frequency in a step-by-step procedure. For hcp Co the pulse bandwidth is $\sim 2/\Delta t_1 \sim 4.0$ MHz for a pulse width ,t_1 , of 0.5 microsec. while the resonance line has a width of approximately 10 MHz.

Linewidths of this magnitude present several special instrumental requirements. First, the pulse spectrometer must be of variable frequency and one must ensure that the r.f. pulse amplitude and the receiver sensitivity remain constant or be accounted for over the entire spectrum. In addition, since the enhancement factor in domain walls is function of position a function of position in the wall, the tuning conditions for a 90^{o} or 180^{o} pulse will change with the position in the wall being sampled at a given frequency.

The r.f. pulse power is assumed to be constant over the range

of the spectrum while the receiver sensitivity is easily calibrated using an r.f. pulse of known amplitude obtained from an r.f. signal generator. Thus for each new frequency (or field) the receiver gain must be measured and the pulse widths adjusted for the optimum echo amplitude. This adjustment also helps to compensate for any variation in the pulse amplitude with frequency, since in the vector model of the spin-echo phenomena, a change in the r.f. amplitude may be compensated for by a change in the width of the pulses.

Because of the large enhancement of the applied r.f. field, very large turning angles are possible for strong pulses in the absence of any dynamic frequency shift resulting from the pulses (4,5), particularly for nuclei within domain walls. It is therefore never totally clear that the pulses form a true 90-180 pair. Furthermore, the optimum pulse sequence when a quadrupole interaction is present is further complicated. Solomon (6) has discussed the formation of multiple echoes for the case of a constant Zeeman energy and an inhomogeneously distributed quadrupole coupling constant and found that the optimum echo amplitude was obtained for a $90^{\circ} - \phi$ pulse sequence where ϕ is around $\pi/5$. As a result of the different form of the nuclear interaction responsible for the broadening due to this inhomogeneous distribution (I_z^2 rather than I_z as in the case of magnetic broadening) the effect of a 180° pulse will leave H_Q, the quadrupole Hamiltonian, unchanged since it results in the change of $|m\rangle$ into $|-m\rangle$. Consequently the sequence of a 90° pulse followed by a 180° pulse will not yield an echo in this situation. Co^{59} has a large quadrupole moment and the pulse sequences that produce the optimum echo amplitude

in both hcp Co and the RCo_5 intermetallic compounds appear to exhibit this type of behaviour. The second, refocussing pulse consistently had a shorter duration than the first pulse which presumably produced a 90^{o} spin rotation. Therefore, the second pulse would seem to represent a spin rotation of considerably less than the 180^{o}.

The variation in the enhancement factor with position for nuclei within domain walls results in an additional uncertainty in conducting the experiments, since it is impossible to satisfy the optimum condition (90-180) for all resonant nuclei simultaneously. This, in turn, could result in a power dependence of the spectrum since the echo amplitude measured at a given frequency would be a function of the r.f. field used. A different r.f. field would produce the optimum tuning conditions for a different set of nuclei in the wall having a suitable enhancement factor.

This problem, however, is of less concern for the case in which there is a large anisotropy in the hyperfine field. At a given frequency the spin-echo experiment should then be quite selective in terms of which nuclei in the domain wall contribute to the signal. At a different power, a different set of nuclei will satisfy the optimum tuning conditions, but these now will be off resonance. This was found to be the situation for the Co^{59} resonance in the materials we have investigated which therefore represents an important simplification for the analysis of the observed spectrum. To avoid any power dependence of the observed spin-echo spectrum in materials containing domain walls, it is therefore important that the pulse bandwidth be much less than the width of the spectrum. To maximize this condition, all spectra were

taken at the lowest r.f. pulse power possible (largest pulse durations), being only large enough to allow adequate signal-to-noise ratio throughout the spectrum. This also ensured that the best possible pulse shape was obtained from the pulsed oscillator.

Of course, this problem could be eliminated completely by removing the domain walls completely with a saturating magnetic field and observing only the "domain" enhanced NMR signal. However, the anisotropy fields for the RCo_5 compounds are of such large magnitude that the enhancement factors are only a factor of 2-3 making the signal unobservable. In addition, since we are interested in measuring the anisotropy in the hyperfine field for these materials, this procedure would require the saturation of the samples in a direction perpendicular to the easy c-axis which would require external fields much larger than what is available ~250 kOe for $SmCo_5$. An additional consideration for this approach would be the effect of the paramagnetic frequency shift that results from the non-vanishing electronic spin susceptibility (7). The latter two considerations eliminate the Mossbauer effect as an alternative experimental technique for the measurement of the anisotropy in the hyperfine field.

Domain wall NMR therefore provides a unique method of obtaining a value for both the perpendicular hyperfine field and the anisotropy in the hyperfine field for materials having a large magnetocrystalline anisotropy such as the RCo_5 compounds. Pulsed NMR provides the additional advantage of yielding an accurate distribution in local fields enhanced but undistorted by the wall enhancement mechanism. Since the driving and response enhancement factors are both proportional

to the rate of spin rotation in the wall (section 4.4) and the density of spins in the wall is inversely proportional to the rate of spin rotation (section 4.7), the local contribution to a composite steady-state signal will vary as $|\sin\theta|$ for a 180° wall. For spin-echo NMR, however, the adjustment of the pulse widths compensates for the angular variation of the driving enhancement factor to obtain the optimum turning angles and the local contribution to the composite spectrum becomes independent of wall structure.

There are several additional advantages to using spin-echo NMR for the study of the Co^{59} resonance in the rare-earth-Co compounds. In the presence of a quadrupole interaction the steady-state lineshape consists of 2I lines with a separation $\Delta\nu_q = a/\pi$ where $a = 3e^2qQ/(4I(2I-1))$. Abe et al (8,9) have calculated the echo amplitude following a density matrix formalism for the case of an inhomogeneously distributed hyperfine field and a constant quadrupole coupling constant, and found that the echo amplitude is modulated as a function of the pulse separation with a modulation period of $\tau_m = \pi/a$. This modulation was also observed for the boron resonance in ferromagnetic Fe_2B and MnB and for the Mn resonance in MnB. The following relationship, therefore, exists between the quadrupole modulation period of the first echo and the multiplet separation of the steady-state spectrum.

$$\Delta\nu_q \tau_m = 1 \qquad (5.3)$$

The period of the spin-echo modulation can therefore be used to determine the local quadrupole splitting. The advantage of this method

of determining $\Delta\nu_q$ is that the static inhomogeneities which obscure the splittings in steady-state experiments will not affect the modulations of the spin-echo, which will still be observed unless the relaxation time T_2 is shorter than the period of the modulation.

The spin-echo technique also can be used to study the line splittings due to magnetic dipolar or indirect spin-spin interactions between inequivalent neighbouring nuclei which will also cause modulations of the transient signals. These experiments were of significance in identifying the origin of the complex line structure observed in steady-state resonance measurements (10,11).

Relaxation measurements by the steady-state technique requires the measurement of the signal strength as a function of the amplitude of the r.f. field. The pulse technique, on the other hand, requires only the measurement of the damping of the free induction and echo signals as a function of the pulse separation.

The major disadvantage of spin-echo NMR is that it is, for the most part, limited to low temperatures for the materials that we are interested in. As a result of the strong temperature dependence of the relaxation times the nuclear magnetization decays to a level too small to be detected in a time shorter than the recovery time of the receiver. Therefore, in order to achieve adequate signal strength, we were limited to liquid He temperatures in taking the NMR spectra for the Co^{59} resonances in the RCo_5 compounds. For $SmCo_5$ adequate signal strength could only be obtained by using a high-capacity mechanical vacuum pump to reduce the He vapour pressure and therefore reduce the He bath temperature to 1.57 K. Many other samples in the RCo_5 series

failed to show any resonance at all at the lowest temperatures possible. This may be of fundamental origin or may purely be a reflection of sample condition. This is an extremely important point, since although in principle NMR would be an extremely useful technique for the study of the microscopic properties of magnetic materials, its practical usefulness lies in one's ability to obtain the required data of sufficient quality to allow reliable and unambiguous interpretation. This point has received considerable attention and will be discussed in greater detail in later sections. The hcp Co resonance could be observed at temperatures as high as room temperature, although it was considerably smaller in amplitude to that observed at liquid N_2 or He temperatures.

Excluding the significant effect of temperature on the signal strength, no appreciable effect on the lineshape or linewidth was observable over the limited temperature range available to us. This is a serious limitation to the use of spin-echo NMR for the study of the Co^{59} hyperfine field anisotropy and the Co sub-lattice contribution to the magnetocrystalline anisotropy in the RCo_5 compounds, which may only be overcome by making significant improvements in the sensitivity of the apparatus. A temperature dependent study of the Co^{59} NMR lineshape and in particular the linewidth would go a long way in determining the detailed nature of the relationship between the above quantities as would additional data from other compounds in the RCo_5 series for which no data could be obtained. We were however able to obtain enough data to at least make a preliminary investigation of the relationship between the anisotropy in the hyperfine field and the

cobalt contribution to the magnetocrystalline anisotropy and this will be presented in the discussion in chapter six.

In addition, we have made what, to our knowledge, is the first systematic study of the nature of the NMR spectra obtained for highly anisotropic materials containing domain walls. In order to do so new experimental techniques were developed to locate and identify domain-wall-edge and centre resonances. These will be described in sections 5.6 - 5.8. Without these techniques it becomes difficult not only to determine the isotropic contribution to the hyperfine field, but also the anisotropic component as well. This is particularly true if the material contains more than one site as is the situation for the RCo_5 compounds which contain two Co^{59} sites, or the R_2Co_{17} compounds which contain four sites. Previous work has, for the most part, studied the isotropic hyperfine fields (12-17) , attempting to separate the net hyperfine field into its various components. This work, however, is done at great risk for materials possessing a large anisotropy in the hyperfine field if the exact nature of the various peaks observed are not first determined.

5.4 Sample Preparation

A magnetic resonance experiment in a metallic substance requires that the r.f. magnetic field should penetrate the sample to as large an extent as possible. The effect of a skin-depth is to confine the nuclear resonance to the nuclei near the surface, with a resulting reduction in the amplitude of the signal. As a consequence experiments

are often performed using metallic powders with the particle size less than the skin-depth if possible.

It is interesting that this effect can also introduce a distortion in the detected lineshape, which arises from the interaction of the induced eddy currents with the nuclei to cause power absorption in analogy with the wall losses detected in ferromagnetic materials (Eqn. 4.13 in section 4.2).

An additional consequence of the finite skin-depth which also tends to reduce the signal-to-noise ratio is the reduction in the Q of the sample coil caused by the lossy metallic sample. The skin-depth is given by

$$\delta = (2/\omega\sigma\mu)^{\frac{1}{2}} \qquad (5.4)$$

where ω is the r.f. frequency, σ is the conductivity and μ is the permeability. This would therefore set an ideal upper limit on the size of the powdered samples. For Co the skin-depth is on the order of one micron at a frequency of 220 MHz.

However, since the observation of a resonance is dependent upon the presence of domain walls, the single domain size sets a lower limit on the particle size. We require that the average particle size be considerably greater than this value. For $SmCo_5$ the single domain particle size is approximately 1.6 micron ; while for YCo_5 it is 0.68, for $CeCo_5$ 0.92, and $PrCo_5$ it is 0.61. For hcp Co the single domain particle size is approximately 0.2 micron. Therefore, in preparing the samples and to obtain an optimum useable filling factor the sample must be crushed or filed into a powder and then passed

through a series of sieves to select particles of the desired size. However, as the skin-depth at the resonance frequencies for these materials are comparable to the single domain particle size, the effective filling factor achievable is considerably less than optimum. The particles must be considerably greater than the single domain size to ensure the presence of walls that can be used to excite the NMR resonance. The optimum size to obtain a maximum useable wall volume is then a complex function of the skin-depth and the magnetic structure. The RCo_5 compounds are characterized by extremely narrow walls separated by wide domains. These parameters vary through the RCo_5 series and, in fact, are functions of particle size for small diameters (less than 100 micron). The wall volume is therefore quite small and the effective wall volume may be even smaller as a result of the skin effect. Table 5.1 shows a list of the domain wall width and domain size taken from Ref. 38 for the samples that we have studied. The ratio of these two quantities is also shown and represents the percentage of the total sample volume taken up by domain walls.

TABLE 5.1

SAMPLE	δ(A)	W (μm)	δ/W (wall vol.)
hex Co	350	1.25	2.8 %
YCo_5	55	1.7	0.3 %
$SmCo_5$	51	4.0	0.13 %
$GdCo_5$	60	14.6	0.04 %

The RCo_5 powdered samples were prepared from arc-melted and homogenized buttons obtained from the U S Air Force Materials Laboratory. The buttons were crushed to a particle size of 10 - 100

micron. The powders were fixed in paraffin in glass tubes to give cylindrical samples approximately 1.0 cm long and 0.6 cm in diameter containing about 0.75 gm of material. The particles were aligned at room temperature with their easy-axis either along or across the cylindrical axis by applying a d.c. magnetic field of 10 kOe while the melted paraffin was solidifying. The hcp Co sample used was 50 micron powder obtained from Alpha Products Ltd. Additional samples in the Y-Co intermetallic series were prepared by melting stoichiometric amounts of the constituents together in an arc furnace. The constituents were 99.9% pure metals also obtained from Alpha Products. The buttons were melted repeatedly to ensure homogeneity and then annealed for seven days at 1100 K in an argon atmosphere. X-ray powder photographs indicated that the samples were predominantly of a single phase. i.e. > 95% RCo_5. The presence of traces of a second phase is not expected to influence the results to any appreciable extent.

The final packing density of the aligned powders was roughly 30% of the density of the pure material. The particle size was selected to be considerably greater than the single domain size to ensure not only that the sample contain an adequate number of domain walls but also to allow adequate penetration of paraffin to securely align the particles as well as to provide an insulation layer between the particles. An additional concern was that too dense packing would effectively screen the particles in the interior from the applied r.f. field. This has been confirmed experimentally since reducing the particle size still further by grinding the powder in a mortar dish actually resulted in a reduction in signal strength.

5.5 Preliminary Experimental Results

NMR studies (18-20) of magnetically ordered materials containing domain walls have reported the observation of two NMR peaks arising from a single site, which have been attributed to nuclei located at the edge and at the centre of domain walls. The origin of this effect is an anisotropic contribution to the hyperfine field, H_a, which leads to a resonance frequency which varies with the direction of the electronic moment and hence with the position of the nucleus in the domain wall. Either an asymmetric electronic spin density in the outer electronic shell, or an anisotropic g-factor (orbital contribution) can lead to this effect (20).

In the case of materials containing two or more inequivalent sites such as the intermetallic compounds of RCo_5 (R is a rare-earth element or Y) which contain two Co sites, the identification of the origin of the observed peaks becomes a problem. This identification is important as it makes it possible to determine the total hyperfine field anisotropy at each of the Co sites which may then be related to the contributions of the two sites in the Co sub-lattice to the magnetocrystalline anisotropy. This identification of the resonances has not been done conclusively in any of the RCo_5 compounds, and any existing attempts to do so that we are aware of have involved only indirect methods based on conclusions made from the following observations (21).

(a) The NMR peaks corresponding to nuclei of atoms located near a wall centre should be largest since the domain wall enhancement factor

and hence the effective r.f. pulse intensity is a maximum here. This is an interpretation apparently taken from steady-state NMR which has questionable general validity to spin-echo pulsed NMR spectra.

(b) Polarized neutron diffraction studies (22) show that the Co atoms at the 2c site (see Fig. 2.15) have a larger orbital moment, a large orbital anisotropy, and therefore a large orbital contribution to the anisotropy in the hyperfine field. The corresponding values for the 3g site are much smaller and more isotropic.

In any microscopic analysis of the magnetocrystalline anisotropy of the RCo_5 compounds it is advisable that the simplest case should be attempted first which would be that of YCo_5 for which there is no Y sub-lattice contribution. However, an analysis of the Co^{59} NMR spectrum is especially difficult since the spectrum consists of only two discernible peaks instead of the expected four. Figure 5.3 shows the spectrum obtained for the Co^{59} resonance in YCo_5 at 1.5 K. Observation (a) would suggest that the two peaks are the domain-wall-centre (DWC) resonances for the two inequivalent Co sites. The domain-wall-edge (DWE) resonances would not be resolvable because of their smaller amplitude. Streever (21,22) has made the suggestion that, based on observation (b), the two peaks in the NMR spectrum be attributed to the DWE and DWC resonances of Co atoms located at the 2c site, with the 3g Co resonance not resolved. Neither of these identifications are by themselves conclusive, and any further analysis would still require the location of the unresolved peaks.

The nuclear spin of Co^{59} is I = 7/2, but as seen in Fig. 5.3 no indication of quadrupole splitting is observable in the spectrum. No

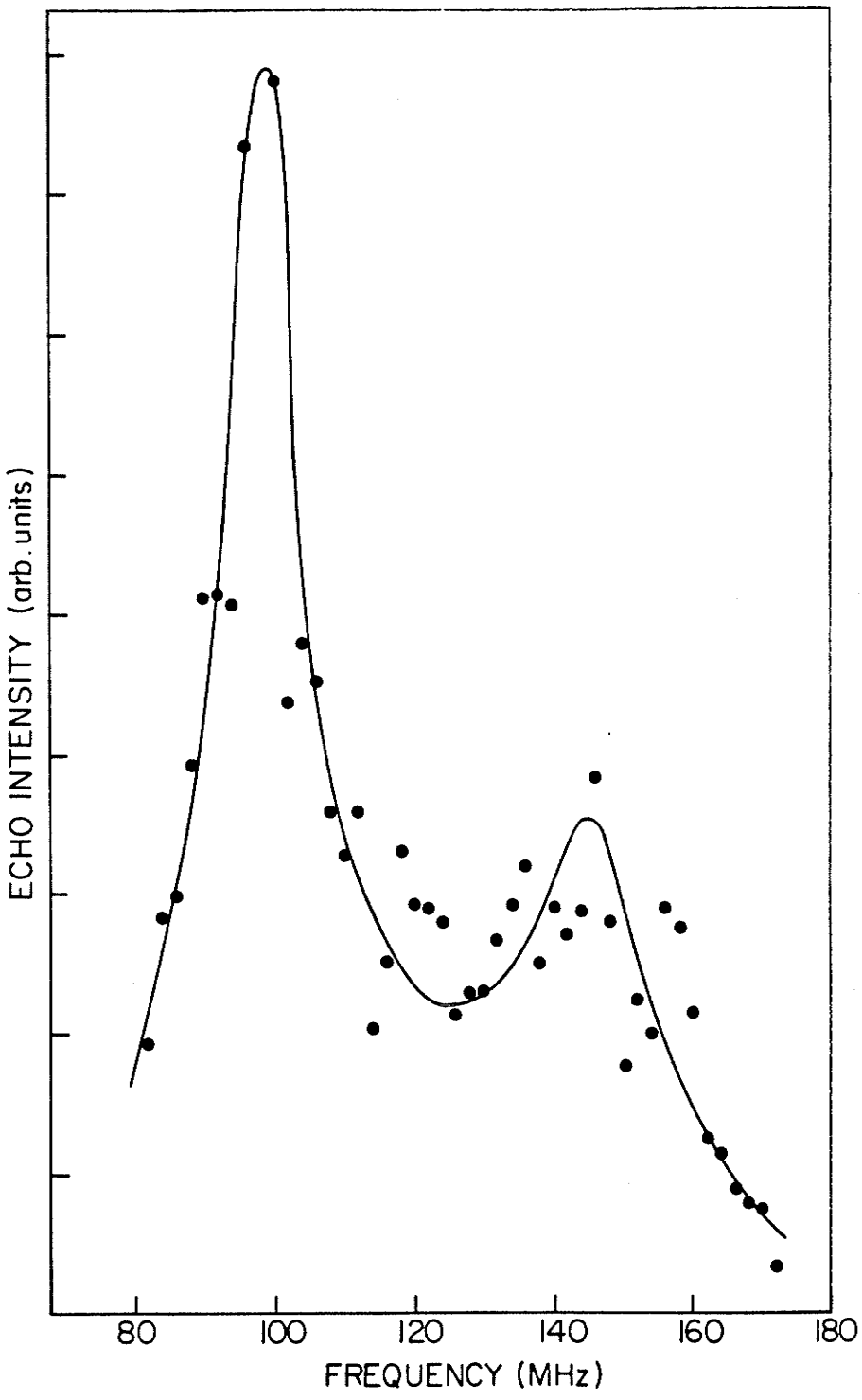

Fig. 5.3 The Co^{59} spectrum for YCo_5 at 1.5 K.

modulation of the spin-echo decay envelope by the quadrupole interaction is observed at any point in the spectrum, the relaxation curves being very nearly exponential with little variation through the line. Quadrupole effects therefore will offer no assistance in locating and identifying the DWE and DWC resonances. Indeed, in none of the RCo_5 compounds that we have examined has a quadrupole splitting been resolved in the spectrum itself. However, a modulation of the echo amplitude as a function of pulse separation was observed in some of the compounds at certain frequencies. The presence of the modulation of the spin-echo amplitude was not in any way related to the domain-wall-edge resonance as was reported for the observation of quadrupole splitting by other workers for various other materials (7,18,20). It therefore can be concluded that quadrupole effects cannot be used to analyse the Co^{59} spectra for the RCo_5 compounds even if these effects are observable. Indeed, the quadrupole effects observed represent an extremely interesting aspect of the nuclear magnetic resonance phenomena in the RCo_5 compounds, requiring further study itself.

5.6 The External Modulation of the Spin-Echo Decay Envelope

In order to analyse the Co^{59} spectra we have developed a particularly unique experimental technique which not only allows us to locate DWE and DWC resonance peaks which do not appear in the spectrum itself, but which potentially could become extremely useful in a more detailed study of the nature of the nuclear magnetic resonance phenomena in domain walls.

Essentially what is measured in this experiment is the relative slope of the hyperfine field distribution in the domain wall. This measurement appears to be considerably more sensitive to the variation in the hyperfine field through the wall than the spectrum itself.

The experiment is quite similar to the direct electron-spin-echo modulation reported by Dupont and Woonton (23) and Srivastava (24) who showed that the effect was related to the ratio of the magnitude of the modulating field, h, to that of the r.f. field during the pulse, H_1.

We first detected a "direct" nuclear-spin-echo modulation of the Mn resonance at the B-site of MnF_2O_4 at 1.5 K. The Mn A-site resonance showed no such modulation at the maximum external modulating field we were able to apply. Kubo et al (25) have shown, using a single crystal of manganese ferrite, that Mn^{3+} located at the B site has a large anisotropic component in its hyperfine field. Davis et al (26,27) in a detailed study of the Mn resonance at the A site found that the anisotropy in the hyperfine field is negligible for this site. Figures 5.4 and 5.5 show the spin-echo decay envelope for the Mn B-site resonance at four different resonance frequencies as well as the corresponding modulation of the echo amplitude that occurs when an 80 kHz modulating signal is applied. A slight variation in the depth of the modulation is observed through the spectrum. Figure 5.4 shows the spin-echo envelope modulation at three different modulation frequencies. Clearly, for the most pronounced effect, the period of the modulating signal must be considerably less than the spin-spin relaxation time, although too rapid a modulation also obscures this effect.

We subsequently observed a similar modulation of the NMR echo

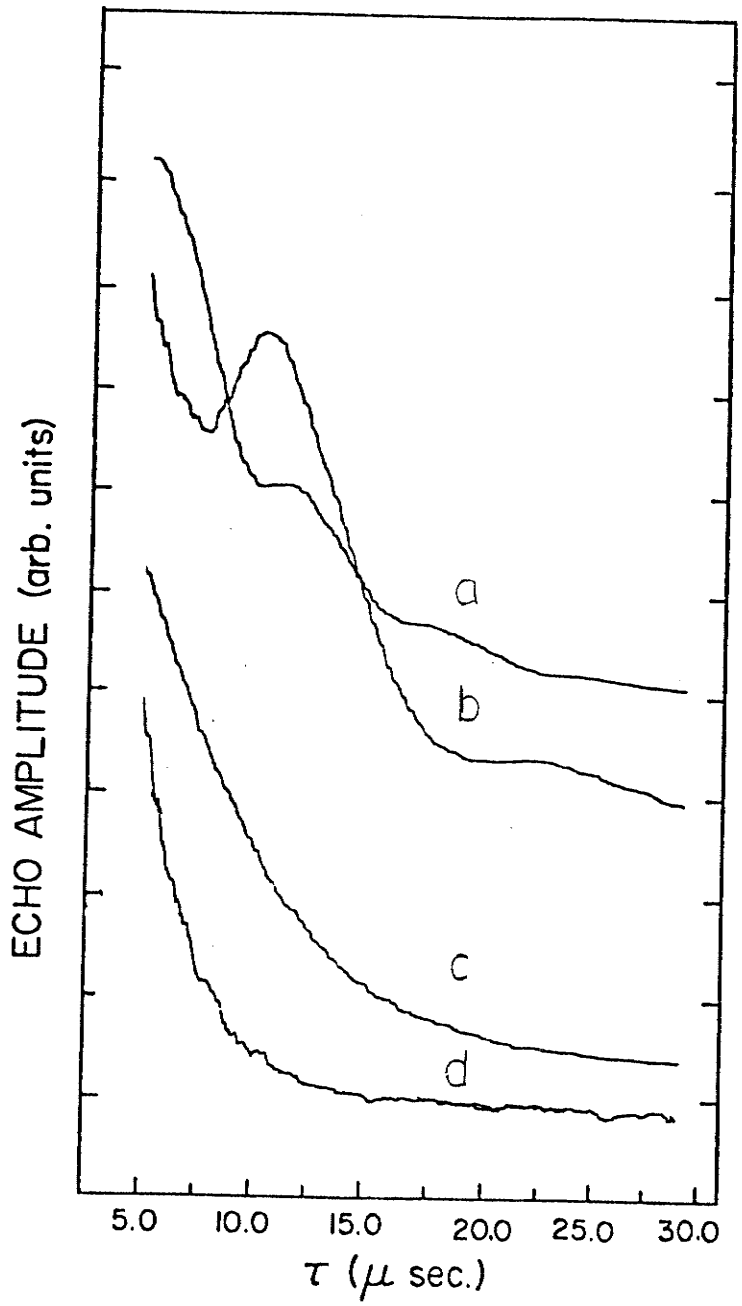

Fig. 5.4 The spin-echo envelope modulation of the Mn B-site resonance in $MnFe_2O_4$ a frequency of 370 MHz. Curve (c) is the unmodulated spin-echo decay envelope while curve (a) was taken at a modulation frequency of 160 kHz, curve (b) was taken at 80 kHz and (d) at 40 kHz.

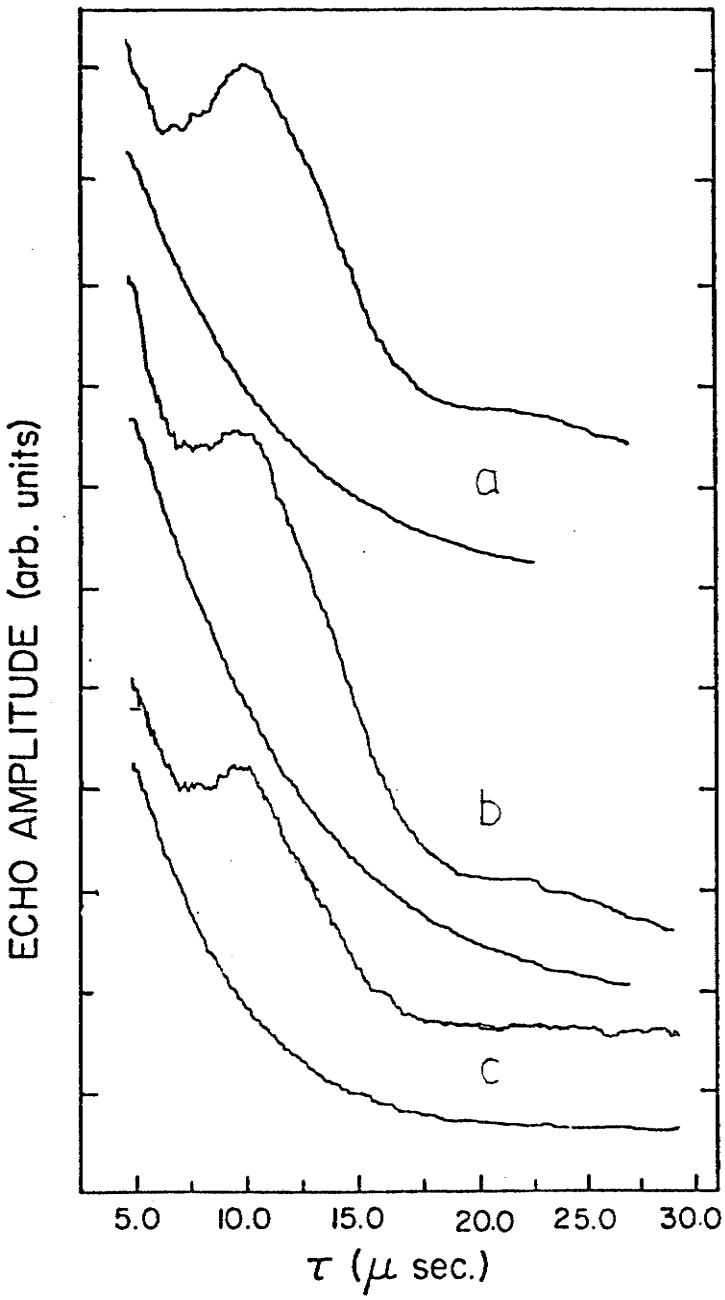

Fig. 5.5 The spin-echo modulation along with the corresponding spin-echo decay envelope for the Mn resonance in $MnFe_2O_4$ at a resonance frequency of (c) 390 MHz, (b) 360 MHz and (c) 340 MHz.

amplitude from Co^{59} in hexagonal Co and YCo_5. The experimental data were taken at 77 K for Co and at 1.5 K for YCo_5. The NMR spin-echo, following a two-pulse sequence, was observed with and without a modulating field, $\vec{H}_m$, applied parallel to the pulsed r.f. field, $\vec{H}_1$.

The NMR signal originates entirely from the domain walls since no echo was observed with H_1 perpendicular to the c-axis, while a relatively strong echo was observed with H_1 parallel to the c-axis. This is consistent with the strong uniaxial magnetocrystalline anisotropy in these materials (28,29) which leads to a very small enhancement factor within the domains.

Figure 5.6 shows the relative spin-echo amplitude for hexagonal cobalt, extrapolated to $\tau = 0$, where τ is the pulse separation, as a function of frequency. The spectrum shows a single peak which by comparison with the spectra reported by others (20) can be identified as a DWC resonance. At higher powers an additional resonance peak can be observed at 217 MHz which presumably is the DWE resonance.

A typical Co spin-echo-decay envelope appears in Fig. 5.7 (a) along with the spin-echo-decay envelope with a modulating field of amplitude H_m = 1.4 Oe and frequency ν_m = 80 kHz applied along the c-axis. The corresponding spin-echo-decay envelopes for YCo_5 are shown in Fig. 5.7 (b). It is apparent that the echo amplitude is modulated with a period of $1/\nu_m$ and has maxima at $\tau = n/\nu_m$, where τ is the pulse separation and n is an integer.

This study produced two startling and unexpected results. The first striking feature is that a modulation of the echo amplitude is

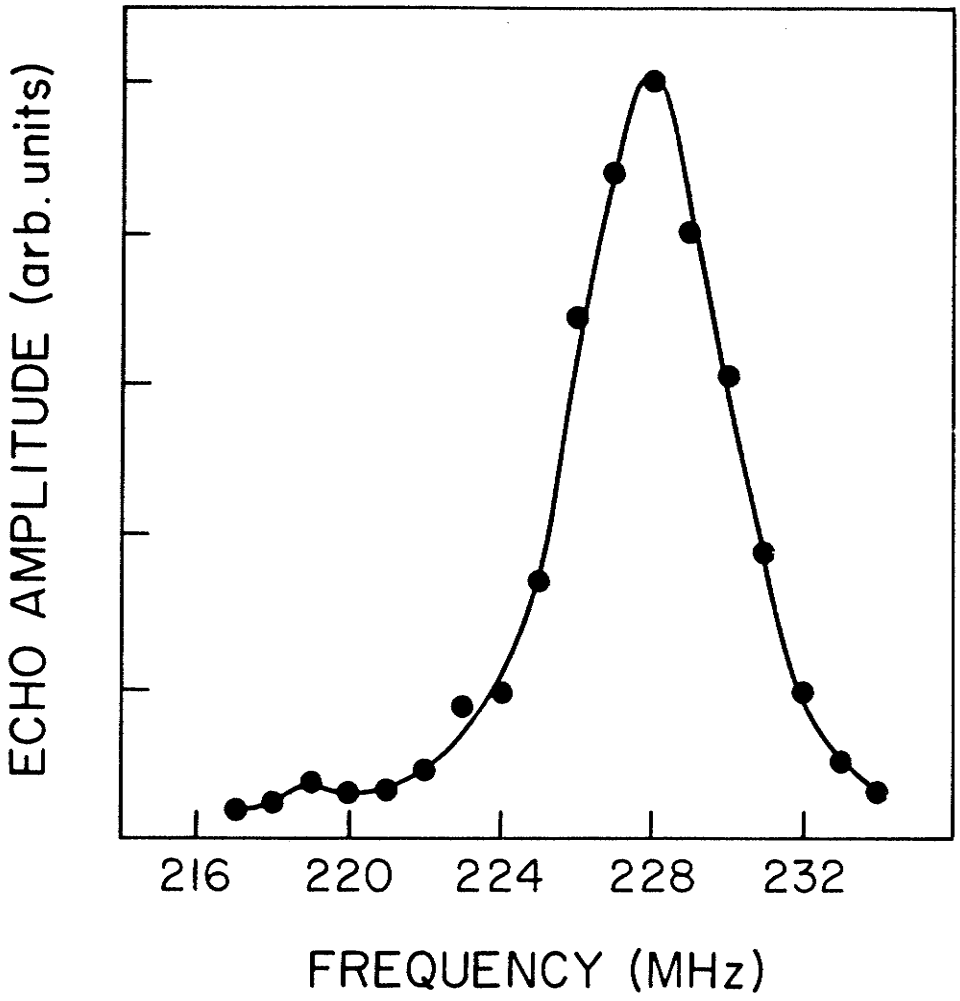

Fig. 5.6 The Co^{59} spectrum of hcp Co at 77 K.

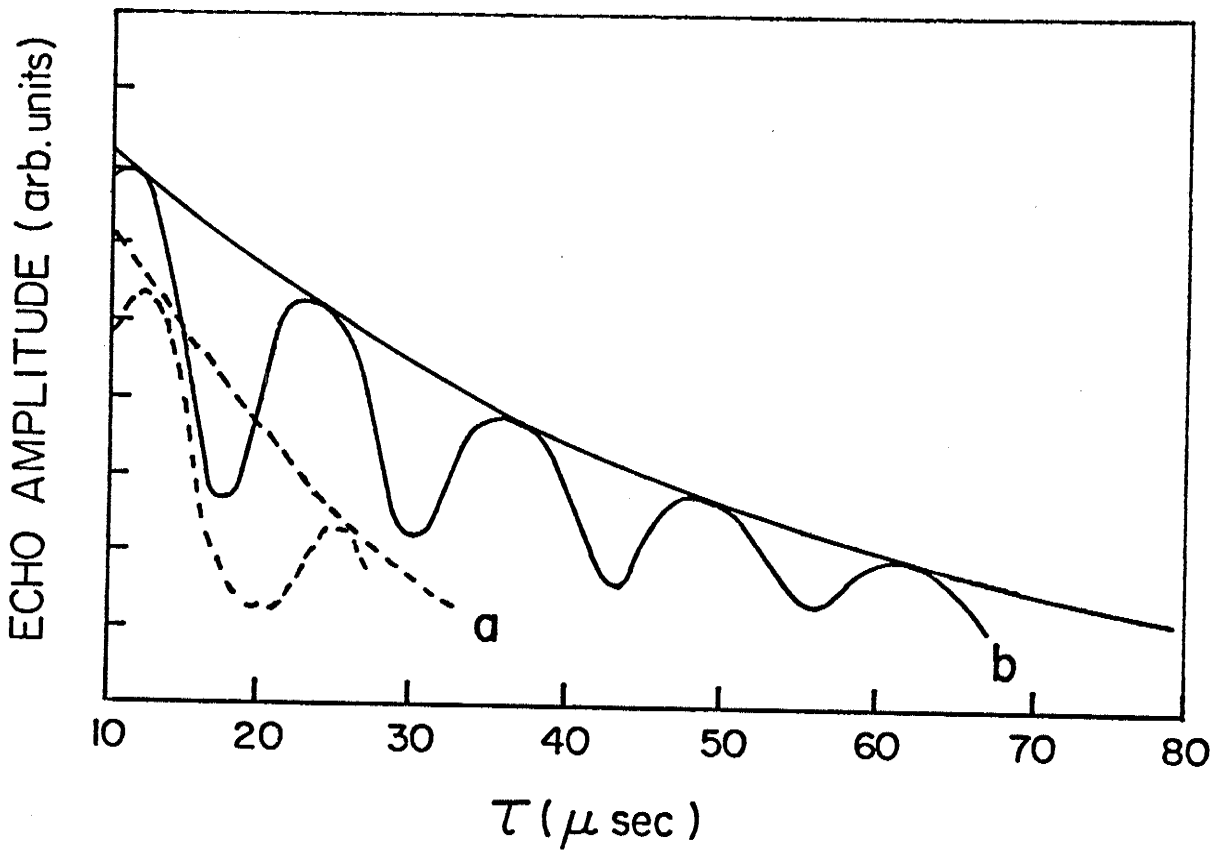

Fig. 5.7 Echo-decay envelopes with and without an 80 kHz modulating field, H_m, applied along the c-axis; (a) hcp cobalt at 224 MHz; H_m = 1.4 Oe (b) YCo_5 at 124 MHz; H_m = 0.1 Oe.

seen at all at these fields, since the modulating fields used are much less than the pulsed r.f. field. In addition, a strong dependence of the depth of modulation upon frequency was observed. For Co the modulation was strongest in the centre of the spectrum and weakest at the high-and-low frequency edges, for a constant H_m. Figure 5.8 is a plot of $A_{min}(H_m)/A_o$ as a function of frequency, for hexagonal Co, where $A_{min}(H_m)$ is a minimum of the modulated echo amplitude and A_o is the unmodulated echo amplitude measured at the same pulse separation τ; H_m and ν_m were maintained at 1.4 Oe and 80 kHz through the entire frequency range. The striking feature shown by these data is that $A_{min}(H_m)/A_o \sim 0.9$ at the low-frequency end of the spectrum, drops through a minimum of ~ 0.1 near the centre and again rises monotonically to large values near the high-frequency edge. Figure 5.9 shows a series of spin echo decay envelopes obtained with and without a 80 kHz modulating field applied at selected frequencies.

Figure 5.10 is the corresponding plot of $A_{min}(H_m)/A_o$ as a function of frequency for the Co resonance in YCo_5. H_m and ν_m were maintained at 0.1 Oe and 80 kHz throughout the entire NMR frequency range. The plot of $A_{min}(H_m)/A_o$ against frequency shows the same basic shape as was obtained for hexagonal cobalt. However, some additional structure does appear which is interpreted as arising from the two inequivalent Co sites in YCo_5. This structure observed on the modulation spectrum is fundamental to the location of the resonance peaks not resolved in the spectrum. At its minimum $A_{min}(H_m)/A_o \sim 0.2$. Figure 5.11 shows representative data used to construct Fig. 5.10.

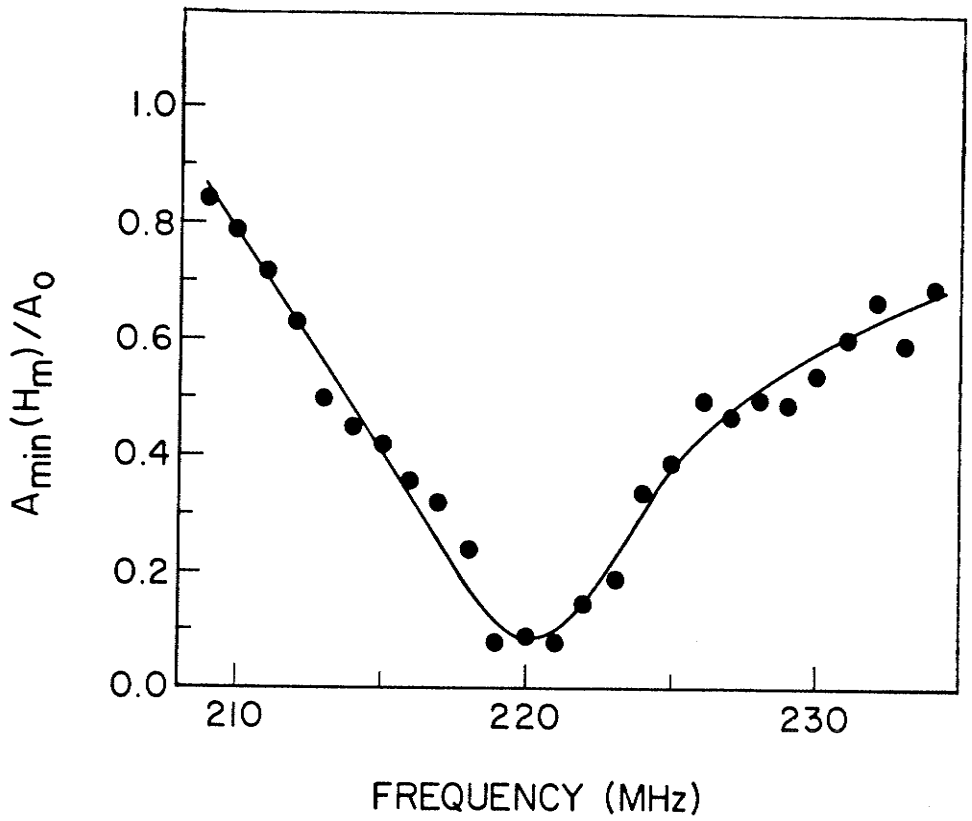

Fig. 5.8 $A_{min}(H_m)/A_o$ as a function of frequency for hexagonal cobalt. $A_{min}(H_m)$ is a minimum of the modulated echo amplitude and A_o is the unmodulated echo amplitude measured at the same pulse separation.

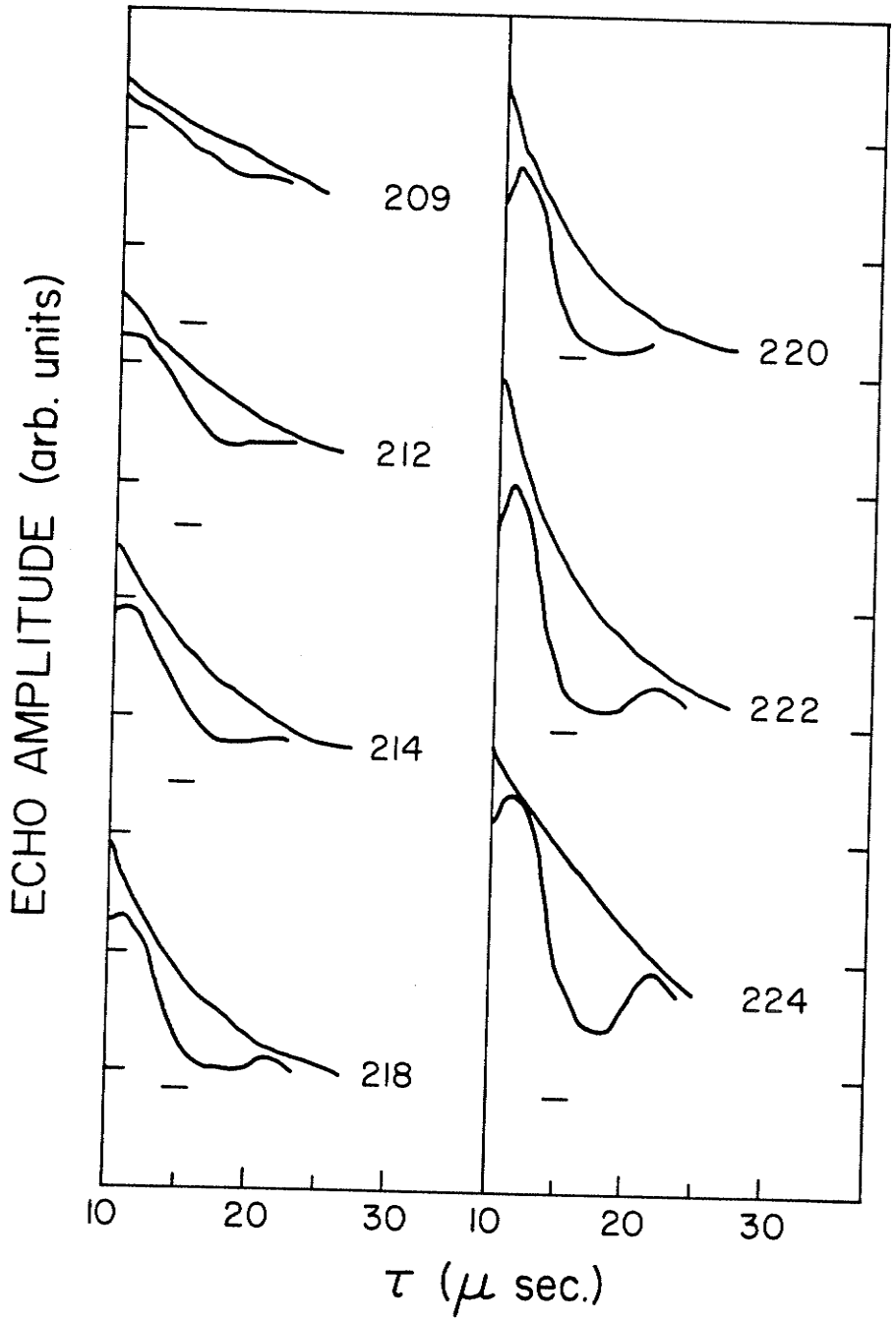

Fig. 5.9 A series of echo-decay envelopes with and without an 80 kHz modulating field applied, for hexagonal cobalt. The level of the zero is indicated by a horizontal line beneath each of the curves. The frequency at which the measurement was taken (MHz) is also shown.

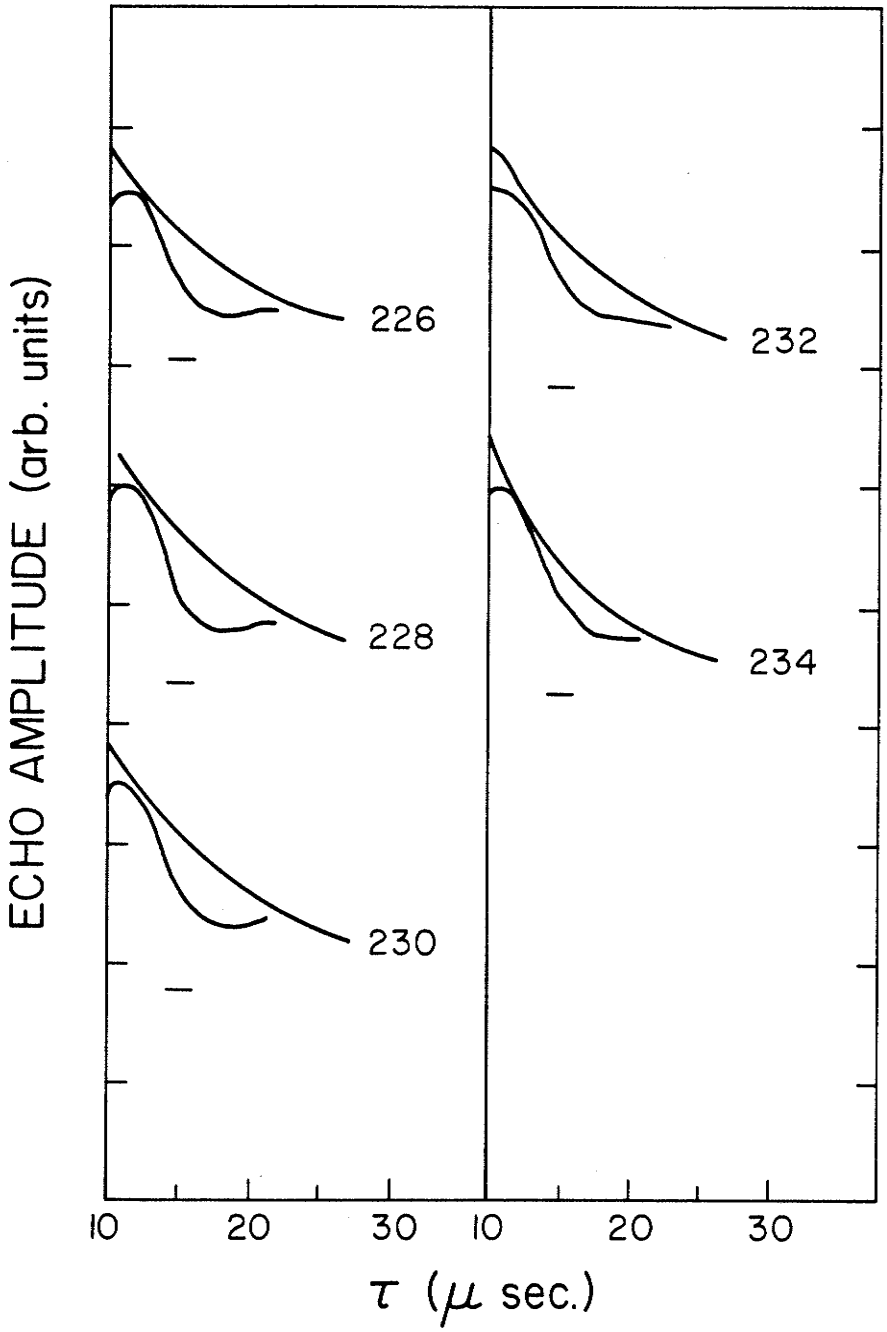

Fig. 5.9 A series of echo-decay envelopes with and without an 80 kHz modulating field applied, for hexagonal cobalt. The level of the zero is indicated by a horizontal line beneath each of the curves. The frequency at which the measurement was taken (MHz) is also shown.

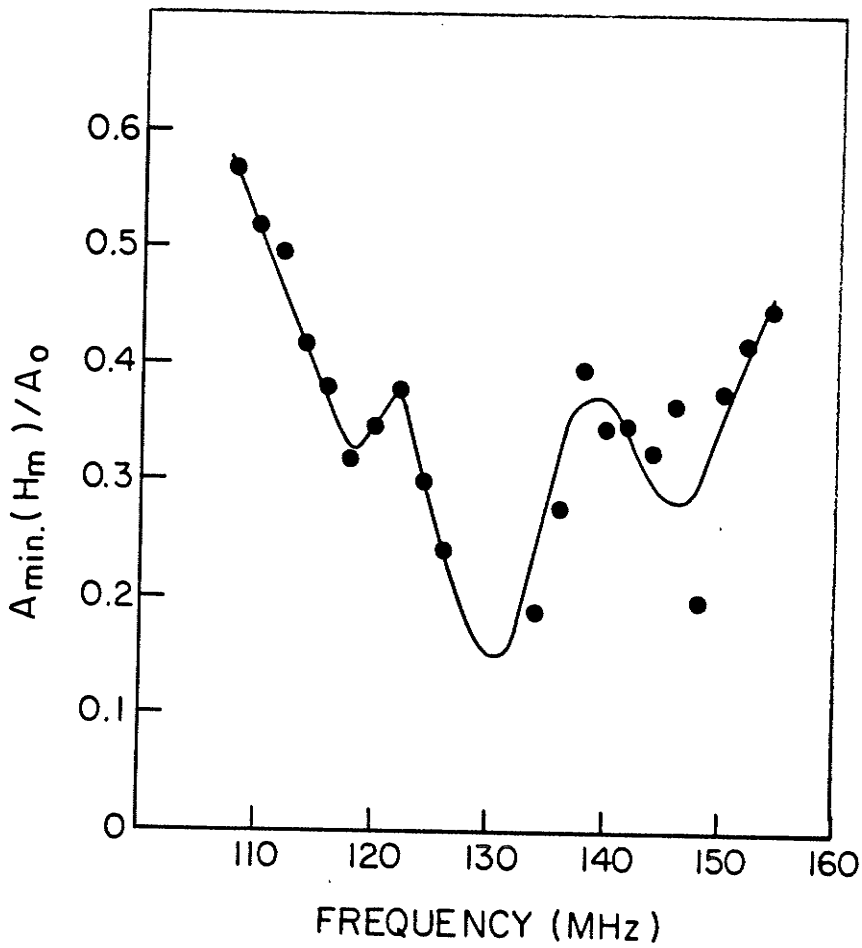

Fig. 5.10 $A_{min}(H_m)/A_o$ as a function of frequency for the Co^{59} resonance in YCo_5.

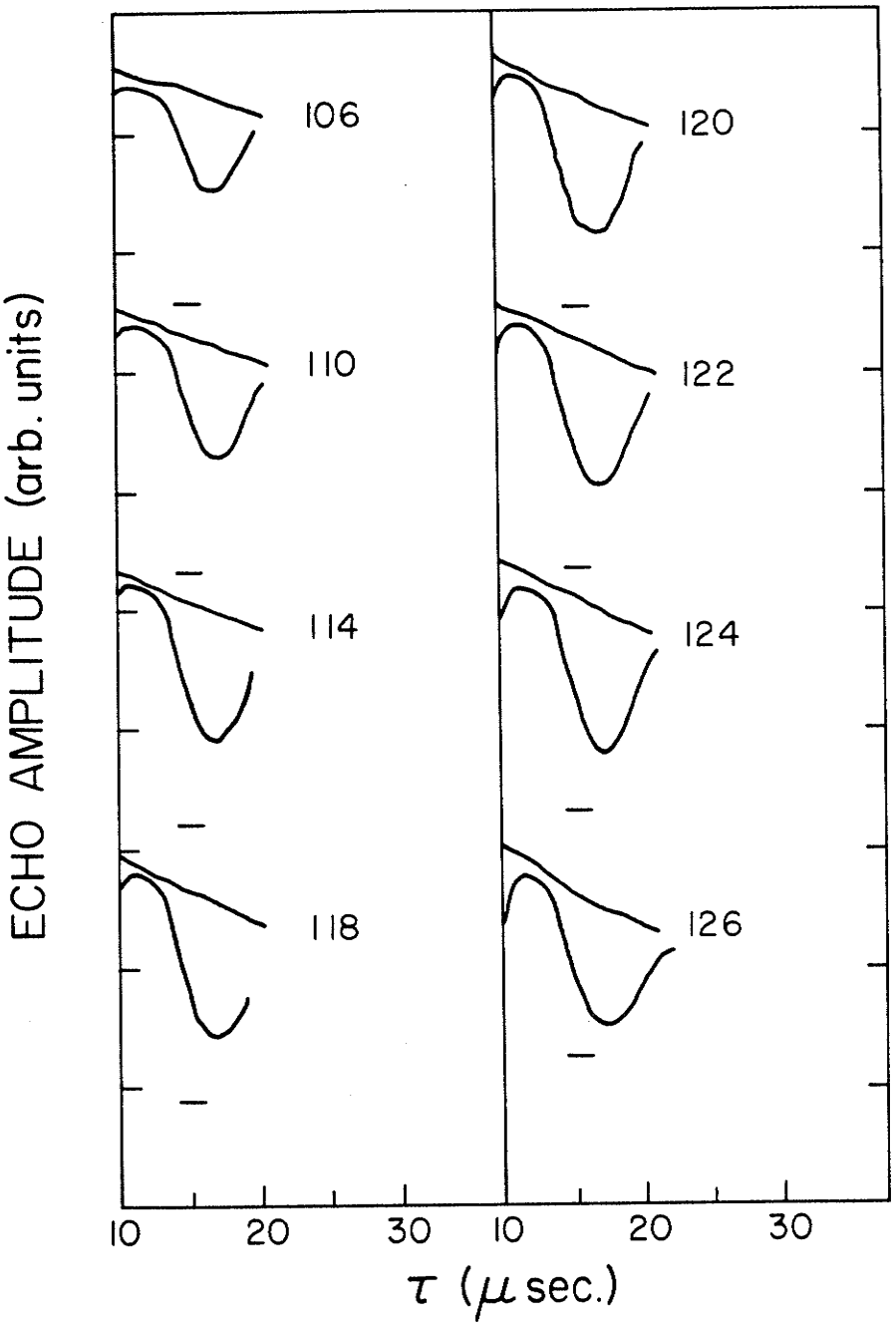

Fig. 5.11 A series of echo-decay envelopes, with and without an 80 kHz modulating field applied, for the Co^{59} resonance in YCo_5. The zero-level is indicated by a horizontal line beneath each of the curves. The frequency at which the measurement was taken (in MHz) is also shown.

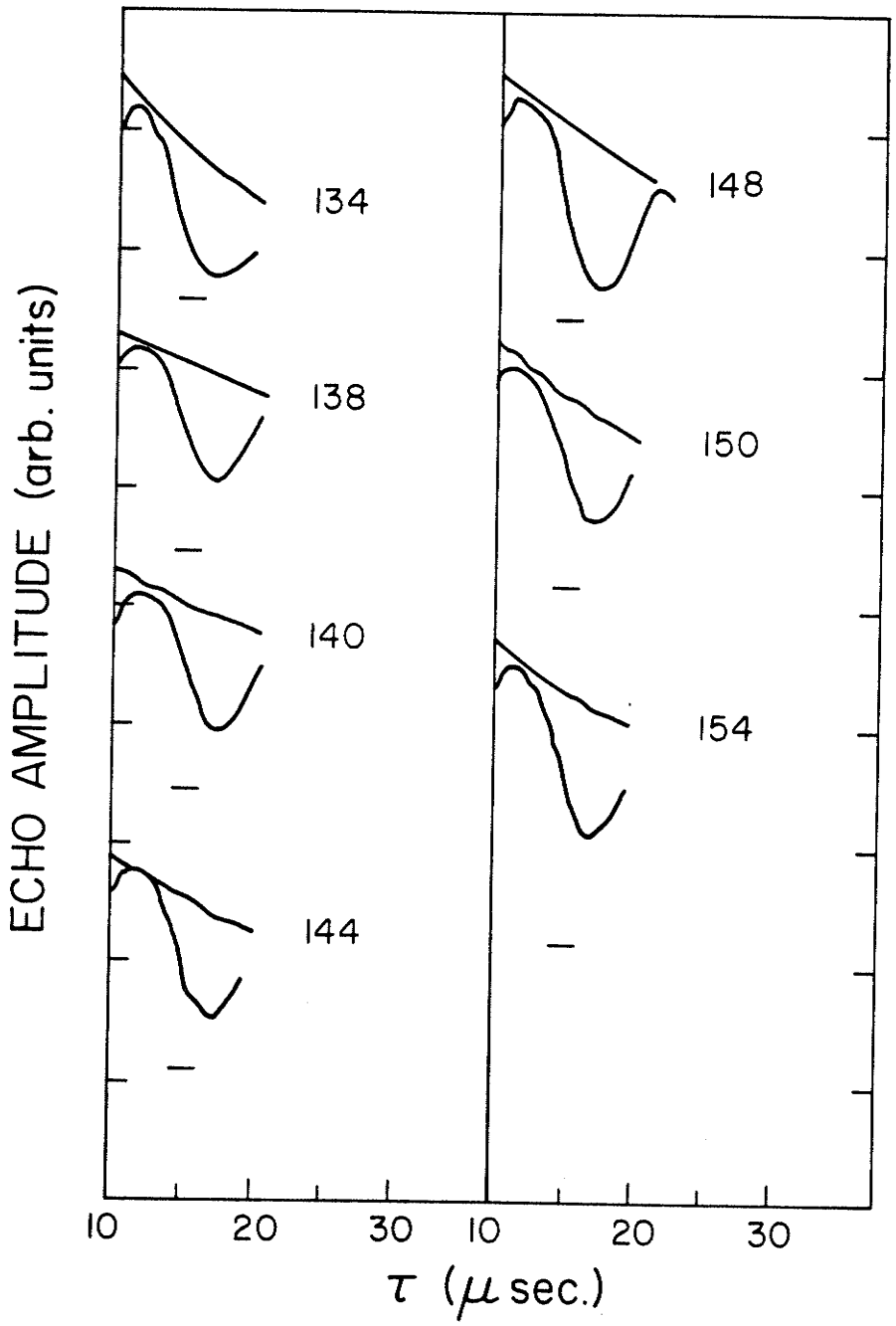

Fig. 5.11 A series of echo-decay envelopes, with and without an 80 kHz modulating field applied, for the Co^{59} resonance in YCo_5. The zero-level is indicated by a horizontal line beneath each of the curves. The frequency at which the measurement was taken (in MHz) is also shown.

Another interesting result from these data was the large difference in the modulating field that is required to obtain approximately the same maximum depth of modulation for the hexagonal Co and YCo_5 samples. This appeared to be directly related to the mechanism responsible for the modulation, as in both cases the applied external modulating field was much smaller than the r.f. field.

A similar investigation of the Co^{59} resonance in Y_2Co_{17} serves to illustrate not only the complexity but also the potential of the modulation technique for the analysis of the NMR spectra obtained from ferromagnetic materials. The Y_2Co_{17} sample was one of a series of Y-Co compounds that we prepared. Figure 5.12 shows the NMR spectrum we obtained for the Co^{59} resonance for Y_2Co_{17}. The spectrum consists of four peaks possibly resulting from the four Co sites in this material.

The modulation spectrum shown in Fig. 5.13 consists of two regions, the three lower frequency peaks displaying a much larger modulation than the high frequency peak. The difference was so large in fact, that the two regions had to be examined separately with different modulating field strengths. The data were then assembled to produce an entire spectrum by compensating for the difference in the modulating field at a few appropriately selected frequencies and then shifting the regions accordingly.

Y_2Co_{17} has a Th_2Ni_{17} hexagonal structure for which the Co (6c) site has a local environment consisting of Co atoms only. As the modulation characteristics for the high frequency peak are quite similar to that found in hexagonal Co it seems reasonable to associate this peak and the low modulation region with the Co (6c) site.

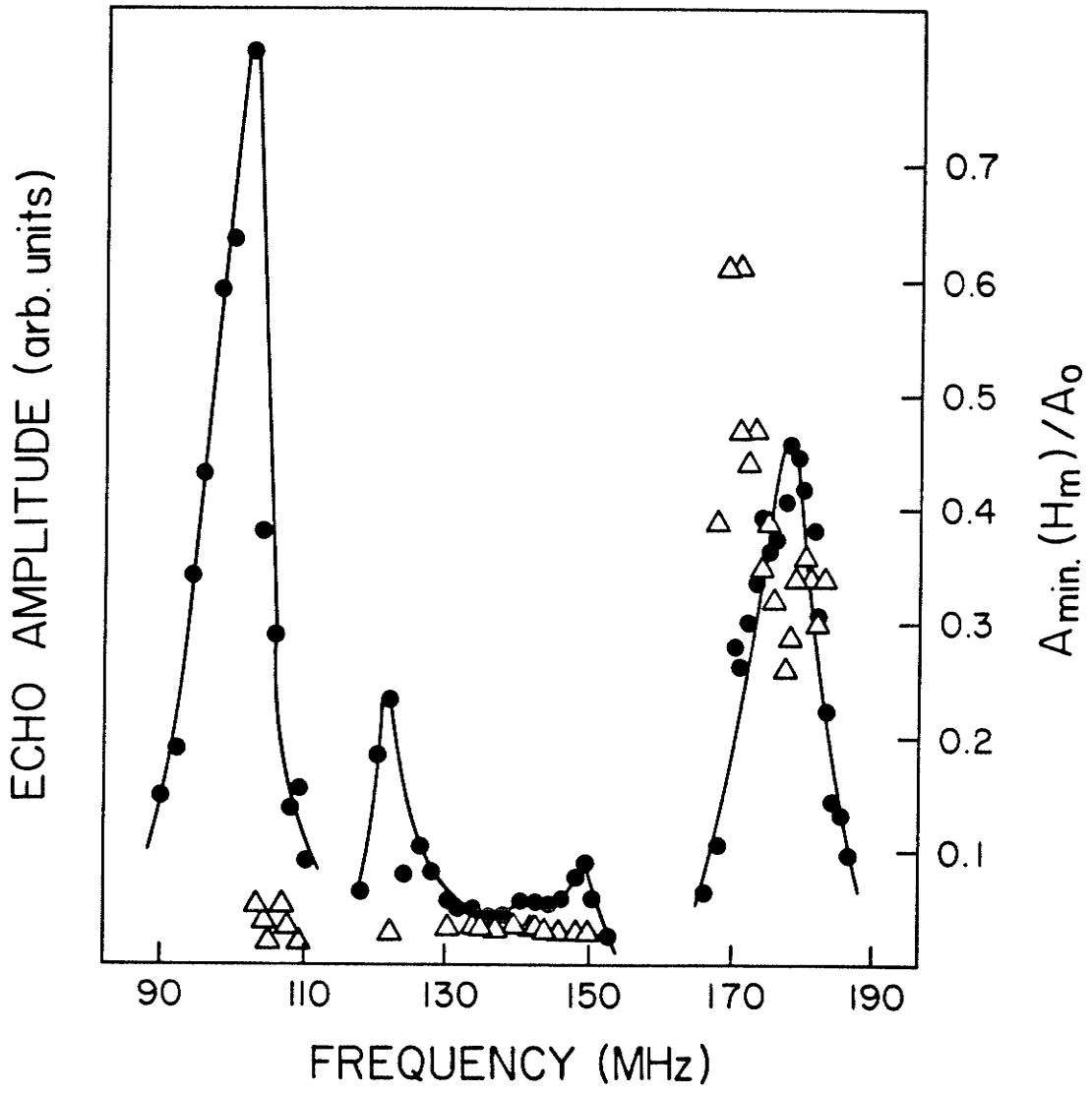

Fig. 5.12 The NMR spectrum for the Co^{59} resonance in Y_2Co_{17}●. Also shown is the external modulation spectrum, $A_{min}(H_m)/A_o$ △.

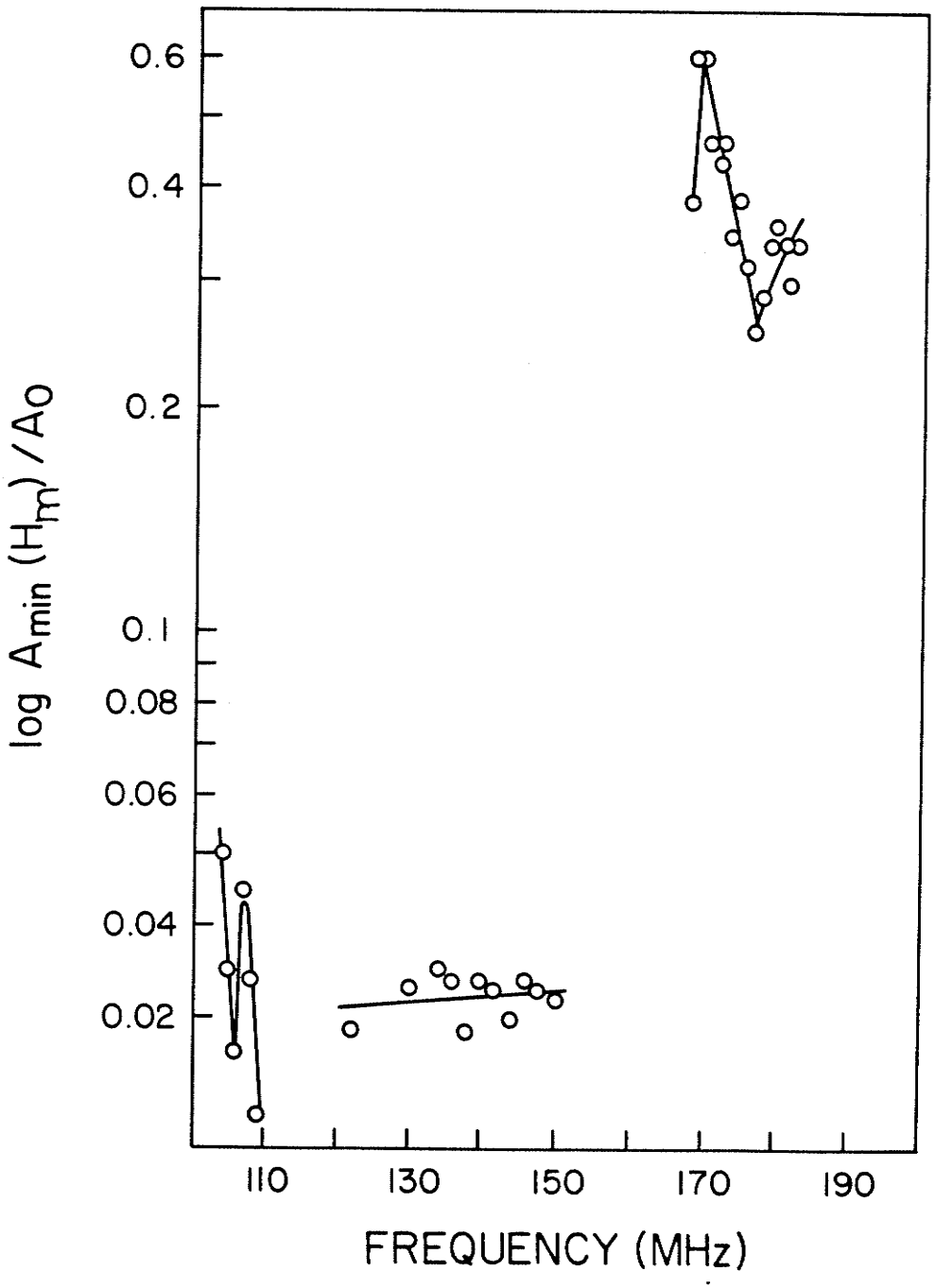

Fig. 5.13 Logarithmic plot of the external modulation spectrum illustrating the extremely large variation observed in different regions of the Y_2Co_{17} spectrum.

5.7 Origin of the Spin-Echo Modulation Effect - The Longitudinal Enhancement Mechanism

In order to determine the origin of the observed modulation, a modification of this experiment is of considerable use. The entire sample circuitry was placed inside a solenoid to generate a field parallel to the axis of the experiment. The field would therefore be parallel to both the r.f. field and the c-axis of the samples. The solenoid was driven by a current generator modulated by a triangular waveform obtained from a low frequency function generator. In this way the sample was driven around a minor loop ideally illustrated in Fig. 5.14(a) and the echo amplitude was recorded as a function of magnetic field at a fixed pulse separation. Figure 5.14(b) illustrates an idealized recording of the echo amplitude while Fig. 5.15 shows experimental data taken at several frequencies for the Co^{59} resonance in YCo_5.

Clearly, the echo amplitude reduction is the result of the wall motion, since reversing the direction of the field sweep (point a in Fig. 5.14) does not lead to an immediate change in the magnetic state of the sample, but does result in an immediate return of the echo amplitude to its maximum value.

Figure 5.16 shows the ratio of the minimum echo amplitude measured in a passage around a minor loop, A_{min}, to the echo amplitude measured when the field sweep is stopped, A_o, plotted as a function of frequency. The zero level, as well as the static echo amplitude, are indicated by tags on the loops in Fig. 5.15 from which the above data

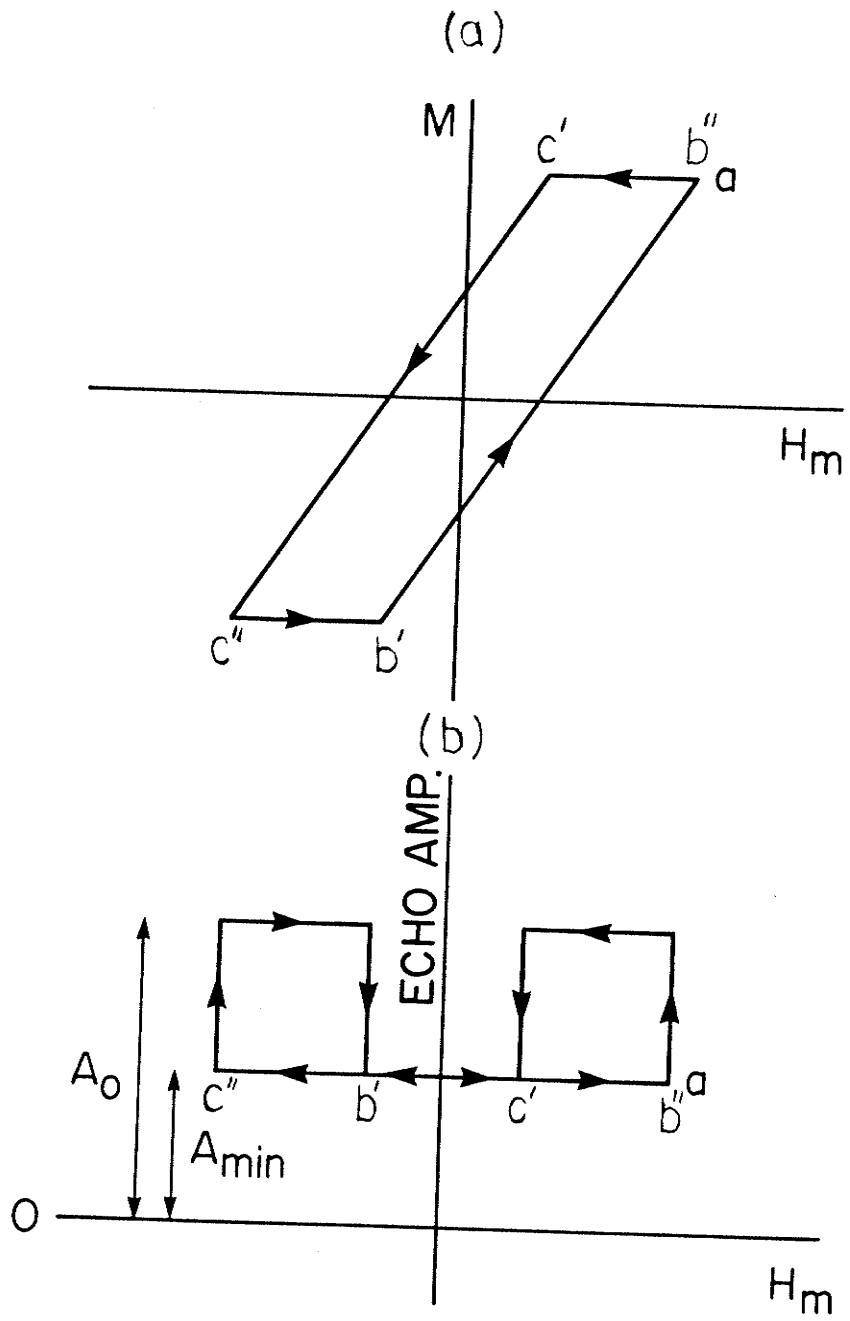

Fig. 5.14 Idealized plot of the echo amplitude versus magnetic field intensity, H_m (b) as the sample is driven around a minor loop (a).

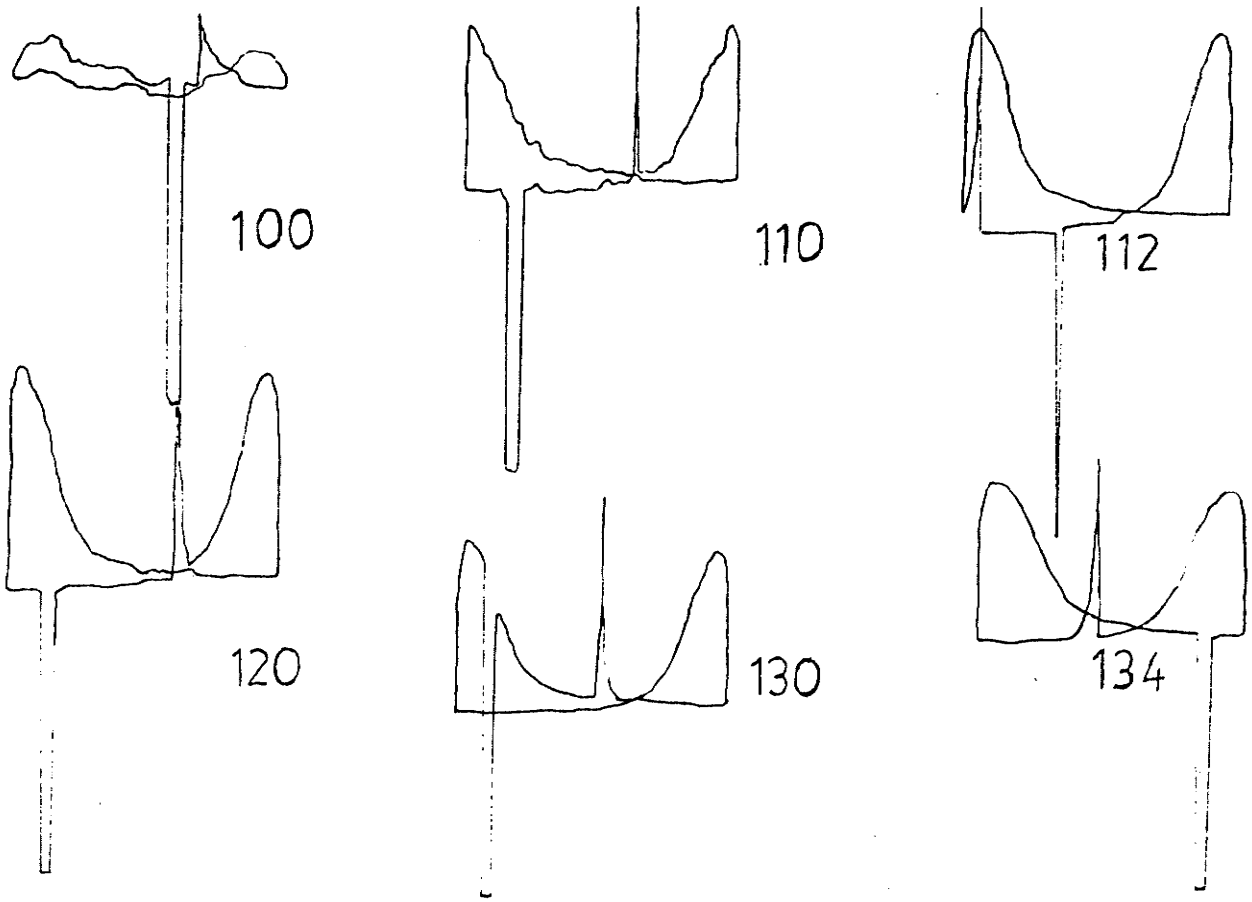

Fig. 5.15 Experimental data showing the echo amplitude versus the magnetic field as the sample is driven around a minor loop for the Co^{59} resonance in YCo_5, at several resonance frequencies.

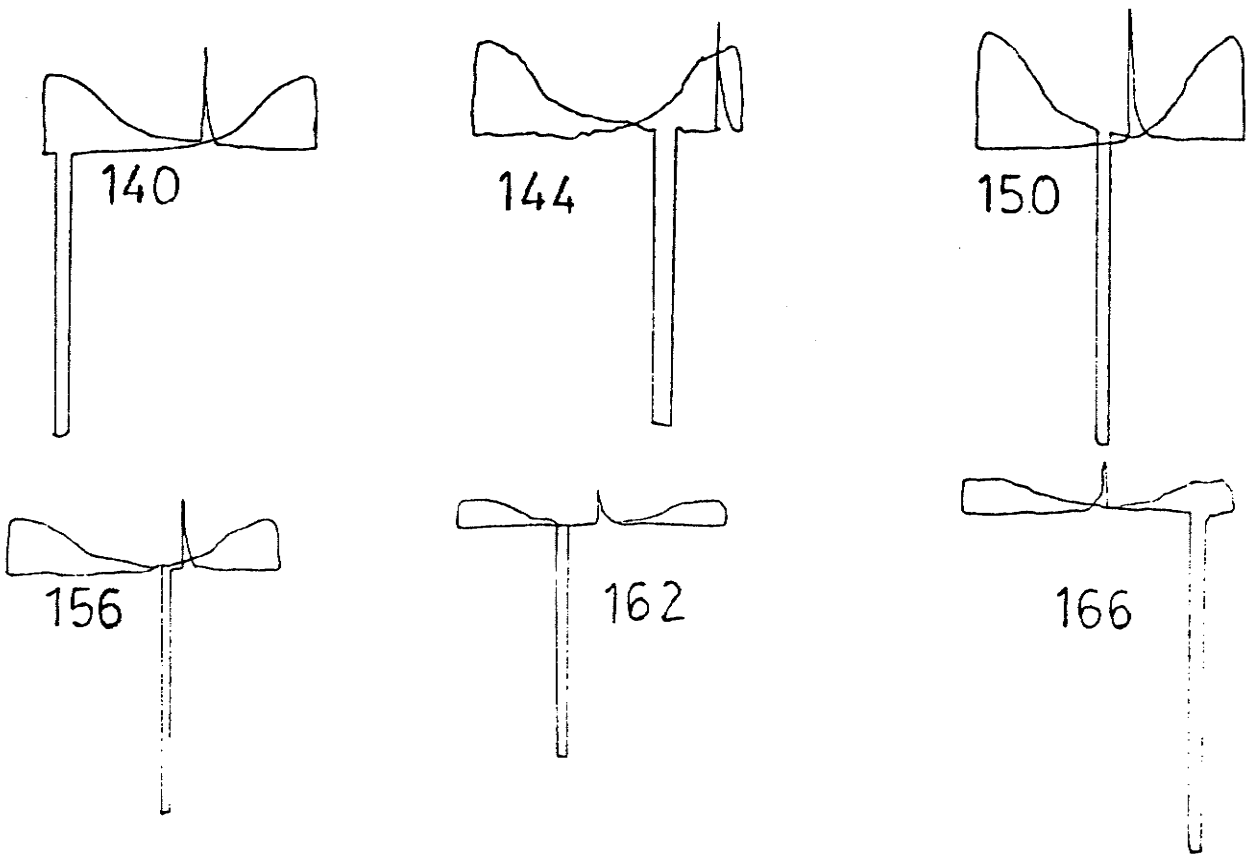

Fig. 5.15 Experimental data showing the echo amplitude versus the magnetic field as the sample is driven around a minor loop for the Co^{59} resonance in YCo_5, at several resonance frequencies.

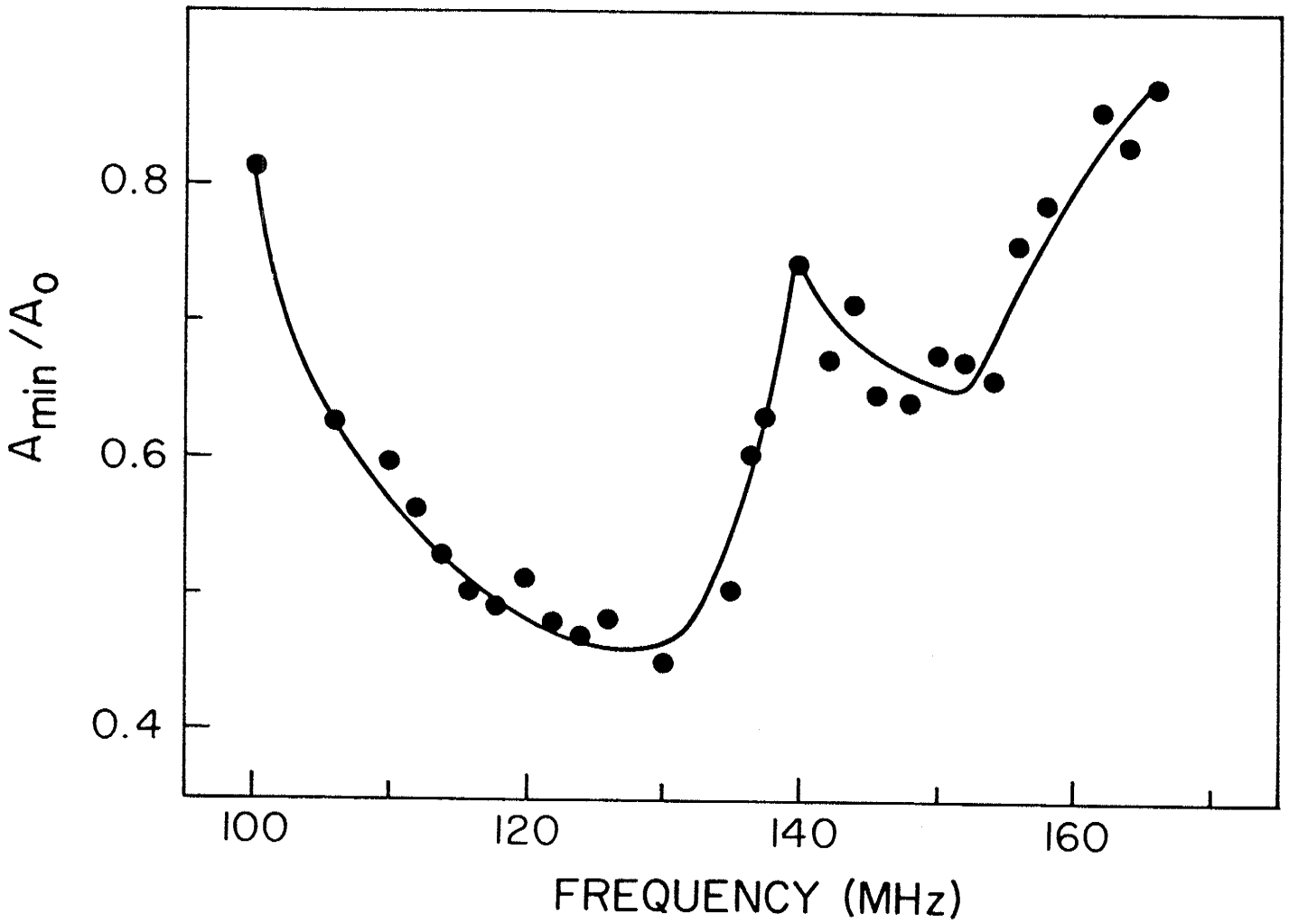

Fig. 5.16 A plot of A_{min}/A_o, measured during a passage around a minor loop, as a function of resonance frequency for YCo_5.

are obtained. This plot closely resembles the modulation spectrum described in the previous section possessing both a central minimum (maximum is the depth of modulation) and a maximum at approximately 140 MHz. The reason the maximum at 121 MHz is not observed may be that the slow sweep method is less sensitive to the structure of the spectrum than the "high frequency" modulation technique. It is felt, however, that both these experiments are making basically the same measurement although the fact that wall motion is inherently involved in the modulation mechanism is only apparent from the slow sweep measurement.

The direct electron spin-echo modulation reported by Dupont and Woonton (23) and Srivastava (24) was related to the ratio of the magnitude of the modulating field, h, to that of the r.f. field during the pulses, H_1. Using the results of their calculations we obtain

$$A_{min}(H_m)/A_o \sim 0.1 \text{ when } h/H_1 = 1.22 \qquad (5.5)$$

We will estimate H_1 for a 90^o pulse, since in the presence of a quadrupole interaction only the first pulse has a well-defined turn angle for an optimum echo amplitude. In a rotating co-ordinate system one may then write $\pi/2 = \gamma_N H_1 t_1$, where γ_N is the gyromagnetic ratio for Co^{59} and t_1 is the pulse width. Using $\gamma_N/2\pi = 1.01 \times 10^3$ Hz/Oe and $t_1 = 0.5$ microsec. one obtains

$$H_1 \sim 495 \text{ Oe} \qquad (5.6)$$

Clearly, H_m is not directly modulating the Co spin-echo envelope since $H_m/H_1 = 1.4/495$ or over two orders of magnitude too small to make any direct effect of H_m experimentally detectable. We

therefore require an enhancement factor of $\eta_{max.} \approx 424$ between the external modulating field and the effective field seen at the nuclei in the domain walls.

We have proposed that this longitudinal enhancement arises out of an anisotropic contribution to the hyperfine field which varies through the domain wall (30), and which is felt by the resonant nuclei as the domain-wall-motion shifts the effective position of the nuclei in the wall. We will assume that the anisotropic contribution to the hyperfine field through the domain wall takes the following form, as in hexagonal Co (20)

$$H_a(x) = H_a \sin^2(\pi x/\delta) \tag{5.7}$$

where δ is the wall width and x is a position in the wall referred to one "edge". Then the enhancement factor for the modulating field parallel to a local quantization direction in the domain wall may be written as

$$\eta_{||} = \frac{h}{H_m} = \frac{\Delta H_a}{H_m} \simeq \frac{\partial H_a}{\partial x} \frac{\Delta x}{H_m} \tag{5.8}$$

where h is the effective modulating field at the nucleus, and Δx is the change in wall location when H_m goes through a half period to satisfy the condition for a minimum in the echo amplitude. One may also write the change in magnetization as

$$m_{||} = \chi_{||} H_m = M_s \frac{2\Delta x}{W} \tag{5.9}$$

where $\chi_{||}$ is the magnetic susceptibility parallel to the c-axis (almost

entirely due to domain wall motion at 77 K), W is the average spacing between walls, and M_s is the saturation magnetization. Using Eqns. 5.7 - 5.9 we obtain

$$\eta_{||} = (\pi W \chi_{||} Ha/2\delta M_s) \sin (2\pi x/\delta) \tag{5.10}$$

The maximum $\eta_{||} = \eta_{max.}$ occurs when $x = 1/4\ \delta$ giving

$$\eta_{max} = \pi W \chi_{||} H_a/2\delta M_s \tag{5.11}$$

The maximum enhancement factor for hexagonal cobalt is experimentally located at ν_o = 220 MHz as seen in Fig. 5.10.

As the depth of the spin-echo modulation is related to the ratio of the enhanced modulating field to the r.f. field, the depth of modulation varies approximately as the longitudinal enhancement factor which, in turn, is dependent on the rate of change of the hyperfine field within the wall.

The spin-echo could be very simply modulated if the modulating field were large enough so that the movement of the domain wall, in the time between r.f. pulses, would be sufficient to remove a significant fraction of the nuclear spins, excited by the first pulse, from the domain wall. This effect can be ruled out, however, since a simple calculation indicates that the ratio of the domain-wall-motion between pulses to domain-wall-width is ~ 10^{-4} for the modulating fields used in the modulation experiments described in the previous section.

The ordinary domain-wall-enhancement factor, η, also depends on the position within the wall (31). This could also lead to an echo envelope modulation. However, the effective change in η between pulses,

$\delta\eta$, would be on the order of the total change through the domain wall $\Delta\eta$, times the ratio of the domain-wall-displacement between pulses to the domain-wall-width. With $\Delta\eta \sim 10\eta$ (31) we have $\delta\eta = 10\eta \times 10^{-4} = \eta \times 10^{-3}$ which is again too small to account for the observed effect.

5.8 Experimental Identification of Domain-Wall-Centre and Domain-Wall-Edge NMR Resonances in Magnetically Ordered Materials

The enhanced modulation of the NMR spin-echo decay envelope resulting from the application of a small a.c. field has been related to the anisotropy in the hyperfine field. Our model described in sections 5.6 and 5.7 predicted that the depth of modulation should be a minimum for nuclei located at the domain-wall-edge and the domain-wall-centre. The modulation spectrum for YCo_5 showed two subsidiary maxima (minima in the modulation depth) which identify the location of the DWE or DWC resonance peaks not observed in the NMR spectrum.

Thus it becomes essential for a complete analysis of the NMR spectra, to be able to experimentally distinguish between the DWC and DWE peaks. The effect of an external magnetic field applied perpendicular to the c-axis on the Co^{59} spin-echo amplitude has been measured for hexagonal Co and YCo_5 (32). The resulting reduction in the echo intensity for hcp Co is largest in that portion of the spectrum associated with the domain-wall-centre and monotonically approaches zero at the lower edge of the spectrum which is associated with the domain-wall-edge. A technique is presented in this section which allows one to make a direct experimental determination of whether an NMR

resonance peak observed in a magnetically ordered material is of the domain-wall-centre or domain-wall-edge type. Such an identification will be necessary for a microscopic analysis of the Co sub-lattice contribution to the magnetocrystalline anisotropy in the RCo_5 compounds. The technique should be generally applicable to magnetically ordered materials in which NMR experiments are conducted.

The samples again consisted of magnetically-aligned powders of the material of interest encased in a wax binder. The r.f. field was applied along the c-axis for maximum coupling with the domain-wall-motion, and the d.c. field H_o was applied in the basal plane.

This technique resembles the methods used by Cobb et al (31) for the analysis of the Cr resonance in $CrBr_3$ (see chapter 4.6). However, a field dependent frequency shift is not easily resolved for the broad peaks characteristic of the RCo_5 compounds.

In our experiment the enhanced r.f. field, H_1, used is much smaller than the total linewidth and only a narrow band of width $\Delta\omega_1 \simeq \gamma_N H_1$, where γ_N is the gyromagnetic ratio for Co^{59}, is excited around the exact resonance frequency ($H_1 \sim 500$ Oe compared with a total linewidth of ~ 10 kOe for hcp Co). To first order the variation of the spin-echo amplitude will be dependent on the degree to which nuclei are shifted out of resonance.

It is assumed that the application of the d.c. field, H_o, does not produce a significant variation in θ, the orientation with respect to the c-axis of the electronic spins located within the domain wall, and consequently does not produce a variation in the hyperfine

field at a given nucleus as a result of the anisotropy in the hyperfine field. The variation in the NMR frequency for $\vec{H}_o \perp \vec{c}$ is then approximately given by the vector sum of the effective external field and the hyperfine field. The effective external field is given by

$$H = H_o - D_\perp M_s \sin(\theta_o) \tag{5.12}$$

where $D_\perp$ is the demagnetization factor perpendicular to the c-axis ($4\pi/3$ for a spherical particle), M_s is the saturation magnetization, and θ_o is the angle the electronic moment of atoms located within domains make with respect to the c-axis. The angle θ_o and hence the direction of the domain magnetization can be obtained from the equilibrium condition between the torque exerted on the magnetization by the external field and the magnetocrystalline anisotropy

$$\frac{-\partial E_c}{\partial \theta} = -\vec{H}_o \times \vec{M} \tag{5.13}$$

where

$$E_c = K_1 \sin^2\theta + K_2 \sin^4\theta \simeq K_1 \sin^2\theta \tag{5.14}$$

is the magnetocrystalline energy.

The resultant magnetic field at a nucleus of an atom whose magnetic moment has an angle θ with respect to the c-axis given by

$$H_t = (H_i^2 + H^2 + 2 H_i H \sin\theta' \cos\phi)^{\frac{1}{2}} \tag{5.15}$$

Here θ' is the angle between the hyperfine field and the c-axis, given by (33) $\tan\theta' = H_\perp / H_{||} \tan\theta$ where $H_{||}$ and $H_\perp$ are the hyperfine fields

when the electronic moments point parallel and perpendicular to the c-axis, respectively, ϕ is the azimuthal angle giving the hyperfine field and electronic moment orientation with respect to the direction of the external field, and H_i is the hyperfine field given by

$$H_i = (H_{||}^2 \cos^2\theta' + H_{\perp}^2 \sin^2\theta')^{\frac{1}{2}} \qquad (5.16)$$

If $H_{||}, H_{\perp} \gg |H_{||} - H_{\perp}|$ and $2H \sin\theta' \cos\phi / H_i \ll 1$ then

$$H_t \simeq H_i \ (1 + H \sin\theta' \cos\phi / H_i) \qquad (5.17)$$

and the shift in the resultant field at the nucleus of an atom with magnetic-moment orientation (θ, ϕ) is

$$H_t - H_i \simeq H \sin\theta' \cos\phi \qquad (5.18)$$

The maximum shift in the resultant magnetic field occurs for nuclei located at the wall centre, while for nuclei at the wall edge there is no shift (to first order).

Kawakami et al (20) have measured the temperature dependence of the DWE and DWC NMR frequencies for hexagonal Co and report that at 77 K the resonances occur at 218 and 227 MHz, respectively. Figure 5.17 shows the field dependence of the hcp Co spin-echo amplitude we have measured at several frequencies. The monotonic decrease of the echo amplitude suggests that the shifting and concentrating of intensity to the low-frequency edge (DWE) of the spectrum does not occur, presumably because the 90 - 180 condition for echo formation cannot be satisfied

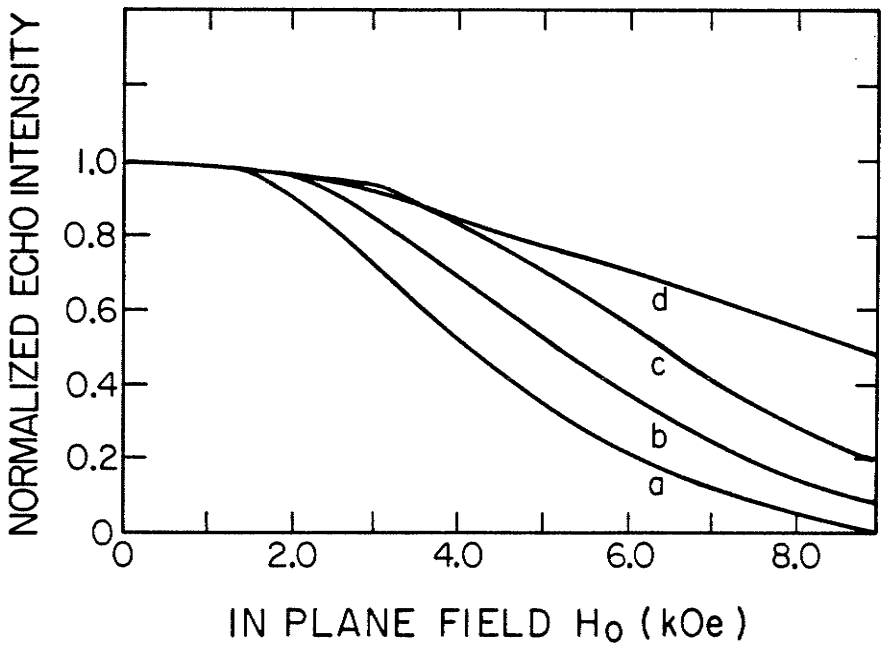

Fig. 5.17 Variation of the spin-echo intensity with applied field $\vec{H}_o \perp$ c-axis for hcp cobalt at 77 K. Curves (a) and (b) are at 230 and 228 MHz, respectively, and are representative of the DWC. Curve (c) is at 224 MHz and curve (d) is at 220 MHz and is representative of the DWE.

for the nuclei experiencing a shifted field. It therefore seems reasonable that to first orde. the reduction in echo amplitude is proportional to the amount of shift.

For the case of the random domain-wall-distribution (the spins at the centre of the walls have all possible orientations in the basal plane with equal probability) the reduction in echo intensity would be proportional to the average shift in the field which is given by

$$\langle H_t - H_i \rangle_{av} = \tfrac{1}{2} H \sin \theta' \qquad (5.19)$$

From Fig. 5.17, curves (a) and (b), it is seen that the domain-wall-signal is reduced to zero for an applied field of approximately 9 kOe. From Eqns. (5.13) and (5.14) and using appropriate values of M_s and K_1, from Ref. 5.34 and 5.29, respectively, we obtain $\theta_o \approx 45^o$ and an effective external field, H_c, of 4.78 kOe assuming the particles to be spherical in shape.

Since, to first order, $A_o - A_H \propto \langle H_t - H_i \rangle_{av}$, it follows that

$$\frac{A_o - A_H}{A_o} = \frac{H \sin \theta'}{H_c} \qquad (5.20)$$

where the experimentally determined parameter, H_c, is twice the effective width of the excitation window. Any deviation of the effective demagnetization factor from the value for a spherical particle is inherently contained within H_c.

The ratio of the echo amplitude in the absence of and with a d.c. magnetic field applied in the basal plane can be expressed as

$$\frac{A_o}{A_H} = \frac{1}{1 - H \sin \theta'/H_c} \qquad (5.21)$$

Figure 5.18 shows the measured and calculated echo amplitude reduction ratio, A_o/A_H, for hcp Co for an applied field of 8 and 4 kOe. θ' is related to the frequency by Eqn. 5.16 and the relation $\nu = \gamma_N H_i$. A_o/A_H rises sharply in that part of the spectrum associated with the domain-wall-centre and monotonically approaches unity at the lower edge of the spectrum associated with the domain-wall-edge. The calculated results are in qualitative agreement with the experimental data.

The experiment, therefore, appears to make it possible to distinguish whether any given NMR resonance peak in a magnetically ordered material is of the DWE or DWC type.

An additional secondary effect, which would be important only in the case where the applied field is not much less than the anisotropy field, H_A, could lead to an increase in the echo amplitude reduction ratio for the domain-wall-edge resonance. As a result of the domain rotation magnetization the domain walls will "unwind" to some extent, shifting the domain-wall-edge resonance frequency from $\nu_{II} = \gamma_N H_{II}$ to $\nu_{II} = \gamma_N (H_{II}^2 \cos^2 \theta_o + H_\perp^2 \sin^2 \theta_o)^{1/2}$ and resulting in an effective echo amplitude reduction for the domain-wall-edge resonance.

Since the anisotropy field, H_A, for hcp cobalt at 77 K is 12.7 kOe ($H_A = 2K_1/M_s$ and again using appropriate values for M_s and K_1 from Ref. 5.34 and 5.29, respectively) an applied field of 8 kOe should produce a substantial domain rotation and shift in the DWE resonance frequency ($\theta_o = 39^o$).

Figure 5.19 shows the echo amplitude reduction ratio as a

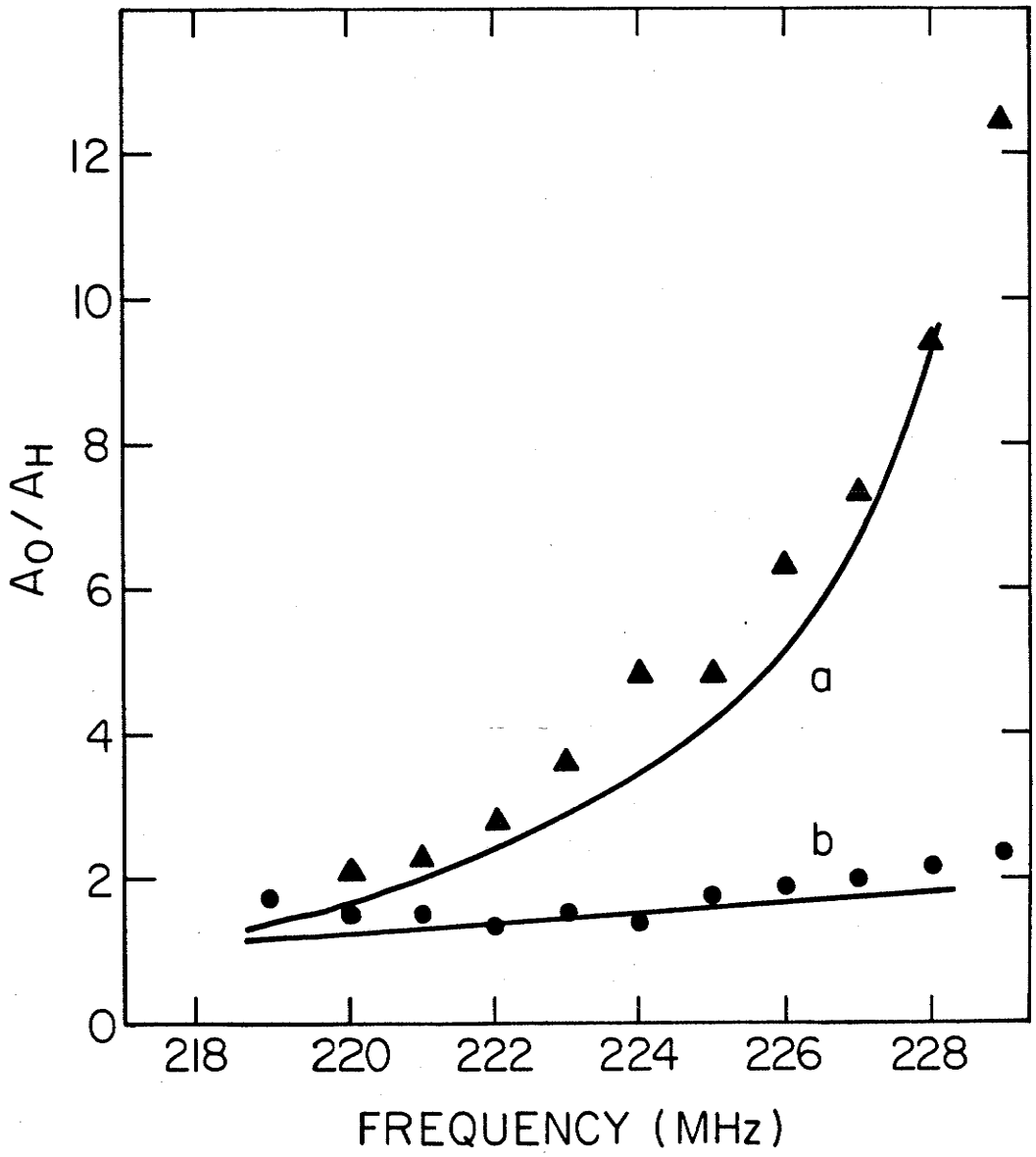

Fig. 5.18 The echo amplitude reduction ratio, A_o/A_H, as a function of frequency for hcp Co at 77 K and with an applied external field of (a) H_o = 8 kOe and (b) H_o = 4 kOe. The solid curves represent the calculated A_o/A_H assuming the echo amplitude reduction is proportional to the field shift.

function of frequency, taken at a larger r.f. field in order to also resolve the domain-wall-edge resonances at 217 MHz. In these data we see the effect of the applied perpendicular d.c. field upon the domain-wall-edge, resulting in a large reduction in the echo amplitude. The data were taken at 77 K for an applied magnetic field of 4 kOe and 8 kOe. The zero-field Co^{59} resonance is also shown.

As the anisotropy fields for the RCo_5 compounds are much larger than for cobalt, this effect should not be of any significance for the application of this technique to these compounds.

Figure 5.20 shows a plot of A_o/A_H as a function of frequency for YCo_5. The ratio is approximately one in the intermediate region between NMR peaks and rises to a larger value as the frequency approaches the region of both peaks. The experimental results therefore indicate that the two observed peaks in the spectrum are both of the DWC type. The two subsidiary maxima (minima in modulation depth) in the modulation spectrum discussed in the previous section would then determine the location of the DWE resonances for the two Co sites. This location of the DWE resonances in the intermediate region between NMR peaks is consistent with the small echo amplitude reduction observed in this region which is characteristic of nuclei located at the domain-wall-edge.

Figure 5.20 also shows the echo amplitude reduction calculated using Eqn. 5.21 for an external field of 9 kOe and for several different values of the parameter, H_c. Although we have located both the DWC and DWE resonances with considerable certainty, it is still not clear which edge resonance to associate with which centre resonance,

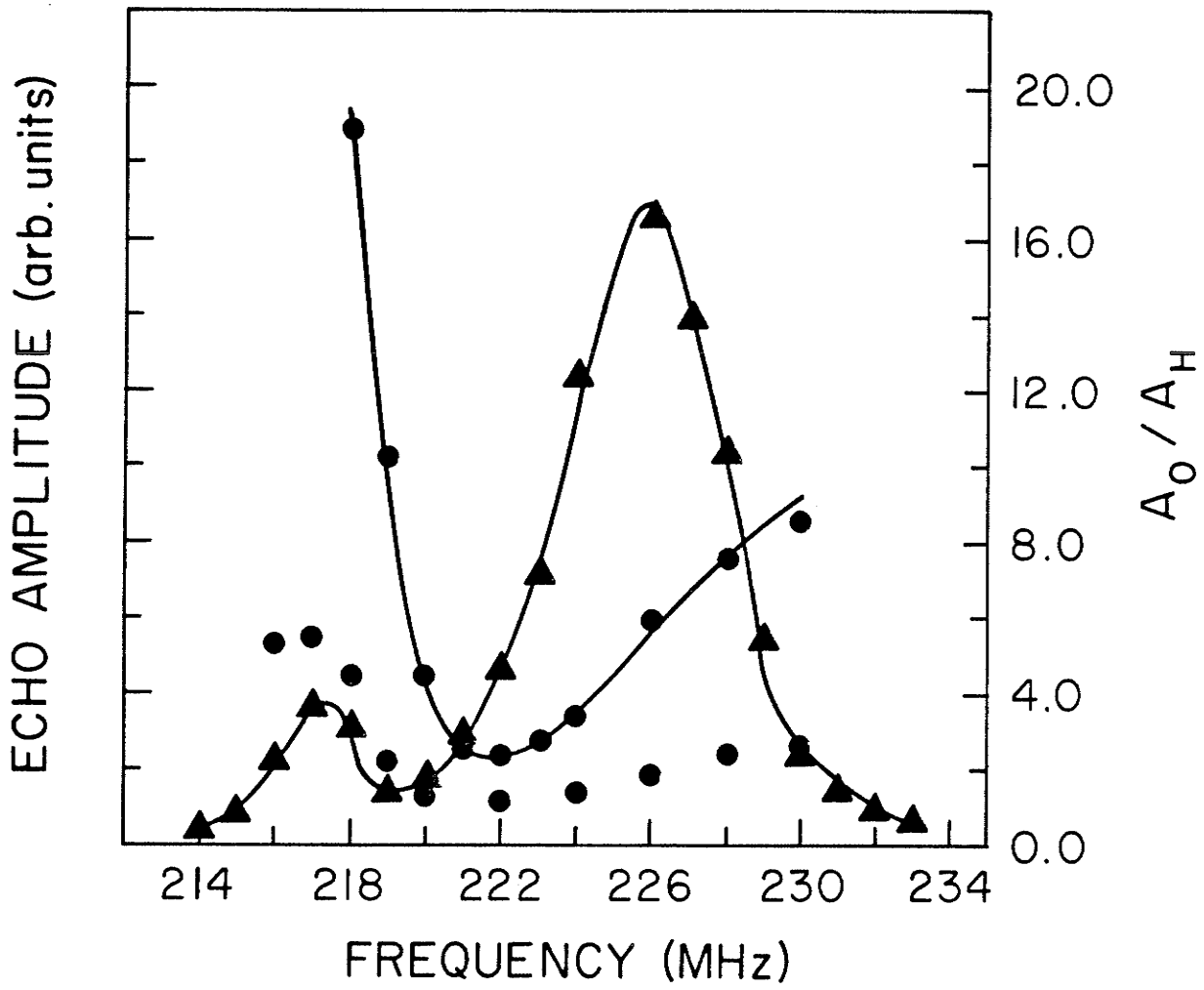

Fig. 5.19 The hcp Co spectrum measured at a large r.f. field ▲. Also shown is the echo amplitude reduction ratio as a function of frequency measured with an applied field of 4 and 8 kOe. ●

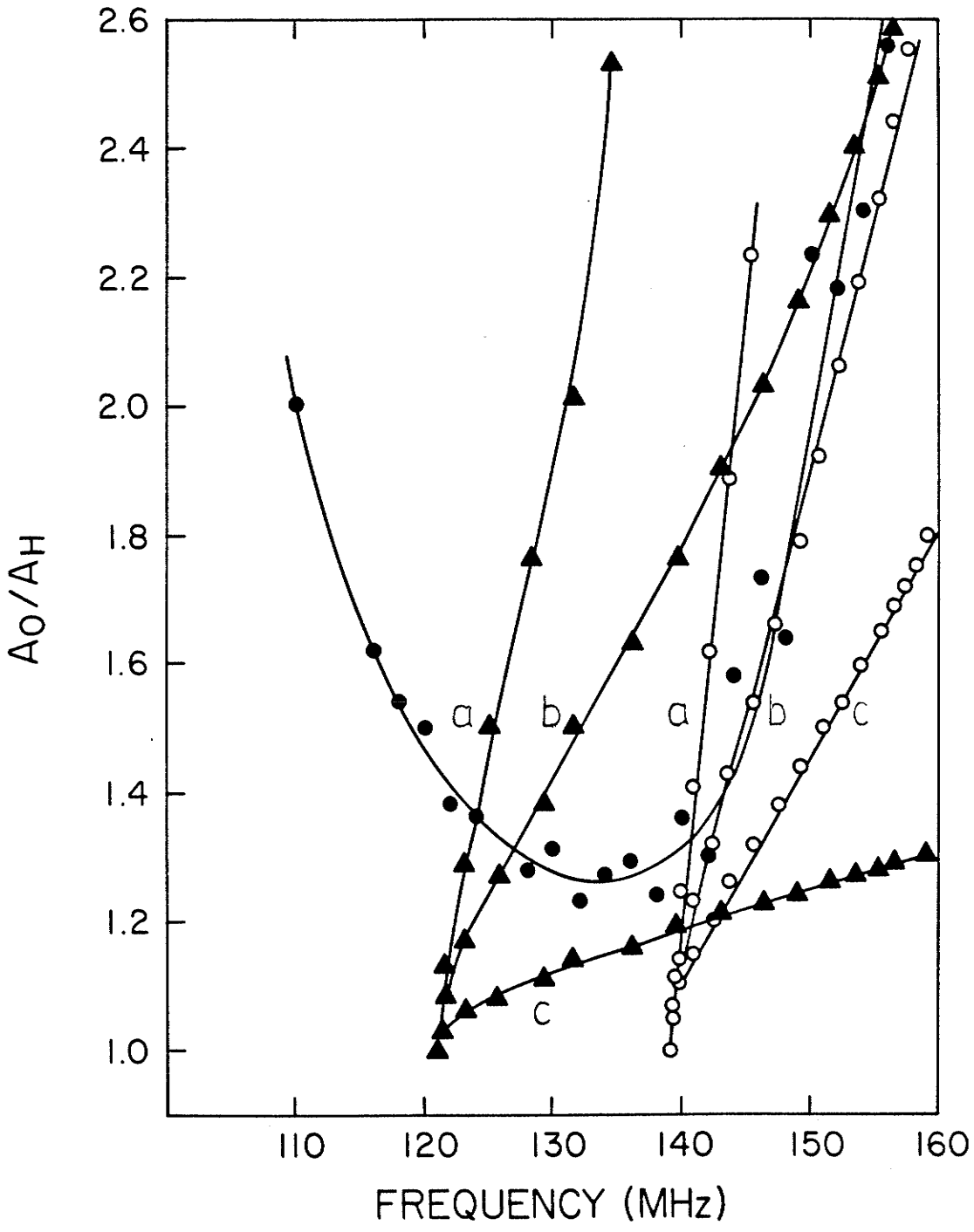

Fig. 5.20 The echo amplitude reduction ratio, A_O/A_H, versus frequency for YCo_5 ●. Also shown is the calculated ratio using Eqn. 7.21 assuming that (1) the 121 MHz DWE resonance is associated with the 146 MHz DWC resonance ▲ or (2) the 138 MHz DWE resonance is associated with the 146 MHz DWC resonance ○. For combination (1) we used H_c values of 9(a), 13.8(b) and 38 kOe(c). For combination (2) we used the same values except for case (c) H_c = 20 kOe.

which is absolutely necessary to determine the anisotropy in the hyperfine field for both Co sites. Therefore we have examined both combinations possible for the high frequency DWC resonance peak. It is felt that the value of H_c is in some way a function of the total linewidth (i.e. the anisotropy in the hyperfine field). The experimental value for hexagonal cobalt was approximately one-half the linewidth. For this particular Co site in YCo_5 the anisotropy in the hyperfine field is then either 26 kOe or 9 kOe. Figure 5.21 shows the field dependence of the echo amplitude for the Co^{59} resonance in YCo_5. Of particular interest are the curves (a) and (b) which correspond to the high frequency DWC resonance. Since $\theta_o \simeq 0$ we have $H_c > 9$ kOe, from which we can conclude that the 121 MHz edge resonance arises from the same site as the 147 MHz centre resonance. However, the calculated fit in Fig. 5.20 is rather poor, the best fit to the experimental data, in fact, being obtained using the other edge resonance with $H_c = 13$ kOe. The poor quantitative agreement is not too surprising considering the nature of the phenomenological model the calculation is based on.

The qualitative agreement, however, between the measured and the calculated frequency dependence of the echo amplitude reduction ratio for hcp Co suggests that this technique can be used to determine whether a NMR resonance peak observed in a magnetically ordered material is of the DWE or DWC type. The results also indicate that the two peaks observed in the Co^{59} resonance of YCo_5 are both of the DWC type and related to the two inequivalent Co sites present.

An approximation inherent to our model for the field reduction

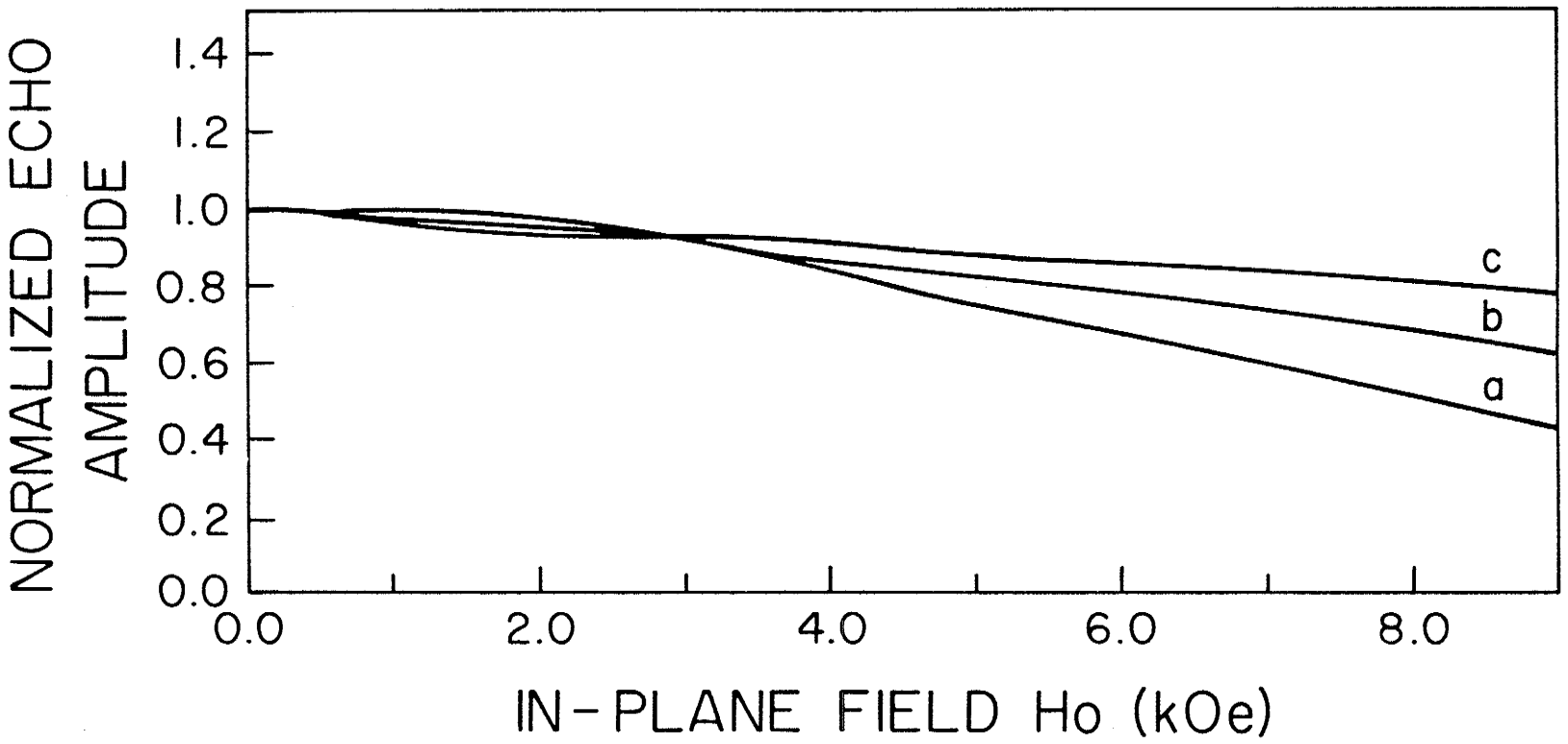

Fig. 5.21 Field dependence of the echo amplitude for the Co^{59} resonance in YCo_5. Curve (a) is at 152 MHz, curve (b) is at 144 MHz and curve (c) is at 132 MHz.

of the echo amplitude is that we have not considered any lineshape, rather, we have assumed a gate-shaped spectrum with the experimentally determined (for hcp Co) DWE and DWC resonance peaks located at the edges. The agreement we obtained between the measured and calculated results indicate that the pulses used excite only a small portion of the entire linewidth and the assumption that the echo amplitude reduction is proportional to the field shift is accurate, and as a consequence the lineshape is not of great significance in this experiment.

5.9 Experimental Results for the RCo_5 Compounds

The identification of the origin of the two NMR peaks observed in the YCo_5 spectrum, as well as the location of the DWE resonances using the enhanced echo-decay envelope modulation results will, as yet, not allow the determination of the individual anisotropy in the hyperfine field of the two Co sites. It is still not known which DWC resonance to associate with which DWE resonance. A slightly more sophisticated analysis of the results than the largely phenomenological approach taken in the previous sections can answer this final question concerning the nature of the Co^{59} resonance spectrum in YCo_5. These results will be presented in the next chapter accompanying a more general examination of the Co spectra in the RCo_5 compounds. In this section we will present the experimental results that were obtained for several other RCo_5 compounds, using the experimental techniques developed in the previous sections. In addition, zero-field quadrupole modulation measurements were also taken, where possible.

The samples again consisted of magnetically aligned powders encased in a wax binder. As the r.f. magnetic field of the dominant mode of the cavity or the field inside the inductor of the L-C tuned circuit were both parallel to the axis of the sample tube, the compounds which maintain an easy c-axis at low temperatures were aligned parallel to the sample tube axis. The compounds which have an easy plane or cone were aligned perpendicular to the sample tube axis (for example, $PrCo_5$, $NdCo_5$). These arrangements would give maximum coupling between the r.f. field and the domain walls.

Figures 5.22 - 5.26 show a summary of the results obtained for $GdCo_5$, $SmCo_5$, YCo_5, $PrCo_5$ and $CeCo_5$. In each case figure (c) gives the relative spin-echo amplitude extrapolated to $\tau = 0$, where τ is the pulse separation, as a function of frequency. Figure (b) gives the echo amplitude reduction as a function of frequency. This data was not taken for $PrCo_5$ since at low temperature this compound has an easy cone making interpretation more difficult, and at the present stage of the study of these materials using NMR it was felt that it would be wise to concentrate the efforts on the simpler uniaxial compounds. Figure (a) shows the modulation spectra obtained for the above compounds. Also shown in Fig.(a) are the observed quadrupole modulation period and depth as a function of frequency. The depth of modulation was defined in the same way as for the spin-echo amplitude modulation observed with the applied modulating field, i.e.: the depth is the ratio of the minimum echo amplitude to the unmodulated echo amplitude at a fixed value of the pulse separation τ. The presence of the quadrupole modulation did not in any way affect the measurement of the NMR spectra or the modulation

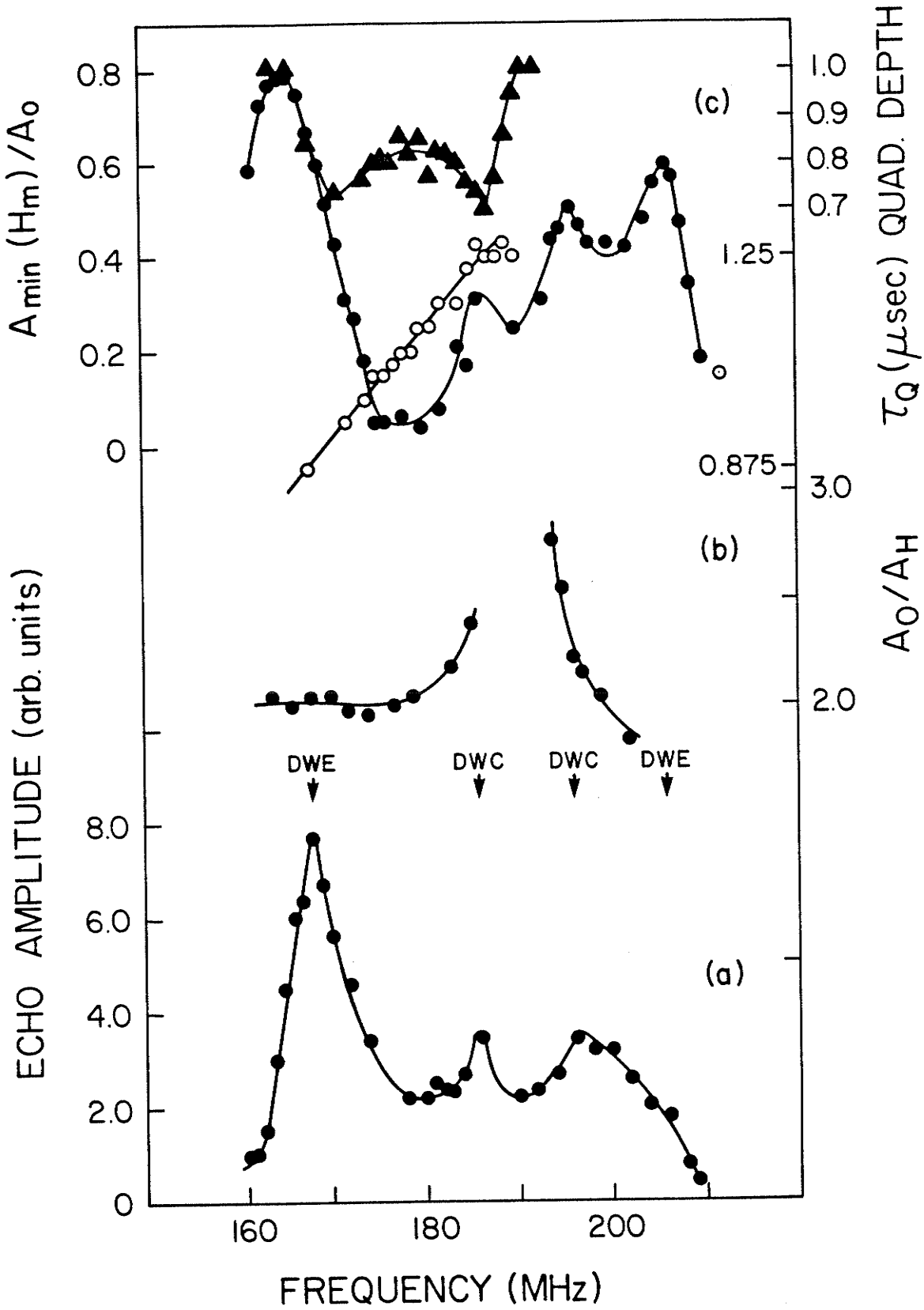

Fig. 5.22 A summary of the experimental results obtained for $GdCo_5$ at 4.2 K. Fig. (a) gives the Co^{59} spectrum, (b) gives the echo amplitude reduction produced by a perpendicular field, as a function of frequency and (c) shows the modulation spectrum. Fig. (c) also shows the quadrupole modulation period O and depth ▲ as a function of frequency.

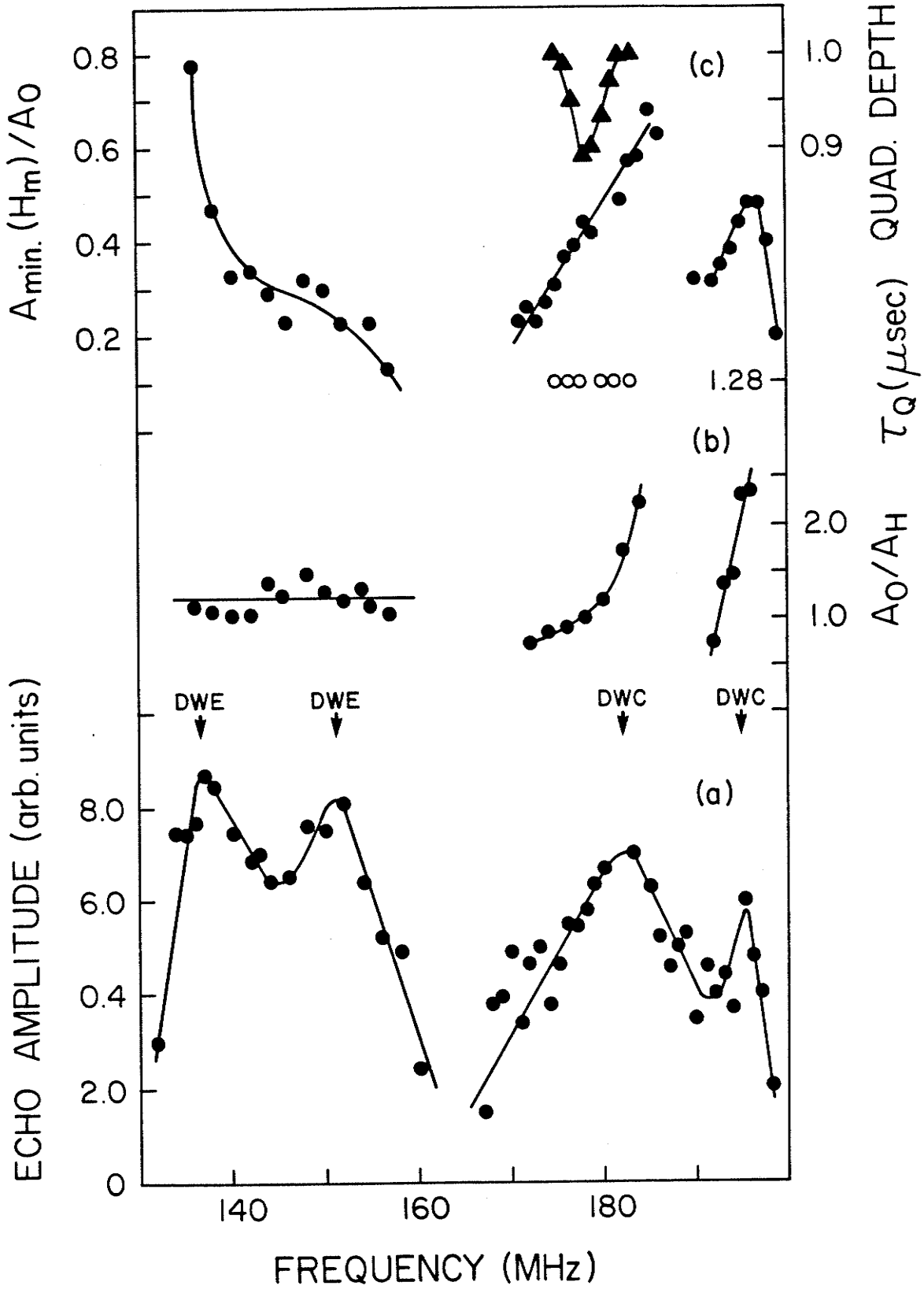

Fig. 5.23 A summary of the experimental results obtained for $SmCo_5$ at 1.5 K. Fig. (a) gives the Co^{59} spectrum, (b) gives the echo amplitude reduction produced by a perpendicular field, as a function of frequency and (c) shows the modulation spectrum. Fig. (c) also shows the quadrupole modulation period O and depth ▲ as a function of frequency.

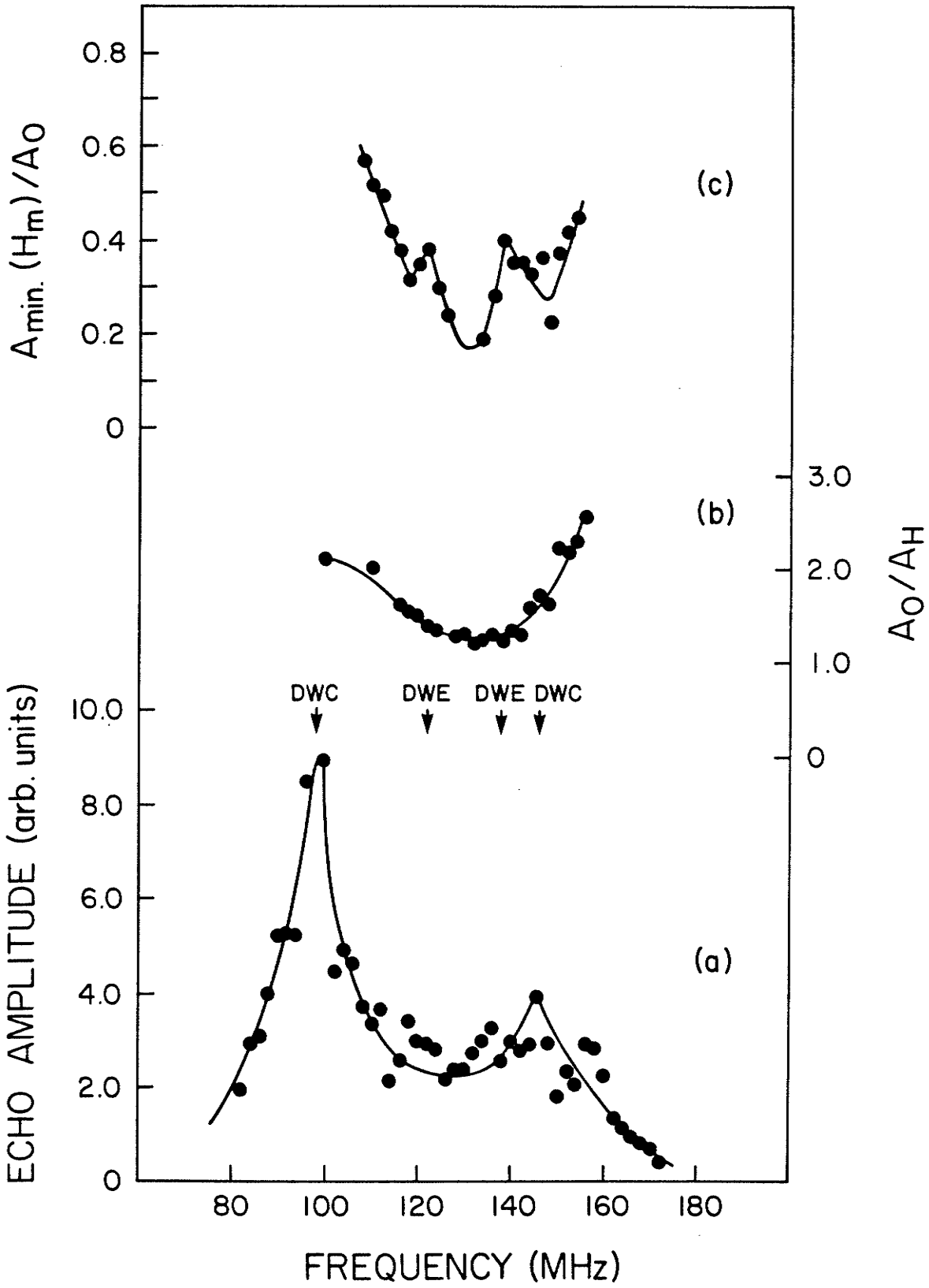

Fig. 5.24 A summary of the experimental results obtained for YCo_5 at 1.5 K. Fig. (a) gives the Co^{59} spectrum, (b) gives the echo amplitude reduction produced by a perpendicular field, as a function of frequency and (c) shows the modulation spectrum.

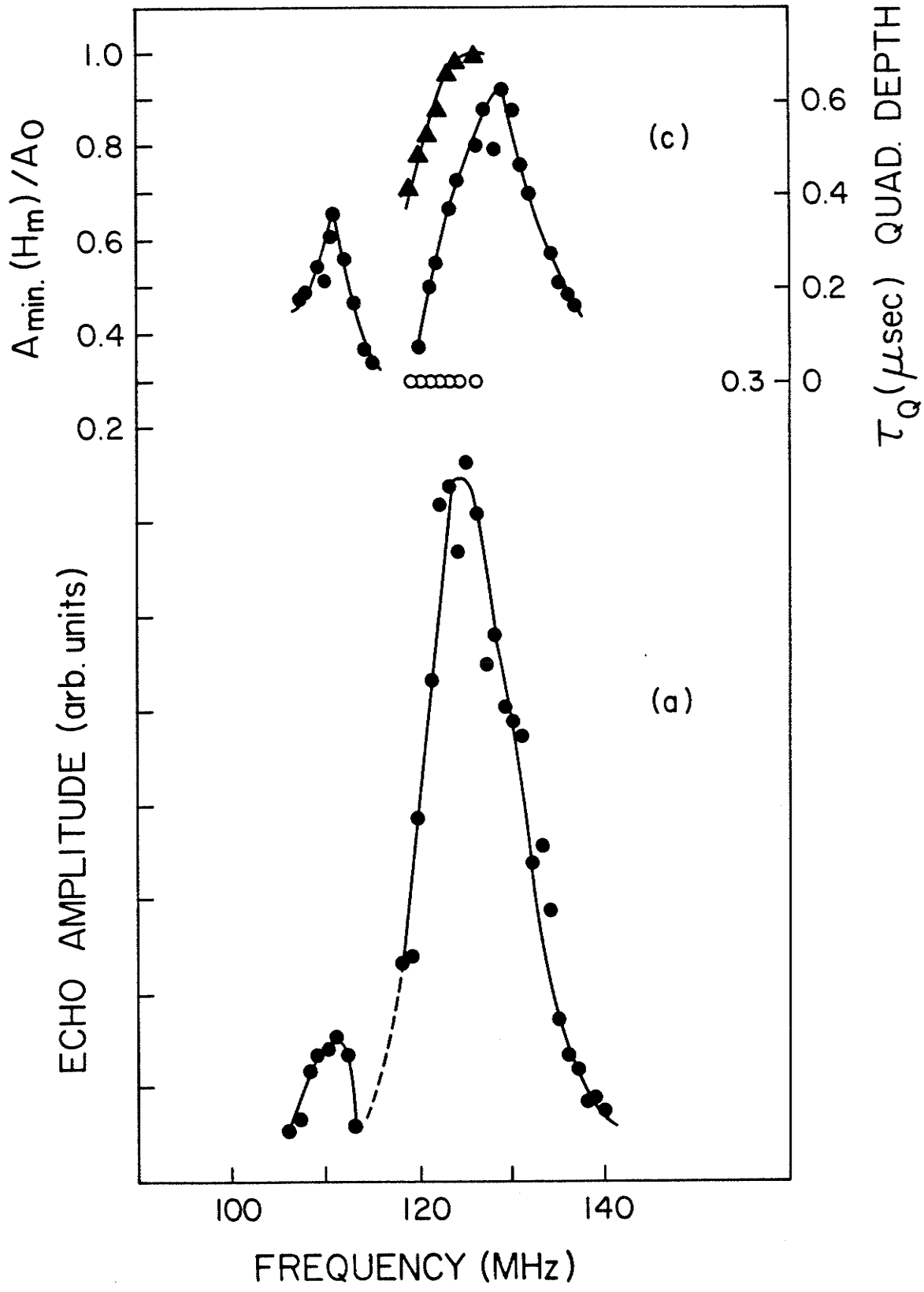

Fig. 5.25 A summary of the experimental results obtained for $PrCo_5$ at 1.5 K. Fig. (a) gives the Co^{59} spectrum and (c) gives the modulation spectrum as well as the quadrupole modulation period O and depth ▲ as a function of frequency.

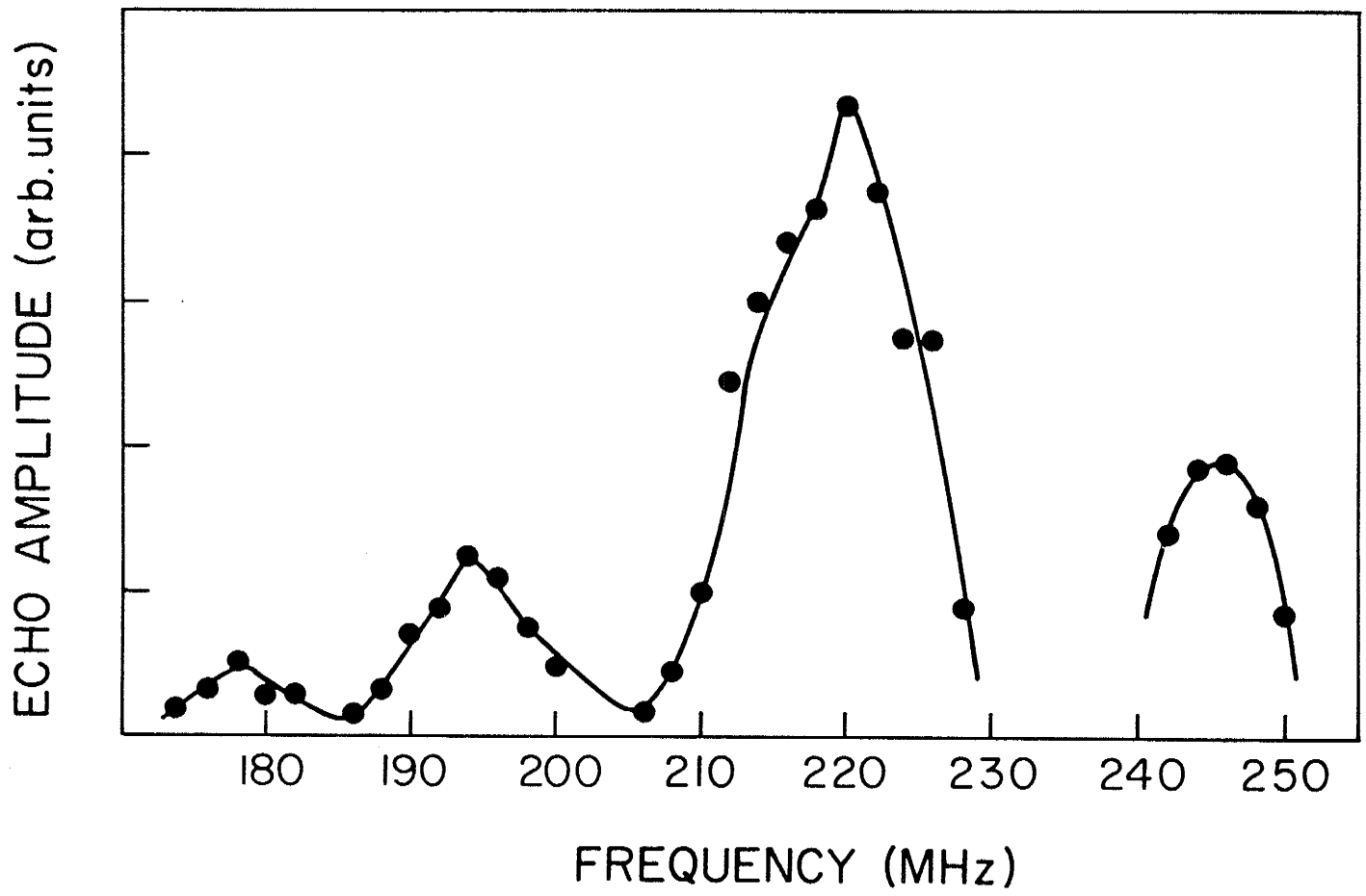

Fig. 5.26 The Co^{59} NMR spectrum obtained for $CeCo_5$ at 1.5 K.

spectra for the compounds used, since the quadrupole modulation is only observed at very small pulse separations and the period is much smaller than the period of the 80 kHz modulating field. The experimental data were taken at 4.2 K for $GdCo_5$ and 1.5 K for $SmCo_5$, $PrCo_5$ and $CeCo_5$.

The most practical arrangement for the measurement of the modulation spectra involved the use of the cavity for the excitation of the NMR signal with a small coil wound around the tail of the glass cryostat to apply the modulating field. Figure 5.27 shows the experimental arrangement used in these measurements. The modulation is not synchronized with the r.f. pulses obtained from the spectrometer. The coil used consisted of 2 1/2 turns of 30 gauge copper wire wound over 2 cm. The error in the calculated value of the modulating field applied to the sample using such a coil could be significant and must be considered in interpreting the data. The calculation of the field itself consisted of a weighted average of the fields produced by a single loop and an infinite solenoid. This calculation was actually only applied to the hexagonal Co sample. The significance of the error in determining the strength of the modulating field for the other samples was then minimized by using a coil of standard geometry and weighting the field by only the current in the coil.

It was also found that the screening effect of the applied r.f. field by the small coil wound around the Helium dewar tail to apply the modulating field significantly reduced the signal intensity. In particular, for the case of the $SmCo_5$ sample, the echo amplitude was so small that we were forced to use a single turn coil to apply the

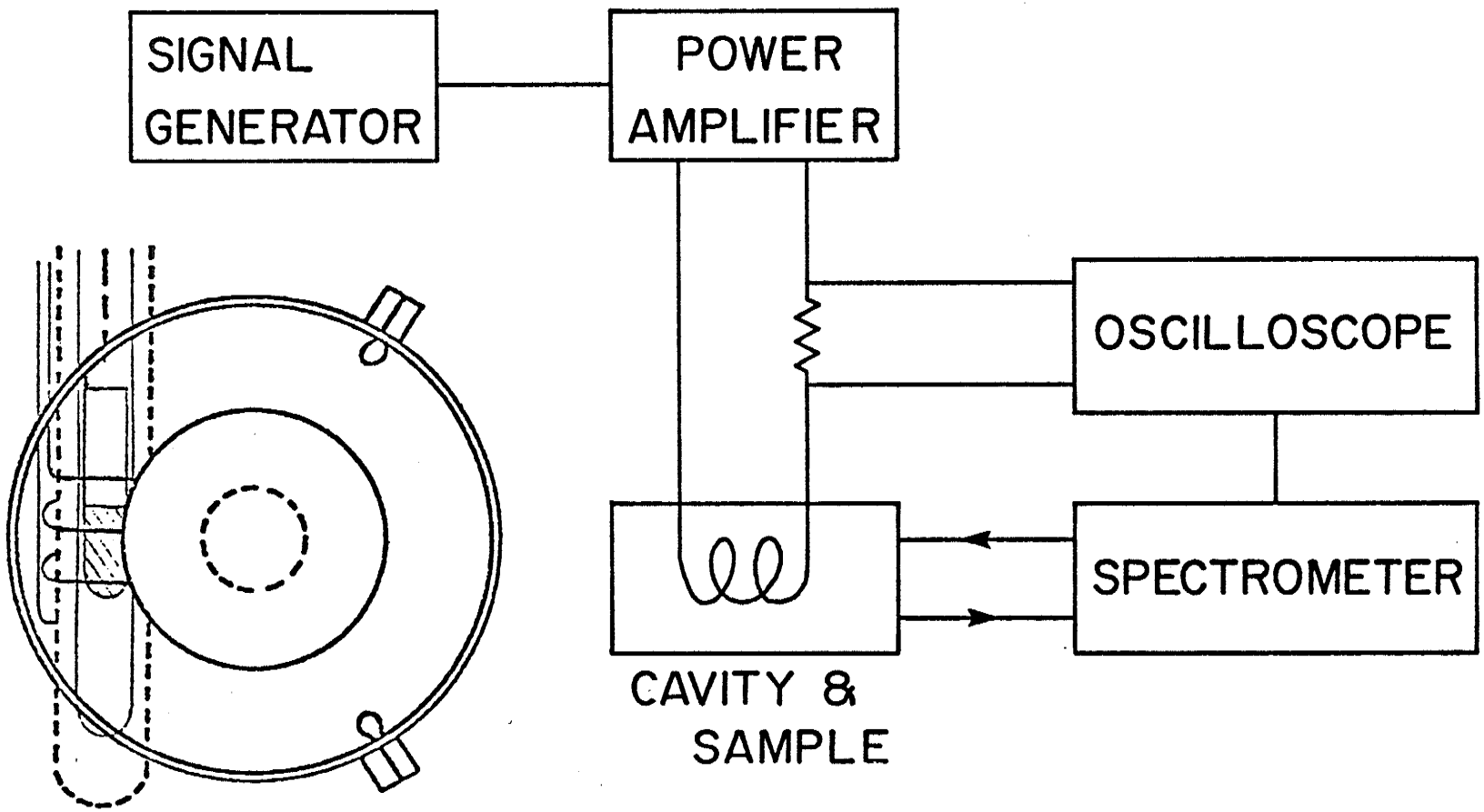

Fig. 5.27 The experimental arrangement used in the external modulation measurements.

modulating field (instead of the standard 2 1/2 turns over 2 cm).

The model for the longitudinal enhancement of the modulating field predicted a maximum enhancement factor of (Eqn. 5.11)

$$\eta_{max} = \pi W \chi_{||} H_a / 2 \delta M_s$$

where W is the average domain width, H_a is the anisotropy in the hyperfine field, and δ is the domain-wall-width. It should be noted that although H_a is the anisotropy in the hyperfine field at a Co site the value of $\chi_{||}$ must be the total susceptibility of the material. This is because the modulating field is enhanced by the anisotropic contribution to the hyperfine field as the domain-wall-motion shifts the effective position of the nuclei. The susceptibility is almost entirely due to domain-wall motion in these materials. M_s also represents the total saturation magnetization.

The magnetic susceptibility $\chi_{||}$ is the susceptibility parallel to the c-axis for easy-axis materials. In the case of an easy-plane or cone material, the situation is considerably more complicated, although $\chi_{\perp}$ might be a reasonable initial value to use.

Table 5.2 shows the experimentally determined values of $\eta_{max.}$ determined from the minima in the modulation spectra (maximum in depth of modulation), A_{min}/A_o. Using the results of Srivastava (24) this ratio may be related to the ratio of the enhanced modulating field, h, to the r.f. field due to the pulses, H_1. H_m is our calculated value for the external modulating field and H_1 is the applied r.f. field calculated from the length of the 90° pulse, t_1 and the relation $\pi/2 = \gamma_N H_1 t_1$.

TABLE 5.2

SAMPLE	A_{min}/A_o	h/H_I	H_m(Oe)	t_p(90°)	H_I(Oe)	$\eta_{max.}$
hex Co	0.1	1.22	1.4	0.5 μsec	495	431
Y Co_5	0.18	1.12	0.1	0.35	707	7918
	0.30	1.0	0.1	0.35	707	7070
Sm Co_5	0.10	1.22	0.05	0.55	450	10980
	0.30	1.0	0.05	0.55	450	9000
Gd Co_5	0.05	1.32	0.4	0.4	620	2046
	0.42	0.88	0.4	0.4	620	1364
	0.25	1.03	0.4	0.4	620	1597

The change in the magnetization resulting from the external modulating field, H_m, is given by Eqn. 5.9

$$m_{||} = \chi_{||} H_m = M_s \frac{2\Delta x}{W}$$

and therefore, $\Delta\chi$, the change in wall location, is

$$\Delta x = \frac{\chi_{||} H_m W}{2 M_s} \tag{5.22}$$

Table 5.3 shows a comparison of the values of $\Delta\chi$ with the corresponding values of δ, the domain wall width. The extremely small values of $\Delta\chi/\delta$ eliminates the simple modulation mechanisms considered in section 5.7.

However, an attempt to obtain quantitative results from our model for the longitudinal enhancement mechanism proved to be quite disappointing. Table 5.4 shows the results of our calculated linewidth, $\Delta\nu = \gamma_N H_a/2\pi$, which used the anisotropy in the hyperfine field obtained from the modulation data and Eqn. 5.11. Although we have as yet not determined the exact anisotropy in the hyperfine field at the two Co sites; a comparison of the overall width of the Co^{59} spectrum obtained experimentally and the predicted linewidths shows, except for $GdCo_5$, an extremely large discrepancy. The values of the maximum enhancement factor, $\eta_{max.}$, do, however, order with the overall widths of the spectrum. The nature of this discrepancy will be examined in detail in the discussion. However, in the calculation it was assumed that the form of the anisotropic contribution to the hyperfine field has the form

$$H_a(x) = H_a \sin^2(\pi x/\delta)$$

This angular dependence has been confirmed for the domain-wall-edge resonance in hexagonal Co by Enokiya (33), and for the domain resonance

TABLE 5.3

SAMPLE	$M_0(\frac{emu}{cm^3})$	W (μm)	$\chi_{II}(\frac{emu}{cm^3 Oe})$	Δx (Å)	δ (Å)	$\Delta x/\delta$
hex.Co	420	1.25	0.32	1.92	350	5.63×10^{-3}
Y Co_5	901	1.7	1.6×10^{-2}	1.51×10^{-2}	55	2.74×10^{-4}
Sm Co_5	855	4.0	3.8×10^{-3}	4.44×10^{-3}	51	3.7×10^{-5}
Gd Co_5	287	14.6	2.19×10^{-2}	2.23	60	3.71×10^{-2}

TABLE 5.4

SAMPLE	$\eta_{max.}$	$\chi_{11}(\frac{emu}{gm.Oe})\times10^{-4}$	$\chi_{11}(\frac{emu}{cm^3.Oe})$	H_a(kOe)	$\Delta\nu$ (MHz)
hex. Co	431	436	0.32	34	34.3
Y Co_5	7918	21.8	1.6×10^{-2}	918	927
	7070			820	828
Sm Co_5	10980	5.2	3.3×10^{-3}	2010	2030
	9000			1650	1667
Gd Co_5	2046	30.0	2.19×10^{-2}	7.0	7.1
	1364			4.68	4.7
	1597			5.48	5.5

by Fekete et al (36). Fekete et al refer to a "recently developed technique which enables the observation of NMR in fully magnetized single crystals of ferromagnetic metals" without elaboration. It is assumed that this refers to the nuclear acoustic echo observed by Taborov (37). Taborov reports that it is precisely in the magnetized state that it becomes easy to observe the nuclear acoustic echo in cobalt.

There is no reason, however, to assume that the angular distribution of the hyperfine field in a domain wall is identical to that in a fully saturated ferromagnet. This possibility will be examined in greater detail in the discussion. As the longitudinal enhancement is the result of a modulation of the hyperfine field resulting from the periodic displacement of the domain wall, a more rapid variation of the hyperfine field as one enters the wall would manifest itself in a larger enhancement factor. This in turn would result in a considerably larger calculated value of H_a, possibly explaining the discrepancy we have observed.

Alternatively, the reliability of the values of the other parameters used in the calculation of H_a must be examined. The values for the saturation magnetization M_s = 1420 emu/cm^3 and the domain-wall-energy γ = 10.7 erg/cm^2 for cobalt was taken from Ref. 5.34. The wall thickness for cobalt was obtained using the expression

$$\delta = \pi\gamma/4\ K_1 \qquad (5.23)$$

and values for γ and K_1 (the anisotropy constant) from Ref. 5.38. We obtained an estimated value for the domain width in 50 micron diameter particles as described in Ref. 5.38. Here we assumed that the result

which is given for a plate of thickness T will not be much different from that of a particle of the same diameter. We obtained W = 1.25 micron and δ = 350 A. The low-field a.c. susceptibility measured at 77 K and 15 kHz was χ_{II} = 0.32 emu/cm^3-Oe. The required values of W, δ and M_s for the RCo_5 compounds were also obtained from Ref. 5.38. The value of M_s obtained from Ref. 5.39 was 901 emu/cm^3. The low-field a.c. susceptibility was measured at the same temperature the NMR data were taken and at a frequency of 15 kHz.

5.10 The Observation of Quadrupole Splitting Effects and its Correlation with the Longitudinal Enhancement Measurements

Figures 5.22 - 5.26 also show a very interesting variation in the depth of the observed quadrupole modulation through the spectra, particularly $SmCo_5$ and $GdCo_5$. In all instances where a modulation could be observed, it is evident that the resolution of the quadrupole splitting is a maximum at neither the domain-wall-edge or the domain-wall-centre, but rather at an intermediate point in the wall. This is particularly well-illustrated by $PrCo_5$ where the depth of quadrupole modulation increases down one side of the resonance peak at 125 MHz. No modulation is observed on the peaks at 125 MHz or 110 MHz. Figure 5.28 shows a series of oscillograms illustrating this effect.

It is interesting to correlate the depth of the quadrupole modulation with the rate of change of the hyperfine field with displacement as given by our external modulation experiment and with the position of the peaks in the NMR spectrum itself. The correlation is quite evident and one can conclude that the NMR peaks occur where the

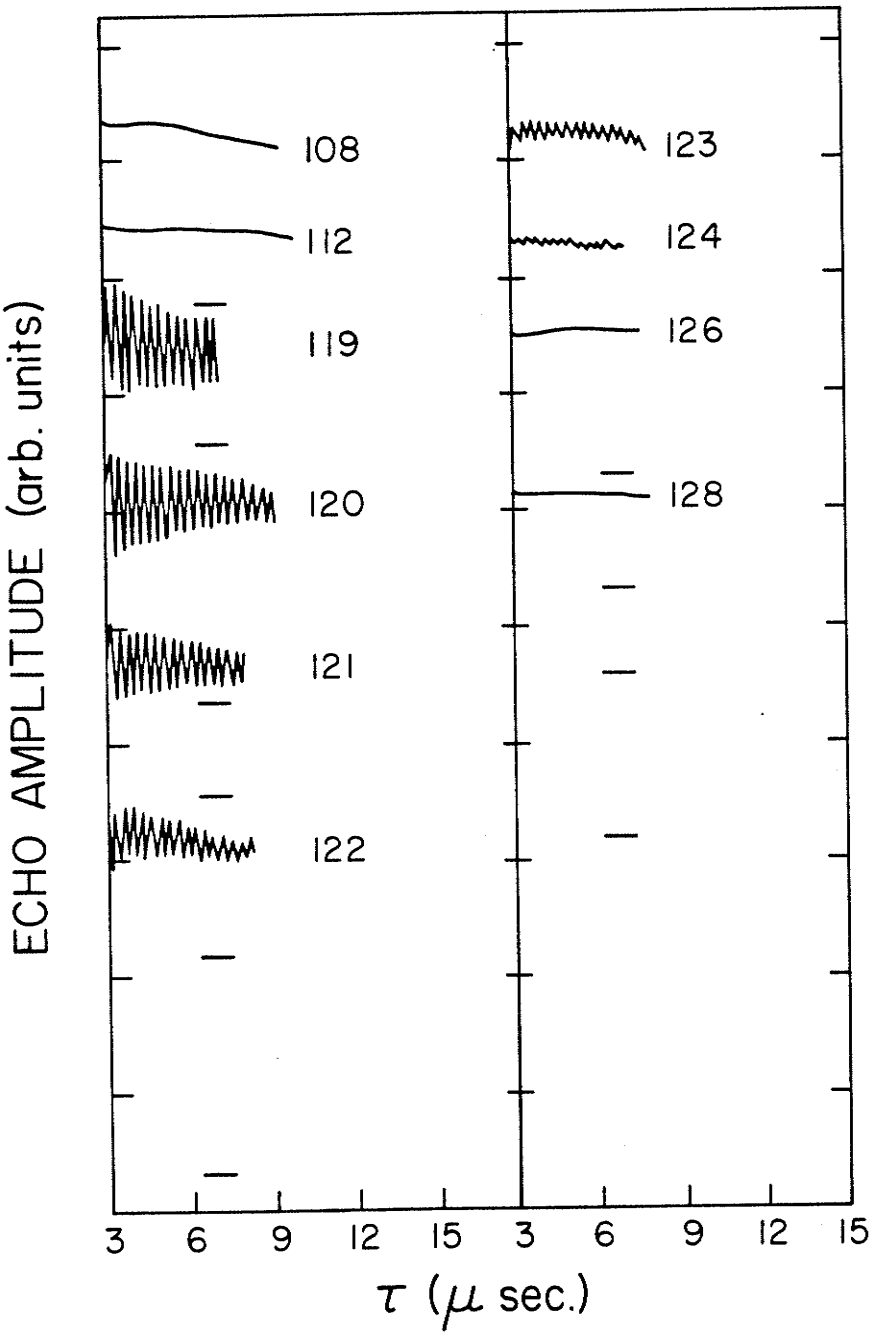

Fig. 5.28 A series of oscillograms illustrating the frequency dependence of the depth of the quadrupole modulation of the spin-echo decay envelope for Co^{59} in $PrCo_5$. The frequency is indicated in MHz.

rate of change of the hyperfine field and the depth of the quadrupole modulation is small. This is not in agreement with the observations of the quadrupole splitting by other workers for various other materials (7,18) as was discussed in chapter 4.6. For these materials the observation of the quadrupole splitting was correlated with the domain-wall-edge resonance and was explained using an angular dependent linewidth which had a minimum at the wall-edge as predicted by Winter (40).

The correlation of the quadrupole modulation with the rate of change of the hyperfine field suggests that the observation of quadrupole effects for the Co^{59} resonance in the RCo_5 compounds is related to the extremely large anisotropies in the hyperfine field characteristic of these materials, and to their extremely narrow domain walls which have a width on the order of 50 A or approximately 10-12 atomic layers. The observation of the quadrupole splitting would appear to be related in these materials to the inhomogeneous broadening resulting from a distribution of spins in the walls about a particular angle for a particular atomic layer. The composite lineshape would therefore consist of not simply 10-12 quadrupole split groups of lines each with a width of dynamic origin (i.e.: determined by T_2) or possibly of width $\gamma_N \eta(\theta) H_1$, and shifted relative to each other because of the anisotropy in the hyperfine field, but rather each of the groups corresponding to a layer in the domain wall would consist of many more groups (representing a distribution over many domain walls) split by the inhomogeneity. This certainly would obscure the quadrupole splitting and presumably also the quadrupole modulation. It seems reasonable to

expect that this effect would be a minimum where the hyperfine field changes most rapidly and there is the least overlap between groups. In this region of the wall the nuclei would also see the most distinct electric field gradient and therefore the most distinct quadrupole splitting since its neighbours have distinctly different electronic structures. The quadrupole modulation is most likely to be observed where the electric field gradient distribution is narrow. This would therefore explain the correlation we have observed between the depth of quadrupole modulation and the rate of change of the hyperfine field as measured by the modulation experiment.

This interpretation is supported by the fact that no quadrupole modulation was observed in any of several powdered, hexagonal Co samples of different origins that were examined. For hexagonal Co we have a wide domain wall (275 A) and a smaller H_a, and therefore a considerably smaller inhomogeneity could obscure this effect. However, a strong modulation was observed in a single crystal of Co which probably has a very much smaller inhomogeneous broadening. Figure 5.29 shows the oscillograms obtained for the sample, displaying an obvious frequency dependence of the depth of modulation. However, the entire spectrum for the Co crystal is shifted to lower frequency relative to the powdered samples, and therefore it is difficult to compare the two results. Riedi (41) has observed a similar frequency dependence of the depth of quadrupole modulation but throughout the entire Co spectrum. Interestingly he reports a maximum in the depth of modulation at 221 MHz which is approximately the frequency at which we observed a maximum in the longitudinal enhancement. Reidi also reports the observation of a

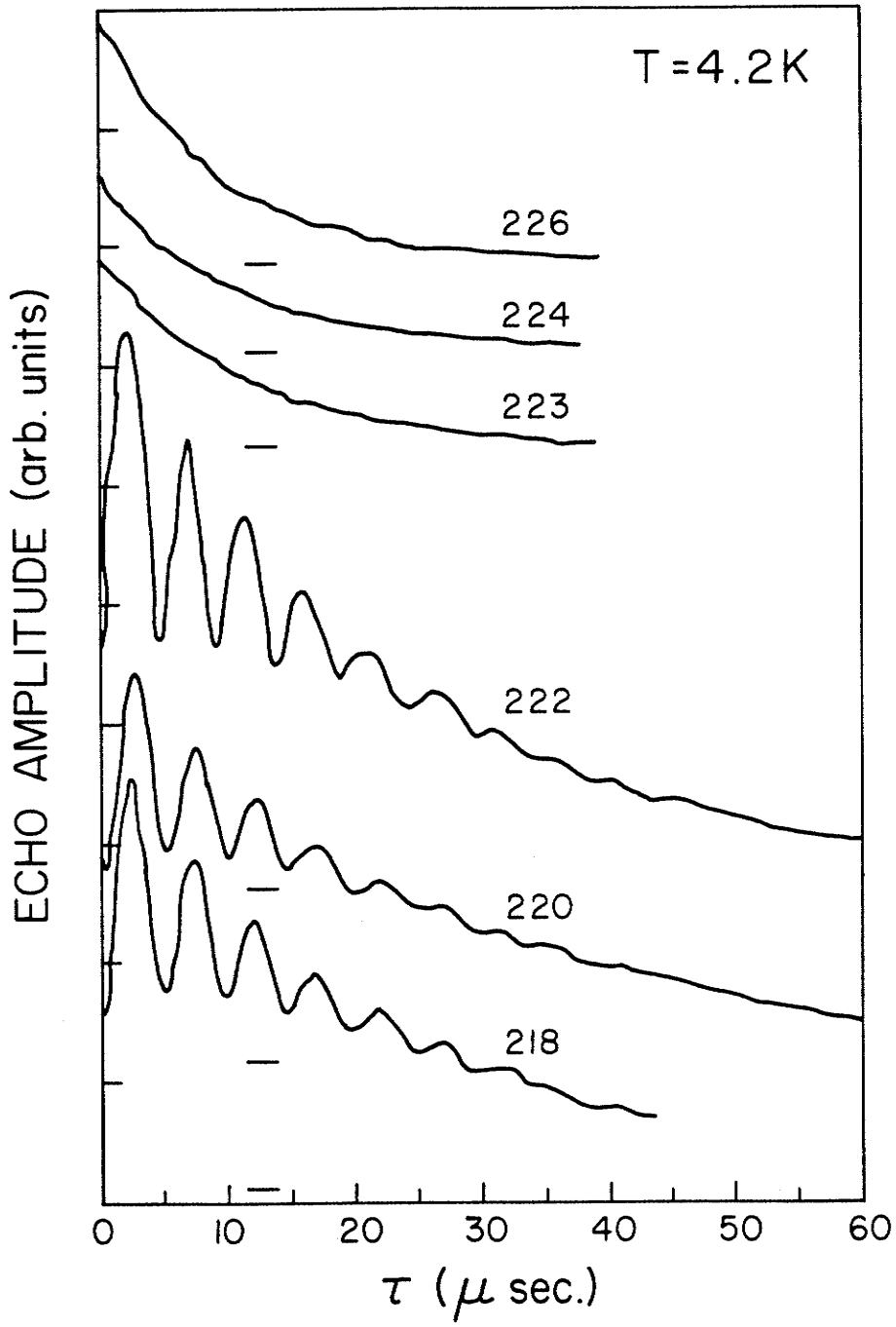

Fig. 5.29 The frequency dependence of the depth of the quadrupole modulation of the spin-echo decay envelope for a hcp Co single crystal.

reduction in the depth of modulation in powders.

L. T. Leung (42) reports that he observed a modulation of the spin-echo-decay envelope for the Mn resonance of $La_{.69}Pb_{.31}MnO_3$ only when he saturated the sample which would presumably remove the inhomogeneity. This was attempted with Co powder but because of the much larger anisotropy no signal could be detected.

It would therefore seem that given that the inhomogeneities in the hyperfine field distribution (and the electric field gradient) are not too large, the depth of the quadrupole modulation should be a minimum wherever the NMR spectrum has a peak and should have a maximum wherever the external modulation experiment shows a minimum (maximum longitudinal enhancement factor).

The quadrupole modulation of the Co spin-echo-decay envelope for $GdCo_5$ and $SmCo_5$ could be observed only over small regions of the spectrum and show some of the above properties (small modulation at an NMR peak). However, we also observe a saturation effect as the depth of the modulation again begins to decrease, although the longitudinal enhancement factor continues to increase. Figures 5.30 and 5.31 show a series of oscillograms which clearly display this effect. This could be explained within the present model by a competition between an ever-increasing rate of change of the hyperfine field within the wall and an opposing increase in the local linewidth. However, the saturation effect is observed as one leaves the DWC resonance peak at 183 MHz for $SmCo_5$ and therefore does not involve such a competition, as might occur as one enters the wall from the edge.

An alternative modulation mechanism which requires a strong

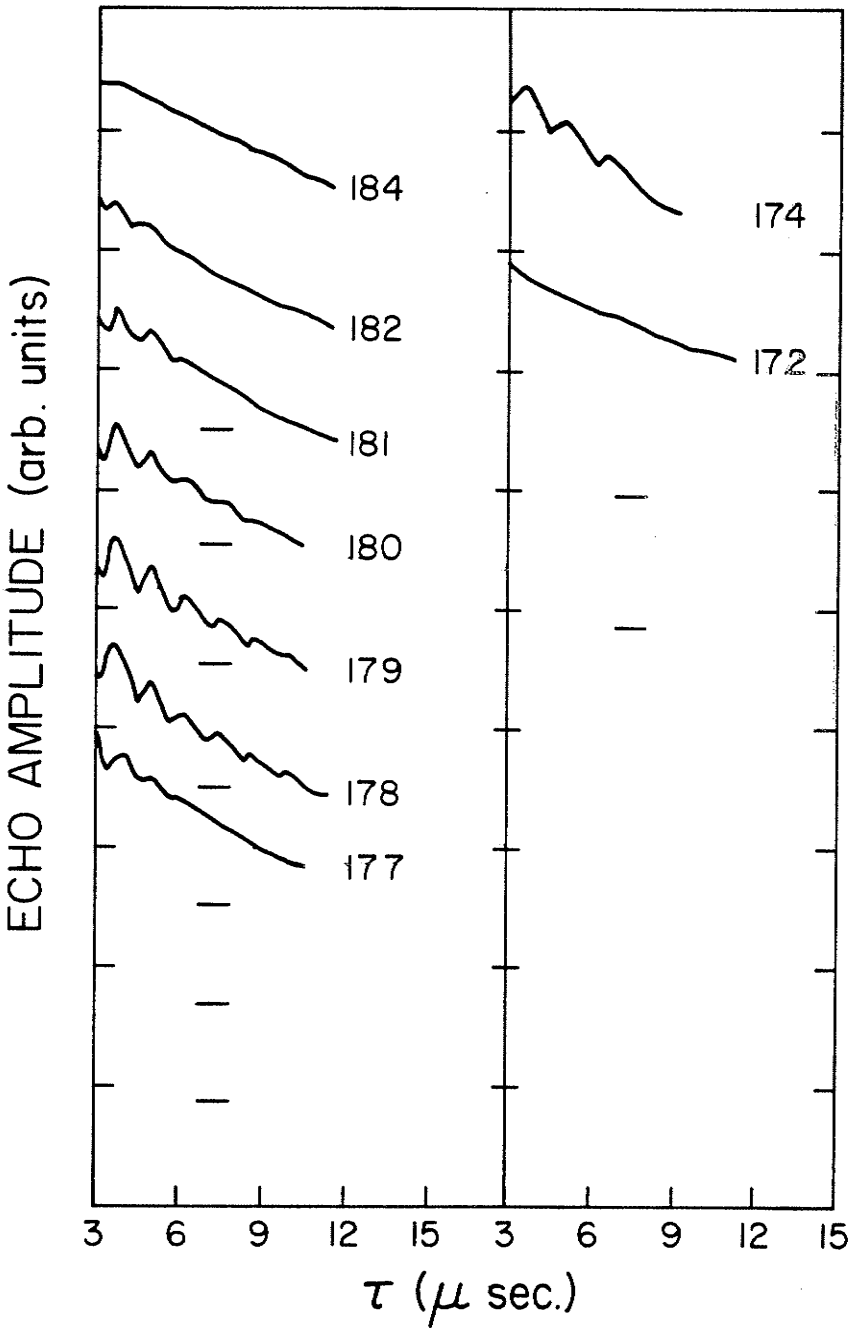

Fig. 5.30 Oscillograms illustrating the frequency dependence of the depth of the quadrupole modulation of the spin-echo decay envelope for Co^{59} in $SmCo_5$. The "saturation" effect is evident when this data is compared to the external modulation data shown in Fig. 5.23.

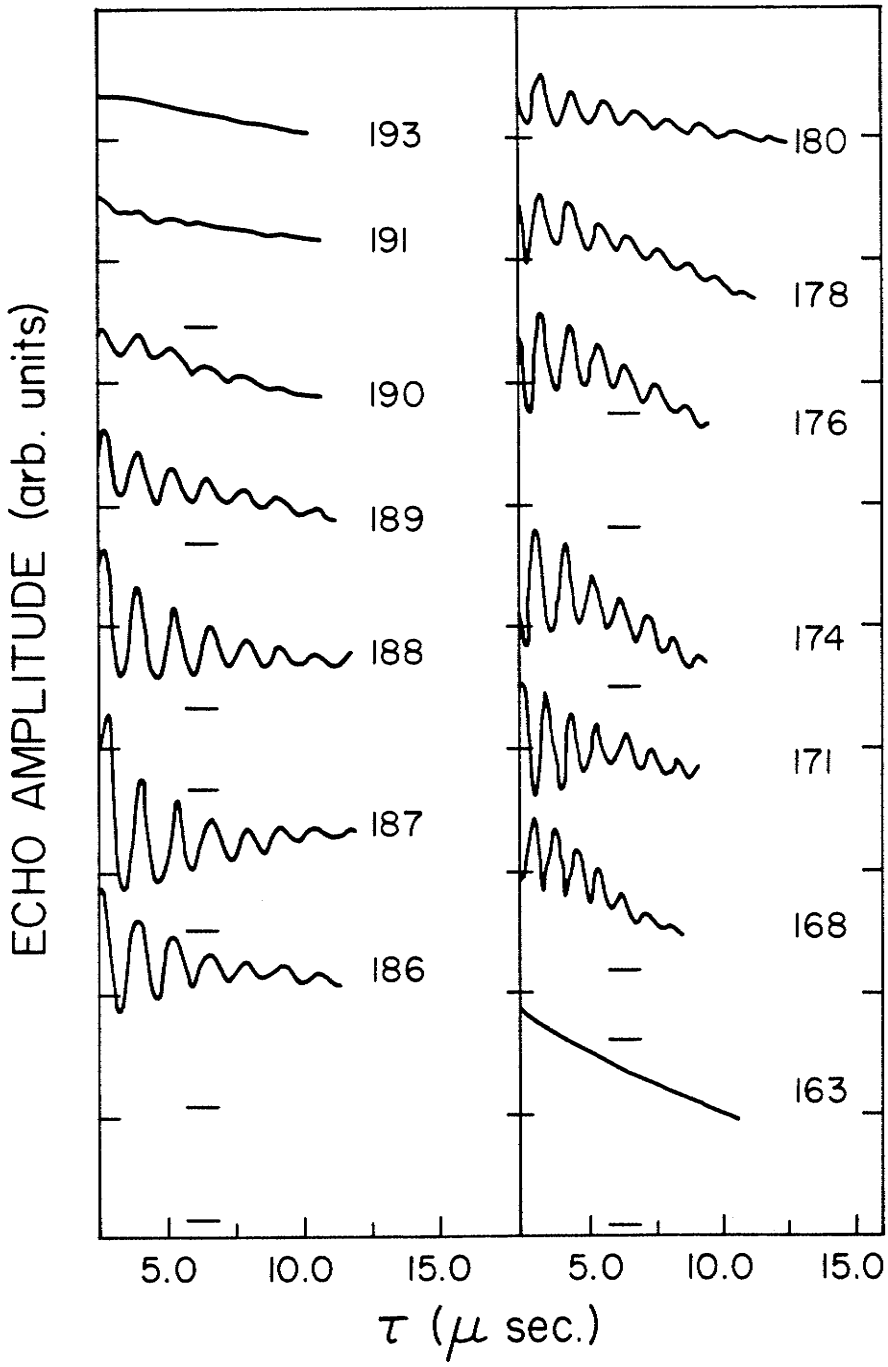

Fig. 5.31 Oscillograms illustrating the frequency dependence of the depth of the quadrupole modulation of the spin-echo decay envelope for Co^{59} in $GdCo_5$.

interaction between neighbouring nuclei as well as an explicit requirement that the neighbouring nuclei have widely different resonance frequencies has been suggested by Froidevaux and Weger (43). Jackson et al (44) first observed a spin-echo decay envelope modulation for Co at 221 MHz and attributed it to this mechanism involving nuclei within and adjacent to a fault structure. However, the modulation frequency ($1/\tau_m$) observed by both Enokiya and Fekete et al showed an approximate ($3\cos^2(\theta) - 1$) dependence on the angle the spins make with respect to the c-axis. This dependence clearly links the modulation mechanism to the quadrupole interaction. Also the modulation period we observed in the wall (~ 5 microsec.) agrees with the period observed by Fekete in the saturated sample.

The modulation mechanism described by Froidevaux and Weger resulted in an oscillation in the spin echo decay envelope with a frequency equal to the strength of the interaction between the neighbouring nuclei. The strength of such an interaction would, of course, be measured by the spin-spin relaxation time, T_2. We observed a small but measurable variation of T_2 through the domain wall for hexagonal Co. We found the value of the spin-spin relaxation time to be somewhat larger at the domain-wall-edge than at the domain-wall-centre, typically 18 microsec. and 12 microsec., respectively. One might expect such a dependence since nuclei with differing resonance frequencies are less capable of interacting and relax more slowly. In the event that this mechanism is responsible for the observed modulation we would expect a further correlation between the rate of change of the hyperfine field in the domain wall as measured by our external

modulation experiment and the spin-spin relaxation time, T_2. This mechanism can explain the reduction in quadrupole modulation depth seen in both $GdCo_5$ and $SmCo_5$. As the rate of change of the hyperfine field increases the strength of the interaction between nuclei would decrease and the spin-spin relaxation time would increase. It is not clear, however, how this mechanism could account for the $(3\cos^2\theta - 1)$ dependence of the modulation frequency observed by Fekete et al (36) as the modulation frequency is given by the spin-spin coupling constant which is related to T_2. Mitchell (45) indicated that in cases where the nuclear quadrupole moment is large and there is p or higher admixture into the conduction band, there is a possibility that strong relaxation occur through the quadrupole interaction with the conduction electrons. This is an attractive possibility but one for which there is little supporting evidence outside of the saturation effect we observed in our quadrupole modulation data.

Enokiya (33) observed a very rapid decrease in the spin-lattice relaxation time, T_1, across the domain wall (two orders of magnitude) for hexagonal Co. As it is generally accepted that the dominant contribution to T_1 in domains is due to thermal fluctuations of d orbital currents (46), it now becomes of interest, as a result of our experimental measurements of the rate of change of the hyperfine field, to investigate whether this same mechanism is important in domain walls. A rapid variation of the hyperfine field (mainly the orbital contribution) in the domain wall could produce such a rapid variation in T_1. However, since the orbital moment at the domain-wall-edge is greater than at the domain-wall-centre ($\nu_{DWE} < \nu_{DWC}$) we have a rapid

reduction in the orbital moment across the wall which should result in a rapid increase in T_1, wheras a rapid decrease is actually observed. From this we can conclude that this relaxation mechanism is not of great importance in domain walls and that relaxation in domain walls for at least hexagonal Co is probably caused by the wall-type excitations discussed by Winter (40).

CHAPTER 6

Discussion

6.1 Introduction

In chapter five (sec. 3) it was indicated that for steady-state NMR the angular variation of the detected signal intensity in a domain wall is proportional to $\eta^2(\theta)n(\theta)$ where η is the transverse enhancement factor and n is the electronic spin density as a function of angle. In addition, $\eta(\theta) \propto 1/n(\theta)$, independent of the wall structure, and therefore the signal intensity is simply proportional to $\eta(\theta)$. For a 180° domain wall the signal is then proportional to $|\sin\theta|$. This is simply the result of the fact that the rate of spin rotation in a simple 180° wall is proportional to $\sin\theta$. The transverse enhancement factor is therefore largest at the wall centre and the spin density is largest at the edge where the rate of rotation is smallest.

For spin-echo NMR, however, one of the factors of $\eta(\theta)$ is eliminated by maintaining a 90-180 (or optimum) pulse sequence. As the detected signal is proportional to the product $\eta(\theta)n(\theta)$, the measured spectrum should represent a distribution in local fields undistorted but enhanced by the domain wall. The enhancement effect on the nuclear signal is the consequence of the coupling of the precessing nuclear spins to the domain wall, the detected signal resulting from domain wall displacements.

The steady-state NMR spectrum represents the product of the

distribution of the enhancement factor and that of the local fields, and therefore would contain considerably less information.

If $S(\omega')\Delta\omega'$ represents the static nuclear magnetization due to "spin packets" in the interval from ω' to $\omega'+\Delta\omega'$ away from the exact resonance frequency, ω_o, then the precessing magnetization which generates the echo is given by

$$A(t) = \int_{-\infty}^{\infty} S(\omega') E(\omega') d\omega' \tag{6.1}$$

A spin packet is a group of nuclear spins which have an independent history of interactions with the r.f. field and with the crystal lattice. $E(\omega')$ represents the contribution of the static magnetization to the precessing moment and therefore to the detected signal

$$E(\omega') = \frac{M_p}{M_o} \tag{6.2}$$

M_o is the static magnetization of the spin packet centered at ω and M_p is the transverse component of the magnetization generated by the pulses.

In order to calculate the transverse component of the magnetization resulting from the application of an r.f. pulse of amplitude H_1 along the x-axis one, as usual, goes into a reference frame rotating at a frequency ω_o. The nuclei experience a fictitious field in the z-direction of magnitude $\Delta\omega/\gamma$ where $\Delta\omega = \omega-\omega_o$ as well as a stationary component of the r.f. field along the x'-axis. The nuclei then precess about the resultant field $\vec{b}$ which makes an angle Ψ with respect to the z-axis as shown in Fig. 6.1. For a pulse of length t_1 the moment, M_o, turns through an angle bt_1 and ends up at an angle α

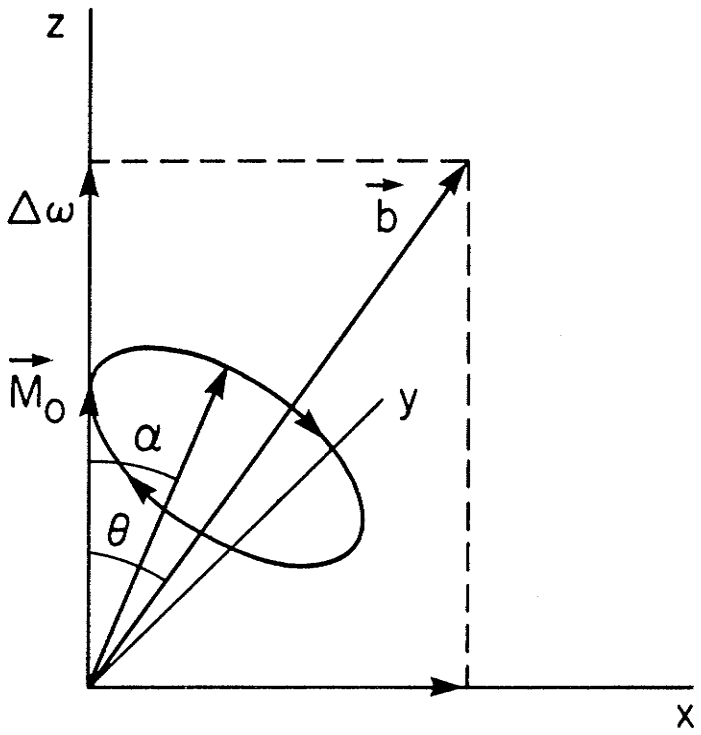

Fig. 6.1 The motion of the nuclear spin in the rotating frame.

with respect to the z-axis. After the pulse the nuclear moment precesses about the z-axis with a frequency ω. The receiving coil is in the x-y plane and therefore sensitive to this component of the nuclear moment. This component is given by

$$\begin{aligned} A(w) &= M_o \sin \alpha \\ &= M_o \sin \psi \left[\sin^2 bt_1 + \cos^2 \psi \, (1 - \cos bt_1)^2\right]^{\frac{1}{2}} \end{aligned} \tag{6.3}$$

where

$$\tan \psi = \gamma H_1 / \Delta w \tag{6.4}$$

and the turning angle bt_1 is given by

$$b \, t_1 = \left[(\Delta w)^2 + (\gamma H_1)^2\right]^{\frac{1}{2}} t_1 \tag{6.5}$$

Because of their spread in resonant frequencies the nuclear spins become spread out in the x-y plane. A second pulse of length t_2 would again rotate the z-components through an angle bt_2 around $\vec{b}$ and we would observe an echo. To calculate the transverse magnetization using the above geometrical approach for a general pulse sequence of two or more pulses would be quite complicated. Mims et al (1) showed that the motion resulting from the application of an r.f. pulse transforms the magnetization in the rotating system $M = (M_x, M_y, M_z)$ to $[R]M$ where $[R]$ is the matrix

$$\begin{bmatrix} s\psi^2 + c\psi^2 c\phi_1 & -c\psi s\phi_1 & s\psi c\psi(1-c\phi_1) \\ c\psi s\phi_1 & c\phi_1 & -s\psi s\phi_1 \\ s\psi c\psi(1-c\phi_1) & s\psi s\phi_1 & c\psi^2 + s\psi^2 c\phi_1 \end{bmatrix} \tag{6.6}$$

and $c\Psi$, $s\Psi$, $c\phi_1$ and $s\phi_1$ stand for $\cos\Psi$, $\sin\Psi$, $\cos\phi_1$ and $\sin\phi_1$ and Ψ is

the angle between the effective field and the z-axis. ϕ_1 is the angle through which the magnetizations turn about the effective field during the pulse time t_1.

The calculation of the resultant of several successive rotations, using the above (3x3) matrix rapidly becomes very tedious. Jaynes (2) and Bloom (3) developed an elegant matrix method to calculate the transverse magnetization and in particular the free induction and echo amplitudes after any general series of pulses.

To each polarization $\vec{M}$, oriented with polar angles θ,ϕ and with components in the axial representation given by

$$\begin{aligned} M_+ &= M \sin\theta\, e^{i\phi} \\ M_- &= M \sin\theta\, e^{i\phi} \\ M_z &= M \cos\theta \end{aligned} \tag{6.7}$$

Jaynes associated a spinor

$$\psi = \begin{bmatrix} u \\ v \end{bmatrix} = \begin{pmatrix} M^{\frac{1}{2}} \cos(\theta/2)\, e^{-i(\phi/2)} \\ M^{\frac{1}{2}} \sin(\theta/2)\, e^{i(\phi/2)} \end{pmatrix} \tag{6.8}$$

To every rotation of M generated by a matrix [R]

$$\vec{M}' = [R]\vec{M} \tag{6.9}$$

there corresponds a unitary transformation of Ψ such that

$$\psi' = Q\psi \tag{6.10}$$

The relationship between the elements of Q and the axis and magnitude of the corresponding rotation is given by

$$Q = \begin{bmatrix} \alpha & \beta \\ -\beta^* & \alpha^* \end{bmatrix} = \exp\left[-i(\hat{n}\cdot\vec{\sigma})\ (\theta/2)\right] \qquad (6.11)$$
$$= [1]\ \cos\ (\theta/2) - i\ [\hat{n}\cdot\vec{\sigma}]\ \sin\ (\theta/2)$$

where $\hat{n}$ is a unit vector defining the axis of rotation, θ is the angle of rotation and $\vec{\sigma}$ represents the Pauli spin matrices. The Cayley-Klein parameters for this rotation are

$$\alpha = \cos\ (\theta/2) - in_z\ \sin\ (\theta/2)$$
$$\beta = -in_-\ \sin\ (\theta/2) \qquad (6.12)$$

To determine the Cayley-Klein parameters corresponding to the rotation occurring during an r.f. pulse we note that the rotation occurs about the vector $\vec{H}_1$ through an angle bt_1. Denoting by ψ the angle between the z-axis and $\vec{b}$, Eqn. 6.12 becomes

$$\alpha = \cos\ (bt_1/2) - i\ \cos\ \psi\ \sin\ (bt_1/2)$$
$$\beta = -i\ \sin\ \psi\ \sin\ (bt_1/2) \qquad (6.13)$$

The R-matrix corresponding to a given Q-matrix takes the following form in the axial representation

$$R = \begin{pmatrix} \delta^2 & -\gamma^2 & 2\gamma\delta \\ -\beta^2 & \alpha^2 & -2\alpha\beta \\ \beta\delta & -\alpha\gamma & (\alpha\delta+\beta\gamma) \end{pmatrix} \qquad (6.14)$$

where $\delta = \alpha^*$ and $\gamma = -\beta^*$.

The precession is clockwise for γ (gyromagnetic ratio) > 0 when viewed from in front of the effective field vector $\vec{b}$. Between pulses the Q-matrix has the special form

$$Q = \begin{pmatrix} e^{-\frac{1}{2} i\Delta\omega t} & 0 \\ 0 & e^{\frac{1}{2} i\Delta\omega t} \end{pmatrix} \tag{6.15}$$

corresponding to precession about the z-axis with angular frequency $\Delta\omega$. The resultant transformation after n time intervals is then given by

$$Q = Q_n \cdots Q_1 = \begin{pmatrix} \alpha & \beta \\ -\beta^* & \alpha^* \end{pmatrix} \tag{6.16}$$

Starting with $\vec{M} = M_z$ we can now compute the transverse nuclear magnetization, M_{x-iy}, as a function of time by evaluating the matrix element $(-2\alpha\beta)$ of Eqn. 6.14. We can determine the α and β by combining the 2x2 Q-matrices to obtain the required three dimensional matrix element which is much simpler than multiplying 3x3 matrices directly.

These relations have been used to calculate NMR spin-echo amplitudes resulting from domain walls in materials possessing a large anisotropy in the hyperfine field. In addition, we will use these relations to examine our experimental techniques in greater detail in order to determine what additional information may be obtained from our results.

We proceed to evaluate the echo amplitude using Eqn. 6.16. After the first pulse the z-component of the magnetization is given by

$$\begin{aligned} M_z^1 &= (\alpha_1\alpha_1^* - \beta_1\beta_1^*)\, M_z \\ &= \{1 - 2 \sin^2 \psi_1 \sin^2 (\tfrac{1}{2} b_1 t_1)\}\, M_z \end{aligned} \tag{6.17}$$

For exact resonance $\Delta\omega = 0$ and $\sin\psi_1 = 1$. Therefore

$$M_z^1 = \cos(b_1 t_1)\, M_z$$

which for $b_1 t_1 = \pi/2$ gives $M_z' = 0$ as expected.

After the second pulse we have

$$\alpha = \alpha_3\alpha_2\alpha_1 - \beta_3\beta_1^*\alpha_2^*$$
$$\beta = \alpha_3\alpha_2\beta_1 \quad \beta_3\alpha_2^*\alpha_1^* \tag{6.18}$$

and the z-component of the magnetization becomes much more complicated.

$$\begin{aligned} M_z'' &= \cos^2(\tfrac{1}{2} b_1t_1)\cos^2(\tfrac{1}{2} b_3t_3) + \cos(2\psi_1)\sin^2(\tfrac{1}{2}b_1t_1)\cos^2(\tfrac{1}{2} b_3t_3) \\ &+ \cos(2\psi_3)\sin^2(\tfrac{1}{2} b_3t_3)\cos^2(\tfrac{1}{2} b_1t_1) \\ &+ \cos^2\psi_1\cos^2\psi_3\sin^2(\tfrac{1}{2} b_1t_1)\sin^2(\tfrac{1}{2} b_3t_3) \\ &- \sin^2\psi_1\cos^2\psi_3\sin^2(\tfrac{1}{2} b_1t_1)\sin^2(\tfrac{1}{2} b_3t_3) \\ &+ \sin^2\psi_1\sin^2\psi_3\sin^2(\tfrac{1}{2} b_1t_1)\sin^2(\tfrac{1}{2} b_3t_3) \\ &- \sin^2\psi_3\cos^2\psi_1\sin^2(\tfrac{1}{2} b_1t_1)\sin^2(\tfrac{1}{2} b_3t_3) \\ &+ \cos(2\psi_3)\cos(2\psi_1)\sin^2(\tfrac{1}{2} b_1t_1)\sin^2(\tfrac{1}{2}3b_3t\ ) \\ &- \sin\psi_1\sin\psi_3\sin(b_1t_1)\sin(b_3t_3)\cos(\Delta\omega_2t_2) \\ &+ \sin(2\psi_1)\sin(2\psi_3)\sin^2(\tfrac{1}{2} b_1t_1)\sin^2(\tfrac{1}{2} b_3t_3)\cos(\Delta\omega_2t_2) \\ &+ \sin(2\psi_1)\sin(\psi_3)\sin^2(\tfrac{1}{2} b_1t_1)\sin(b_3t_3)\sin(\Delta\omega_2t_2) \\ &+ \sin(\psi_1)\sin(2\psi_3)\sin(b_1t_1)\sin^2(\tfrac{1}{2} b_3t_3)\sin(\Delta\omega_2t_2) \end{aligned} \tag{6.19}$$

Here the subscripts label the time interval and therefore t_1 and t_3 are pulse durations and t_2 is the pulse separation. $\Delta\omega_2$ is the off-resonance frequency which may not be equal to $\Delta\omega$ if a dynamic frequency shift occurs due to the change in nuclear magnetization resulting from the first pulse (i.e. M_z').

To evaluate the transverse component of the nuclear magnetization from which both the free induction and the echo amplitude may be obtained we must evaluate the matrix element $(-2\alpha\beta)$ where if $\beta_2, \beta_4 = 0$ (Eqn. 6.15)

$$\alpha = \alpha_4\alpha_3\alpha_2\alpha_1 - \alpha_4\beta_3\beta_1^*\alpha_2^*$$
$$\beta = \alpha_4\alpha_3\alpha_2\beta_1 + \alpha_4\beta_3\alpha_2^*\alpha_1^* \tag{6.20}$$

Using Eqn. 6.13 we obtain for the echo amplitude

$$\begin{aligned} &- \sin(2\psi_1) \sin^2\psi_3 \sin^2(\tfrac{1}{2} b_1 t_1) \sin^2(\tfrac{1}{2} b_3 t_3)\, e^{i\Delta\omega_2 t_2}\, e^{i\Delta\omega_4 t_4} \\ &+ i \sin\psi_1 \sin^2\psi_3 \sin(b_1 t_1) \sin^2(\tfrac{1}{2} b_3 t_3)\, e^{i\Delta\omega_2 t_2}\, e^{-i\Delta\omega_4 t_4} \end{aligned} \tag{6.21}$$

and for the free induction amplitude

$$\begin{aligned} &- \sin(2\psi_3) \cos(2\psi_1) \sin^2(\tfrac{1}{2} b_1 t_1) \sin^2(\tfrac{1}{2} b_3 t_3)\, e^{-i\Delta\omega_4 t_4} \\ &- \sin(2\psi_3) \sin^2(\tfrac{1}{2} b_3 t_3) \cos^2(\tfrac{1}{2} b_1 t_1)\, e^{-i\Delta\omega_4 t_4} \\ &- i \sin\psi_3 \cos(2\psi_1) \sin^2(\tfrac{1}{2} b_1 t_1) \sin(b_3 t_3)\, e^{-i\Delta\omega_4 t_4} \\ &- i \sin\psi_3 \cos^2(\tfrac{1}{2} b_1 t_1) \sin(b_3 t_3)\, e^{-i\Delta\omega_4 t_4} \end{aligned} \tag{6.22}$$

Here

$$\psi_1 = \tan^{-1}(\gamma H_1/\Delta\omega) = \tan^{-1}(\gamma\eta H_{rf}/\Delta\omega)$$

$$b_1 = |\gamma H_1 + \Delta\omega| = |H_{eff}|$$

$$\psi_3 = \tan^{-1}(\gamma H_1/\Delta\omega_2)$$

$$b_3 = |\gamma H_1 + \Delta\omega_2|$$

6.2 The Basic Principles of the Analysis

To analyse our experimental results in more detail we note that the effect of both the a.c. modulation as well as the perpendicular d.c. field is to introduce an angular dependent field shift into the spin-echo experiment. The local field at a particular position in the wall is given by

$$H_{loc}(\theta) = H_{hf}(\theta) + \Delta H(\theta) + h(\theta) \tag{6.23}$$

where H_{hf} is the hyperfine field which has an anisotropic component and therefore is angular dependent, ΔH is the local linewidth and h is the angular dependent field shift. In a system of co-ordinates rotating about the z-axis with a frequency ω_1, the effective field is given by

$$H_{eff} = [(H - \omega_1/\gamma)^2 + H_1^2]^{\frac{1}{2}} \tag{6.24}$$

and the cosine of the angle Ψ between H_{eff} and the z-axis is given by

$$\begin{aligned} \cos \psi_1 &= (H - \omega_1/\gamma)/H_{eff} \\ &= (\omega - \omega_1)/[(\omega - \omega_1)^2 + (\omega H_1/H)^2]^{\frac{1}{2}} \\ &= \frac{(\omega - \omega_1)/(\omega H_1/H)}{\{1 + [(\omega - \omega_1)/(\omega H_1/H)]\}^{\frac{1}{2}}} \\ &= (x + \eta)/[1 + (x+\eta)^2]^{\frac{1}{2}} \end{aligned} \tag{6.25}$$

where $x = \Delta\omega/H_1$ and $\eta = h/H_1$ Similarly

$$\sin \psi_1 = 1/[1 + (x + \eta)^2]^{\frac{1}{2}} \tag{6.26}$$

and

$$\begin{aligned} b_1 t_1 &= [(\omega - \omega_1)^2 + (\omega H_1/H)^2]^{\frac{1}{2}} t_1 \\ &= \gamma H_1 t_1 [1 + (x + \eta)^2]^{\frac{1}{2}} \\ &= \phi_1 [1 + (x + \eta)^2]^{\frac{1}{2}} \end{aligned} \tag{6.27}$$

$$\begin{aligned} b_3 t_3 &= \gamma H_1 t_3 [1 + (x' + \eta)^2]^{\frac{1}{2}} \\ &= \phi_2 [1 + (x' + \eta)^2]^{\frac{1}{2}} \end{aligned} \tag{6.28}$$

where $x' = \Delta\omega_2/H_1$ in the presence of a dynamic frequency shift. For most of our calculations we will, however, take $\Delta\omega_4 = \Delta\omega_2 = \Delta\omega$ and therefore $x' = x$. The notation used above is quite convenient and was

taken from the work of Srivastava (4). To calculate the echo amplitude we now combine Eqns. 6.25-6.28 with Eqn. 6.21, 6.2 and 6.1 and obtain

$$A(w_i) = + i \int_{-\infty}^{\infty} F(x) \frac{\sin \{\phi_1[1 + (x \mp \eta)^2]^{\frac{1}{2}}\}}{[1 + (x \mp \eta)^2]^{\frac{1}{2}}}$$

$$x \frac{\sin^2 \{(\phi_2/2)[1 + (x' \pm \eta)^2]^{\frac{1}{2}}\}}{1 + (x' \pm \eta)^2} e^{i\Delta\omega_2 t_2} e^{-i\Delta\omega_4 t_4}$$

$$- \frac{2(x \mp \eta) \sin^2\{(\phi_1/2)[1 + (x \mp \eta)^2]^{\frac{1}{2}}\}}{[1 + (x \mp \eta)^2]} \qquad (6.29)$$

$$x \frac{\sin^2 \{(\phi_2/2)[1 + (x' \pm \eta)^2]^{\frac{1}{2}}\}}{[1 + (x' \pm \eta)^2]^{\frac{1}{2}}} e^{i\Delta\omega_2 t_2} e^{-i\Delta\omega_4 t_4} dx$$

where F(x) is the composite lineshape for the wall NMR resonance.

Equation 6.29 is the fundamental equation upon which our analysis is based. To evaluate the echo amplitude as a function of frequency we set $\eta = 0$ and perform the integration. The exact form of for the modulation experiment will depend on the variation of the hyperfine field through the domain wall. For a hyperfine field which varies as $\sin^2 \theta'$ (see Eqn. 4.46) η will take the form

$$\eta(\theta) = \pm \eta_o \sin(2\theta')$$

For the modulation experiment the lower signs are used in Eqn. 6.29. This is a result of the fact that a maximum in the depth of modulation occurs when the field shift is a maximum in opposite directions during the two r.f. pulses. This corresponds to the condition (4) that a minimum in the modulation envelope occurs when the pulse separation τ =

$(n + 1/2)T$ where n is an integer and T is the period of the modulation. To compare the calculated to the experimental results we calculate the ratio of the echo amplitude with η to the echo amplitude with $\eta = 0$.

For the effect of a field applied perpendicular to the c-axis η takes the form of Eqn. 5.18.

$$\eta = H \sin\theta' \cos\phi$$

For this calculation we use the upper sign in Eqn. 6.29 and for comparison to the experimental echo amplitude reduction ratio, A_o/A_H, we calculate the ratio of the echo amplitude with $\eta = 0$ to the echo amplitude with η given by Eqn. 5.18.

Two basic models for the composite lineshape F(x), based on either a continuous or a discrete wall structure, have been used. For either model the values of $H_{||}$ and $H_{\perp}$ and therefore the total anisotropy in the hyperfine field, H_a, is taken from experiment and the hyperfine field is assumed to take a particular form. The discrete wall structure certainly allows one to more realistically model the situation. We associate with each atomic layer in the wall a set of quadrupole split lines which may also have an angular dependent linewidth. With these models we attempted to reproduce some of the general features that we observe in our experimental data.

In most instances we found it adequate to consider the simpler continuous wall model with a hyperfine field which either explicitly varied as $\sin^2\theta'$ through the wall, or we assumed a gate shape for the composite lineshape F(x). This model still implicitly assumes a $\sin^2\theta'$ variation of the hyperfine field for the calculation of the modulation spectrum as we took $\eta(\theta) = \eta_o \sin(2\theta')$.

For the first model the spectral amplitude at a frequency ω_i is given by

$$A(\omega_i) = \int_0^{\pi} F(\theta)E(\theta)d(\theta) \qquad (6.30)$$

which is equivalent to Eqn. 6.29 using Eqns. 4.45 and 4.46 to relate θ and $\Delta\omega$ and we take $F(\theta) = 1$. θ represents the angle of the electronic spin with respect to the c-axis and the integration over θ indicates an assumption of a uniform rotation of the electronic spins in the wall. However, as we have indicated earlier, the angular distribution of electronic spins is inversely proportional to the transverse enhancement factor and therefore we may take $F(\theta) = 1$. The effect of the distribution in transverse enhancement factors will still manifest itself in an angular dependence of ϕ_1, ϕ_2 and H_1. However, when the experimental data was taken it was observed, to our surprise, that the optimum tuning conditions (pulse lengths) remained the same, within experimental error, throughout each of the spectra. The pulse lengths shown in Table 5.2 and therefore the measured values of H_1 were taken at the frequency at which the maximum modulation of the spin-echo-decay envelope was observed. In actual fact no measurable change in the tuning conditions throughout the spectrum could be observed. For the time being, and for these calculations, it was therefore assumed that ϕ_1, ϕ_2 and H_1 are independent of angle.

6.3 The Calculation of the Modulation Spectrum and the Identification of NMR Resonance Peaks

Figure 6.2 shows the domain-wall NMR spectrum and the

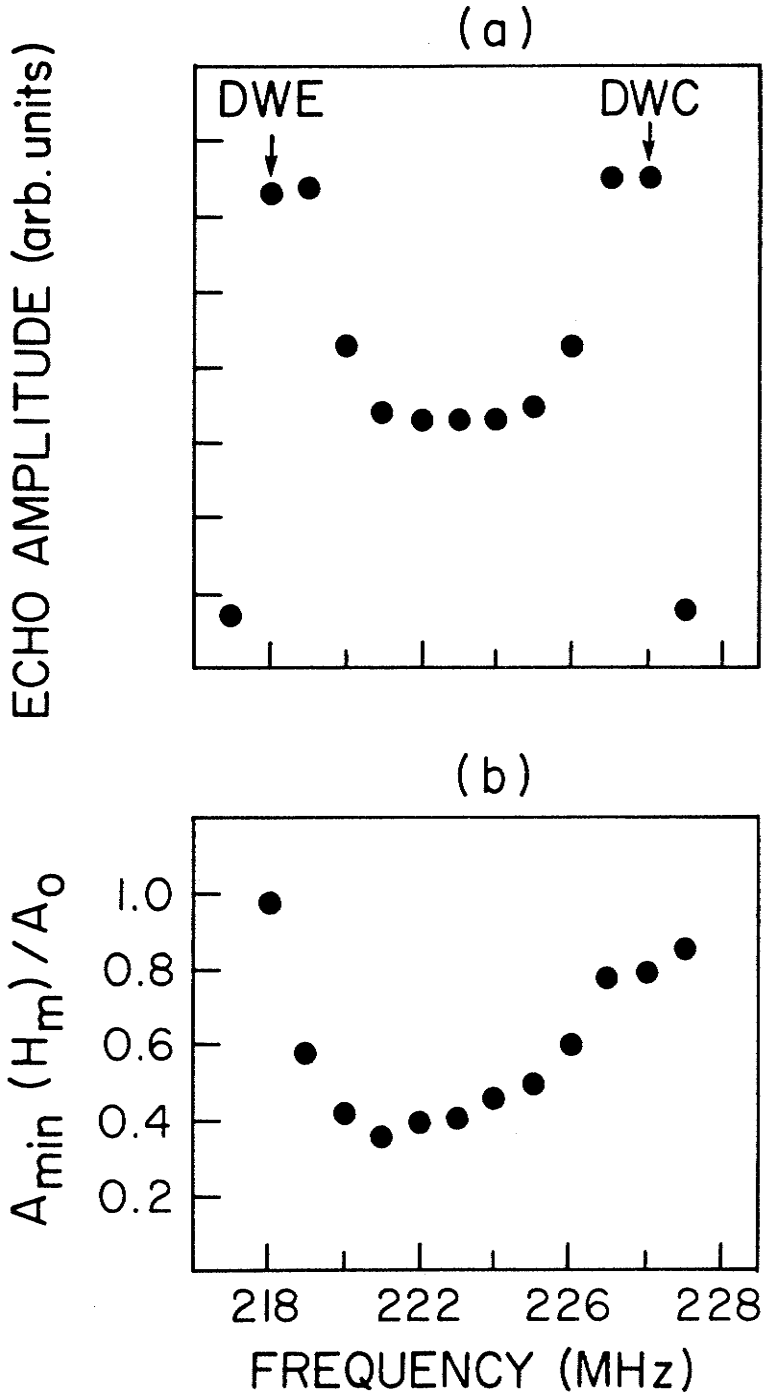

Fig. 6.2 The domain-wall NMR spectrum (a) and the corresponding modulation spectrum (b) for hexagonal Co assuming a $\sin^2\theta'$ variation of the hyperfine field through the domain wall. The curves were calculated using Eqn. 6.30.

corresponding modulation spectrum for hexagonal Co, calculated using Eqn. 6.30. The values of $H_{\parallel}$ and $H_{\perp}$ were taken from our experimental results and the value of η_o was simply adjusted to obtain a modulation spectrum which resembled that obtained experimentally. For the time being we will not concern ourselves with the mechanism which generates these apparently large values of the field shifts, η; we will only attempt to reproduce the general shapes of our experimental results in order to complete our identification of the NMR peaks in the spectra we have obtained, and thereby determine the values of the anisotropy in the hyperfine field at the two Co sites in the RCo_5 compounds we have examined. Figures 6.3 - 6.6 show the calculated spectra and the corresponding modulation spectra obtained using Eqn. 6.30 for the Co resonance in YCo_5, $SmCo_5$ and $GdCo_5$. Although we have experimentally identified the domain-wall-edge and centre resonances, we, as yet, have not determined which to associate to a given Co site. We therefore calculated the modulation spectra for each possible combination adjusting the ratio of the value of η_o for the two sites to be equal to the ratio of the corresponding anisotropies in the hyperfine field and scaling the absolute value of the η_o to best reproduce the experimental results. This calculation was not done using a fitting routine, rather it involved the selection of the best qualitative fit from a series of calculated curves.

Figures 6.7 - 6.15 show similarly calculated results using the gate-shaped composite lineshape. These results, in fact, qualitatively reproduce our results with better accuracy, although the calculated spectra do not clearly distinguish the DWE and DWC peaks. The reason

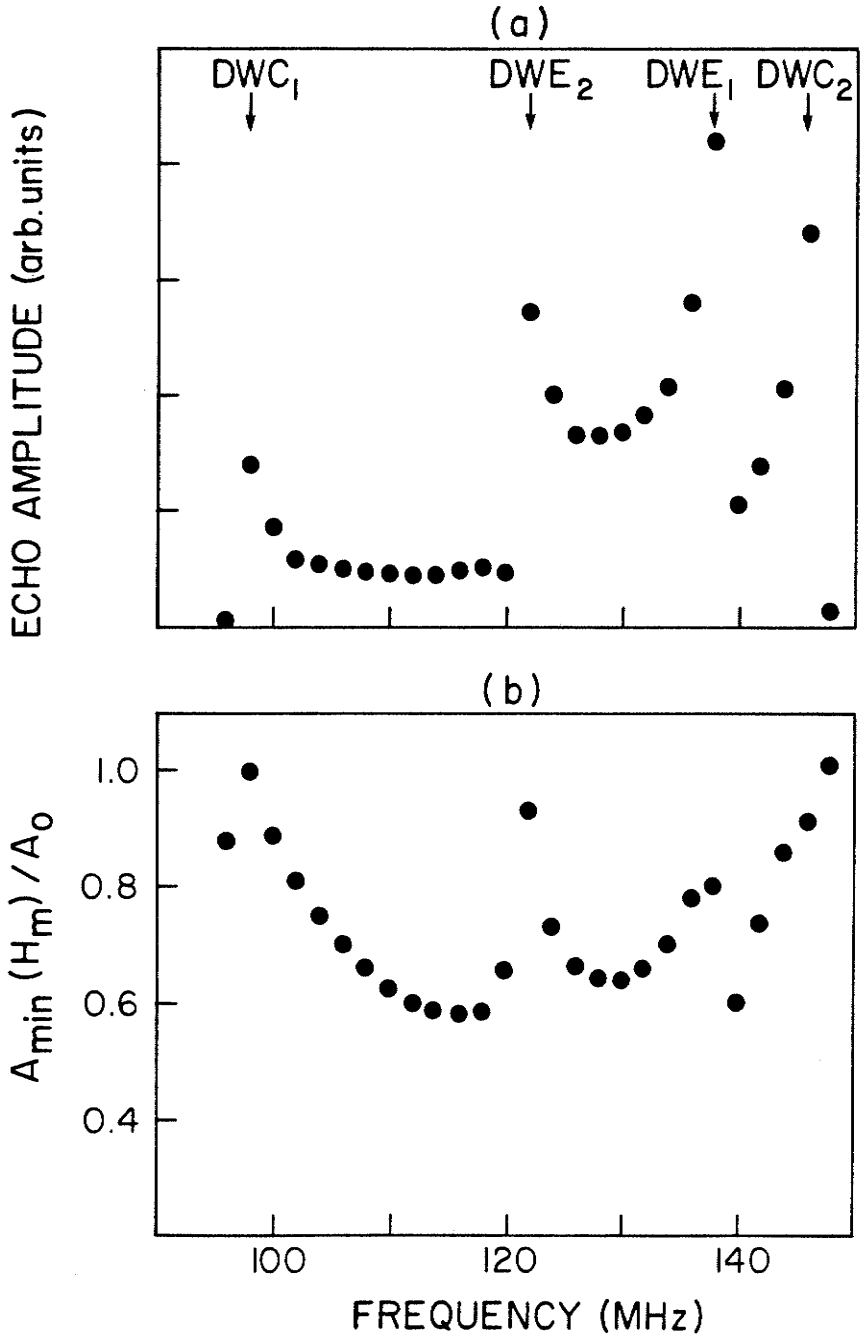

Fig. 6.3 The calculated domain-wall NMR spectrum (a) and the corresponding modulation spectrum (b) for Co in YCo_5 assuming a $\sin^2 \vartheta'$ variation of the hyperfine field through the domain wall. The values of the parameters used in the calculation are $H_\perp(2)$ = 146 MHz, $H_{//}$ (2) = 122, $H_\perp(1)$ = 98 and $H_{//}$ (1) = 138. Also η_o^1 = 0.7, η_o^2 = 0.7 and H_1 = 1.0 kOe.

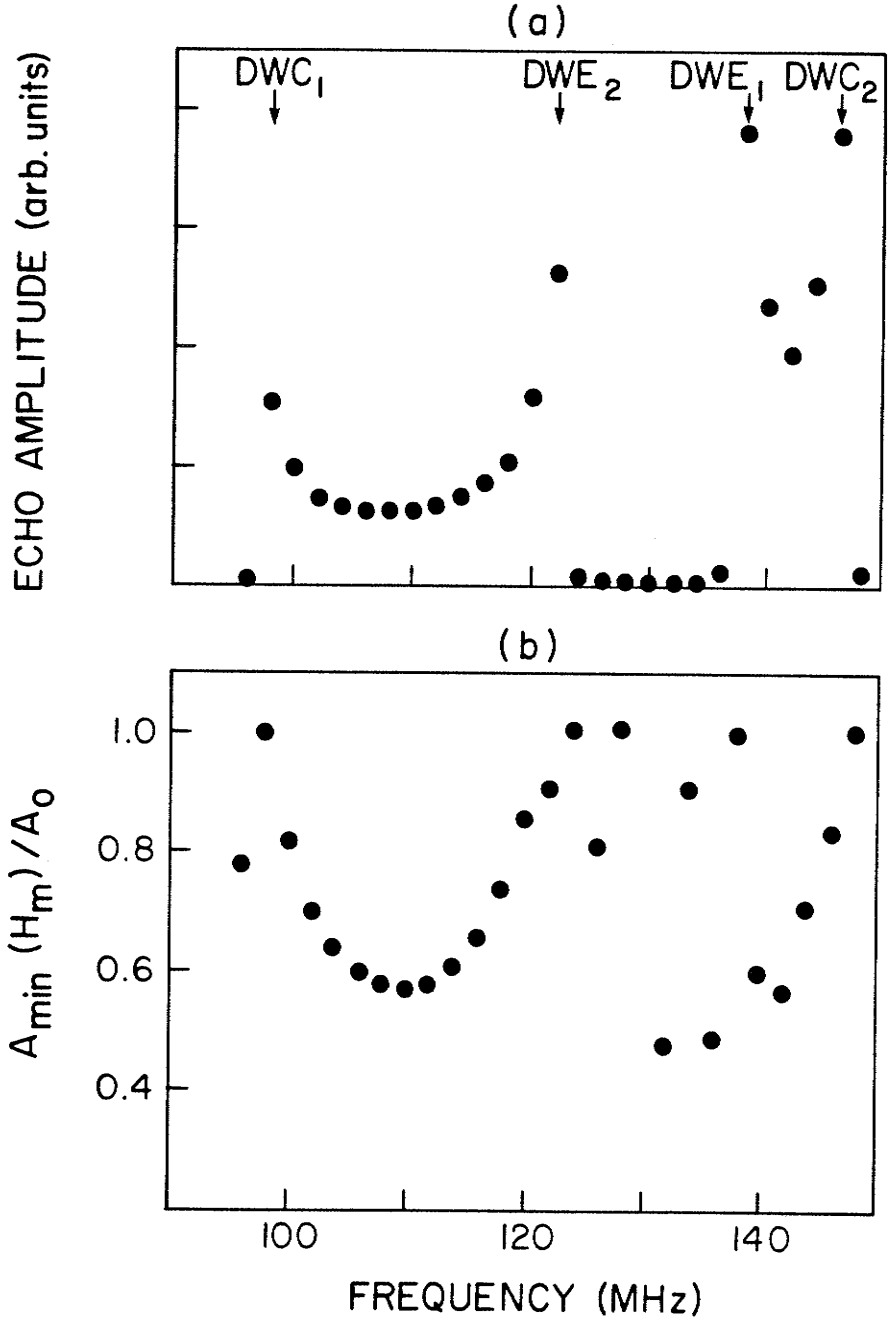

Fig. 6.4 The calculated domain-wall NMR spectrum (a) and the corresponding modulation spectrum (b) for Co in YCo_5. Here, as in Fig. 6.3, we take $\eta_o^1 = \eta_o^2 = 0.7$ and $H_1 = 1.0$ kOe but the peaks of the NMR spectrum are identified as follows: $H_\perp(2) = 146$ MHz, $H_{//}(2) = 138$, $H_\perp(1) = 98$ and $H_{//}(1) = 122$.

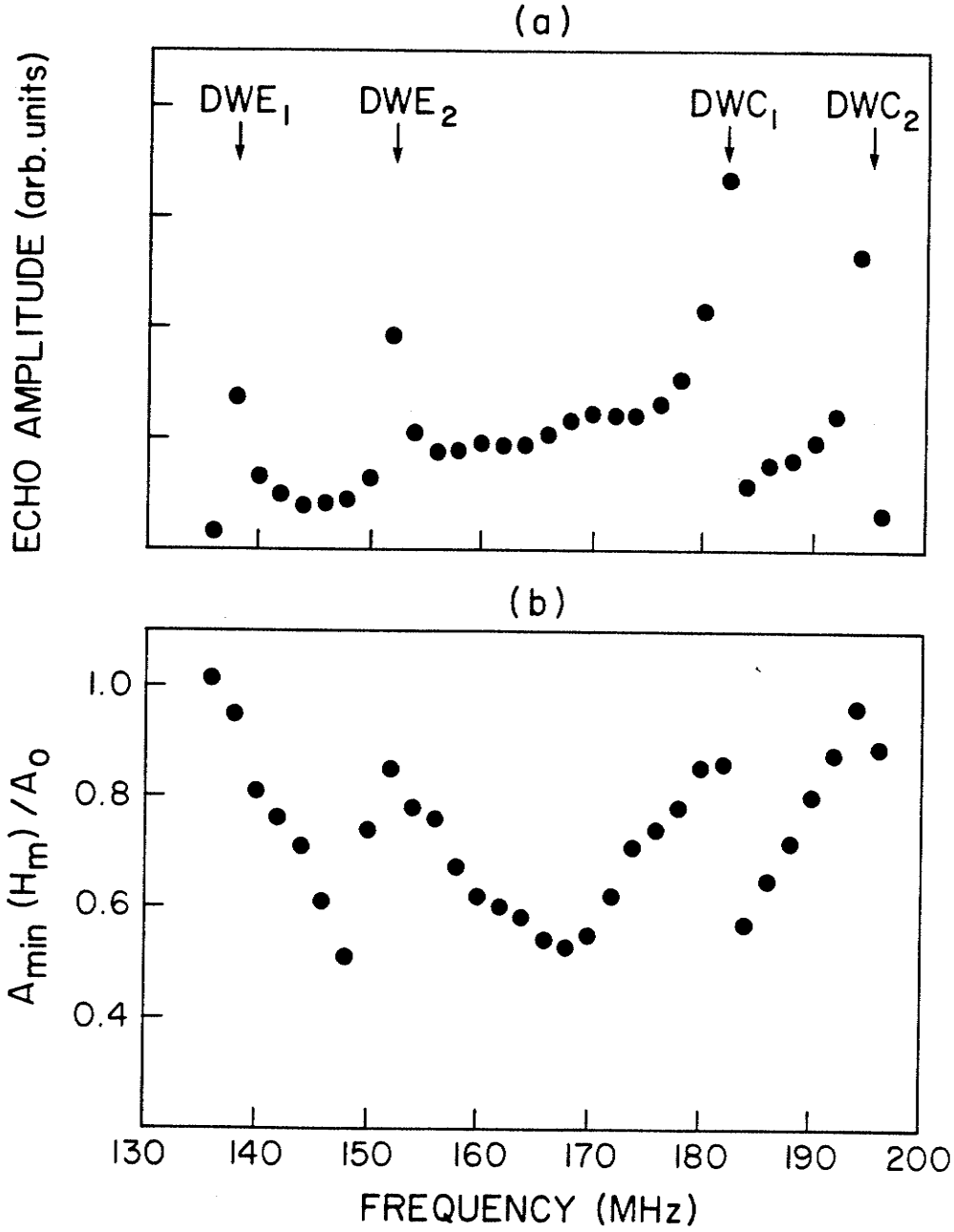

Fig. 6.5 The calculated domain-wall NMR spectrum (a) and the corresponding modulation spectrum (b) for Co in $SmCo_5$ assuming a $\sin^2 \theta'$ variation of the hyperfine field through the domain wall. The values of the parameters used was $\eta_o^1 = \eta_o^2 = 0.7$, $H_1 = 1.0$ and the peaks are identified as $H_\perp(2) = 195$, $H_{//}(2) = 151$, $H_\perp(1) = 182$, $H_{//}(1) = 137$.

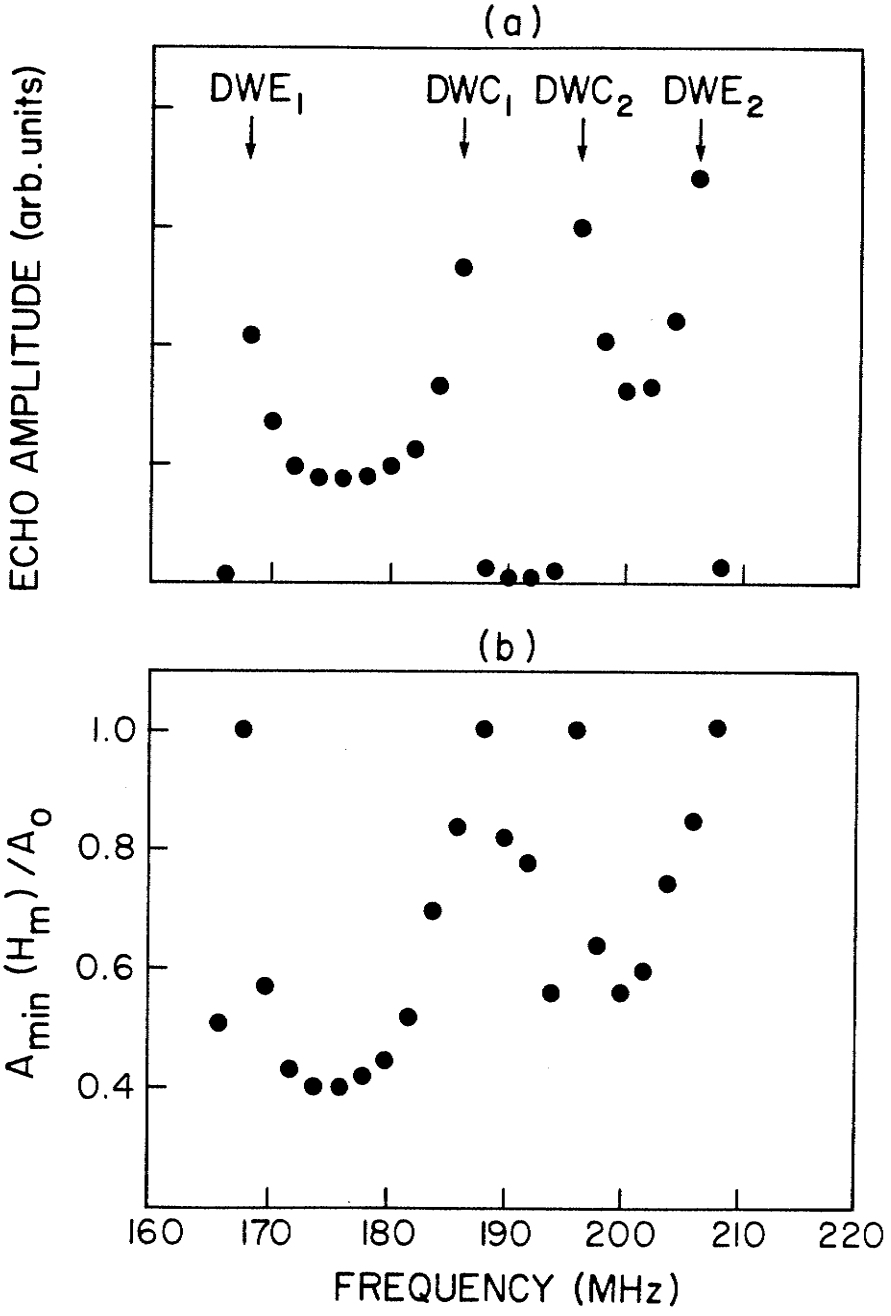

Fig. 6.6 The calculated domain-wall NMR spectrum (a) and the corresponding modulation spectrum (b) for Co in $GdCo_5$ assuming a $\sin^2 \theta'$ variation of the hyperfine field through the domain wall. Here, we take $\eta_o^1 = 1.0$, $\eta_o^2 = 0.7$, $H_1 = 1.0$ kOe and identify the peaks as $H_\perp^o(2) = 196$ MHz, $H_{//}(2) = 206$, $H_\perp(1) = 186$ and $H_{//}(1) = 168$.

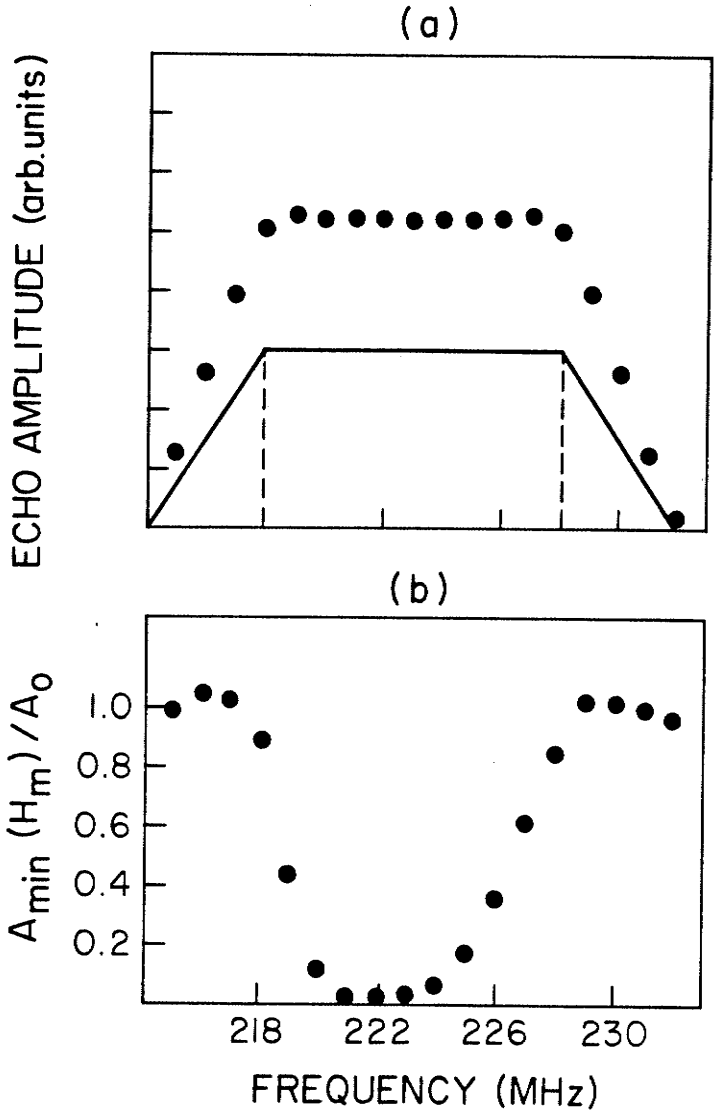

Fig. 6.7 The domain-wall NMR spectrum (a) and the corresponding modulation spectrum (b) for hexagonal Co calculated using Eqn. 6.29 assuming a gate-shaped distribution in the hyperfine field illustrated by the solid line in Fig. (a). The values of the parameters used in the calculation are $H_{\perp}$ = 228 MHz, $H_{//}$ = 218 and η_o^1 = 1.0, H_1 = 1.0 kOe.

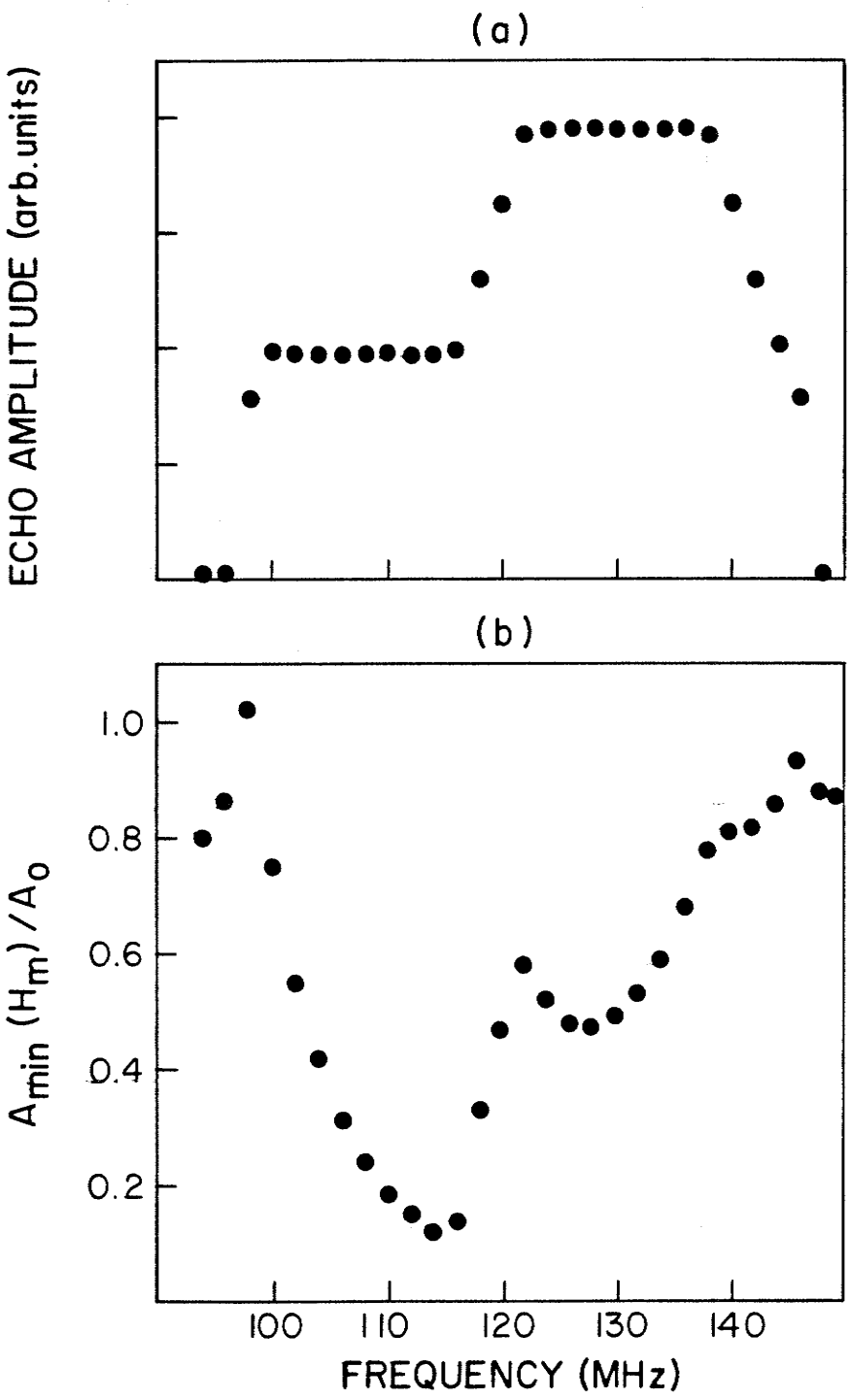

Fig. 6.8 The domain-wall NMR spectrum (a) and the corresponding modulation spectrum (b) for Co in YCo_5 assuming a gate-shaped distribution in the hyperfine field. The triangular edges to the spectrum have widths of Lw1 = 6.0 and Lw2 = 1.0. The values of the other parameters in the calculation are $\eta_o^1 = 0.9$, $\eta_o^2 = 0.54$ and $H_1 = 1.0$. The peaks in the spectrum are identified as $H_\perp(2) = 146$ MHz, $H_{//}(2) = 122$, $H_\perp(1) = 98$ and $H_{//}(1) = 138$.

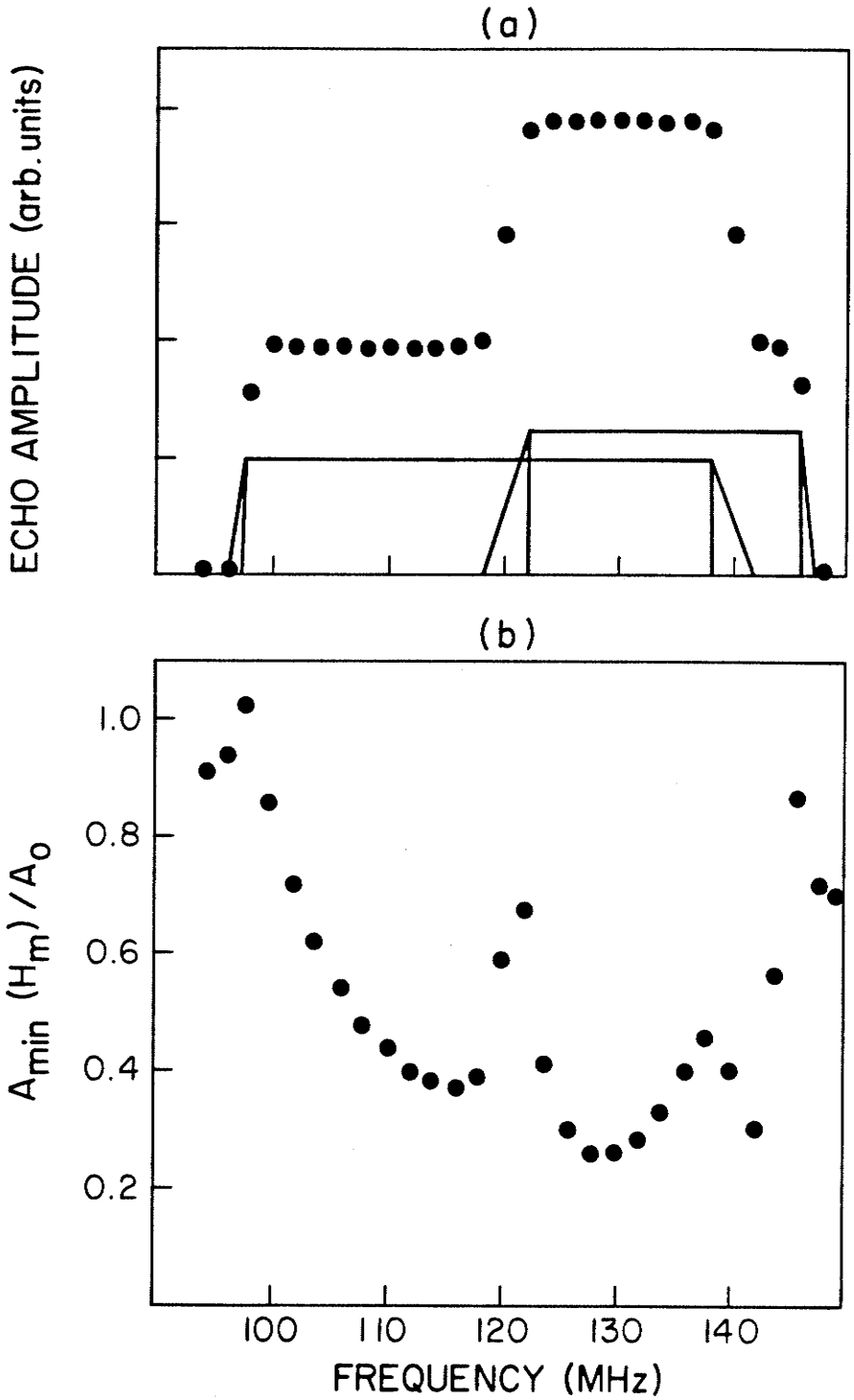

Fig. 6.9 The domain-wall NMR spectrum (a) and the corresponding modulation spectrum (b) for Co in YCo_5. The triangular edges shown in Fig. (a) on the gate-shaped distribution have widths of Lw1 = 4.0 and Lw2 = 1.0. The values of the other parameters used in the calculation are $\eta_1^o = 0.7$, $\eta_2^o = 1.1$ and $H_1 = 1.0$. The peaks in the spectrum are identified as $H_\perp(2) = 146$ MHz, $H_{//}(2) = 122$, $H_\perp(1) = 98$ and $H_{//}(1) = 138$.

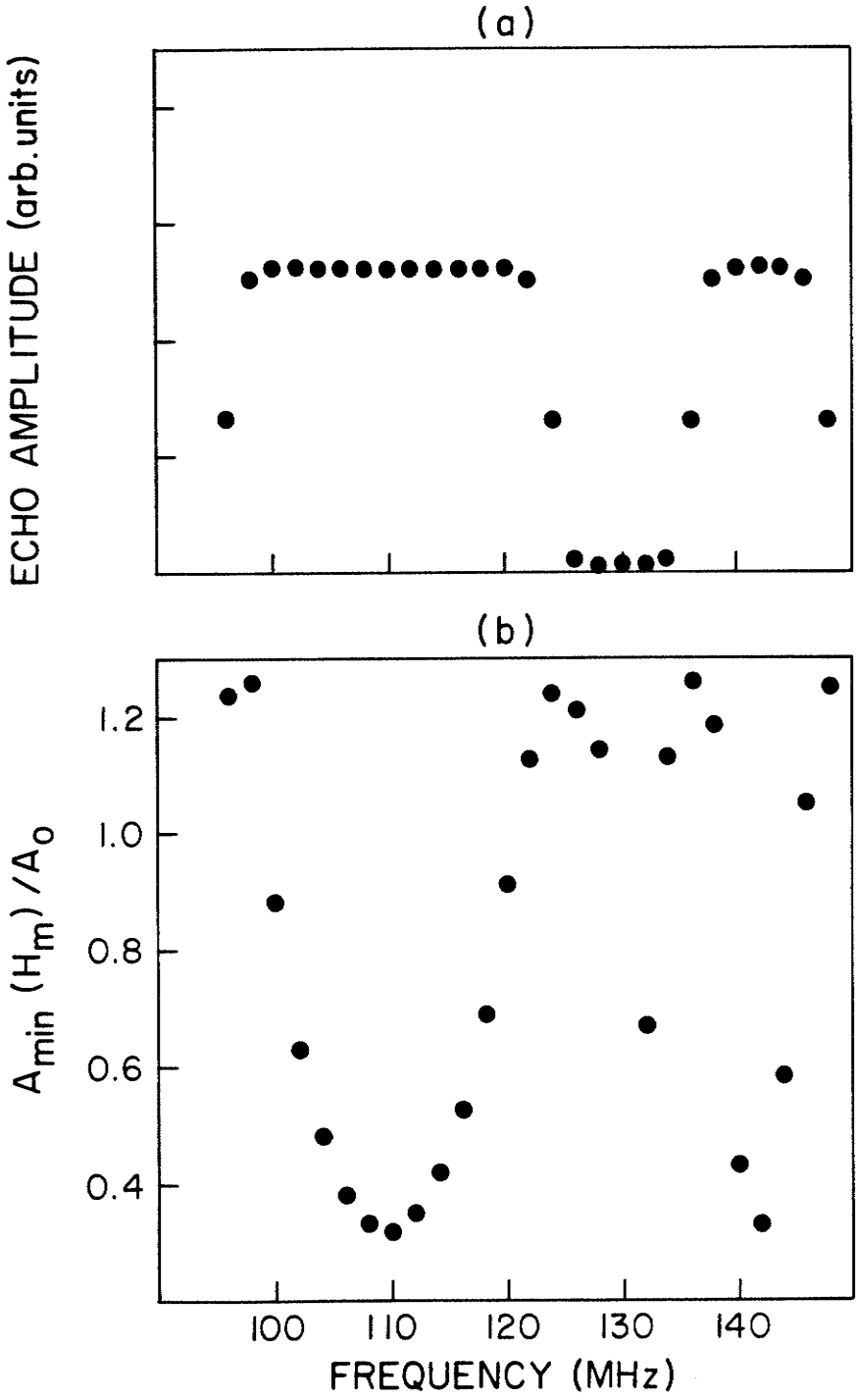

Fig. 6.10 The domain-wall NMR spectrum (a) and the corresponding modulation spectrum (b) for Co in YCo_5. The values of the parameters in the calculation are Lw1 = 4.0, Lw2 = 4.0, $\eta_o^1 = 0.7$, $\eta_o^2 = 0.7$, $H_1 = 1.0$. The peaks in the spectrum are identified as $H_\perp(2) = 146$ MHz, $H_{//}(2) = 138$, $H_\perp(1) = 98$ and $H_{//}(1) = 122$.

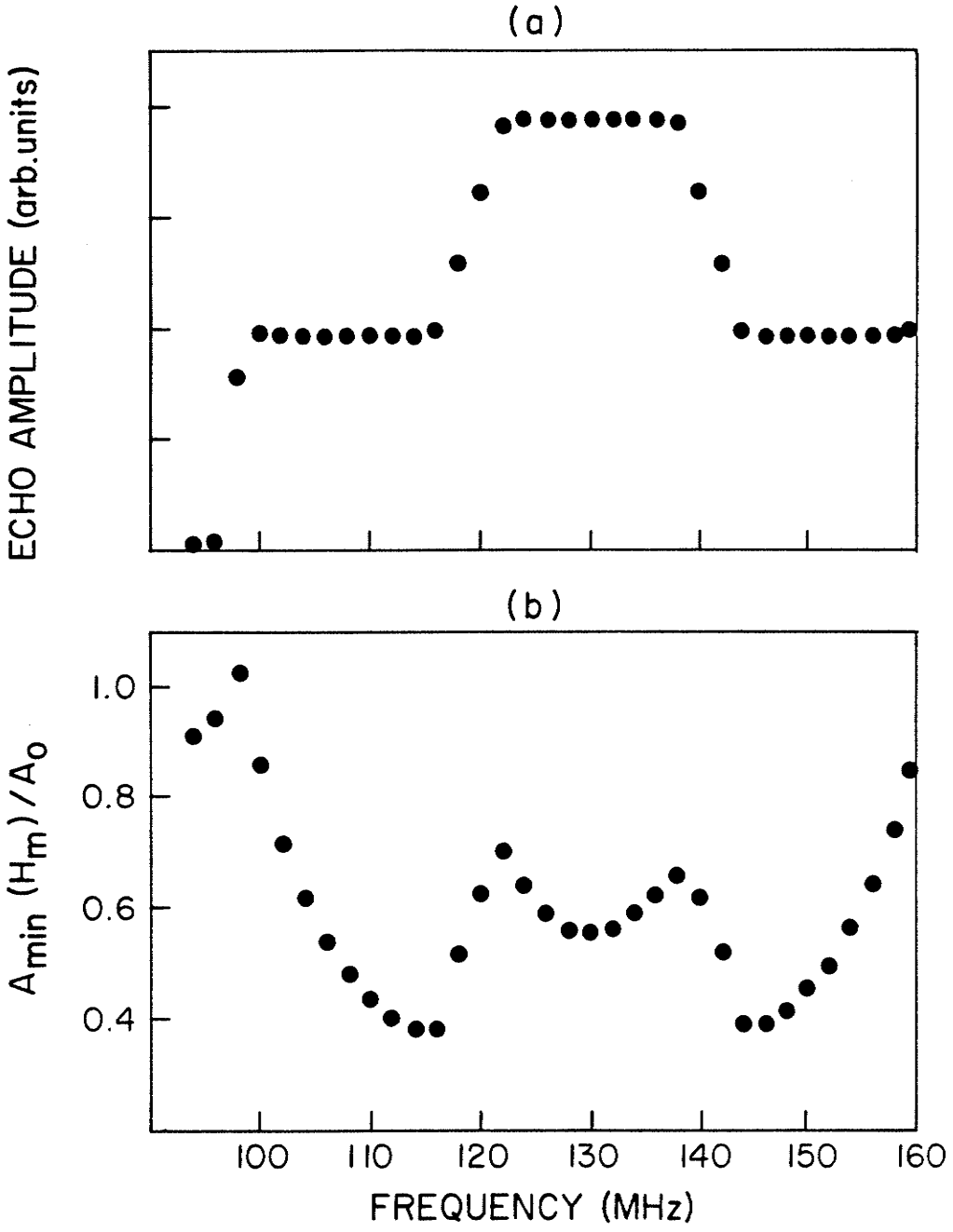

Fig. 6.11 The domain-wall NMR spectrum (a) and the corresponding modulation spectrum (b) for Co in YCo_5. The values of the parameters in the calculation are Lw1 = 6.0, Lw2 = 1.0, $\eta_1^o = \eta_2^o = 0.7$ and $H_1 = 1.0$. The peaks in the spectrum are located at $H_\perp(2)$ = 162 MHz, $H_{//}(2)$ = 122, $H_\perp(1)$ = 98 and $H_{//}(1)$ = 138.

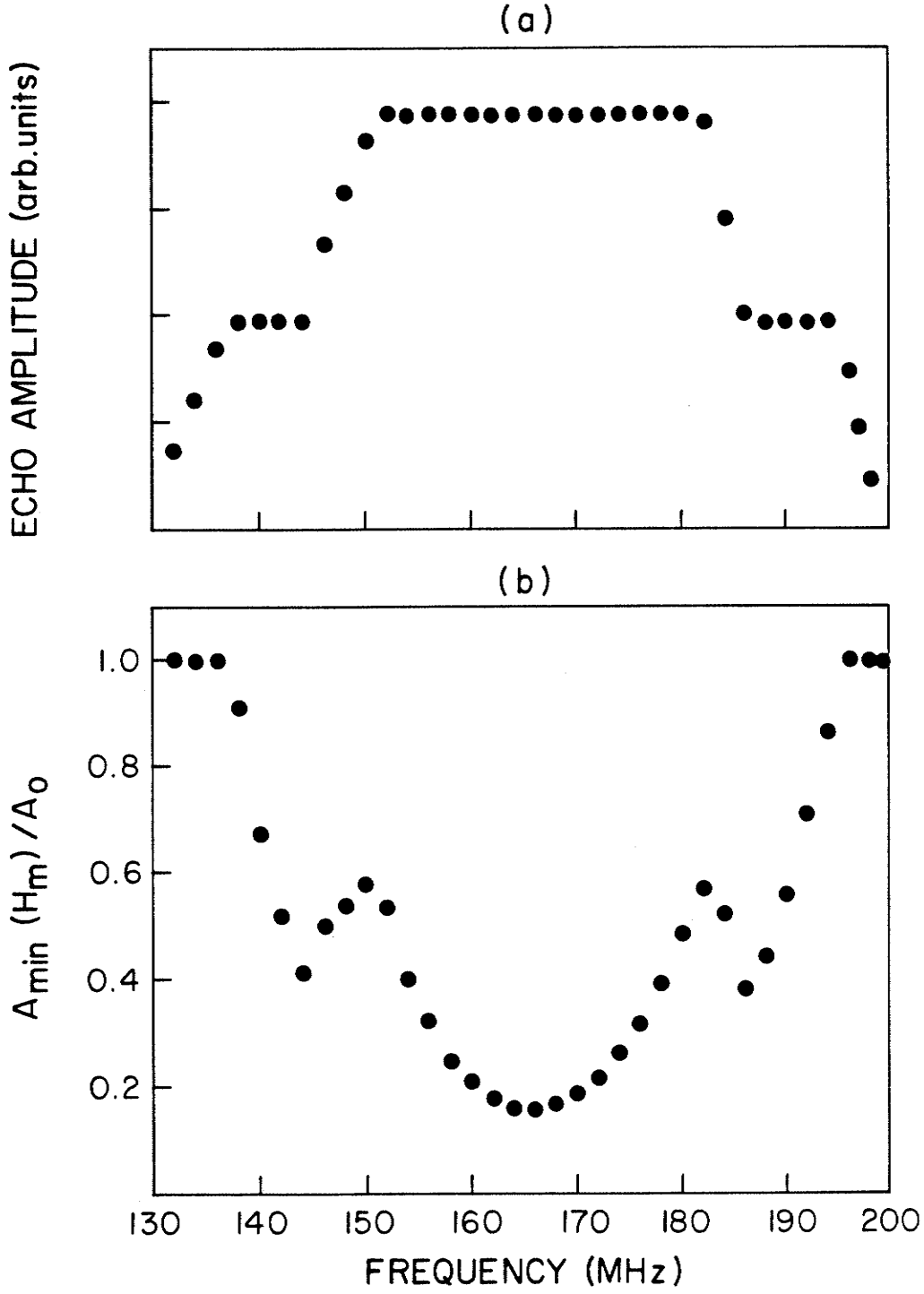

Fig. 6.12 The domain-wall NMR spectrum (a) and the corresponding modulation spectrum (b) for Co in $SmCo_5$. The values of the parameters in the calculation are Lwl = 8.0, Lw2 = 4.0, H_1 = 1.0, and $\eta^1 = \eta^2 = 0.9$. The peaks in the spectrum are identified as ${}^{o}H_{\perp}(2^{o})$ = 195 MHz, $H_{//}$ (2) = 151, $H_{\perp}(1)$ = 182 and $H_{//}$ (1) = 137.

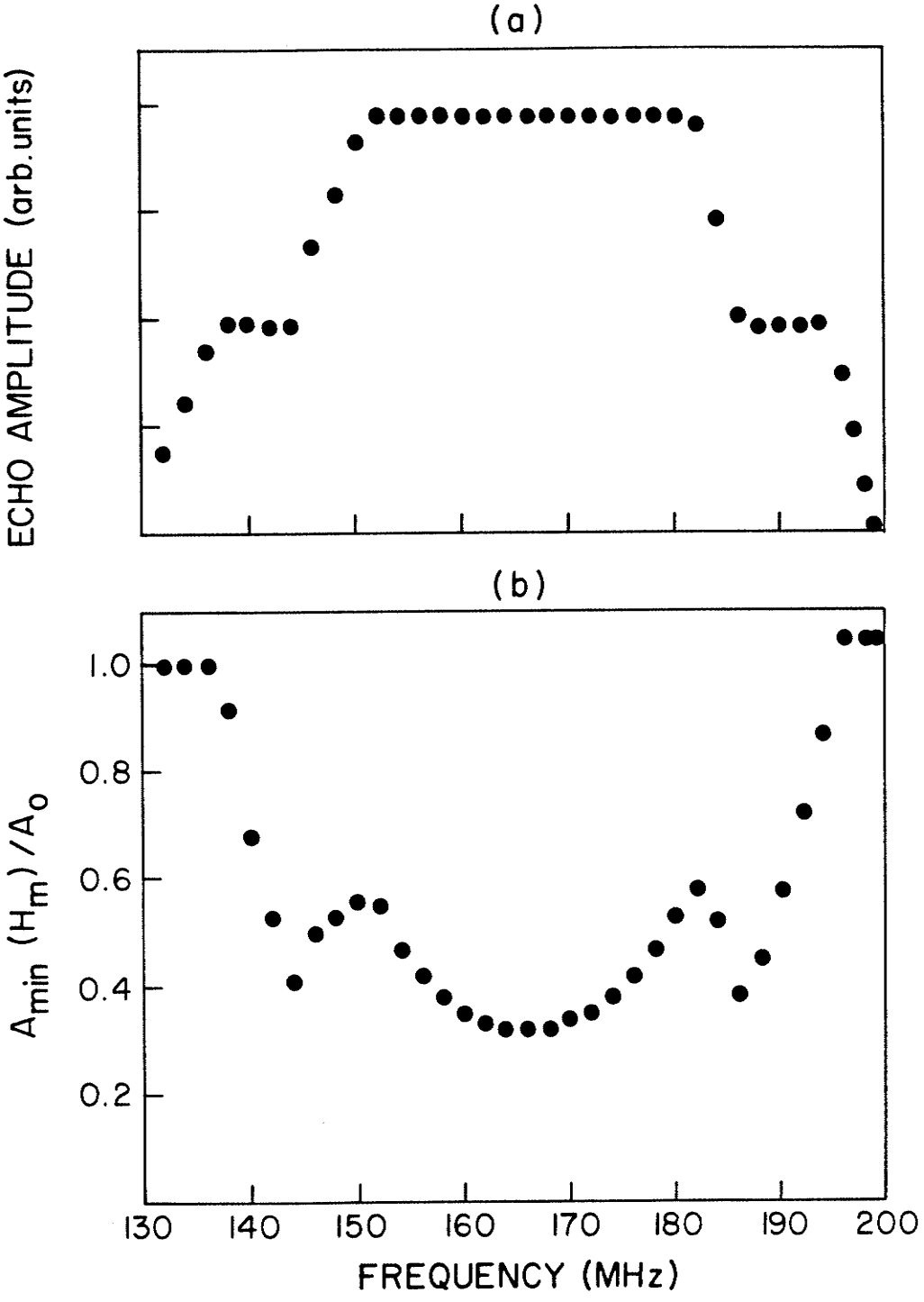

Fig. 6.13 The domain-wall NMR spectrum (a) and the corresponding modulation spectrum (b) for Co in $SmCo_5$. The values of the parameters in the calculation are Lw1 = 8.0, Lw2 = 4.0, H_1 = 1.0 and η_o^1 = 0.5, η_o^2 = 1.0. The peaks in the spectrum are identified as $H_\perp(2)$ = 195 MHz, $H_{//}$ (2) = 137, $H_\perp(1)$ = 182 and $H_{//}$ (1) = 151.

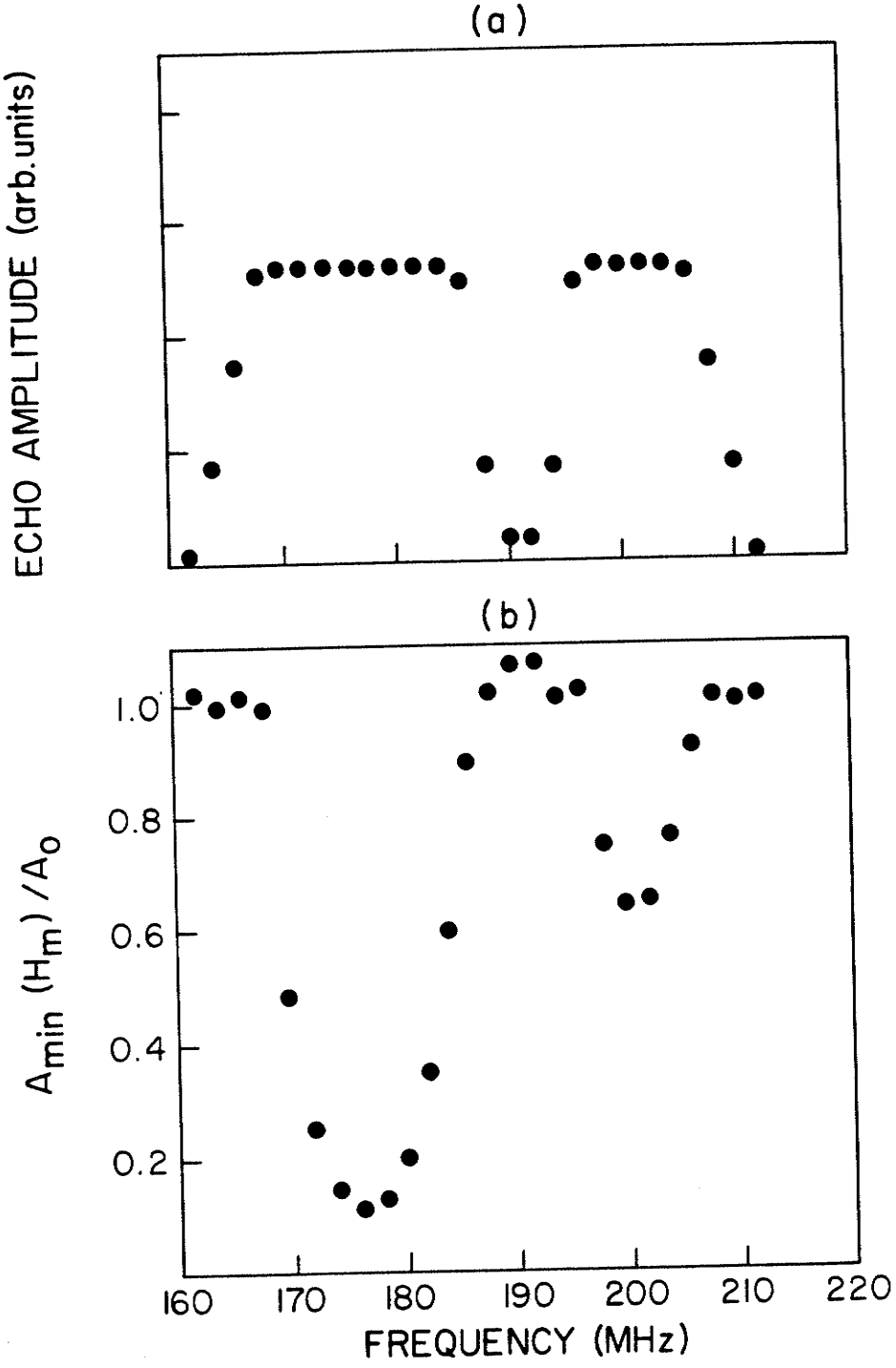

Fig. 6.14 The domain-wall NMR spectrum (a) and the corresponding modulation spectrum (b) for Co in $GdCo_5$. The values of the parameters in the calculation are Lw1 = 6.0, Lw2 = 3.0, H_1 = 1.0 and η_o^1 = 0.9, η_o^2 = 0.5. The peaks in the spectrum are identified as $H_\perp^o(2)$ = 196 MHz, $H_{//}$ (2) = 206, $H_\perp(1)$ = 186 and $H_{//}$ (1) = 168.

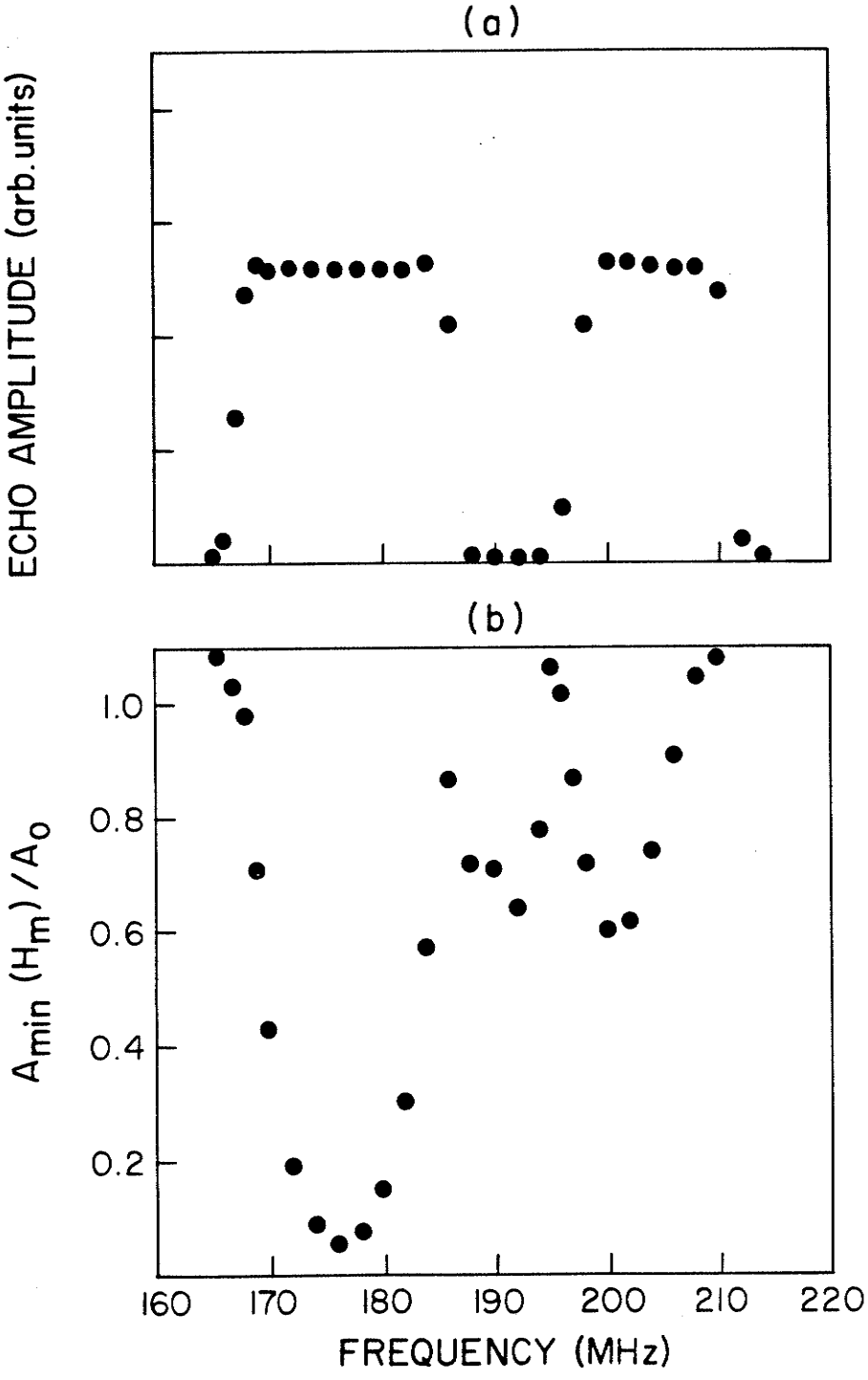

Fig. 6.15 The domain-wall NMR spectrum (a) and the corresponding modulation spectrum (b) for Co in $GdCo_5$. Here the values of the parameters used in the calculation are Lw1 = 2.0, Lw2 = 1.0, H_1 = 1.0 and η_o^1 = 0.95, η_o^2 = 0.53. The peaks in the spectrum are identified $H_\perp(2)^o$ = 196 MHz, $H_{//}$ (2) = 206, $H_\perp(1)$ = 186 and $H_{//}$ (1) = 168.

for the better results for the calculated modulation spectrum probably lies in this very fact. The experimental spectra were characterized by generally broad peaks which smoothly overlapped and thus actually resembled these spectra more closely than the abrupt peaks generated by the first model and shown in Figs. 6.2 - 6.6.

Essentially this procedure involved the use of the modulation spectrum obtained for a single site, as shown in Fig. 6.2 or Fig. 6.7, as a building block to construct the spectrum for a material having more than one site. In particular, the modulation spectra for each site, i, will have to be weighted by the contribution to the overall spectrum arising from that site, i.e. the observed depth of modulation at a given frequency will be given by

$$\frac{\sum_i A^i_{min}(H_m)}{\sum_i A^i_o} = \frac{A^i_o}{\sum_i A^i_o} \times \sum_i \frac{A^i_{min}(H_m)}{A^i_o} \qquad (6.31)$$

where $A^i_{min}(H_m)/A_o{}^i$ is the depth of modulation resulting from site i only.

Figure 6.8 shows the calculated modulation spectrum for the Co resonance in YCo_5 assuming that the DWC peak at 146 MHz arises from the same site as the DWE peak at 122 MHz and the peaks at 98 MHz and 138 MHz belong to the other site. According to our procedure we then have

$$\frac{\eta^1_o}{\eta^2_o} = \frac{H^1_a}{H^2_a} = \frac{40}{24}$$

The calculated spectrum does not show the deep central minimum shown by the experimental data (Fig. 5.24) but basically does show similar features. A better looking curve is obtained by choosing $\eta^1_o = 0.70$ and

$\eta_o^2 = 1.10$ as shown in Fig. 6.9. Figure 6.10 shows the calculated modulation spectrum if we associate the DWC peak at 146 MHz with the DWE peak at 138 MHz and the DWC peak at 98 MHz with the DWE peak at 122 MHz, the other possibility which still exists. We choose $\eta_o^1 = \eta_o^2 = 0.70$ and clearly establish that this identification cannot reproduce the type of shape we obtain experimentally. The sites do not overlap in this situation and large fluctuations in the calculated depth of modulations are obtained in the intermediate region. This is the result of the small amplitude of the calculated spectrum in this region which consists of an off-resonance contribution only which, is highly sensitive to the field shift but which would not be observed experimentally. This is the result of the sharp cut-off of the assumed hyperfine field distribution and the addition of triangular edges (as shown in Fig. 6.7a) to ensure a non-negligible intensity in this region (as is observed experimentally) is able to eliminate these fluctuations to produce a more realistic result. We denote the width of the triangular edges on the DWE side of the distribution as Lw1 and the DWC side as Lw2.

Clearly the case of non-overlapping sites for YCo_5 cannot reproduce the modulation spectrum we have observed experimentally since we then would have only two minima without an additional deep central minimum. We conclude that for the Co^{59} spectrum we have observed in YCo_5 the peaks at 98 and 138 MHz originate from one Co site which therefore has an anisotropy in the hyperfine field of 40 kOe. The peaks we observed at 122 MHz and 146 MHz are then associated with the other Co site which would have an anisotropy in the hyperfine field of 24 kOe.

Streever (5) has obtained the Co^{59} resonance for YCo_5 and

observed peaks at 98 MHz and 162 MHz, whereas we observed the high frequency peak at 146 MHz. We are unable to account for this discrepancy, although large discrepancies in the reported resonance frequencies are common in the literature for these materials (6,7). Figure 6.11 shows the calculated modulation spectrum assuming that the peak at 146 MHz should be at 162 MHz. We use $\eta_o^1 = \eta_o^2 = 0.7$ but obtain a spectrum which is quite different from the experimental curve.

The experimental results for $SmCo_5$ identified the wall edge and centre resonances (Fig. 5.23) but here again we were left uncertain about which edge peak to associate with which centre peak. Figures 6.12 and 6.13 show the calculated modulation spectra for the two remaining possibilities. We again select the values of η_o^i as we did for the calculations for YCo_5. The results are not as clear cut, however, as they were for YCo_5. Figure 6.12 shows a more defined central minimum and therefore we tentatively conclude that in $SmCo_5$ we have one site $H_\perp$ = 195 kOe and $H_{||}$ = 151 kOe and for the other site $H_\perp$ = 182 kOe and $H_{||}$ = 137 kOe. Both sites have therefore approximately the same anisotropy in the hyperfine field of 45 kOe.

The identification of the peaks in the Co^{59} resonance in $GdCo_5$ was in fact complete with the experimental results. From Fig. 5.22 we have that for one site $H_\perp$ = 196 kOe and $H_{||}$ = 206 kOe and therefore H_a is 10 kOe; and for the other site $H_\perp$ = 186 kOe and $H_{||}$ = 168 kOe and therefore H_a = 18 kOe. As in the case of YCo_5 the modulation data were able to detect a resonance peak (the DWE peak at 206 MHz) not detected in the spectrum itself. Figures 6.14 and 6.15 show the calculated modulation spectra for $GdCo_5$ which now represent a

case of non-overlapping sites. Figure 6.14 shows the calculated modulation spectrum using Lw1 = 6.0 MHz and Lw2 = 3.0 MHz to control the intensity of the resonance in the intermediate region. Using the values Lw1 = 2.0 MHz and Lw2 = 1.0 MHz one can more accurately reproduce the experimental modulation spectrum (Fig. 5.22c) as shown in Fig. 6.15.

Basically the same conclusions can be obtained from Figs. 6.2 - 6.6 which were calculated using Eqn. 6.30.

6.4 Calculation of the Effect of a Perpendicular Magnetic Field on the Echo Amplitude

In this section we will calculate the effect of a d.c. field applied perpendicular to the c-axis on the echo amplitude. For this calculation we again use Eqn. 6.29 with η now given by (Eqn. 5.18)

$$\eta = H \sin\theta' \cos\phi$$

where H is the effective applied field given by

$$H = H_o - DM_s \sin(\theta_o)$$

and H_0 is the applied external field, D is the demagnetization factor, M_s is the saturation magnetization and θ_o is the angle the electronic moments in the domains make with respect to the c-axis.

The domain structure of the RCo_5 compounds, as well as hexagonal cobalt, is labyrinth-like rather than of the ideal planar form, as a result of the small in-plane anisotropy. Initially, it was assumed that the spins at the centre of the wall will rotate to be aligned along the direction of the external field. However, the calculated results proved to be entirely inconsistent with experiment, the calculated field dependence being much stronger than that obtained experimentally. The spin rotation is presumably limited by the wall

demagnetizing energy. In these calculations the directions of the spins at the centre of the walls are therefore assumed to be distributed randomly in the basal plane. The evaluation of Eqn. 6.29 now becomes a double integral over ϕ as well as over θ or the frequency. The relationship between θ and the hyperfine field is again assumed to be of the form $\sin^2\theta'$ where the relationship between θ' and θ is given by Eqn. 4.45, and the relationship between the frequency and the hyperfine field is given by $\nu = \gamma_N H_{hf}$.

These calculations were performed using the gate-shaped composite lineshape and the experimentally determined values for $H_\perp$ and $H_{||}$. Figure 6.16 shows the effect on the idealized Co spectrum of a field applied perpendicular to the c-axis. The field shift, η, for this experiment is zero for the domain-wall-edge resonance and is a maximum for the domain-wall-centre. The additional ϕ dependence of η introduces a distribution in the field shift at any given position in the wall which ranges from $+H \sin\theta'$ to $-H \sin\theta'$. The application of an external field results in the redistribution of the resonant frequencies in the wall and a corresponding change in the shape of the spectrum as illustrated in Fig. 6.16 (b), (c), and (d). This calculation assumed that nuclei shifted into resonance by the field contribute to the detected signal to the same extent as the nuclei that were at resonance at zero field. However, these nuclei lie in a different part of the domain wall and therefore may have a different enhancement factor, and accordingly may not have the optimum tuning conditions (90° - 180° pulses). Figure 6.16 shows an increase in amplitude of the DWE resonance as well as a shift of a portion of the DWC resonance to higher

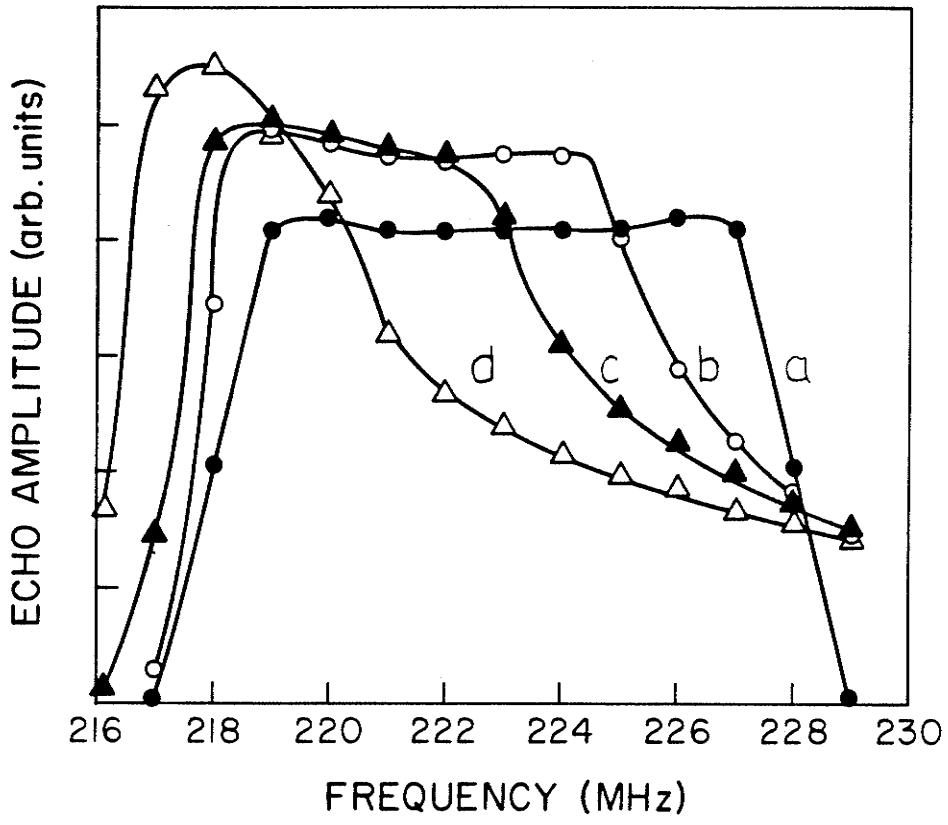

Fig. 6.16 The effect on the Co spectrum of a field applied perpendicular to the c-axis. A gate-shaped distribution in the hyperfine field is assumed with Lw1 = Lw2 = 0 and H_1 = 1.0 kOe. The spectrum is calculated for an applied field of H_o = 0 (a), 6 kOe (b), 10 kOe (c) and 16 kOe (d).

frequencies. Figure 6.17 (a), curve (a), shows the predicted increase in the echo amplitude with field at 218 MHz. An examination of curve (a) in Fig. 5.17 shows that this effect is not observed experimentally, presumably because the shifted nuclei do not satisfy the optimum tuning condition.

In order to account for this effect in our calculation we must make the r.f. field and the turn angles dependent on the angle θ. We therefore introduce into Eqn. 6.29 the following relationships:

$$\begin{aligned} H_1 &= H_1^D \ (1 + \Delta\eta \sin(\theta))/(1+\Delta\eta \sin\theta_1) \\ \phi_1 &= (\pi/2) \ (1 + \Delta\eta \sin\theta)/(1 + \Delta\eta \sin\theta_1) \\ \phi_2 &= (\pi) \ (1 + \Delta\eta \sin\theta)/(1 + \Delta\eta \sin\theta_1) \end{aligned} \qquad (6.32)$$

where H_1^D is the enhanced r.f. field at resonance and $\Delta\eta$ is the factor by which the enhancement factor varies through the domain wall which Cobb et al report as approximately 10 in $CrBr_3$ (8). The angle θ_1 is the angle the electronic spins of the particular spin packet considered in the integration makes with respect to the c-axis.

Figure 6.17 (a), curve (b), shows the results of this calculation for the field dependence of the echo amplitude at the wall edge. Figure 6.18, curve (c), shows the corresponding result on the spectrum. Curve "b" in this figure is the zero field spectrum and curve "a" is the spectrum with a field of 6 kOe applied perpendicular to the c-axis. For these calculations we used a value of $\Delta\eta$ of twelve to suppress the increase of the echo amplitude with field at the wall edge.

The experimental data in Fig. 5.17, in fact, shows a decrease

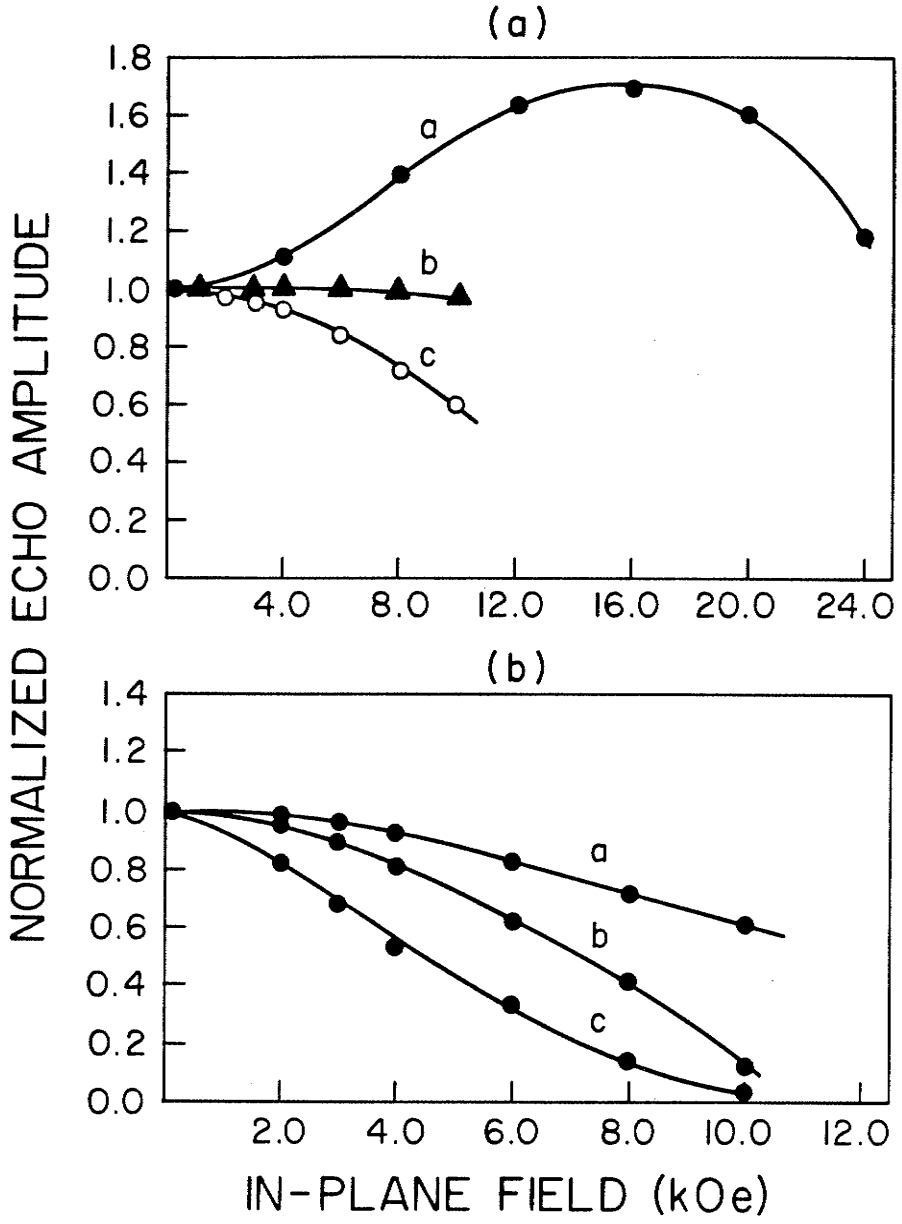

Fig. 6.17 a) The normalized echo amplitude calculated for the wall edge resonance of cobalt (frequency of 218 MHz) as a function of the perpendicular field. Curve (a) shows an initial increase in echo amplitude with the applied field. Curve (b) uses a position dependent transverse enhancement factor to suppress this increase, $\Delta\eta = 12$, and curve (c) uses a field dependent enhancement factor to further decrease the echo amplitude.

b) The normalized echo amplitude versus perpendicular field for Co calculated at a frequency (a) 218 MHz, (b) 224 MHz and (c) 228 MHz. The transverse enhancement factor is assumed to vary through the domain-wall with $\Delta\eta = 12$ and a field dependent enhancement factor is also used. These calculated results are to be compared to the experimental results of Fig. 5.17.

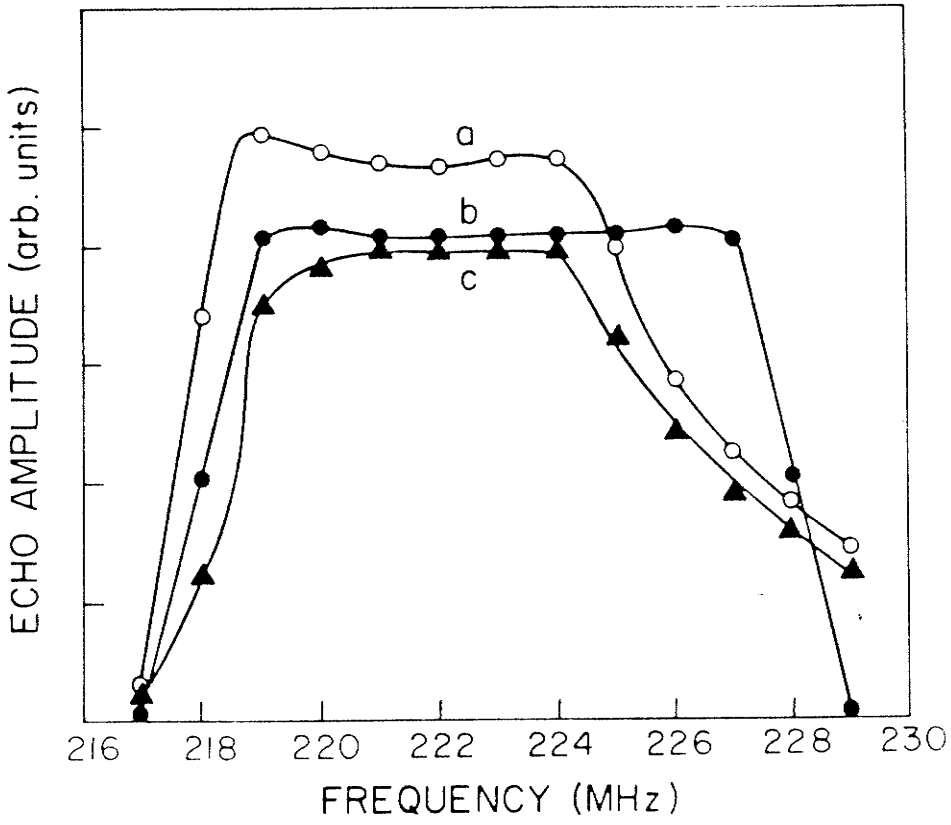

Fig. 6.18 The effect of a distribution of enhancement factors on the field dependence of the Co spectrum. Curve (b) is the zero-field spectrum, curve (a) is the calculated spectrum for H_o = 6 kOe (curve (b) in Fig. 6.16) and curve (c) includes the effect of a distribution of enhancement factors at H_o = 6 kOe.

in echo amplitude with applied field at the wall edge. This could not be accounted for by the above effect for reasonable values of $\Delta\eta$ and we were forced to introduce a field dependence of the enhancement factor to reproduce the experimental results.

Muller and Sher (9) have examined the effect on the enhancement factor of a d.c. field applied perpendicular to the easy axis. In the uniform wall approximation they obtained the following expression for the enhancement factor

$$\eta = \frac{1}{\sqrt{2}\sin\phi_o} = \frac{H_{hf}}{4\pi M_s}\frac{D}{\delta_o}\left(1 + 2\cos^2\phi_o - \frac{3\sin(2\phi_o)}{2\phi_o}\right)^{\frac{1}{2}} \qquad (6.33)$$

Here all variables represent the same parameters as before and $\phi_o = M_s H_o / 2K_1$ where M_s is the saturation magnetization, H_o is the external field and K_1 is the anisotropy constant. The application of an external field therefore changes the r.f. enhancement factor by a factor

$$\frac{\eta(H)}{\eta(o)} = \frac{1}{\sin\phi_o}\left(1 + 2\cos^2\Phi_o - \frac{3\sin(2\phi_o)}{2\phi_o}\right)^{\frac{1}{2}} \qquad (6.34)$$

We therefore are required to multiply the H_1, ϕ_1 and ϕ_2 in Eqn. 6.32 by the additional factor given by Eqn. 6.34 and introduce this into Eqn. 6.29.

Figure 6.17 (a), curve (c), shows the calculated spin-echo amplitude for the domain-wall-edge resonance which is now seen to decrease monotonically with increasing field. Figure 6.19 shows the resulting effect of the field dependence of the enhancement factor on the spectrum, for external fields of 0, 6 kOe, 10 kOe and 16 kOe.

We are now at a stage where we can attempt to reproduce some of

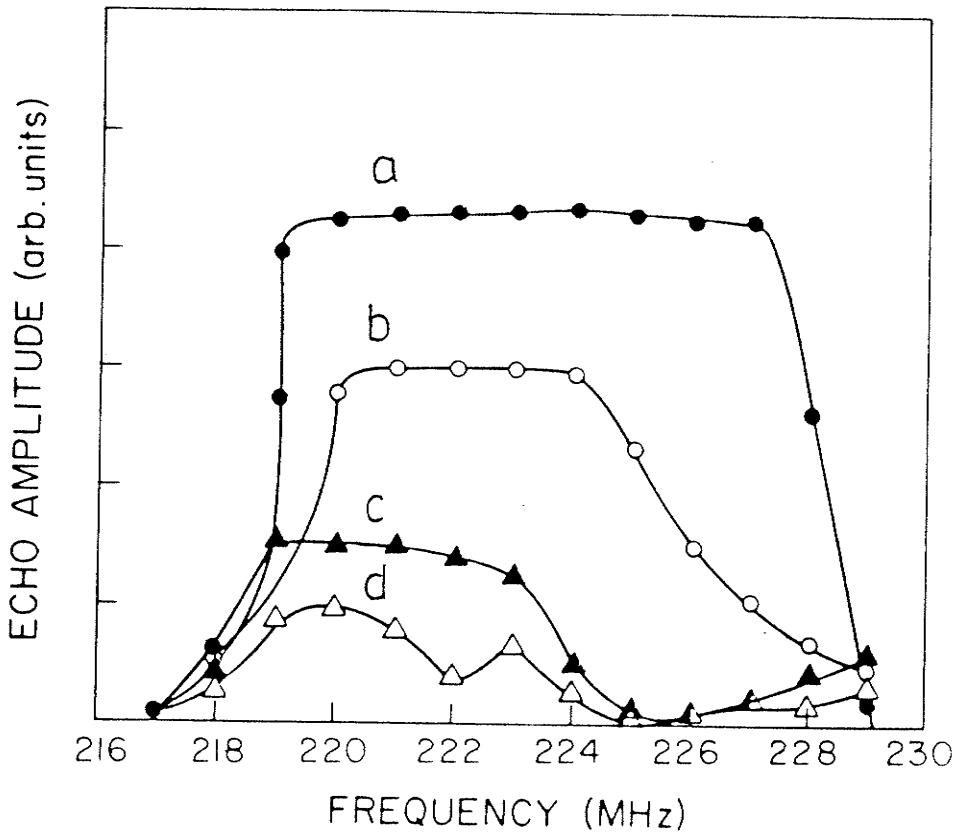

Fig. 6.19 The effect of the field dependence of the enhancement factor on the Co spectrum for perpendicular fields of (a) 0 kOe, (b) 6 kOe, (c) 10 kOe and (d) 16 kOe. To be compared to the behaviour illustrated in Figs. 6.16 and 6.18.

our experimental results. Figure 6.17 (b) shows the calculated field dependence of the echo amplitude for hexagonal cobalt at 218, 224 and 228 MHz using $\Delta\eta = 12$ and including the field dependence of the transverse enhancement factor. A comparison with the experimental results in Fig. 5.17 shows good agreement. We therefore feel that we have not only developed a technique which can distinguish between DWE and DWC NMR resonances in materials with a large anisotropy in the hyperfine field but we have also isolated the dominant effects which influence the quantitative results obtained from this experiment.

In the application of this form of calculation to the RCo_5 compounds two observations can first be made. Since all the compounds we have examined have an extremely large anisotropy constant the demagnetizing field will be negligible and the internal field, H, will approximately equal the applied field, H_o. Secondly, as a result of large anisotropy constant, K_1; $\phi_o = M_s H_o / 2K_1$ will also be negligible and the factor describing the field dependence of the transverse enhancement factor will be approximately one and can also be neglected.

Figure 6.20 shows the calculated frequency dependence of the echo amplitude reduction ratio, A_o/A_H for YCo_5 for an applied field of H_o = 9 kOe. Comparison with the experimental data in Fig. 5.20 indicates good agreement. In the calculation the values for the position of the wall edge and centre resonances were taken as they were identified in the previous section and the value of $\Delta\eta$ used was $\Delta\eta = 12$. A similar calculation for $SmCo_5$ again produced good results using a $\Delta\eta$ of 12 and identifying the centre resonance at 195 MHz with the edge

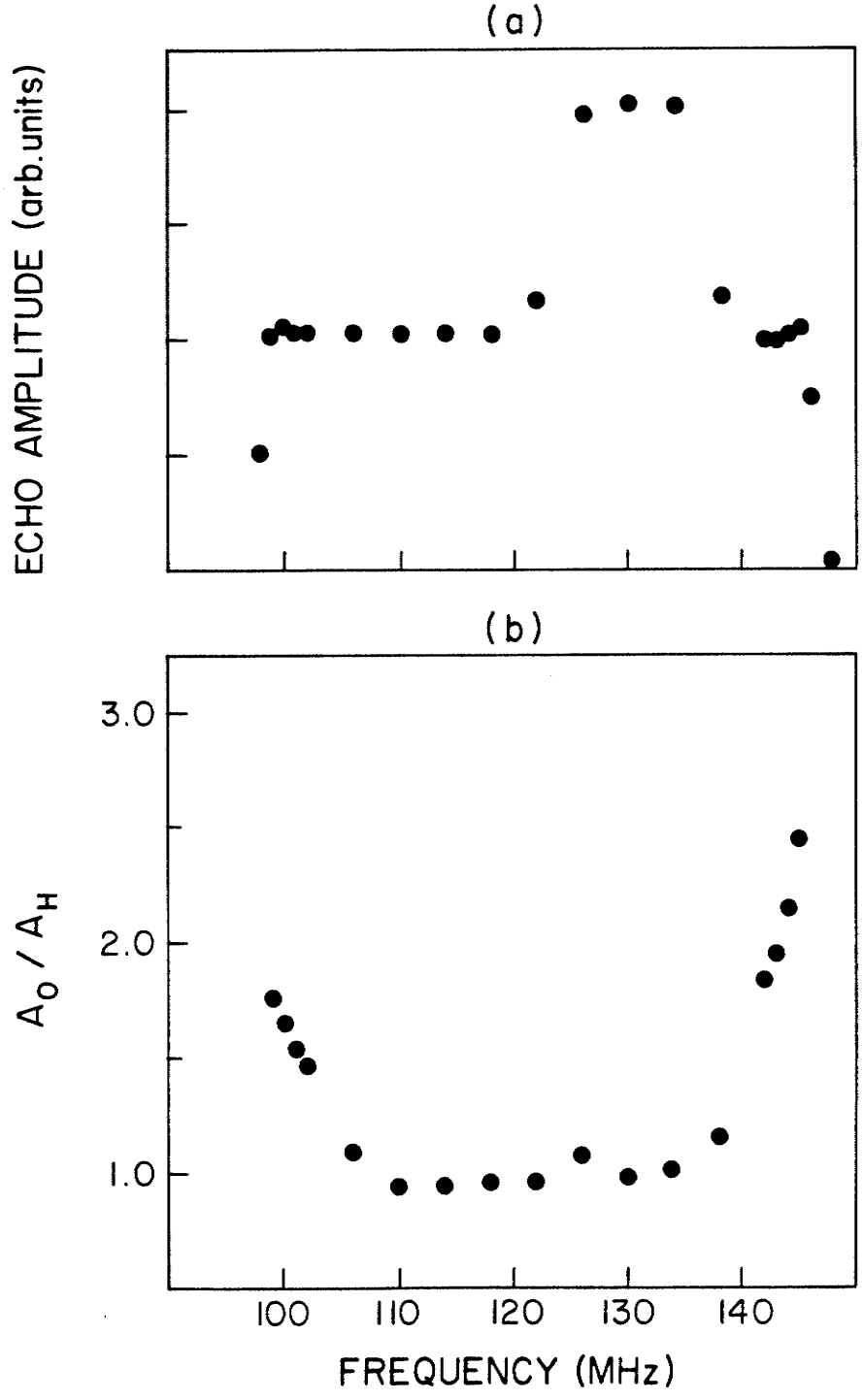

Fig. 6.20 The calculated frequency dependence of the echo amplitude reduction ratio, A_O/A_H, for YCo_5 for a perpendicular field of 9 kOe. The values of the parameters used in the calculation are Lw1 = Lw2 = 0.0, H_1 = 1.0, $\Delta\eta$ = 12 and we locate $H_\perp(2)$ = 146 MHz, $H_{//}(2)$ = 122, $H_\perp(1)$ = 98 and $H_{//}(1)$ = 138.

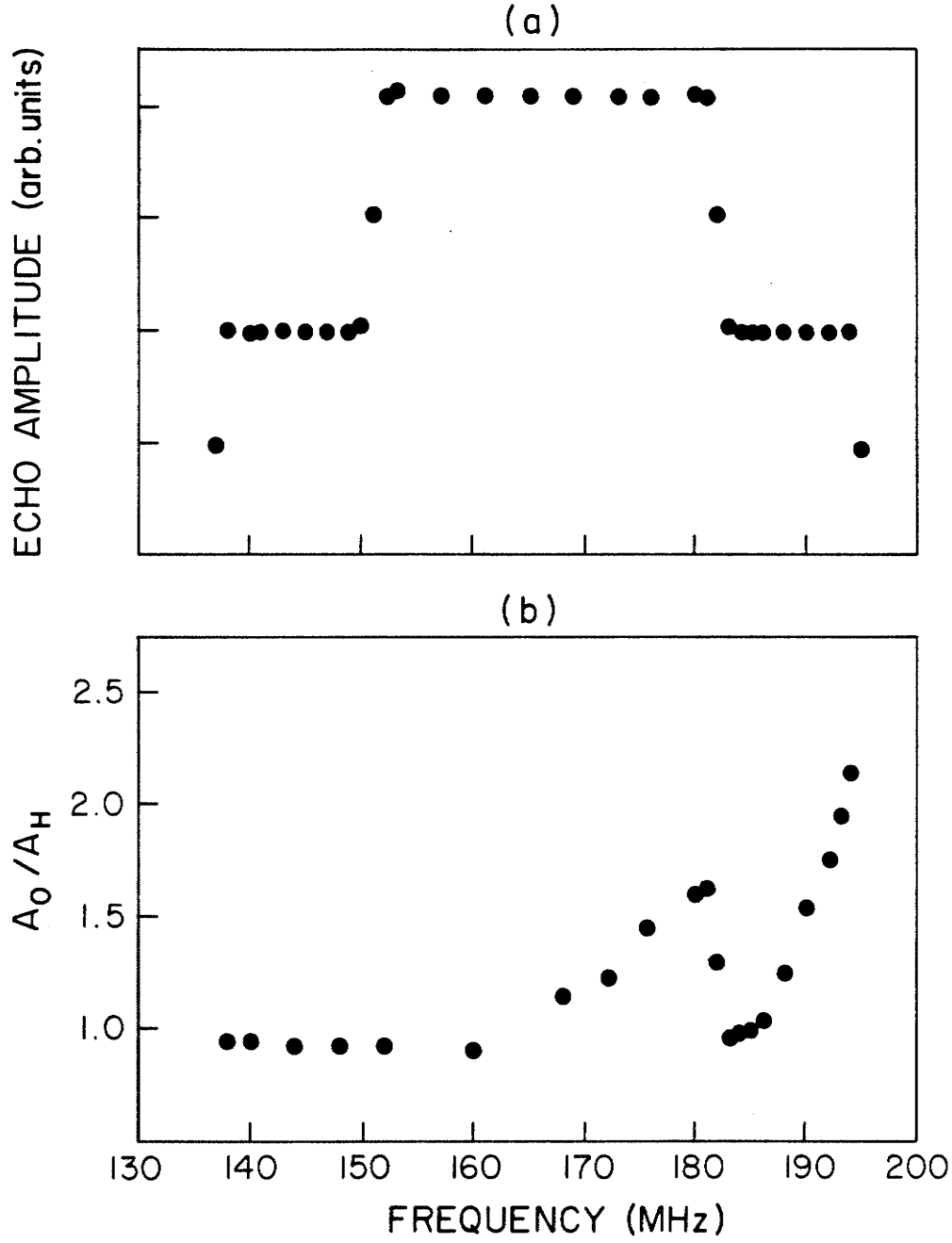

Fig. 6.21 The calculated frequency dependence of the echo amplitude reduction ratio, A_O/A_H, for $SmCo_5$ for a perpendicular field of 9 kOe. The values of the parameters used in the calculation are Lw1 = Lw2 = 0.0, H_1 = 1.0 and $\Delta\eta$ = 12 and we locate $H_\perp(2)$ = 195 MHz, $H_{//}(2)$ = 151, $H_\perp(1)$ = 182 and $H_{//}(1)$ = 137.

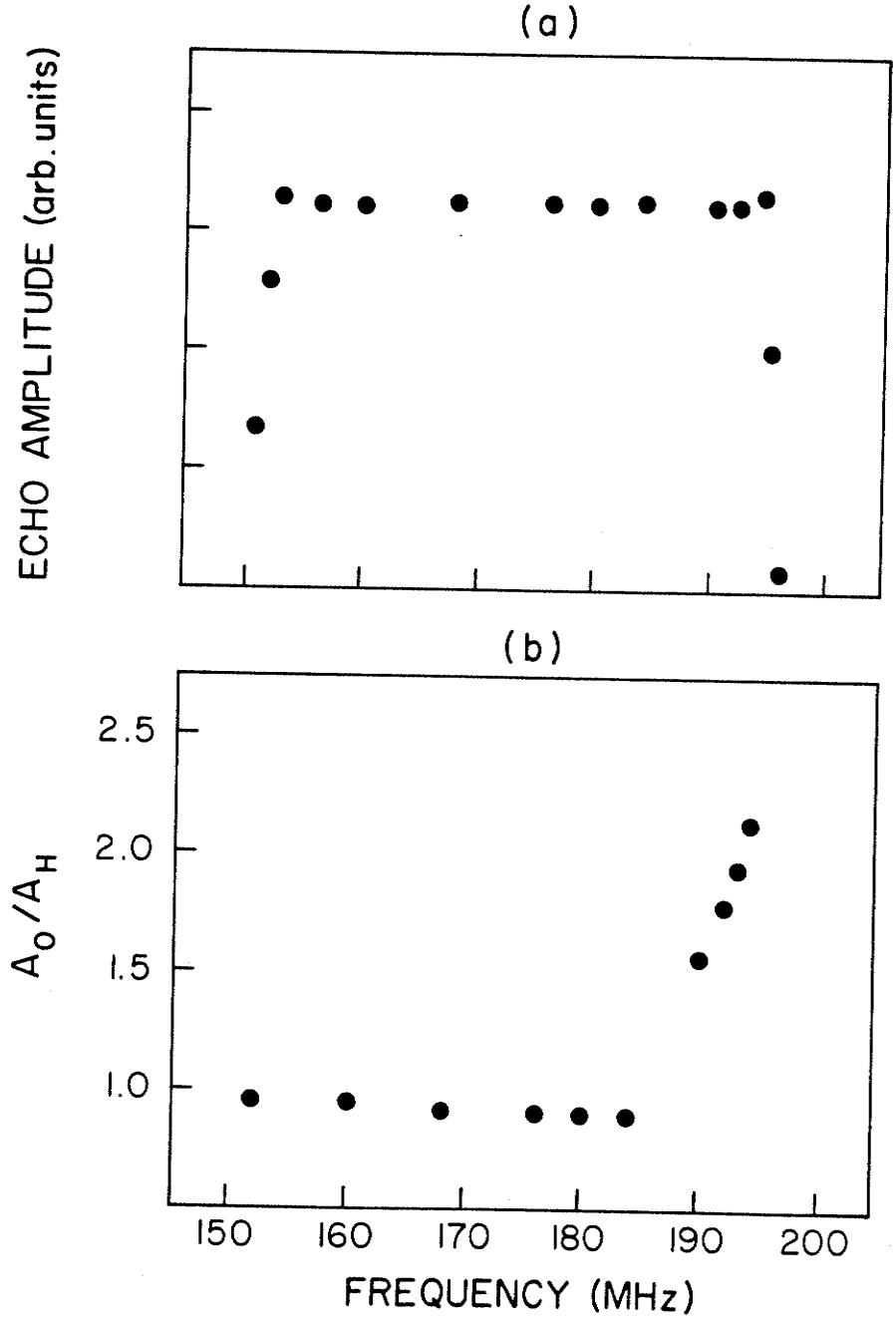

Fig. 6.22 The calculated frequency dependence of the echo amplitude reduction ratio, A_o/A_H, for the individual site in $SmCo_5$ for which we identify $H_\perp$ = 195 MHz and $H_{//}$ = 151. We use the same parameter values as for Fig. 6.21.

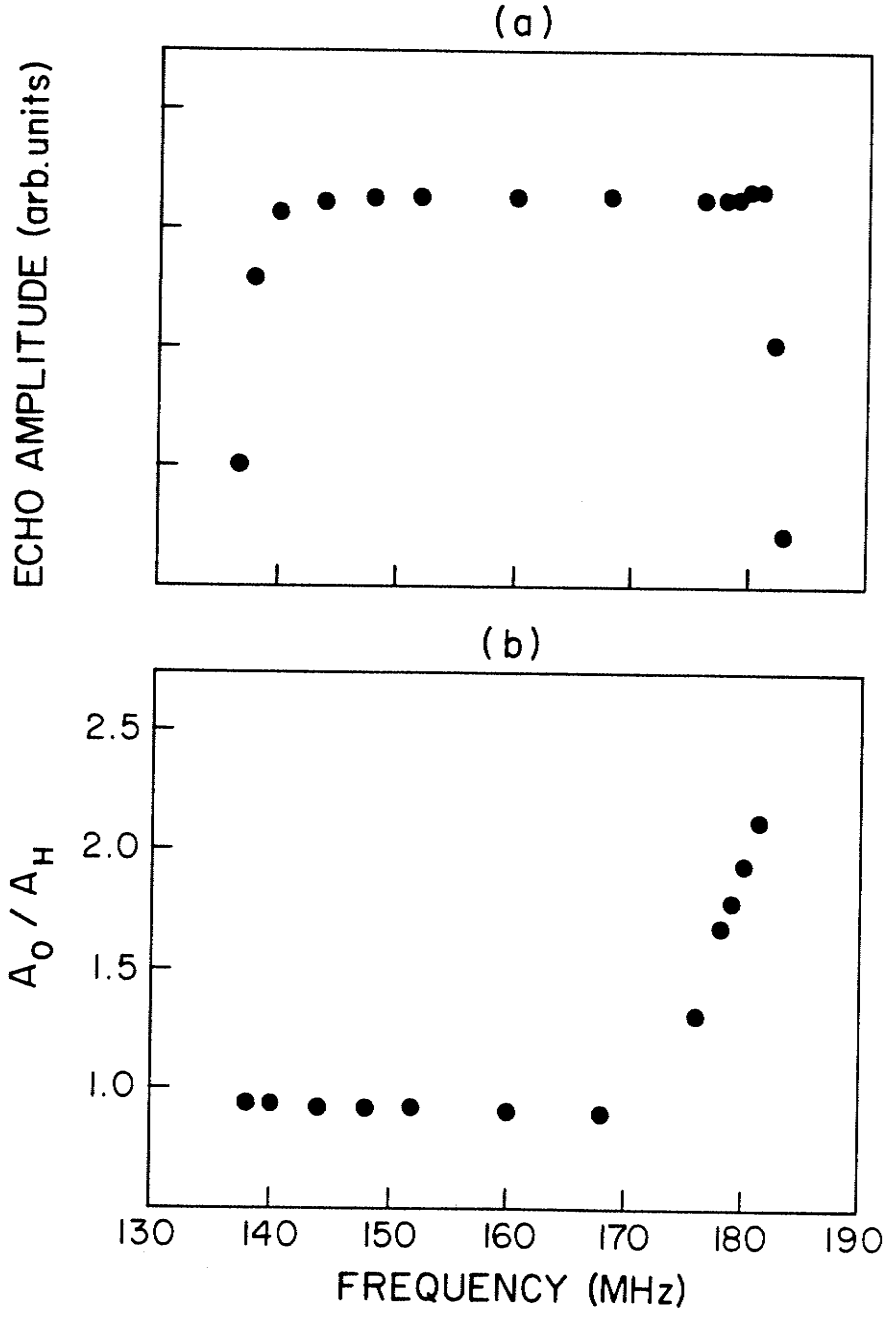

Fig. 6.23 The calculated frequency dependence of the echo emplitude reduction ratio, A_O/A_H, for the individual site in $SmCo_5$ for which we identify $H_\perp$ = 182 MHz and $H_{//}$ = 137. We use the same parameter values as for Fig. 6.21.

resonance at 151 MHz and the centre resonance at 182 MHz with the edge resonance at 137 MHz as was tentatively done in the previous section. Figure 6.21 shows these results while Figs. 6.22 and 6.23 give the calculated results for each site individually. Clearly the overall results are a type of weighted sum of the results obtained from the individual sites.

6.5 The Discrete-Wall Model and the Hyperfine Field Distribution within the Domain Wall

In chapter five (sec. 3) we commented on the generally small intensity of the NMR signal that we observed from the Co sub-lattice of the RCo_5 compounds. We will elaborate on this difficulty to a greater extent in a later section of this chapter, but at this time we will examine the relative strengths of the peaks observed in our spectra in order to see if a consistent interpretation can be found for the details of the spectra. Of course, as the spectra are extremely broad and smooth, the most obvious "detail" is the relative intensity of the DWE and DWC resonance peaks. Other details of interest are the frequency dependence of the depth of quadrupole modulation, the nature of the apparently extremely large longitudinal enhancement factors we measured in our modulation experiment, and of particular interest, because this is the quantity that is probably most directly related to the Co sub-lattice contribution to the magneto-crystalline anisotropy, is not only the total anisotropy in the hyperfine field at the two Co sites but also the sign of the anisotropy in the hyperfine field.

Figures 5.22 - 5.26 showed a summary of the results obtained for

the Co resonance in the RCo_5 compounds. In these figures we have also identified the DWE and DWC resonance peaks. From this identification it is apparent that the DWC resonance peak is not necessarily greater than the DWE peak as is generally assumed for domain wall NMR resonances. This is the case for YCo_5 but for $SmCo_5$ all resonance peaks are approximately of the same magnitude and for $GdCo_5$ the low frequency domain-wall-edge peak is considerably larger than the corresponding centre resonance. For hexagonal Co the DWC resonance is also much greater than the barely detectable DWE resonance.

In order to investigate these details it is necessary to consider a more realistic model for the wall structure than the simple continuous wall assumed up till now. For this discussion we will use a discrete wall structure. However, before we proceed it is worthwhile to first comment on the deficiencies of our earlier models.

Clearly, our simple gate-shaped spectrum will not be very successful in explaining the details we are now concerned with. The continuous wall model which assumes an explicit $\sin^2\theta'$ dependence of the hyperfine field through the domain wall shows well-defined peaks of differing amplitudes for the DWC and DWE resonances for a given site. A $\sin^2\theta$ dependence of the hyperfine field would result in domain-wall-edge and domain-wall-centre resonance peaks of equal magnitude. However, the existence of an anisotropy in the hyperfine field results in a deviation of the direction of the hyperfine field from the direction of the local spin. This deviation is given by Eqn. 4.45 where it is assumed that the hyperfine coupling constants $A_{//}$ and $A_{\perp}$ are independent of angle. We have

$$\tan \theta' = H_{\perp}/H_{||} \quad \tan \theta$$

where θ' is the angle the hyperfine field makes with respect to the c-axis and θ is the angle the spin makes with respect to the c-axis. An examination of this equation indicates that the hyperfine field vector is colinear with the electronic spin at $\theta = 0$ and $\pi/2$, i.e.: at the domain-wall-edge and at the domain-wall-centre. In between the hyperfine field vector will lag behind the spin if $H_{\perp} < H_{||}$ and lead the spin if $H_{||} < H_{\perp}$. Within the uniform rotation model, if the hyperfine field vector lags behind the spin, the DWE peak will be greater than the DWC peak, and if the hyperfine field leads the spin the DWC peak will be largest. Comparing this with the corresponding sign of the anisotropy in the hyperfine field (i.e. whether $H_{\perp} < H_{||}$ or $H_{||} < H_{\perp}$) indicates that inherently the higher frequency peak, whether it is of the DWE or DWC type, will be of largest amplitude. A comparison with the experimental results shows that this is not the dominant effect influencing the relative amplitude of the peaks observed in our spectra, as several definite contradictions are observed. For example, the low frequency peak in the Co^{59} spectrum of YCo_5 is a DWC resonance and the corresponding DWE peak lies at higher frequency but is not resolved in our spectrum.

At this point the possibility was investigated that the discrepancy we observed in the longitudinal enhancement was the result of the non-colinear rotation of the hyperfine field and the electronic spins. As the hyperfine field and the electronic spins must be colinear at $\theta = 0$ and $\pi/2$, if the hyperfine field initially lags the spin as one enters the wall it must at some point rotate faster than the spin in

order to catch up at $\theta = \pi/2$. For a $\sin^2\theta'$ variation of the hyperfine field the resulting change in the hyperfine field as a result of a spin rotation of $\Delta\theta$ and a rotation of the hyperfine field of $\Delta\theta'$ is given by

$$\Delta H_a = H_a \, \Delta\theta' \sin(2\theta') \tag{6.35}$$

The required value of ΔH_a to produce the observed modulation can be obtained from Table 5.2 and the required value of $\Delta\theta'$ can then be calculated. Table 6.1 shows a list of the rotation angle that would be required to generate the magnitude of the longitudinal modulating field we have observed. Also shown is the value of $\Delta\theta$ using the values of the wall displacements given in Table 5.3 and assuming a uniform wall rotation so that

$$\Delta\theta = \frac{\pi\Delta x}{\delta} \tag{6.36}$$

Also shown in the table is a listing of $d\theta'/d\theta$ at various positions in the domain wall for hexagonal cobalt. This list shows that, using the experimentally obtained values for $H_\perp$ and $H_{//}$, the hyperfine field vector rotates at a maximum of approximately 4 per cent faster than the electronic spins and at the position in the wall where the spin rotates most rapidly (i.e. at $\theta = 45^o$) the hyperfine field vector is rotating at approximately the same rate. Therefore, this can in no way account for the quantitative results we obtained in our modulation experiments.

The discrete wall models that we considered consisted of N atomic layers within the domain wall where N is simply given by the domain wall thickness for the material in question devided by the lattice spacing. As a result of the inverse dependence of the transverse enhancement factor and the spin density on the rate of

TABLE 6.1

SAMPLE	$\Delta\theta'$ (req'd)	$\Delta\theta$	θ (rad)	$d\theta'/d\theta$
hex. Co	3.46°	1.01°	0.157	1.043
			0.314	1.037
Y Co_5	1.13	0.05°	0.471	1.026
	1.69		0.628	
Sm Co_5	0.70	0.016°	0.785	
	0.57		0.942	0.985
Gd Co_5	2.61	6.68°	1.100	
	1.74		1.257	0.964
	3.66		1.413	0.958
			1.571	

electronic spin rotation in the wall we consider the domain wall to consist of N atomic layers with spins that effectively rotate at a uniform rate. Therefore the angle, θ_n, that the layer makes with respect to the c-axis is (n-1)/(N-1) X $\pi/2$ and the effective r.f. field seen by the nuclei is given by

$$H_1 = H_1^D (1 + \Delta\eta \sin \theta_n) \tag{6.37}$$

The turn angles that are produced by the two r.f. pulses are now more generally given by

$$\begin{aligned} \phi_1 &= 2\pi H_1 t_1 \\ \phi_2 &= 2\pi H_1 t_2 \end{aligned} \tag{6.38}$$

To calculate the echo amplitude we continue to use Eqn. 6.29 with the only significant change in the calculation being in the nature of F(x). The composite lineshape now consists of the sum of N locally produced lineshapes resulting from the N atomic layers and shifted with respect to one another due to the anisotropy in the hyperfine field. We may also associate with each atomic layer in the wall a local lineshape and a corresponding angular dependent linewidth of the form given in Eqn. 4.43.

$$\Delta = \Delta_d + \delta \sin\theta_n$$

where Δ_d is the linewidth in the domain and δ is the variation in the linewidth through the wall. We assume for the local lineshape a Lorentzian distribution of the form

$$\frac{\Delta}{\Delta^2 + (\nu - \nu')^2}$$

where ν' is the mean resonance frequency for the nth layer which is a function of the hyperfine field distribution in the domain wall and ν is the variable of integration. To include also the quadrupolar splitting

we associate with each atomic layer in the wall a total of 2I lines separated by the quadrupolar splitting which is incorporated into the value of ν as given by Eqn. 4.48. The evaluation of Eqn. 6.29 now involves the double sum over the 2I lines associated with each of the N layers as well as an integration over x, the deviation of ν from the frequency of the r.f. field.

In chapter five (sec. 9) it was suggested that there was no obvious reason to assume that the angular distribution of the hyperfine field in a domain wall is identitical to that in a fully saturated ferromagnet. The $\sin^2\theta$ relationship has been confirmed for the domain-wall-edge Cr^{53} resonance in $CrBr_3$ by Cobb et al (8) and for the domain-wall-edge resonance in hexagonal cobalt by Enokiya (10). However, these measurements were done by applying a d.c. field perpendicular to the c-axis and measuring the field dependence of the domain-wall-edge resonance frequency. These results may, therefore, be more characteristic of the domain than of the domain wall. Fekete et al (11) have confirmed this angular dependence in a fully saturated sample of hexagonal cobalt. Enokiya also observed the angular dependence of the quadrupole splitting for the domain-wall-edge resonance using the echo decay envelope modulation relationship established by Abe et al (12). However, they noticed a significant deviation from the expected $(3\cos^2\theta' - 1)$ dependence given by Eqn. 4.32 in the high angle range. This deviation was attributed to either a dependence of the principal value of the EFG on θ or an asymmetry of the EFG resulting from a change in the 3d charge distribution due to the spin-orbit interaction. Enokiya favoured the latter explanation and consequently

considered the following expression for the quadrupole splitting in the presence of a deviation from axial symmetry of the EFG tensor (13).

$$\Delta\nu = \frac{\nu_q}{2} \quad (3\cos^2\theta' - 1 - \zeta \sin^2\theta' \cos 2\phi') \qquad (6.39)$$

where θ' and ϕ' are the polar angles defining the direction of the hyperfine field in the frame of the principal axes of the EFG tensor, the z-axis of which is along the c-axis; and $\zeta = (V_{xx}-V_{yy})/V_{zz}$ is the asymmetry parameter as was defined in Eqn. 4.47. Enokiya obtained a good fit to the data using a value of the asymmetry parameter $\zeta \sim 0.5$ which appeared to be rather large and presumably is the result of the nearly spherical charge distribution in hexagonal cobalt. A small asymmetry in the charge distribution could then result in a large value of ζ. A similar variation of the EFG due to the electronic spin rotation was observed in hexagonal MnBi by Hihara and Koi (14). Hihara and Koi observed the temperature dependence of the domain-wall-edge quadrupole splitting taking advantage of the rotation of the magnetic moments in the domain from along the c-axis to a direction within the basal plane. They observed a quadrupole splitting of 2.1 MHz at 140 K which decreased to approximately 1.2 MHz, below 90 K at which temperature the spins have rotated into the basal plane. The quadrupole splitting compares favourably with the domain-wall-centre value observed above 140 K. However, the splitting does not pass through zero and therefore these results represent an extremely large distortion from the $(3\cos^2\theta' - 1)$ angular dependence that might be expected. Alternatively if we take the quadrupole splitting as a quantity which can be used to determine the angle between the hyperfine field and the

c-axis we obtain $\theta' \sim 30^{\circ}$ for nuclei at the centre of the domain wall. The hyperfine field therefore would take an extremely large angle with respect to the electronic spins in the basal plane. This, however, is inconsistent with uniaxial symmetry which would require that, at least for $\theta = 0$ and $\pi/2$, the hyperfine field and the direction of the electronic spins be colinear. Therefore a more likely explanation is a large asymmetry in the EFG induced when the spin direction is inclined to the c-axis. A change in the charge distribution of the 3d electrons will be caused by the admixture of the excited states by the spin-orbit interaction.

Fekete et al (11) also observed the angular dependence of the quadrupole splitting and delineated it into an isotropic and an angular dependent term. The angular dependent term took a $(3 \cos^2 \theta' - 1)$ form and was interpreted to arise from a contribution to the field gradient due to the hexagonal lattice. Kawakami et al (15) observed that the quadrupole splitting had a similar temperature dependence as the deviation of the c/a lattice parameter ratio from ideal. Fekete et al observed a similar correlation between the quadrupole splitting and the lattice parameters, and clearly established that the lattice makes a major contribution to the electric field gradient. The isotropic contribution to the electric field gradient mentioned by Fekete was attributed to an exchange splitting of the d electrons which for the nearly spherical charge distribution could be significant. Zevin et al (16) showed that the angular dependence of this term is negligible in hexagonal Co. Fekete et al also established the existence of a relationship between both an isotropic and an angular dependent orbital

angular momentum and the corresponding contribution to the electric field gradient. The orbital angular momentum, therefore, also depends on the exchange polarization of the 3d band. A $(3\cos^2\theta - 1)$ dependence of the orbital angular momentum and therefore also of the orbital contribution to the hyperfine field would lead to the situation where both the DWE and DWC resonance peaks would be of equal amplitude since the entire NMR spectrum would be simply a sum of local field distributions which are themselves symmetrically distributed about $\theta = 0$ and $\pi/2$. The $(3\cos^2\theta - 1)$ dependence observed experimentally (10,11) for the hyperfine field was obtained either for a fully saturated sample or using the domain-wall-edge resonance only, and it seems not unreasonable to expect that the angular dependence in a domain wall would be somewhat different. The local field could change quite abruptly as the electronic spins rotate through the domain wall, possibly the result of a reduction in the effective exchange field seen by a particular Co atom due to the fact that the neighbouring spins are no longer parallel.

If we accept that the exchange field seen by the first few atomic layers in the wall will be basically the same as in the domain, and consequently there will be no change in electronic strucuture for these atoms, then we can explain the variation in the DWE and DWC resonance amplitudes for hexagonal Co as well as the RCo_5 compounds. For hexagonal Co we have a wide domain wall (275 A). If the electronic structure varies rapidly after a few layers, then almost the entire wall will contribute to the DWC resonance. This is, of course, what we found experimentally since the DWE resonance was virtually undetectable. The

RCo_5 compounds have very narrow walls (~50 A or 10-12 atomic layers) and we immediately can foresee the possibility that the DWE resonance may be comparable or even greater in amplitude than the DWC resonance, which is again consistent with our experimental results.

An interesting result, which supports the suggestion that the electronic structure of an atom in a domain wall with a spin at an angle θ with respect to the c-axis is different from an atom in a saturated sample at the same angle, is that we observe no change in the quadrupole splitting throughout the spectra. However, as we are able to observe the corresponding quadrupole modulation only over portions of the spectrum, it is also possible that this region of the spectrum comes from a specific position in the domain wall. Riedi (17) was, however, able to observe the quadrupole modulation through a large portion of the spectrum and did not detect a change in the modulation period. The modulation period observed at all frequencies was 5.5 microsec. which compares favourably to a period of modulation that we observed in a Co crystal of 5.0 microsec. Both these results also agree with the period observed by Fekete in the saturated sample with the spins aligned along the c-axis. The quadrupole splitting through large portions of the domain wall in these materials appears to be strongly influenced by the domains. In particular, for the RCo_5 compounds which are characterized by extremely narrow domain walls and very wide domains (see Table 5.3), it is entirely conceivable that the electronic structure of atoms in the domain wall are strongly influenced by long-range exchange interactions from the domains. In chapter two (sec. 4) we examined in detail the magnetic properties of the RCo_5 compounds

and established that the dominant effects influencing the Co magnetic moment is band filling with electrons contributed by the rare-earth sub-lattice and the influence of the rare-earth-Co exchange interaction on the exchange splitting of the 3d band. The discussion presented in chapter two can therefore be used as supporting evidence for the influence in these metals of long-range exchange interactions with the domains on the magnetic moment of atoms located in the domain wall.

6.6 The Nature of the "Anomalously" large Longitudinal Enhancement Factor

A rapid change in the magnetic moment and therefore the hyperfine field as one enters the wall could explain the very large longitudinal enhancement factor we observed. To investigate this possibility we considered two alternative possibilities for the distribution of the hyperfine field within the framework of our discrete wall model to determine whether this could account for the results of our modulation experiment.

The first possibility considered a frequency distribution within the wall which varied as in Eqn. 6.39. However, the experimental work by Fekete et al (11) using a fully saturated sample, resulted in measured values of the resonance frequencies parallel and perpendicular to the c-axis which were identical to the frequencies that we measured for the domain-wall-edge and domain-wall-centre resonances. A relationship of the type described by Eqn. 6.39 would predict a shift in the resonance frequency of the domain-wall-centre relative to the resonance frequency measured with the sample magnetized in a direction

perpendicular to the c-axis. We therefore considered a field distribution within a discrete domain wall which remained constant at the value of the hyperfine field at the wall edge for a certain number of layers and then decreased exponentially at an adjustable rate to finally attain the experimentally determined value of $H_{\perp}$ at the domain-wall-centre. We have

$$H_{hf} = H_{||} \qquad x \leq x_1$$
$$H_{hf} = H_{||} + H_a\,[1 - \exp(-x/x_o)] \qquad x > x_1 \qquad (6.40)$$

Figure 6.24(a) shows the calculated spectrum for the first atomic layer within a domain wall in hexagonal cobalt. Because of the extremely small value of the quadrupole splitting in cobalt, which has a value of 0.2 MHz as calculated from the quadrupole modulation, the quadrupole splitting can only be resolved for sufficiently small values of the local linewidth, Δ_d, and the r.f. field H_1. It was concluded in chapter five (sec. 10) that the depth of the quadrupole modulation should be a minimum whenever the NMR spectrum has a peak and should have a maximum wherever our applied field modulation experiment shows a minimum (maximum longitudinal enhancement factor). Figure 6.24(b) shows the calculated spectrum for hexagonal Co using our discrete wall model and assuming an exponential variation of the hyperfine field through the wall. We attempted to resolve the quadrupole splitting in an actual calculation of the Co spectrum by adjusting the values of the local linewidth and the r.f. field. However, using the experimentally determined values for $H_{||}$ and $H_{\perp}$ we were unable to resolve any structure

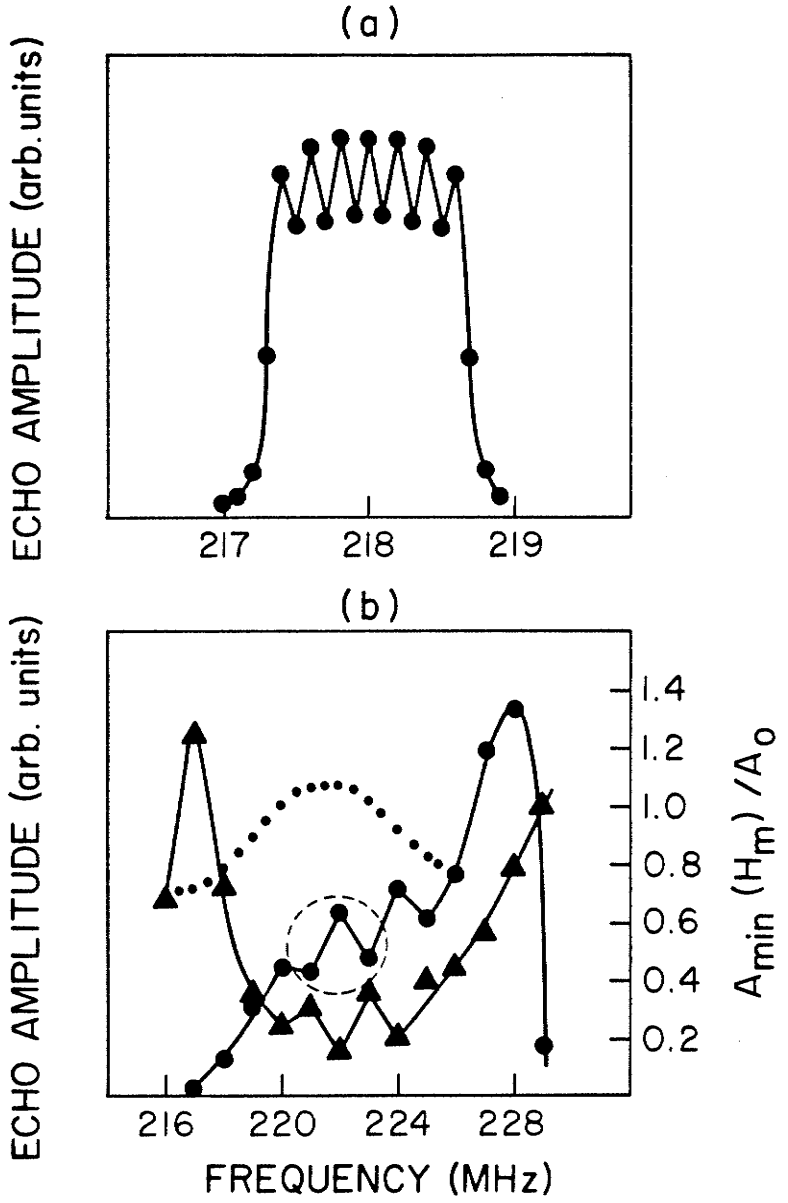

Fig. 6.24 a) The calculated spectrum for a single atomic layer within a domain wall. The parameter values are Δ_d = 0.05 MHz, τ_m = 5.0 μsec., H_1 = 0.1 kOe, t_1 = 2.5 μsec. and t_2 = 5.0 μsec.

b) The calculated spectrum for hcp Co ● assuming an exponential variation of the hyperfine field through the wall. The parameter values are the same as in (a) with, in addition η_o = 1.0, x_o = 2 and x_1 = 1. An enlargement of the peak enclosed in a dashed circle is shown in the inset. Also shown is the calculated modulation spectrum ▲ .

for reasonable values of Δ_d and H_1 and for reasonable values of x_o, the distance over which the hyperfine field will change by 63% of the total anisotropy in the hyperfine field. Using values of Δ_d and H_1 small enough to resolve the quadrupole splitting for a single layer we were still unable to resolve this splitting in the composite lineshape, and no structure appeared unless the width of the domain wall was reduced to twenty atomic layers. The structure that appears in Fig. 6.24(b) represents only the individual atomic layers which become visible for the values chosen for Δ_d, H_1 and x_o. The inset in Fig. 6.24(b) shows in detail one of the peaks arising from an atomic layer from which it can be seen that the quadrupole splitting remains obscured. The calculation illustrates, however, that the resolution of the hyperfine structure including the quadrupole splitting should be greatest where the rate of change of the hyperfine field is largest.

The field shift produced by a wall shift Δx for this type of hyperfine field distribution is given by

$$\Delta H_{hf} = \frac{H_a}{x_o} \exp[- x/x_o] \Delta x$$
$$= \eta_o \exp[- x/x_o] \qquad (6.41)$$

Figure 6.24(b) was calculated with an x_o of two and an x_1 of two, in units of lattice spacings. Also shown in Fig. 6.24(b) is the modulation spectrum calculated assuming

$$\eta_o = \frac{H_a}{x_o} \times \Delta x = 1.0$$

The frequency dependence of the depth of modulation is well-pronounced,

and Fig. 6.24(b) illustrates the relationship between the resolution of structure in the spectrum, and therefore the quadrupole splitting and the rate of change of the hyperfine field as predicted by our model. The resolution of the quadrupole splitting and the observation of the quadrupole modulation of the spin-echo decay envelope, which is what we have observed experimentally, are directly related.

Table 6.2 shows the calculated "skin depth" for the variation of the hyperfine field as one enters the domain wall from the edge in units of the lattice spacing, a. In this calculation we have used the wall displacement Δx which was calculated from our measured susceptibility, and the values of the total anisotropy in the hyperfine field at the Co sites were obtained from our identification of the resonance peaks in the NMR spectra. Of particular interest are the values of x_o/a for YCo_5 and $SmCo_5$. The required values of x_o to account for our observed longitudinal enhancement for these samples would be substantially less than one lattice spacing. It seems unlikely that the effect of the domains on the variation of the hyperfine field in the wall would be constant over several atomic layers and change abruptly over a distance less than a lattice spacing. This would be the situation for $SmCo_5$ which shows domain-wall-edge resonance peaks of comparable amplitude to the domain-wall-centre peaks. Also in this situation it is unclear whether there would be sufficient numbers of atoms located in this very small region of the wall to produce the pronounced reductions in the echo amplitude we observed in our experiments. Too large an r.f. field may also affect the echo amplitude reduction, not only as a result of the reduction in $\gamma_1 = h/H_1$

TABLE 6.2

SAMPLE	H_a (kOe)	Δx (Å)	$h=\Delta H_{hf}$(Oe)	X_o/a
hex. Co	+ 10	1.97	604	
$Y Co_5$	+ 25	1.51×10^{-2}	792	0.19
	− 39			0.30
$Sm Co_5$	+ 45	4.44×10^{-3}	549	0.15
	+ 44			0.14
$Gd Co_5$	− 10	2.23	818	
	+ 18			

upon which the depth of modulation depends, but also as a result of the larger off-resonance contribution from the domain-wall-centre to the signal. As the maximum depth of modulation is located between the DWE and DWC peaks in a region of relatively low intensity, a contribution to the signal from a region in the wall that has a low modulation will decrease the overall effect. This is illustrated in Fig. 6.25(b) for which an H_1 of 2 kOe was assumed.

Figure 6.25(a) shows the calculated spectrum with $x_1 = 4$ and $x_o = 2$, illustrating the situation in which the DWE and the DWC resonance peaks would be of comparable amplitude. For this spectrum we used $\Delta_d = 0.5$ which was sufficiently large to obscure all detail of the discrete structure of the wall.

We therefore must conclude that although the "exchange polarization" of the narrow domain walls by the domains may occur and may, in fact, account for the systematics of the NMR spectra obtained in these materials, it is unlikely that the "anomalous" magnitude of the longitudinal enhancement effect that we have observed is an indication that this is occurring. Before our enhanced modulation of the spin-echo decay envelope measurement will be applicable not only to the location of DWE and DWC resonances, but also to the study of the hyperfine distribution in the wall, it will be necessary to account for the magnitude of the observed enhancement. In order to do so we examined the details of this experiment and eventually came to the conclusion that the large discrepancy between the calculated and measured longitudinal enhancement factor was most likely related to the value used for the susceptibility.

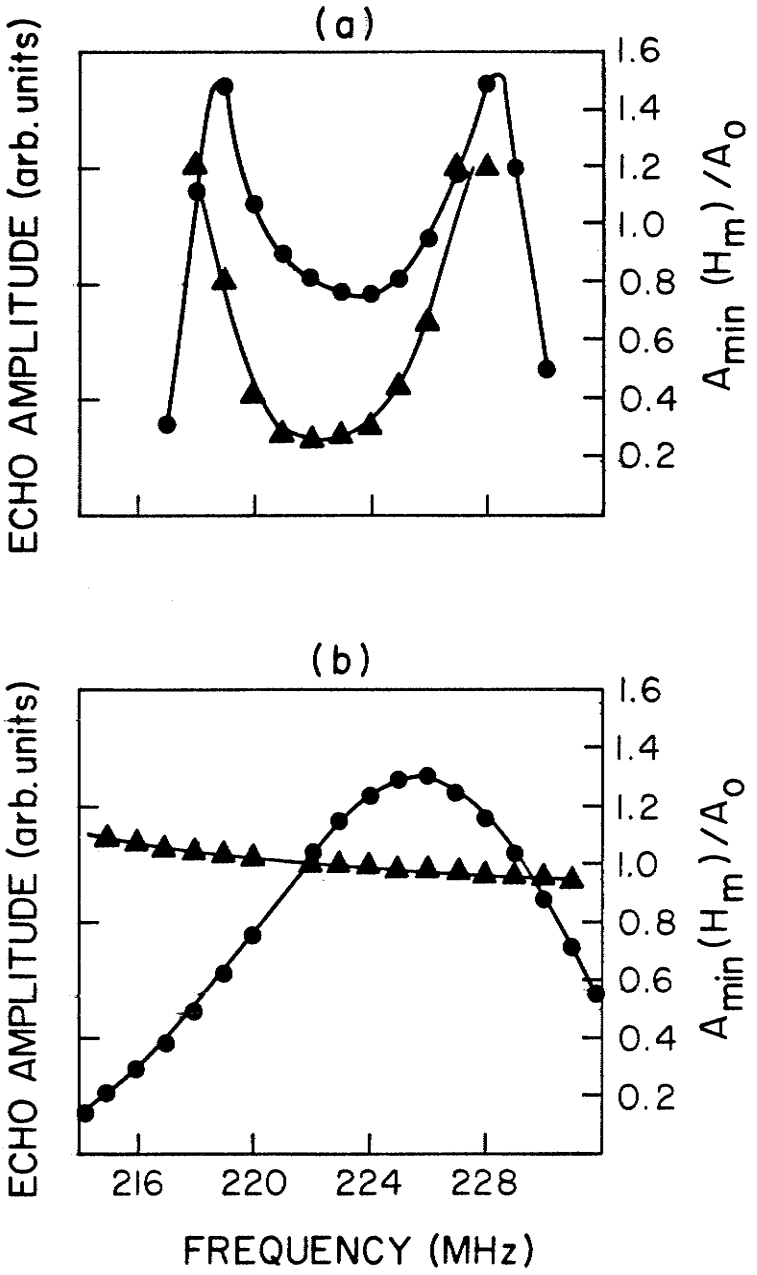

Fig. 6.25 a) The calculated spectrum ● as well as the modulation ▲ spectrum for hcp Co assuming an exponential variation of the hyperfine field through the wall. Here, $x_1 = 4$, $x_o = 2$, $\eta_o = 1.0$ and $\Delta_d = 0.5$ MHz, $H_1 = 0.1$ kOe, $t_1 = 2.5$ μsec and $t_2 = 5.0$ μsec.

b) The effect of a large r.f. field on the modulation spectrum ▲ . Here $H_1 = 2.0$ kOe and $t_1 = .125$ μsec., $t_2 = .25$ μsec. and $x_1 = 1$, $x_o = 2$.

Several other possible contributing factors were examined but dismissed. As was mentioned in the presentation of the experimental results in chapter five (sec. 9) the value of the external modulating field was determined using a weighted average of the field produced by a single loop and an infinite solenoid. This average was calculated using a formula which, it was felt, would most likely overestimate the actual field produced by the coil.

The fact that the modulation was not synchronized with the r.f. pulses will also affect the experimentally observed depth of the modulated spin-echo decay envelope. In our calculations it was assumed that the r.f. pulses are applied at the peaks of the modulation field. Experimentally, however, the pulses are applied at random relative to the modulation. Therefore, the effective modulation field will actually be less than the peak value calculated. Again, this effect would result in a larger value of the longitudinal enhancement factor, and therefore cannot account for the large values that we measured.

As a result of the polycrystalline nature of the samples that we used, the alignment of the particles will in effect align only the dominant grains along the desired direction with all other grains in the particles randomly orientated relative to this direction. For these other grains both the modulating field and the r.f. field will be reduced by the same factor, and therefore the modulating field experiment will not be affected. This will, however, influence the absolute intensity of the detected resonance signal, as the nuclear spins in these grains which are exactly on resonance will not experience the optimum tuning conditions because of the reduced r.f. field driving

the domain walls.

None of the above-mentioned factors can therefore be responsible for the anomalously large longitudinal enhancement factor we have measured. We therefore examined the reliability of the values of the various parameters we used in the calculation of the longitudinal enhancement factor. It becomes immediately evident that the only possible cause of the discrepancy would arise from the value of the wall susceptibility. A large frequency dependence of the wall susceptibility arising from a wall resonance phenomena could possibly give a much larger susceptibility at 80 kHz, the modulation frequency, than at 15 kHz, the frequency at which the susceptibility was measured. Alternatively, the measured susceptibility may not correctly describe the mobility of the domain walls which contribute most to the resonance signal.

To investigate the first possibility, we note from Eqn. 5.22 that the change in wall location upon the application of a field H_x along the c-axis is given by

$$\Delta x = \frac{\chi_{||} W H_x}{2 M_s}$$

where $\chi_{||}$ is the wall susceptibility parallel to the c-axis and the rest of the variables have the same meaning as before. The transverse enhancement factor, using a calculation similar to that used to obtain Eqn. 5.11 describing the longitudinal enhancement factor, is given by

$$\eta_{\perp} = \frac{H_1}{H_x} \simeq \frac{H_{hf} \Delta\theta}{H_x} = \frac{H_{hf}}{H_x} \frac{\pi \Delta x}{\delta} \qquad (6.42)$$

assuming a uniform spin rotation in the wall so that $\theta = \pi x/\delta$. Substituting for Δx using Eqn. 5.22 yields

$$\eta_{\perp} = \frac{\pi W \chi_{||} H_{hf}}{2\delta M_s} \tag{6.43}$$

Combining with Eqn. 4.25 yields an expression for the wall susceptibility

$$\chi_{||} = \frac{4M_s^2}{W} \frac{(\alpha - \mu\omega^2) - i\beta\omega}{(\alpha - \mu\omega^2) + \beta^2\omega^2} \tag{6.44}$$

where $\omega_o = (\alpha/\mu)^{1/2}$ is the wall resonance frequency. Using the standard formula (18) for the wall stiffness constant $\alpha = 4M_s^2/\chi_o W$ and for the wall mass $\mu = 1/8\pi\gamma^{-1}\delta$ where χ_o is the initial susceptibility and γ is the wall energy; and using our measured susceptibilities and the same values for the other parameters that were used earlier yields a wall resonance frequency of 7400 Hz for cobalt and 22,600 Hz for YCo_5. For cobalt the wall resonance frequency is below the frequency at which the susceptibility was measured, 15 kHz, and well below the modulation frequency of 80 kHz. For YCo_5 the wall resonance frequency is much closer to 15 kHz than to 80 kHz. Therefore, we conclude that the susceptibility at 80 kHz will, if anything, be lower than the measured susceptibility.

As a result we are forced to conclude that it is most likely that the measured susceptibility does not accurately describe the

mobility of the domain walls which make the largest contribution to the resonance signal. It should be noted that except for the cobalt sample the measured susceptibility was very much smaller than the theoretical value of $3/4\pi \sim 0.24$ for a sphere. If we assume only the most mobile domain walls contribute significantly to the resonance signal and that these walls have the theoretically expected susceptibility, then we can recalculate the anisotropy in the hyperfine field as predicted by our modulation experiment. Table 6.3 shows these results along with the results we obtained from the measured susceptibility. A comparison of these results with the experimental values of the anisotropy in the hyperfine field shown in Table 6.2 indicates a large improvement, especially for YCo_5 and $SmCo_5$ which had the largest discrepancies before this adjustment was made. Values for $GdCo_5$ are now much smaller than the experimentally determined anisotropy in the hyperfine field, and the value for hexagonal Co has actually increased. These discrepancies are not, however, as extreme as those that existed for YCo_5 and $SmCo_5$ before the adjustment. It is felt that this remaining discrepancy easily falls within the range of possible error in the values of the various other parameters which were used. In particular, the domain width could be substantially different from the value that we used. Livingston and McConnell (19) studied the thickness dependence of the domain width for a plate of YCo_5 and found a rapid increase in the range of plate thicknesses of 10-90 micron. The average domain size varied from approximately 1.7 micron to 7 micron for this range of thickness. This study was conducted at room temperature, and therefore additional uncertainty is created in using these values to

TABLE 6.3

SAMPLE	$\chi_{\parallel}(\frac{emu}{cm^3 Oe})$	$\eta_{max.}$	$\Delta\nu$ (MHz)	$\chi_{\parallel}(\frac{emu}{cm^3 Oe})$	H_a(MHz)	$\Delta\nu$ (MHz)
hex. Co	0.32	431	34.3	0.24	45.3	45.8
Y Co_5	1.6×10^{-2}	7918	927	0.24	61.2	61.8
		7070	828		54.7	55.2
Sm Co_5	3.8×10^{-3}	10980	2030	0.24	31.8	32.1
		9000	1667		26.1	26.4
Gd Co_5	2.19×10^{-2}	2046	7.1	0.24	0.64	0.65
		1364	4.7		0.43	0.43
		1597	5.5		0.50	0.51

compute something at temperatures as low as 1.5 K, although the temperature dependence of W is not expected to be too strong.

From these considerations, however, it is clear that we can expect only an order-of-magnitude agreement between the values of H_a obtained from the modulation experiment and the values obtained directly from the spectra. The fact that only the most mobile domain walls contribute significantly to the resonance signal could also be an important factor determining the strength of the detected signal.

6.7 The Relationship between the Magnetocrystalline Anisotropy and the Anisotropy in the Hyperfine Field

In this section we will present a phenomenological theory that was developed in the hope that it would give a relatively simple explanation for the major features involving both the magnitude and sign of the anisotropy in the hyperfine field and the magnetocrystalline anisotropy. In this model all detail of the distribution of the spin and charge density and the interaction between the spin and orbital momentum and the orbital momentum and the crystal field are described by coupling constants. We consider the following expression for the potential of a uniaxial ferromagnet.

$$E = \lambda \vec{S} \cdot \vec{L} + \lambda_A \vec{S}_\perp \vec{L}_\perp + \tfrac{1}{2} K \vec{L}^2 + \tfrac{1}{2} \Delta K \vec{L}_\perp^{\,2} \qquad (6.45)$$

where the first two terms are the isotropic and anisotropic contributions to the spin-orbit interaction energy and the last two terms are the isotropic and anisotropic components of the interaction of

the orbital momentum with the crystal field. Additional terms may be added, if desired, to include the exchange interaction energy and the hyperfine interaction of the spin and orbital moments with the nuclear moment.

At equilibrium we require that

$$\frac{\partial E}{\partial L_{||}} = \frac{\partial E}{\partial L_{\perp}} = 0 \tag{6.46}$$

where as before the symbols $||$ and $\perp$ denote directions parallel and perpendicular to the uniaxial axis. From Eqns. 6.45 and 6.46 we obtain

$$L_{||} = -\frac{(\lambda + \lambda_A)}{(K + \Delta K}\, S \qquad L_{\perp} = -\frac{\lambda}{K}\, S \tag{6.47}$$

where λ_A is the anisotropy in the spin-orbit coupling constant and ΔK is the anisotropy in the crystal field. In addition, for the uniaxial axis to be an easy axis it is required that

$$\frac{d^2E}{dL^2} < 0 \quad \rightarrow \quad K < 0$$

and for the direction perpendicular to the uniaxial axis to be a hard direction it is required that

$$\frac{d^2E}{dL^2} < 0 \quad \rightarrow \quad (K+\Delta K) > 0$$

Substitution of Eqn. 6.47 into Eqn. 6.45 gives the following expression for the anisotropy energy per atom.

$$\Delta E = E_{||} - E_{\perp} = \frac{\lambda^2 S^2}{2(K+\Delta K)} - \frac{\lambda^2 S^2}{2K} + \frac{\lambda \lambda_A S^2}{K+\Delta K} + \frac{\lambda_A^2 S^2}{2(K+\Delta K)} \tag{6.48}$$

We also get an anisotropy in the orbital angular momentum of

$$\Delta L = L_{||} - L_{\perp} = \frac{\lambda S}{K}\left[\frac{\lambda_A}{\lambda} - \frac{\Delta K}{K}\right] \Big/ \left[1 + \frac{\Delta K}{K}\right] \tag{6.49}$$

where the major quantities in brackets have been expressed as fractions since we know very little about the absolute values of these parameters. The orbital contribution to the anisotropy in the hyperfine field will simply be written as

$$\Delta H_L = H_{||} - H_{\perp} = A_L \Delta L \qquad (6.50)$$

where A_L is the orbital hyperfine coupling constant.

In chapter four (sec. 6) we were able to conclude that, based on data published by Kawakami et al (15), the dominant contribution to the anisotropy in the hyperfine field at low temperature for hexagonal cobalt was the orbital contribution. Of particular interest was that, from the temperature dependent study of the steady-state resonance, it could also be concluded that at the temperature at which the easy direction of hexagonal cobalt begins to rotate into the basal plane and therefore the first anisotropy constant, K_1, goes negative, the dominant contribution to the anisotropy in the hyperfine field remains the orbital contribution, and furthermore, the sign of the anisotropy in the hyperfine field remains positive, as it was at low temperature.

This observation was the first indication that the relationship between the anisotropy in the hyperfine field and the magnetocrystalline anisotropy may not be as straight forward as we initially had hoped. The anticipated procedure had been to follow Streever (5,20) and use Eqn. 4.36

$$(H_{||} - H_{\perp}) = 2\mu_B(\Delta L) \langle r^{-3} \rangle$$

where $\Delta L = \langle L_{||} \rangle - \langle L_{\perp} \rangle$ is the difference in the unquenched orbital angular momentum for the two orientations, to compute ΔL. If we assume that the dominant contribution to the anisotropy in the hyperfine field

is an orbital contribution, then our identification of the DWE and DWC resonance peaks would allow the determination of ΔL for each of the Co sites. The contribution of the spin-orbit interaction energy to the Co anisotropy energy can be written as

$$E_{||} - E_{\perp} = \lambda[\langle L_{||}\rangle\langle S_{||}\rangle - \langle L_{\perp}\rangle\langle S_{\perp}\rangle] \qquad (6.51)$$

which, if $\Delta S/\langle S\rangle \ll 1$ becomes

$$E_{||} - E_{\perp} = \lambda\langle S\rangle\Delta L \qquad (6.52)$$

Since λ is negative for hexagonal Co metal (21), for an easy axis we require $\Delta L > 0$ or $H_{\perp} > H_{||}$ which is the situation for hexagonal Co at low temperature. However, at high temperature the anisotropy energy becomes negative but the anisotropy in the hyperfine field does not change sign. An examination of the anisotropy in the hyperfine field for the two Co sites in YCo_5 displays a similar complicating factor. The yttrium sub-lattice is non-magnetic and makes no contribution to the magneto-crystalline anisotropy energy. The compound YCo_5 has an easy c-axis at all temperatures but an examination of the anisotropy in the hyperfine field at the two Co sites as determined by our experiments and listed in Table 6.2 shows one site which apparently favours an easy plane ($H_{\perp} - H_{||} = -39$ kOe) and one site which apparently favours an easy axis ($H_{\perp} - H_{||} = +25$ kOe). Equation 6.52 represents the anisotropy energy per Co atom and to assess the strength of the contribution from each type of site one must also consider the number of Co atoms of each type per formula unit.

A polarized neutron diffraction study (22) of YCo_5 indicated a very large orbital contribution to the magnetic moment on the Co (2c) site. The magnetization density around the Co (3g) site, which lies in

planes which contain no yttrium atoms, is nearly isotropic, whereas the Co (2c) site, which lies in the plane containing yttrium, exhibits a very pronounced anisotropy. The magnetization density is extended in the basal plane relative to the free atom. This spatial anisotropy is accompanied by a large orbital contribution to the magnetic moment, much larger than the Co (3g) site or pure Co (23), which suggests that the major part of the anisotropy originates from this site as a result of the coupling of the spins to the crystallographic axes via the spin-orbit coupling.

For the RCo_5 compounds three different types of substitutions are known to occur; substituted Ni prefers to occupy the Co (2c) site, Fe atoms favour the Co (3g) site and additional cobalt replaces yttrium atoms in pairs above and below the plane containing the yttrium atoms. Deportes et al (24) have measured the anisotropy constant, K_1, for YCo_5 as a function of Ni concentration and found that the value of K_1 closely follows the concentration of Co atoms in the 2c site.

If we associate the high frequency resonance peaks having an anisotropy in the hyperfine field of +25 kOe with the Co (2c) site and note in addition that the number of Co (2c) atoms per formula unit is two, it is apparent that this calculation would predict an easy plane for YCo_5, at least at low temperature where the NMR data were taken.

This difficulty is not directly apparent from the NMR results we obtained for the Co resonance in $SmCo_5$ and $GdCo_5$. $SmCo_5$ has the largest magnetocrystalline anisotropy of all the RCo_5 compounds which favours an easy c-axis. Both the sites, as identified using our experimental techniques, have a positive anisotropy in the hyperfine

field and therefore would favour an easy axis. $GdCo_5$ is also known to favour an easy axis and in our experimental results we found that one Co site favours an easy axis ($H_\perp > H_{||}$) and the other site favours an easy plane ($H_{||} > H_\perp$). However, in contrast to the situation for YCo_5, for this material the anisotropy in the hyperfine field ($H_a = H_\perp - H_{||}$) is larger for the site favouring an easy axis. If one considers the relative abundance per formula unit of each type of Co atom, however, the Co sub-lattice only marginally favours an easy axis. For $SmCo_5$, however, the rare-earth sub-lattice may contribute significantly to the magnetocrystalline anisotropy, particularly at low temperature (25-27) and therefore no further conclusions about the influence of the Co sub-lattice on the magnetic properties of the RCo_5 compounds can be achieved until one understands more about the relative importance of the two sub-lattices.

Experimental studies of the magnetocrystalline anisotropy of the RCo_5 compounds have been undertaken by a number of authors (28,29). These measurements of the temperature dependence of the anisotropy constants showed that the constants K_1 are positive and have comparable values for all compounds at high temperature. Certainly, the cobalt sub-lattice gives the main contribution to the anisotropy constant K_1 of the compounds YCo_5, $LaCo_5$ and $CeCo_5$ because Y, La and Ce have no magnetic moment in these compounds. The comparable behaviour of the other compounds at high temperature suggest that this may also be the case for these RCo_5 compounds.

At low temperatures the K_1 values are different for various RCo_5 compounds, not only in magnitude but also in sign. The easy axis

is retained by $SmCo_5$ and $GdCo_5$ as well as $CeCo_5$, YCo_5 and $LaCo_5$. A transition occurs to a cone of easy axes for $PrCo_5$ and $HoCo_5$ or to an easy plane for $NdCo_5$, $TbCo_5$ and $DyCo_5$. One can suppose that the behaviour of the anisotropy of the RCo_5 compounds is determined at low temperatures by the contribution of the single-ion anisotropy of the rare-earth sub-lattice. Greedan and Rao (25) were able to correctly predict the magnetic behaviour of the RCo_5 compounds at low temperatures by considering the rare-earth sub-lattice only.

In any event the large values of K_1 for YCo_5, $CeCo_5$ and $LaCo_5$ at low temperature suggests that the Co sub-lattice contribution is significant and worthy of investigation. Of particular interest would be the microscopic investigation of ternary series involving either a non-magnetic rare-earth such as La, Ce or Y and the substitution of Ni or Fe for Co or the substitution of a non-magnetic rare-earth for a magnetic rare-earth such as Sm. Such an investigation would allow the relative importance of the two Co sites to the magnetocrystalline anisotropy to be determined from the first series since Ni and Fe substitute with a known preference into the two Co sites. Also, the influence of the rare-earth partner on the Co contribution could be investigated using the second series. The dependence of the magnetic properties of the Co sub-lattice upon the rare-earth partner was discussed in chapter two (sec. 4) and it is not clear that the anisotropy arising from the two sub-lattices should necessarily be independent. The general approach that has been taken for these materials is to assume that the Co contribution to K_1 is constant throughout the series, and is given by the value of K_1

obtained for YCo_5. The difference between this value and the value for another member of the RCo_5 series was then attributed to the rare-earth sub-lattice.

A microscopic study of the Co sub-lattice contribution to the magnetocrystalline anisotropy using our NMR techniques would be extremely helpful in understanding the nature of the extremely large magnetocrystalline anisotropy possessed by these important materials. Before this can be done, however, a greater understanding of the nature of the anisotropy in the hyperfine field at the two Co sites will be required, as well as a better understanding of how it correlates with the magnetocrystalline anisotropy. To achieve this it is advisable to restrict oneself to hexagonal cobalt and to the RCo_5 compounds which have a non-magnetic rare-earth sub-lattice.

We will therefore limit ourselves to a more detailed examination of both hexagonal cobalt and YCo_5. A resonance could also be detected in a $CeCo_5$ sample that we had and the spectrum was shown in Fig. 5.26. However, we were unable to obtain a complete set of data for the Co^{59} resonance in $CeCo_5$, and therefore we are able to examine only the two samples in detail.

For this purpose we have used the phenomenological expressions for the anisotropy energy and the orbital contribution to the anisotropy in the hyperfine field, given by Eqns. 6.48 and 6.49 respectively, to attempt to account in a consistent manner for the major features observed in the study of these materials. To first order in the anisotropy in the crystal field, ΔK, and in the anisotropy in the spin-orbit interaction, λ_A, the expression for the anisotropy energy

becomes

$$\Delta E = -\frac{\lambda^2 S^2}{2K^2}\Delta K + \frac{\lambda\lambda_A S^2}{K} \tag{6.53}$$

Similarly, to first order the anisotropy in the orbital contribution to the hyperfine field is

$$\Delta H_L = \frac{A_L \lambda S}{K}\left[\frac{\lambda_A}{\lambda} - \frac{\Delta K}{K}\right] \tag{6.54}$$

An additional measurable quantity for which data exist and which we will want to account for consistently is the anisotropy in the magnetization. Almeda et al (30,31) conducted high field magnetization measurements on YCo_5 and reported a 4% magnetization anisotropy at 4.2 K with $M_{\parallel} - M_{\perp} > 0$. In conjunction with the neutron diffraction experiments by Schweizer and Tasset (22) they concluded that the magnetization anisotropy in the RCo_5 comes from the large orbital contribution to the Co (2c) moment. Rebouillat (32) measured an anisotropy in the magnetization of hexagonal cobalt of +.45% at 4.2 K by measuring the magnetization up to 50 kOe. In terms of our phenomenological model the anisotropy in the magnetization is given by

$$\Delta L = \frac{\lambda S}{K}\left[\frac{\lambda_A}{\lambda} - \frac{\Delta K}{K}\right] \tag{6.55}$$

and to be consistent with the experimentally determined sign we require $\Delta L > 0$ for both Co and YCo_5.

At low temperature to have an easy axis we require that $\Delta E < 0$.

For these materials $\lambda < 0$ and $A_L < 0$ as well since the orbital contribution to the hyperfine field is anti-parallel to the orbital moment. For an easy axis at low temperature we would simply require from Eqn. 6.53 that the first term dominate with $\Delta K > 0$. It is known that Co acquires an easy plane at higher temperatures (520 K) and therefore the anisotropy energy ΔE will have to pass through zero and become positive. From the experimental data of Kawakami et al (15) we know that at this point the anisotropy in the orbital hyperfine field, although decreasing in magnitude with increasing temperature retains its positive sign. We therefore have a non-simultaneous transition through zero of the quantities ΔE and ΔH_L. To examine how this may come about we will consider Eqns. 6.53 and 6.54 in more detail. First of all, the point at which the transition to an easy plane occurs is defined by setting $\Delta E = 0$ which gives

$$\Delta K = \frac{2K\lambda_A}{\lambda} \tag{6.56}$$

Substituting Eqn. 6.56 into Eqn. 6.54 determines the value of ΔH_L at this point of transition. We have

$$\Delta H_L = - \frac{A_L \lambda_A}{K} S \tag{6.57}$$

which is positive if λ_A and K have the same sign. For convenience we express both ΔK and λ_A in reduced units defined by

$$\Delta k = \frac{\lambda^2 S^2}{K^2} \Delta K \quad \text{and} \quad \lambda_a = \frac{\lambda S^2}{K} \lambda_A \tag{6.58}$$

Equations 6.53 and 6.55 now become respectively

$$\Delta E = -\tfrac{1}{2}\Delta k + \lambda_a \qquad (6.59)$$

$$\lambda S\Delta L = -\Delta k + \lambda_a \qquad (6.60)$$

Figure 6.26 shows a simultaneous plot of these two equations as a function of Δk for positive and negative values of λ_a as well as for $\lambda_a = 0$.

Kawakami et al (15) also reported that the total anisotropy in the hyperfine field and the quadrupole splitting had approximately the same temperature dependence as the deviation of the ratio of the lattice constants c/a from ideal, i.e. deviation = $(8/3)^{1/2} - c/a$. It therefore seems reasonable to associate our crystal field term involving Δk with a crystallographic distortion which produces a non-ideal c/a ratio. A general increase of c/a towards the ideal value with increasing temperature is well-established (33). We therefore expect that this temperature dependence will influence both the magnetocrystalline anisotropy ΔE and the anisotropy in the hyperfine field as a result of their dependence on Δk. At high temperature $\Delta k \to 0$ and since Kawakami et al have shown using NMR that ΔH_{hf} is still large and positive at high temperature we require that either λ_a be positive or that the dipolar contribution to the anisotropy in the hyperfine field be dominant at high temperature. However, in chapter four (sec. 6) we were able to show, using the available data, that even at high

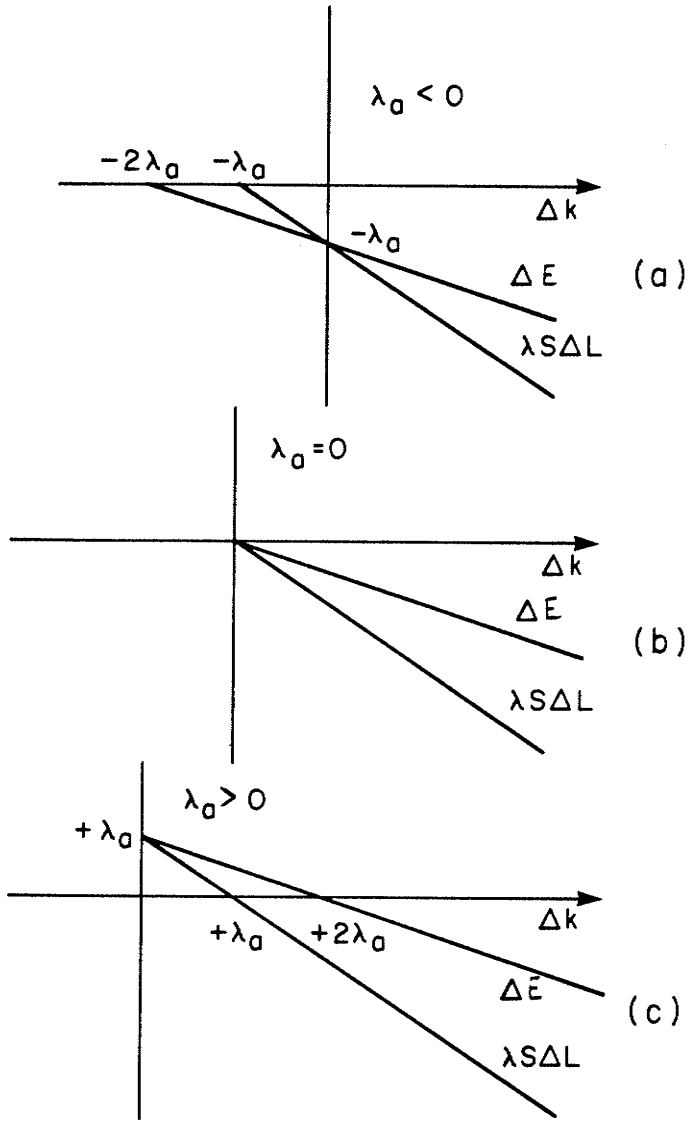

Fig. 6.26 ΔE and ΔL as a function of Δk, for (a) $\lambda_a<0$, (b) $\lambda_a=0$ and (c) $\lambda_a>0$.

temperature the major contribution is from the orbital motion. Therefore, we conclude that λ_a is positive which corresponds to case (c) in Fig. 6.26.

Our model for hexagonal cobalt, therefore, requires that Δk be large ($\Delta k > +2\lambda_a$) and positive at low temperature. As the temperature increases, Δk decreases as a result of lattice expansion until $\Delta k \sim +2\lambda_a$ at which temperature the easy direction begins to rotate into the basal plane. In the discussion in chapter four (sec. 6) it was concluded that the orbital contribution at this temperature was approximately one-half the value at low temperature. From this conclusion we can project using Fig. 6.26 (c) that at low temperature $\Delta k \sim 3\lambda_a$. As the temperature increases beyond the transition temperature ΔE is positive and the second term in Eqn. 6.59 begins to dominate. As $\Delta k \rightarrow 0$ we have an anisotropy energy per atom of $\Delta E = \lambda_a$. Vonsovskii (34), in fact, suggested in 1938 that an anisotropy in the spin-orbit interaction was the reason that the easy direction for Co rotated into the plane at high temperature, but this seems to have been forgotten.

A qualitative explanation of our experimental results for the RCo_5 compounds can also be made. An examination of the local co-ordination of the two Co sites shows two distinctly different environments. The Co (2c) site has a h.c.p. Co - like environment. All the neighbouring ions in the same plane tend to turn the orbital moment of the central Co ion along the c-axis. The electron distribution is concentrated in the basal plane because of the positive ions located in this plane. This effect is compensated by the effect of the ions in the neighbouring planes when the lattice is not too compact,

i.e. c/a small. The degree to which complete compensation is not achieved will be determined by the deviation of c/a from the ideal structure. The crystalline potential energy in the point charge approximation for a h.c.p Co lattice taking the z-axis parallel to the c-axis is given by $B_2^0 \langle 3z^2 - r^2 \rangle$ where

$$B_2^o = -3 \left[16 \frac{x^2 - 2/3}{(x^2+4/3)^{5/2}} - 1 \right] \frac{q}{a^3}$$

$$= -1.22(1.633 - \frac{c}{a}) \frac{q}{a^3} \quad \text{for } x = \frac{c}{a} \simeq 1.633 \qquad (6.61)$$

Our phenomenological expression for the anisotropy energy shows $\Delta E \propto \Delta k$ and since Δk is proportional to the deviation from the ideal hexagonal structure, we can compile the Table 6.4 which uses lattice parameters taken from the review article by Buschow (35) and compares the magnitude of the deviations to the composite anisotropy constant K_1. As these lattice parameters were room temperature values we must compare these to the room temperature values of K_1 taken from Table 1.1. Of particular importance are the first three compounds which because they do not contain a magnetic rare earth are the most easy to study. For these compounds the anisotropy constant K_1 orders with the deviation of the c/a ratio from ideal, as predicted by our model.

TABLE 6.4

SAMPLE	a (A)	c (A)	c/a	K_1 (ergs/cm^3)
$CeCo_5$	4.922	8.032	1.6318	5.2×10^7
YCo_5	4.935	7.928	1.6065	5.5×10^7
$LaCo_5$	5.105	7.932	1.5538	6.3×10^7
$SmCo_5$	5.004	7.938	1.5863	11.2×10^7
$GdCo_5$	4.973	7.938	1.5962	5.3×10^7
$PrCo_5$	5.013	7.960	1.5879	6.9×10^7
$NdCo_5$	5.020	7.954	1.5845	

We also expect that for the Co (2c) site the DWC frequency will be greater than the DWE frequency for all the RCo_5 compounds. All our spectra have at least one set of peaks for which we have identified that $\nu_{DWC} > \nu_{DWE}$ and we can therefore associate this set with the Co (2c) site. From the expression for ΔL (Eqn. 6.60) it is seen that the anisotropy in the hyperfine field is also proportional to Δk. We therefore have $\Delta H_L\ (SmCo_5) > \Delta H_L\ (YCo_5) > \Delta H_L\ (Co)$ in agreement with experiment. The data for $GdCo_5$ does not follow this trend, however. It is possible that the second term in λ_α is substantial and subtracts from the term in Δk to produce the narrower NMR spectrum observed.

An examination of the co-ordination of the Co (3g) site suggests that a more complete compensation is possible for this site, or the orbital moment may even favour an easy plane. A point charge expression for the crystal field potential is

$$\frac{16}{a^3}\left\{q_1\left[18\sqrt{3}\,\frac{c^2}{a^2} - 3\sqrt{3}\right]/\left[1 + \frac{3c^2}{a^2}\right]^{5/2} + q_2\left[\frac{2c^2}{a^2} - 1\right]/\left[1 + \frac{c^2}{a^2}\right]^{5/2} - q_3\right\} \tag{6.62}$$

where the first two terms represent contributions from the nearest planes and the third term is an in-plane contribution. Taking $c/a \sim 1.633$, Co charges q_1 and q_3 of +2e and a rare-earth charge q_2 of

+3e gives an energy of

$$-0.84\ (16/a^3)$$

The negative sign indicates that the orbital moment would lie along the c-axis. This could be the case in $SmCo_5$ where we have for both sites that $\nu_{DWC} > \nu_{DWE}$. However, as mentioned earlier, the substitution of Ni and Fe in YCo_5 has shown (24) that K_1 is determined by the Co (2c) site. To account for this we require that Δk be small for the 3g site (at least for YCo_5). This could probably be achieved if there were considerable screening of the crystal field in the plane of the 3g site. The anisotropy in the hyperfine field is still found to be large for this site, but this could be predominantly from the λ_a term. Whether $\nu_{DWC} < \nu_{DWE}$ (as in YCo_5) or $\nu_{DWC} > \nu_{DWE}$ ($SmCo_5$) would be determined by the sign of λ_a.

From the above discussion we would come to the tentative conclusion that the resonance properties of the Co (3g) site would be determined predominantly by the spin-orbit interaction, while the properties of the Co (2c) resonance would be determined largely by crystal field effects.

Our expressions for the orbital angular momentum and also the orbital contribution to the hyperfine field do not contain an explicit angular dependence. From Eqn. 6.55 we can write the angular dependence as

$$L(\theta) = L_{||}\left[1 + \frac{\lambda_A(\theta)}{\lambda} \quad \frac{\Delta K(\theta)}{K}\right] \tag{6.63}$$

where $L_{//}$ is the orbital momentum when the spins are aligned along the

c-axis. The second term in brackets containing λ_A is probably equivalent to the relativistic term mentioned by Fekete et al (11), and although Fekete indicates this term has only a small angular dependence in a totally magnetized sample, this may not be the case in a domain wall. This is the essence of our earlier suggestion regarding the distribution of the hyperfine field in the domain wall as it is related to both the enhanced modulation of the echo-decay envelope and the composite lineshape.

The discussion on the previous pages was based on the assumption that λ_A/λ, $\Delta K/K << 1$. Fekete's (11) expression for the expectation value of the orbital angular momentum contained a second term which had an angular dependence of $(3\cos^2\theta - 1)/2$ which is the angular dependence observed experimentally in a saturated sample. If $\Delta K/K$ also has this same angular dependence, then, since from magnetization and neutron diffraction measurements both $L_{||}$ and $L_{\perp}$ are greater than zero (i.e. $L_{||}$ and $L_{\perp}$ are parallel to the electronic spin S and therefore the g-factors $g_{||}$ and $g_{\perp} > 2.0$) we require that

$$\frac{\lambda_A}{\lambda} > \tfrac{1}{2}\frac{\Delta K}{K}$$

This is in agreement with the conclusion that at high temperature where $\Delta K \sim 0$, the orbital contribution to the hyperfine field is approximately one-half the contribution at low temperature.

Our phenomenological model based on Eqn. 6.45 also predicts that as the spin rotates away from the c-axis the spin and orbital moments become non-colinear. We have

$$\tan \theta' = \frac{1 + \frac{\Delta K}{K}}{1 + \frac{\lambda_A}{\lambda}} \tan \theta \qquad (6.64)$$

where θ is the angle between the spin and the c-axis and θ' is the angle between the orbital angular momentum, L, and the c-axis. The total hyperfine field is then given by

$$H_{hf} = \left[H_s^2 + H_L^2 - 2H_s H_L \cos(\theta - \theta')\right]^{\frac{1}{2}} \qquad (6.65)$$

where H_s is the total non-orbital contribution to the hyperfine field which is a constant. Figure 6.27 illustrates how the total hyperfine field now consists of a vector sum of an angular independent non-orbital (Fermi-contact) contribution and an angular dependent orbital contribution. It was originally hoped that whether the orbital moment lags or leads the spin moment, which depends on the signs of λ_A/λ and $\Delta K/K$, could determine whether the DWC or DWE resonance peak is larger. It turns out, however, that Eqns. 6.64 and 6.65 contain no more freedom than Eqn. 4.45 where

$$\tan \theta' = H_{\perp}/H_{||} \tan \theta$$

As in this situation we found that the resonance peak which has the higher frequency also has the larger amplitude which is contradicted by experiment. This aspect of our model, therefore, remains merely a point of interest, there being no experimental evidence of the hyperfine field significantly deviating from the direction of the elecronic spin.

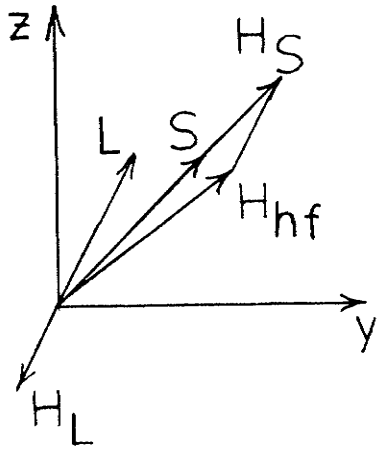

Fig. 6.27 The vector addition of orbital and non-orbital (Fermi contact) contributions to the hyperfine field to produce the total hyperfine field.

6.8 The Absolute Intensity of the Co^{59} Resonances

It was concluded earlier that the difference in the intensity of the resonance observed from the various members of the RCo_5 series may either be of intrinsic origin or may simply reflect the condition of the particular sample used.

Stearns (36,37) has measured the free induction decay amplitude and the spin-echo amplitude dependence on the frequency, r.f. field and pulse length for Fe. The experimental results were not consistent with the usually considered model of rigid oscillating domain walls with a position dependent enhancement factor. It became necessary to postulate that perhaps the domain walls behaved more like vibrating circular membranes which are held immobile along its perimeter. The wall oscillation therefore resembles a vibrating drumhead, and therefore this is referred to as the drumhead model. As a consequence of this model Stearns indicated that the enhancement factor should be smaller for less pure samples. If impurities enhanced the domain nucleation this would produce on average more and smaller domain wall segments which would result in smaller enhancement factors. Alternatively wall pinning would also reduce the domain wall area, although at higher temperatures less pinning should occur, and therefore the domain wall area should increase resulting in an increase in the enhancement factor. Both these effects reflect the possible influence of the sample condition on the intensity. Any restriction in the wall displacement will reduce the enhancement factors resulting in a reduction in the signal strength, but as indicated earlier should not result in any distortion of the spectrum obtained from spin-echo spectrometry. The strength of the detected signal will depend upon the magnitude of the wall displacements produced

by the precessing nuclear spins.

In order to determine the nature of the variation of the signal intensity, several experiments were conducted. Clearly, the NMR behaviour of these materials is quite complex and a more careful study is required to learn more about what is occurring in pulsed NMR experiments. Many of the factors which influence the signal strength have already been identified in previous sections. These factors include the skin depth, the wall volume and the wall mobility. The procedure which was undertaken involved the use of a powdered sample of YCo_5 for which a resonance could be observed and subjecting it to various treatments. The signal strength before and after treatment was compared at a fixed frequency and r.f. power level. Etching the powdered sample in nitric acid resulted in little change in signal strength when the powder was carefully recovered, to prevent any sample loss, and aligned in a wax binder in the same sample tube used in the initial measurement. Annealling the powdered sample at $1100^{o}C$ for 48 hours in an argon atmosphere and then quenching to room temperature in water resulted in only a 50% increase in the signal strength. Using this latter procedure on RCo_5 samples for which no resonance had been detected was not successfull in improvng the situation.

Initially these procedures were undertaken simply to determine what could be done to increase the strength of the signals observed in the various RCo_5 compounds and to improve the possibility of observing a resonance for samples in which no signal could be detected. As the study developed, however, it became apparent that obtaining sufficient data of adequate quality to allow definite conclusions to be drawn about

the nature of the Co sub-lattice contribution to the magnetocrystalline anisotropy would be a major problem.

The variation in the wall volume per unit sample volume may be the source of an intrinsic variation of resonance intensity through the series. Evidence of an intrinsic origin to the variation in the signal intensity through the RCo_5 series comes from the observation that the signal strength orders inversely with the low temperature values of the anisotropy constant, K_1 as well as with the anisotropy in the hyperfine field, H_a. Table 6.5 shows a list of the samples that were examined in the order of decreasing signal strength along with low temperature values of K_1 and our experimentally determined values of H_a.

TABLE 6.5

SAMPLE	K_1 (ergs/cm^3)	H_a (kOe)
hcp Co	9.1×10^6	10
$GdCo_5$	3.0×10^7	18,10
YCo_5	6.8×10^7	24,40
$PrCo_5$		
$SmCo_5$	29.5×10^7	45,45

The reduction in signal strength with increasing anisotropy in the hyperfine field would be expected since the number of nuclei contributing to the detected signal at a given frequency would be reduced. The ordering with K_1 may be the consequence of the relationship between the magnetocrystalline anisotropy and the anisotropy in the hyperfine field. It may also have a more direct effect on the signal intensity via its influence on the domain size and

therefore on the wall volume per unit sample volume. Inomata (38) has examined the Co resonance in $Y_2(Fe_xCo_{1-x})_{17}$ and found that the intensity changes are consistent with the changes in the magnetic anisotropy, an intensity minimum indicating a maximum in the magnetic anisotropy.

CHAPTER 7

Conclusion

In order to be able to determine the anisotropy in the hyperfine field at the two cobalt sites in the highly anisotropic rare earth RCo_5 compounds we have developed several techniques to locate and identify the domain wall edge and the domain wall centre resonances. Of particular interest is the external modulation of the nuclear spin echo decay envelope which has been observed and which is the result of a longitudinal enhancement of the modulating field. The enhancement mechanism is related to the anisotropy in the hyperfine field and occurs as the result of wall motion produced by the external field. The longitudinal enhancement effect can be compared to the transverse enhancement effect first observed by Gossard and Portis (1) which has made it possible to observe NMR resonances in many ferromagnetic materials. The measurement of the depth of the nuclear spin echo modulation as a function of frequency has made it possible to locate resonances not resolved in the NMR spectrum as well as obtain information on the rate of change of the hyperfine field in the domain wall. The presence of peaks in the NMR spectrum has been correlated with a slow variation of the hyperfine field and therefore a minimum in the depth of the modulation of the spin echo modulation. A correlation has also been made between the rate of change of the hyperfine field and the depth of the observed quadrupole modulation, therefore giving additional support to our interpretation of the experimental results.

Calculations designed to reproduce the general features of the results make it possible to complete the analysis of the domain wall spectrum by determining which of the edge and centre resonances to associate with a particular cobalt site.

Using these experimental techniques we have been able to determine the anisotropy in the hyperfine field at both Co sites of a series of RCo_5 compounds. A phenomenological model applied in particular to hexagonal Co and YCo_5 has been able to account for the basic features of the magnetocrystalline anisotropy, the anisotropy in the magnetization and the anisotropy in the hyperfine field. We predict a relationship between the magnetocrystalline anisotropy and the anisotropy in the hyperfine field, which involves contributions from two possible mechanisms: one involving an anistropy in the crystalline field and the other involving an anisotropy in the electronic spin-orbit interaction.

The theoretical problem of describing the magnetocrystalline anisotropy may be divided into two parts ; the nature of the intrinsic anisotropy that would be measured at absolute zero and the temperature dependence which in part involves a change in the intrinsic value of the anisotropy and in part is due to an increase in the angular deviations of the individual spins from their average direction as the temperature increases (2-5). At higher temperatures the individual spins sample the anisotropy over a larger angle and the average energy becomes more isotropic. We were, however, only concerned with the intrinsic anisotropy in this study.

It is generally agreed that a principal source of the

ferromagnetic anisotropy, particularly in transition metals, comes from the electronic spin orbit coupling; a proposal first made by Powell (6) and Bloch and Gentile (7). Two approaches have been used to calculate the effect of the spin orbit interaction in a ferromagnet; one approach, first taken by Van Vleck (8), represents an atomic model which has the advantage of providing a simple physical explanation of the cause of anisotropy. The other approach, first attempted by Brooks (9), uses an itinerant electron model.

Carr (10,11) suggested a different mechanism which arose from the interaction of the orbital moment and the resulting distortion in the charge distribution with the crystal field. The charge distribution is affected by the spin through the spin orbit coupling which induces an orbital momentum in the spin direction and consequently distorts the electronic distribution.

Our experimental results and the model that we have developed to account for these results reflect aspects of both these mechanisms. It therefore is likely that both mechanisms make important contributions to the magnetocrystalline anisotropy and the anisotropy in the hyperfine field (and the anisotropy in the magnetization for that matter) for hexagonal Co and the RCo_5 compounds and that both mechanisms will have to be considered in any detailed study of these materials. This appears to be the direction in which Yang (12,13) was headed when he derived an expression for the temperature dependence of the anisotropy constants of hexagonal Co and Gd in terms of both one-ion crystal-field interactions and the two-ion pseudo-dipolar and pseudo-quadrupolar interactions (8). Yang did not consider the intrinsic value of these interactions; rather

his calculation was concerned only with the temperature dependence introduced by thermal fluctuations in the directions of the electronic spins. The agreement Yang obtained with experimental data on the temperature dependence of the anisotropy constants is largely fortuitous, however, as his expressions contain a large number of adjustable parameters.

The use of NMR to study the microscopic origin of anisotropy is much more direct than the various attempts to simply fit the macroscopic anisotropy constants with a particular model and therefore must be considered to be much more reliable. Also the amount of information that would be obtained would far exceed that obtained from such macroscopic studies.

It is recognized that the work presented here is not a complete study of this problem. It does, however, identify a promising direction that could be taken in the experimental study of the microscopic properties of the RCo_5 compounds. The analysis techniques that would be required have been developed and presented. Further work would be dependent on the availability of additional data either through the improvements of the sensitivity of the apparatus or the increase in the strength of the detected signal.

Of particular interest would be the microscopic investigation of ternary series involving either a non-magnetic rare-earth such as La, Ce or Y and the substitution of Ni or Fe for Co or the substitution of a non-magnetic rare-earth for a magnetic rare-earth such as Sm. Such an investigation would allow the relative importance of the two Co sites to the magnetocrystalline anisotropy to be determined from the first

series, since Ni and Fe substitute with a known preference into the two Co sites. Also the influence of the rare-earth partner on the Co contribution could be investigated using the second series.

References

References for Chapter 1

1. G. W. Urbain, P. Weiss, and F. Trombe, Compt. Rend. 200, 2132 (1935).
2. E. A. Nesbitt, J. H. Wernick, and E. Corenzwit, J. Appl. Phys. 30, 365 (1959).
3. W. M. Hubbard, E. Adams, and J. U. Gilfrich, J. Appl. Phys. 31, 3685 (1960).
4. G. Hoffer and K. Strnat, IEEE Trans. Magnetics 2, 487 (1966).
5. A. H. Morrish, The Physical Principles of Magnetism, p.312, John Wiley & Sons,Inc., New York, (1965).
6. A. S. Ermolenko, IEEE Trans. Magnetics 12, 992 (1976).
7. D. L. Martin and M. G. Benz, IEEE Trans. Mag. 8, (1972).
8. E. A. Nesbitt, G. Y. Chin, G. W. Hull, R. C. Sherwood, M. L. Green, and J. H. Wernick, Proc. 1972 Conf. on Magnetism and Magnetic Materials, A.I.P. Conf. Proc. 10, (1973).

References for Chapter 2

1. M. A. Ruderman and C. Kittel, Phys. Rev. 96, 99 (1954).
2. T. Kasuya, Progr. Theor. Phys., Kyoto. 16, 45 (1956).
3. K. Yoshida, Phys. Rev. 106, 893 (1957).
4. P. G. de Gennes, J. Phys. Radium 23, 510 (1962).
5. D. Gignoux, D. Givord and A. Del Moral, Solid State Comm. 19a, 891 (1976).
6. H. J. Wallbaum, Z. Kristallogr. 103, 147 (1941).
7. H. Nowotny, Z. Metallk. 34, 22 (1942).
8. J. H. Wernick and S. Geller, Trans. Met. Soc. AIME 218, 866 (1960).
9. H. J. Williams, J. H. Wernick, E. A. Nesbitt and R. C. Sherwood, J. Phys. Soc. Jpn. 17 Suppl. B-I, 91 (1962).
10. K. H. Mader and W. E. Wallace, J. Chem. Phys. 49, 1521 (1968).
11. W. M. Swift and W. E. Wallace, J. Phys. Chem. Solids 29, 2053 (1968).
12. D. Mattis and W. E. Donath, Phys. Rev. 128, 1618 (1962).
13. K. Sekizawa and K. Yasukochi, J. Phys. Soc. Jpn. 21, 684 (1966).
14. W. M. Swift and W. E. Wallace, J. Solid State Chem. 3, 180 (1971).
15. V. Jaccarino, B. T. Matthias, M. Peter, H. Suhl and J. H. Wernick, Phys. Rev. Lett. 5, 251 (1960).
16. V. Jaccarino, J. Appl. Phys. 32, 1025 (1961).
17. R. G. Barnes, F. Borsa and D. Peterson, J. Appl. Phys. 36, 940 (1965).
18. V. U. S. Rao and R. Vijayaraghavan, Phys. Lett. 19, 168 (1966).
19. K. H. J. Buschow, J. F. Fast, A. M. Van Diepen and H. W. de Wijn, Phys. Stat. Solidi 24, 715 (1967).
20. R. E. Watson, S. Koida, M. Peter and A. J. Freeman, Phys. Rev.

139, A167 (1965).
21. G. T. Alfieri, E. Banks, and K. Kanematsu, J. Appl. Phys. 37, 1254 (1966).
22. J. Pierre, C. R. Acad. Sci. Paris 265B, 1169 (1967).
23. J. Pierre, Solid State Comm. 7, 165 (1969).
24. A. Oppelt, E. Dormann and K. H. J. Buschow, Phys. Stat. Solidi b51, 275 (1972).
25. A. Oppelt, E. Dormann and K. H. J. Buschow, Int. J. Magn. 3, 55 (1972).
26. K. Eckrich, E. Dormann, A. Oppelt, and K. H. J. Buschow, Z. Phys. B23, 157 (1976).
27. K. H. J. Buschow, A. Oppelt and E. Dormann, Phys. Stat. Solidi b50, 647 (1972).
28. K. H. J. Buschow and C. J. Schinkel, Solid St. Comm. 18, 609 (1976).
29. F. Dintelmann and K. H. J. Buschow, Z. Ang. Phys. 31, 181 (1971).
30. E. Dormann and K. H. J. Buschow, J. Appl. Phys. 47, 1662 (1976).
31. E. Dormann, L. Schaafhausen and K. H. J. Buschow, J. Mag. Magn. Mat. 2, 177 (1976).
32. Y. Berthier and R. A. B. Devine, J. Phys. F: Metal Phys. 8, L113 (1978).
33. E. Dormann, M. Huck and K. H. J. Buschow, J. Mag. Magn. Mat. 4, 47 (1977).
34. E. Dormann, M. Huck and K. H. J. Buschow, Z. Phys. B27, 141 (1977).
35. M. Peter, J. Appl. Phys. 32, 338 (1961).
36. A. C. Gossard, V. Jaccarino and J. H. Wernick, J. Phys. Soc. Jpn. 17 Suppl. B-I, 88 (1962).
37. W. E. Wallace, Prog. Rare Earth Sci. Tech. 3, 1 (1968).
38. M. B. Stearns, J. Appl. Phys. 36, 913 (1965).
39. A. M. van Diepen, H. W. de Wijn and K. H. J. Buschow, J. Chem. Phys. 46, 3489 (1967).
40. A. M. van Diepen, K. H. J. Buschow and H. W. de Wijn, J. Chem. Phys. 51, 5259 (1969).
41. R. Vijayaraghavan, S. K. Malik, U. U. S. Rao, Phys. Rev. Lett. 20, 106 (1968).
42. H. W. de Wijn, K. H. J. Buschow and A. M. van Diepen, Phys. Stat. Solidi 30, 759 (1968).
43. K. H. J. Buschow, A. M. van Diepen and H. W. de Wijn, J. Appl. Phys. 41, 4609 (1970).
44. V. Niculescu, I. Pop and M. Rosenberg, Phys. Stat. Solidi b53 701 (1972).
45. J. H. N. Creighton, P. R. Locher and K. H. J. Buschow, Phys. Rev. B7, 4829 (1973).
46. I. A. Campbell, J. Phys. F: Metal Phys. 2, L47 (1972).
47. I. Shidlovsky and W. E. Wallace, J. Solid State Chem. 2, 193 (1970).
48. W. Fulling, K. Moeller and R. Vogel, Z. Metallk. 34, 254 (1942).
49. E. W. Pugh, B. R. Coles, A. Arrott and J. E. Goldman, Phys. Rev. 105, 814 (1956).
50. J. S. Wollam and W. E. Wallace, J. Phys. Chem. Solids. 13, 212 (1960).

51. E. A. Skrabek and W. E. Wallace, J. Appl. Phys. 34, 1356 (1963).
52. J. Farrell and W. E. Wallace, Inorg. Chem. 5, 105 (1966).
53. J. W. Ross and J. Crangle, Phys. Rev. 133, A509 (1964).
54. W. E. Wallace, H. P. Hopkins, Jr. and K. Lehman, J. Solid State Chem. 1, 39 (1969).
55. E. A. Nesbitt, H. J. Williams, J. H. Wernick and R. C. Sherwood, J. Appl. Phys. 33, 1674 (1962).
56. R. Lemaire and D. Paccard, C. R. Acad. Sci. Paris. 270, 1131 (1970).
57. W. E. Wallace, T. V. Volkmann and H. P. Hopkins, Jr., J. Solid State Chem. 3, 510 (1971).
58. I. Nowik and J. H. Wernick, Phys. Rev. 140, A131 (1965).
59. W. E. Wallace and M. Aoyasi, Chem. Monatsh. 102, 1455 (1971).
60. J. Faforest, R. Lemaire, D. Paccard and R. Pauthenet, C. R. Acad. Sci. Paris 264, 676 (1967).
61. P. D. Carfagna and W. E. Wallace, J. Appl. Phys. 39, 5259 (1968).
62. E. A. Nesbitt, J. H. Wernick and E. Corenswit, J. Appl. Phys. 30, 365 (1959).
63. K. Nassau, L. V. Cherry and W. E. Wallace, J. Phys. Chem. Solids 16, 131 (1960).
64. W. E. Wallace, T. V. Volkmann and H. Hopkins Jr., J. Solid State Chem. 3, 510 (1971).
65. B. Bleaney, in Rare Earth Res., Proc. Rare Earth Conf. 3rd, Vol. 2, p.499, Gordon and Breach, New York, (1964).
66. R. Lemaire, Cobalt 32, 132 (1966).
67. R. Lemaire and J. Schweizer, J. Phys. 28, 216 (1967).
68. J. Schweizer, Phys. Lett. 24A, 739 (1967).
69. R. M. Moon, W. C. Koehler and J. Farrell, J. Appl. Phys. 36, 978 (1965).
70. K. Strnat, G. Hoffer, W. Ostertag and J. C. Olson, J. Appl. Phys. 37, 1252 (1966).
71. R. Lemaire, D. Paccard, R. Pauthenet and J. Schweizer, J. Appl. Phys. 39, 1092 (1968).
72. A. R. Piercy and K. N. R. Taylor, J. Appl. Phys. 39, 1096 (1968).
73. K. N. R. Taylor, Phys. Lett. A29, 372 (1969).
74. A. R. Piercy and K. N. R. Taylor, J. Phys. C., 1, 1112 (1968).
75. C. A. Poldy and K. N. R. Taylor, Rare Earth Conf. Dig.-Inst. Phys. (London) (1971).
76. K. H. J. Buschow, Phys. Stat. Solidi a7, 199 (1971).
77. E. Burzo, Solid State Comm. 14, 1295 (1974).
78. J. Friedel, G. Leman and S. Olszewski, J. Appl. Phys. 32, 325S (1961).
79. E. Burzo, D. P. Lazar and M. Ciorascu, Phys. Stat. Solidi b65, K 145 (1974).
80. V. Jaccarino and L. R. Walker, Phys. Rev. Lett. 15, 259 (1965).
81. A. Blandin and J. Friedel, J. Phys. Radium 20, 160 (1959).
82. M. Brouha and K. H. J. Buschow, J. Phys. F: Metal Phys. 5, 543 (1975).
83. M. Brouha and K. H. J. Buschow, J. Appl. Phys. 46, 1355 (1975).
84. K. H. J. Buschow, M. Brouha, J. W. M. Biesterbos and A. G. Dirks, Physica 91B, 261 (1977).

85. E. Burzo, Phys. Rev. B6, 2882 (1972).
86. J. A. Cannon, J. I. Budnick and T. J. Burch, Solid State Comm. 17, 1385 (1975).
87. K. H. J. Buschow and R. P. van Stapele, J. Physique 32-Suppl. C1, 672 (1971).
88. E. T. Miskinis, K. S. V. L. Narasimhan, W. E. Wallace and R. S. Craig, J. Solid State Chem. 13, 311 (1975).

Additional general references:

89. K. H. J. Buschow, Rep. Prog. Phys. 40, p.1179-1256, (1977).
90. K. H. J. Buschow, Rep. Prog. Phys. 42, p.1373-1477, (1979).
91. K. N. R. Taylor, Adv. Phys. 20, p.551-660, (1971).
92. W. E. Wallace, Rare Earth Intermetallics, Academic Press, New York, (1973).
93. R. E. Smallman, Modern Physical Metalurgy, p.120-180, Butterworths, London, (1970).
94. C. S. Barrett and T. B. Massalski, Structure of Metals, p.223-270, Pergamon Press, New York, (1980).
95. D. A. Porter and K. E. Easterling, Phase Transformations in Metals and Alloys, Van Nostrand Reinhold, New York, (1981).
96. Electronic Structure and Alloy Chemistry of the Transition Elements, edited by P. A. Beck, Interscience Publishers, New York, (1963).
97. U. R. Evans, Metals and Metallic Compounds-Vol. 1, p. 197-222, Edward Arnold and Co., London, (1923).

References for Chapter 3

1. I. I. Rabi, J. R. Zacharias, S. Millman and P. Kusch, Phys. Rev. 55, 526 (1939).
2. C. J. Gorter, Physica 3, 995 (1936).
3. F. Bloch, W. W. Hansen and M. E. Packard, Phys. Rev. 69, 127 (1946).
4. E. M. Purcell, H. C. Torrey and R. V. Pound, Phys. Rev. 69, 37 (1946).
5. N. Bloembergen, E. M. Purcell and R. V. Pound, Phys. Rev. 73, 679 (1948).
6. F. Bloch, Phys. Rev. 70, 460 (1946).
7. I. I. Rabi, N. F. Ramsay and J. Schwinger, Rev. of Modern Physics 26, 167 (1954).
8. H. C. Torrey, Phys. Rev. 76, 1059 (1949).
9. E. L. Hahn, Phys. Rev. 80, 580 (1950).
10. I. J. Lowe and R. E. Norberg, Phys. Rev. 107, 46 (1957).
11. H. Y. Carr and E. M. Purcell, Phys. Rev. 94, 630 (1954).
12. S. Meiboom and D. Gill, Rev. Sci. Instrum. 29, 688 (1958).
13. J. S. Waugh, L. M. Huber and U. Haeberlen, Phys. Rev. Lett. 20, 180 (1968).

References for Chapter 4

1. F. Bloch, W. W. Hansen and M. E. Packard, Phys. Rev. 69, 127 (1946).
2. E. M. Purcell, H. C. Torrey and R. V. Pound, Phys. Rev. 69, 37 (1946).
3. A. C. Gossard and A. M. Portis, Phys. Rev. Letters 3, 164 (1959).
4. R. G. Shulman, Phys. Rev. Letters 2, 459 (1959).
5. E. D. Jones, Phys. Rev. 151, 315 (1966).
6. R. G. Shulman and K. Knox, Phys. Rev. Letters 4, 603 (1960).
7. A. M. Portis and A. C. Gossard, J. of Appl. Phys. 31, 2055 (1960).
8. A. G. Redfield, Phys. Rev. 98, 1787 (1955).
9. C. Kittel and J. K. Galt, Solid State Physics Vol. 3, edited by Frederick Seitz and David Turnbull, Academic Press Inc., New York, 1956.
10. A. C. Gossard, A. M. Portis, M. Rubinstein and R. H. Lindquist, Phys. Rev. 138A, 1415 (1965).
11. W. Doring, Z. Nafurforsch 3A, 373 (1948).
12. A. Hirai, J. A. Eaton and C. W. Searle, Phys. Rev. B3, 68 (1971).
13. E. F. Mendis and L. W. Anderson, Phys. Stat. Solidi 41, 315 (1971).
14. A. M. Portis, Phys. Rev. 100, 1219 (1955).
15. M. A. Butler, Phys. Rev. B8, 5122 (1973).
16. T. Hihara and E. Hirahara, J. Phys. Soc. Jpn. 20, 873 (1965).
17. H. Nagai, T. Hihara and E. Hirahara, J. Phys. Soc. Jpn. 29, 622 (1970).
18. T. Hihara and Y. Koi, J. Phys. Soc. Jpn. 29, 342 (1970).
19. E. Koster and B. G. Turrell, Phys. Lett. A39, 211 (1972).
20. M. Kawakami, T. Hihara, Y. Koi and T. Wakiyama, J. Phys. Soc. Jpn. 33, 1591 (1972).
21. C. H. Cobb, V. Jaccarino, M. A. Butler, J. P. Remeika and H. Yasuoka, Phys. Rev. B7, 307 (1973).
22. Y. A. Turov, A. P. Tankeyev and M. A. Kurkin, Metal Metalloved 28, 385 (1969).
23. Y. A. Turov, A. P. Tankeyev and M. A. Kurkin, Metal Metalloved 29, 747 (1970).
24. J. M. Winter, Phys. Rev. 124, 452 (1961).
25. M. Weger, Phys. Rev. 128, 1505 (1962).
26. A. C. Gossard, V. Jaccarino and J. P. Remeika, J. Appl. Phys. 33, 1875 (1962).
27. A. C. Gossard, V. Jaccarino and J. P. Remeika, Phys. Rev. Lett. 7, 122 (1961).
28. C. H. Cobb and V. Jaccarino, J. Appl. Phys. 42, 1310 (1971).
29. D. L. Cowan and L. W. Anderson, Phys. Rev. 135, A1046 (1964).
30. E. F. Mendis and L. W. Anderson, Phys. Rev. B2, 569 (1970).
31. J. B. Forsyth, S. J. Pichart and P. J. Brown, Proc. Phys. Soc. 88, 333 (1966).
32. G. P. Felcher, J. Appl. Phys. 37, 1056 (1966).
33. G. B. Benedek and T. Kushida, Phys. Rev. 118, 46 (1960).
34. G. B. Benedek and J. Armstrong, Jour. of Appl. Physics 32 Suppl.,

106S (1961).
35. M. A. Butler, G. K. Wertheim and P. N. E. Buchanan, Phys. Rev. B5, 990 (1971).
36. H. Suhl, Bull. Am. Phys. Soc. 5, 175 (1960).
37. Y. Koi, A. Tsusimura, T. Hihara and T. Kushida, Proc. Int. Conf. Magnetism and Crystallography, Kyoto, 1961, J. Phys. Soc. Jpn. 17 Suppl. B-I, 96 (1962).
38. W. Sucksmith, F. R. S. and J. E. Thompson, Proc. Roy. Soc. A225, 362 (1954).
39. R. Pauthenet, Y. Barnier and G. Rimet, Proc. Int. Conf. Magnetism and Crystallography, Kyoto 1961, J. Phys. Soc. Jpn. 17 Suppl. B-I, 309 (1962).
40. E. F. Bertaut, A. Delapalme and R. Pauthenet, Solid State Comm. 1, 81 (1963).
41. G. J. Perlow, C. E. Johnson and W. Marshall, Phys. Rev. 140, A875 (1965).
42. R. M. Moon, Phys. Rev. 136, A195 (1964).
43. A. Abragam, J. Horowitz and M. H. L. Pryce, Proc. Roy. Soc. A230, 169 (1955).
44. J. P. Rebouillat, Intern. Conf. Magnetics, Kyoto (1972).
45. A. J. P. Meyer and G. Asch, J. Appl. Phys. 32, 330S (1961).
46. G. A. Murray and W. Marshall, Proc. Phys. Soc. 86, 315 (1965).
47. K. H. Stewart, Ferromagnetic Domains, Cambridge University Press, (1954).
48. M. A. Butler, Int. J. Magn. 4, 131 (1973).
49. H. Suhl, Phys. Rev. 109, 606 (1958).
50. T. Nakamura, Prog. Theoret. Phys. (Kyoto) 20, 542 (1958).
51. M. H. Cohen and F. Reif: Solid State Physics ed. F. Seitz and D. Turnbull (Academic Press, New York, 1957) Vol. 5, p. 321.
52. A. Abragam: The Principles of Nuclear Magnetism (Clarendon Press, Oxford, 1961) p. 232.

References for Chapter Five

1. W. G. Clark, Rev. Sci. Instr. 35, 316 (1964).
2. R. A. McKay and D. E. Woessner, J. Sci. Instr. 43, 838 (1966).
3. I. J. Lowe and C. E. Tarr, J. Sci. Instr. (J. Phys. E) Series 2 1, 320 (1968).
4. P. G. DeGennes, P. A. Pincus, F. Hartmann-Boutron and J. M. Winter, Phys. Rev. 129, 1105 (1963).
5. A. J. Heeger and T. W. Houston, Phys. Rev. 135, A661 (1964).
6. I. Solomon, Phys. Rev. 110, 61 (1958).
7. C. H. Cobb, V. Jaccarino, J. P. Remeika, R. Silberglitt and H. Yasuoka, Phys. Rev. B3, 1677 (1971).
8. H. Abe, H. Yasuoka, M. Matsuura, A. Hirai and T. Shinjo, J. Phys. Soc. Jpn. 19, 1491 (1964).
9. H. Abe, H. Yasuoka and A. Hirai, J. Phys. Soc. Jpn. 21, 77 (1966).
10. E. B. McNeil, C. P. Slichter and H. S. Gutowsky, Phys. Rev. 84,

1245 (1951).
11. E. L. Hahn and D. E. Maxwell, Phys. Rev. 84, 1246 (1951).
12. S. Kobayashi, K. Asayama and J. Itoh, J. Phys. Soc. Jpn. 21, 65 (1966).
13. K. N. R. Taylor and J. T. Christopher, J. Phys. C2 Ser. 2, 2237 (1969).
14. M. B. Stearns, Phys. Rev. B8, 4383 (1973).
15. M. B. Stearns, Phys. Rev. B9, 2311 (1974).
16. A. Heidemann, D. Richter and K. H. J. Buschow, Z. Phys. B22, 367 (1975).
17. H. Figiel, A. Oppelt, E. Dormann and K. H. J. Buschow, Phys. Stat. Solidi a36, 275 (1976).
18. H. Nagai, T. Hihara and E. Hirahara, J. Phys. Soc. Jpn. 622 (1970).
19. E. Koster and B. G. Turrell, Phys. Lett. A39, 211 (1972).
20. M. Kawakami, T. Hihara, Y. Koi and T. Wakiyama, J. Phys. Soc. Jpn. 33, 1591 (1972).
21. R. L. Streever, Phys. Lett. A65, 360 (1978).
22. F. Tasset, PhD thesis, as quoted from R. L. Streever, Phys. Rev. B19, 2704 (1979).
23. M. Dupont and G. A. Woonton, Can. J. Phys. 46, 87 (1968).
24. V. C. Srivastava, J. Appl. Phys. 39, 5837 (1968).
25. T. Kubo, A. Hirai and H. Abe, J. Phys. Soc. Jpn. 26, 1094 (1969).
26. J. H. Davis and C. W. Searle, Phys. Rev. B9, 323 (1974).
27. J. H. Davis and C. W. Searle, Phys. Rev. B14, 2126 (1976).
28. G. Hoffer and K. Strnat, IEEE Trans. Mag. 2, 487 (1966).
29. W. Sucksmith and J. E. Thompson, Proc. R. Soc. A225, 362 (1954).
30. C. W. Searle, H. P. Kunkel, S. Kupca and I. Maartense, Phys. Rev. B15, 3305 (1977).
31. C. H. Cobb, V. Jaccarino, M. A. Butler, J. P. Remeika and H. Yasouka, Phys. Rev. B7, 307 (1973).
32. H. P. Kunkel and C. W. Searle, Phys. Rev. B23, 65 (1981).
33. H. Enokiya, J. Phys. Soc. Jpn. 42, 796 (1977).
34. J. Kaczer, Sov. Phys. JETP 19, 1204 (1964).
35. M. W. Muller and A. Sher, Phys. Rev. Lett. 8, 85 (1962).
36. D. Fekete, H. Boasson, A. Grayevski, V. Zevin and N. Kaplan, Phys. Rev. B17, 347 (1978).
37. V. F. Taborov, JETP 26, 529 (1977).
38. J. D. Livingston and M. D. McConnell, J. Appl. Phys. 43, 4756 (1972).
39. W. G. D. Frederick, PhD thesis (University of Cincinnati, 1973).
40. J. M. Winter, Phys. Rev. 124, 452 (1961).
41. P. C. Riedi and R. G. Scurlock, Physics Letters 24A, 42 (1967).
42. L. K. Leung and A. H. Morrish, Phys. Rev. 815, 2485 (1977).
43. C. Froidevaux and M. Weger, Phys. Rev. Lett. 12, 123 (1964).
44. R. F. Jackson, R. G. Scurlock, D. B. Utton and T. H. Wilmshurst, Proc. Intl. Conf. on Magnetism. Nottingham 1964 (Institute of Physics and the Physical Society) p. 384.
45. A. H. Mitchell, J. Chem. Phys. 26, 1714 (1957).
46. T. Moriya, J. Phys. Soc. Jpn. 19, 681 (1964).

References for Chapter Six

1. W. B. Mims, K. Nassau and J. D. McGee, Phys. Rev. 123, 2059 (1961).
2. E. T. Jaynes, Phys. Rev. 98, 1099 (1955).
3. A. L. Bloom, Phys. Rev. 98, 1105 (1955).
4. V. C. Srivastava, J. Appl. Phys. 19, 5837 (1968).
5. R. L. Streever, Phys. Lett. A65, 360 (1978).
6. H. Yoshie, J. Phys. Soc. Jpn. 43, 862 (1977).
7. H. Yoshie, M. Matsushima, N. Miyagi, T. Unate, H. Nagai and A.Tsujimura, J. Phys. Soc. Jpn. 41, 41 (1976).
8. C. H. Cobb, V. Jaccarino, M. A. Butler and J. P. Remeika, Phys. Rev. 7, 307 (1973).
9. M. W. Muller and A. Sher, Phys. Rev. Lett. 8, 85 (1962).
10. H. Enokiya, J. Phys. Soc. Jpn. 42, 796 (1977).
11. D. Fekete, H. Boasson, A. Grayevski, V. Zevin and N. Kaplan, Phys. Rev. B17, 347 (1978).
12. H. Abe, H. Yasuoka and A. Hirai, J. Phys. Soc. Jpn. 21, 77 (1966).
13. M. H. Cohen and F. Reif, Solid State Physics-Vol.5, p.321 edited by F. Seitz and D. Turnbull, Academic Press, New York, (1957).
14. T. Hihara and T. Koi, J. Phys. Soc. Jpn. 29, 343 (1970).
15. M. Kawakami, T. Hihara, Y. Koi and T. Wakiyama, J. Phys. Soc. Jpn. 33, 1591 (1972).
16. V. Zevin, D. Fekete and N. Kaplan, Phys. Rev. B17, 355 (1978).
17. P. C. Riedi and R. G. Scurlock, Phys. Lett. 24A, 42 (1967).
18. C. Kittel and J. K. Galt, in Solid State Physics-Vol.3, edited by F. Seitz and C. Turnbull, Academic Press, New York, (1956).
19. J. D. Livingston and M. D. McConnell, J. Appl. Phys. 43, 4756 (1972).
20. R. L. Streever, Phys. Rev. B19, 2704 (1979).
21. N. Mori, T. Ukai and H. Yoshida, J. Phys. Soc. Jpn. 37, 1272 (1974).
22. J. Schweizer and F. Tasset, J. Phys. F 10, 2799 (1980).
23. R. M. Moon, Phys. Rev. 136, 195 (1964).
24. J. Deportes, D. Givord, J. Schweizer and F. Tasset, IEEE Transactions on Magnetics 12, 1000 (1976).
25. J. E. Greedan and V. U. S. Rao, J. Solid State Chem. 6, 1 (1972).
26. K. H. J. Buschow and A. M. van Diepen, Solid State Comm. 15, 903 (1974).
27. S. G. Sankar, V. U. S. Rao, E. Segal, W. E. Wallace, W. G. D. Frederick and H. J. Garrett, Phys. Rev. B11, 435 (1975).
28. A. S. Ermolenko, IEEE Trans. on Magnetics 12, 992 (1976).
29. H. P. Klein and A. Menth, Physica B80, 153 (1975).
30. J. M. Alameda, J. Deportes, D. Givord, R. Lemaire and Q. Lu, J. Magn. Mag. Mat. 15, 1257 (1980).
31. J. M. Alameda, D. Givord, R. Lemaire and Q. Lu, J. Appl. Phys. 52, 2079 (1981).
32. J. P. Rebouillat, Int. Conf. Magnetics, Kyoto, 1972.
33. S. Muller, P. Bunner and N. S. Pranghe, Z. Angew. Phys. 21, 403 (1967).
34. S. V. Vonsovskii, JETP 8, 1104 (1938).

35. K. H. J. Buschow, Rep. Prog. Phys. 40, p.1240, (1977).
36. M. B. Stearns, Phys. Rev. 162, 496 (1967).
37. M. B. Stearns, Phys. Rev. 187, 648 (1969).
38. K. Inomata, Jpn. J. Appl. Phys. 15, 821 (1976).

References for Chapter 7

1. A. C. Gossard and A. M. Portis, Phys. Rev. Lett. 3, 164 (1959).
2. N. S. Akulov, Z. Physik 100, 197 (1936).
3. C. Zener, Phys. Rev. 96, 1335 (1954).
4. F. Keffer, Phys. Rev. 100, 1692 (1955).
5. H. B. Callen and E. J. Callen, J. Phys. Chem. Solids 27, 1271 (1966).
6. F. C. Powell, Proc. Roy. Soc. (London) A130, 167 (1930).
7. F. Bloch and G. Gentile, Z. Physik 70, 395 (1931).
8. J. H. Van Vleck, Phys. Rev. 52, 1178 (1937).
9. H. Brooks, Phys. Rev. 58, 909 (1940).
10. W. J. Carr, Phys. Rev. 108, 1158 (1957).
11. W. J. Carr, Phys. Rev. 109, 1971 (1958).
12. T. T. Yang, J. J. Yang and L. B. Robinson, Solid State Comm. 13, 53 (1973).
13. T. T. Yang, Jpn. J. Appl. Phys. 15, 279 (1976).